

Choosing the Optimal Production Strategy by Multi-Objective Optimization Methods

Ján Čabala, Ján Jadlovský

jan.cabala@tuke.sk, jan.jadlovsky@tuke.sk

Faculty of Electrical Engineering and Informatics, Technical University of Košice,
Letná 9, 04001 Košice, Slovakia

Abstract: This paper presents the solution of multi-objective optimization of the production process of an automated assembly line model, where combination of conventional mathematical methods and methods of artificial intelligence is used. Paper provides the description of methods used in this process, modifications that were realized in the computational process of NSGA - II evolutionary algorithm as well as the solution of the production process optimization respecting all the defined constraints. The first part of the solution, the definition of the set of non-dominated (Pareto optimal) alternatives, is realized by the modified NSGA – II evolutionary algorithm. From the Pareto optimal solutions, choosing the best solution using various mathematical metrics is presented. Approach for the synthesis of the results obtained from various mathematical metrics used to resolve the task is also mentioned with the scope of objectivization of the optimization process.

Keywords: assembly systems; genetic algorithms; optimization methods; mathematical programming; Pareto optimization

1 Introduction

The optimization process is usually used for choosing the best possible solution of a particular task. To ensure that this solution can be found in a qualified manner, it is necessary to create a mathematical model as accurately as possible in order to describe the optimization task properly. The model itself includes quantifiable parameters (objective functions) for measuring the rate of success of optimized criteria (e.g. profit). The model may also contain constraints (e.g. maximum amount of invested capital). Modelling is followed by finding a solution for a given optimization task using a suitably chosen algorithm. It is also necessary to verify and evaluate the obtained solution (whether it is a valid solution to the resolved task) and to interpret the result correctly.

Methods of mathematical programming are used to solve optimization tasks with one objective function. Depending on the type of objective function, these methods can be divided into linear or non-linear programming methods, integer programming methods, parameter programming methods, stochastic programming methods, etc. The overview of optimization algorithms for solving various optimization tasks can be found in [24].

In the process of optimization of production lines, one of the main requirements is the definition of optimization goals, what may include the minimizing number of workstations (posts), minimizing the time of production cycle, maximizing production line efficiency, cost minimization, maximizing profit, maximizing or minimizing the various factors affecting operations performed at a weak spots of the production line. Each of these objectives should be defined by an objective function, which values should be minimized or maximized (depending on the goal of the optimization process). [3]

In most cases, there is more than one objective, which should be optimized to satisfy the needs of the decision-maker. There are two basic types of methods used for resolving multi-objective optimization (MOO) tasks:

- Conventional methods – these are represented by mathematical metrics for choosing the best solution within the defined portfolio of alternative solutions
- Methods of artificial intelligence (AI) - represented by a number of algorithms VEGA (Vector Evaluated Genetic Algorithms) group, mostly used for defining the set of non-dominated solutions.

For defining the Pareto optimal set of solutions, conventional approaches aggregate the objective functions into a simple parametrized objective function. Several runs with different parameters of this objective function are realized in order to approximate the Pareto front. [31]

Except for conventional methods, artificial intelligence methods (especially evolutionary and genetic algorithms) are also used to solve the problems of MOO. Evolutionary algorithms represent the approach for finding the best solutions with trying a relatively small number of possible solutions, as the scope of possible solutions is very extensive in many cases. Some evolutionary algorithms from this group can cope with various forms of objective functions and resolve tasks with complicated Pareto sets (MOEA/D or NSGA-II) [18]. This complexity was one of the reasons for choosing the NSGA-II algorithm for finding the Pareto optimal solutions. The evolutionary algorithm is based on the population of individuals. This population usually contains more individuals, often hundreds or even thousands. The first population is typically generated randomly. This population is then reproduced and the best individuals are kept in the evolutionary process, while the worst are excluded. [5]

For solving multi-objective optimization problems, VEGA (Vector Evaluated Genetic Algorithms) are used. Closer description of this group of algorithms can

be found in [5] and [1]. The motivation for choosing the combination of conventional and AI methods to solve the MOO problem of the production process on assembly line model placed within Center of Modern Control Techniques and Industrial Informatics (CMCT&II) within DCAI FEEI TUKE arose seeing the wide application potential of these methods. In system reliability, redundancy allocation problem was resolved using the NSGA algorithm in [28]. In assembly line balancing, the use of multi-objective genetic algorithm (MOGA) is presented in [19], ant colony algorithms are described and applied in [2] and [25], tabu search algorithm is mentioned in [17]. Genetic algorithms can be also be used for solving assembly sequence planning, which is shown in [11]. Other application possibilities are mentioned in [14]. Other possibilities of using AI methods for optimization is described in [29], while the novel AI optimization approaches and algorithms are presented in [23], [27], [22].

The goal of the MOO process described in the paper is definition of the number of different types of products, satisfying the goals (maximizing profit and maximizing the amount of saved time) and respecting the constraints (limited supplies, limited storage capacity) of the optimization process. Combination of 2 different approaches used for solving the MOO task, as well as synthesis of partial results obtained by using different conventional methods is considered as a novel approach in the field assembly line optimization.

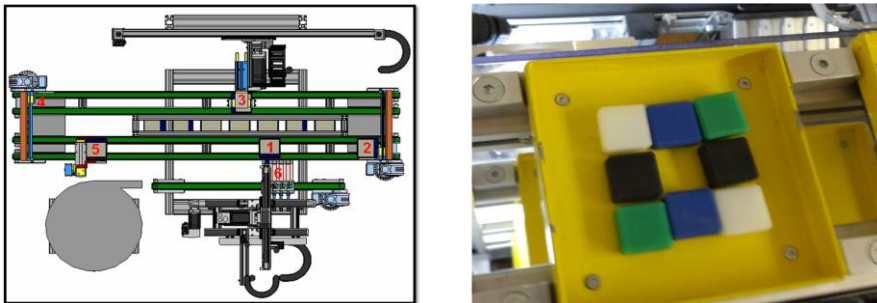


Figure 1

Schematic view on the assembly line model and the final product

In the first phase of the multi-objective optimization, artificial intelligence methods were used, namely the modified NSGA-II evolutionary algorithm for specifying the Pareto front of this multi-objective optimization task. It is also possible to use conventional methods to identify the Pareto front, but especially in the complex types of objective functions, it is easier to use evolutionary algorithms. In the second phase, from the Pareto front solutions, the optimal solution to the MOO task is chosen using conventional methods. Since there are many optimal solution selection methods, synthesis of solutions obtained by various methods was realized and the optimal solution for this task was chosen.

Within the paper, methods used for solving MOO tasks are presented in the second chapter, where 2 main approaches are described: conventional mathematical approach and artificial intelligence approach. Using the combination of these approaches for solving the optimal production process of assembly line model is presented in the Chapter 3.

2 Multi-Objective Optimization Task and Methods

The optimization task generally has the form of minimizing (maximizing) an objective function

$$f = \{x_1, x_2, \dots, x_n\} \quad (1)$$

while taking into account the restrictive conditions (constraints)

$$g_i = \{x_1, x_2, \dots, x_n\}, \text{ for } i = 1, 2, \dots, n \quad (2)$$

The multi-objective optimization (MOO) task is defined by the mathematical description of optimized system. This system is characterized by the functional $J(\mathbf{x}) = (J_1(\mathbf{x}), J_2(\mathbf{x}), \dots, J_k(\mathbf{x}))$, where $\mathbf{x} = (x_1, x_2, \dots, x_n)$ is the vector of variables used to define the mathematical model of the system. Solution of the MOO task is $\mathbf{x}^* \in \{X\}$, which is the optimal solution of the functionals $J_1(\mathbf{x}), J_2(\mathbf{x}), \dots, J_k(\mathbf{x})$.

2.1 Conventional Methods

Conventional methods of MOO are closely described in [16]. Solving the MOO task using the conventional methods applied on the economical investments is part of [7].

2.1.1 Methods Defining the Set of Non-Improving Points

In this group of methods there is no hierarchy of objectives. MOO task can be defined as minimization of vector $J(\mathbf{x}) - J(\mathbf{x}_\alpha)$, where \mathbf{x}_α is the optimal solution of α^{th} objective of MOO task.

Quadratic Metric

The most common decision parameter using this metric is minimum of the squared difference between values of objective functions for solution \mathbf{x} and values of objective functions for ideal solution \mathbf{x}_α .

$$R(x) = \sum_{\alpha=1}^k (J_\alpha(\mathbf{x}) - J_\alpha(\mathbf{x}_\alpha))^2 \quad \alpha = 1, 2, \dots, k \quad (3)$$

$$\text{opt } R(x) = \min_{x \in \{X\}} \sum_{\alpha=1}^k (J_{\alpha}(x) - J_{\alpha}(x_{\alpha}))^2 \quad (4)$$

Frequently, the deciding parameter of this metric is furtherly divided by values of optimal solution, in order to get a result in dimensionless form. The formula for this metric is defined as:

$$R(x) = \sum_{\alpha=1}^k \frac{(J_{\alpha}(x) - J_{\alpha}(x_{\alpha}))^2}{J_{\alpha}(x_{\alpha})^2} \quad (5)$$

$$\text{opt } R(x) = \min_{x \in \{X\}} \sum_{\alpha=1}^k \frac{(J_{\alpha}(x) - J_{\alpha}(x_{\alpha}))^2}{J_{\alpha}(x_{\alpha})^2} \quad (6)$$

Linear Metric

This metric is defined as the sum of variations between the values of objective functions for every solution and optimal values of particular objective functions. Optimal value $R(x)$ is counted as:

$$R(x) = \left| \sum_{\alpha=1}^k (J_{\alpha}(x) - J_{\alpha}(x_{\alpha})) \right| \quad (7)$$

$$\text{opt } R(x) = \min_{x \in \{X\}} \left(\sum_{\alpha=1}^k (J_{\alpha}(x) - J_{\alpha}(x_{\alpha})) \right) \quad (8)$$

Generalized Metric

The formula for finding the optimal value $R_L(x)$ is given as

$$R_L(x) = \sum_{\alpha=1}^k \left\{ (J_{\alpha}(x) - J_{\alpha}(x_{\alpha}))^L \right\}^{\frac{1}{L}} \quad (9)$$

2.1.2 Compromising Methods

This group of metrics is based on adding the weights of optimized objectives into the optimization process. The search for the optimal solution of the MOO task is realized by minimizing the function

$$\beta_1 J_1(x) + \beta_2 J_2(x) + \dots + \beta_k J_k(x) \quad (10)$$

where β_1, \dots, β_k are weight coefficients. It is recommended to set their values to $\beta_1 = 1/J_{10}, \beta_2 = 1/J_{20}, \dots, \beta_k = 1/J_{k0}$, where J_{k0} are values reached by optimization of k^{th} criterion. These metrics are used, if the decision maker is able to define the importance of optimized criteria before the start of optimization process. Weights of particular optimized criterion will be labelled as λ . [16]

Weighted Sum of Values of Objective Functions

The metric is defined as

$$\text{opt } R(x) = \text{opt} \sum_{\alpha=1}^k \lambda_{\alpha} J_{\alpha}(x) \quad (11)$$

Optimal solution is represented as the maximum or minimum of the weighted sum of values of all objective functions.

Weighted Sum of Deviations

Using this metric, the formula for calculating the $R(x)$ parameter is defined as:

$$R(x) = \sum_{\alpha=1}^k \lambda_{\alpha} * (J_{\alpha}(x) - J_{\alpha}(x_{\alpha})) \quad (12)$$

while the optimal solution is the minimum of the $R(x)$:

$$\text{opt } R(x) = \min_{x \in \{X\}} \left(\sum_{\alpha=1}^k \lambda_{\alpha} * (J_{\alpha}(x) - J_{\alpha}(x_{\alpha})) \right) \quad (13)$$

Some other mathematical metrics with their description and usage can be found in [7] and [30].

2.2 Methods of Artificial Intelligence

When solving multi-objective optimization problems, an evaluation function is used which returns a real number representing the suitability of the solution. The higher the value, the better the solution. This function corresponds to the objective function of mathematical methods. This function can represent a number of criteria, which are frequently in conflict. In this case, the goal is to find the Pareto-optimal front, which consists of a set of non-dominated solutions.

Basic evolutionary algorithm process is shown in Fig. 2.

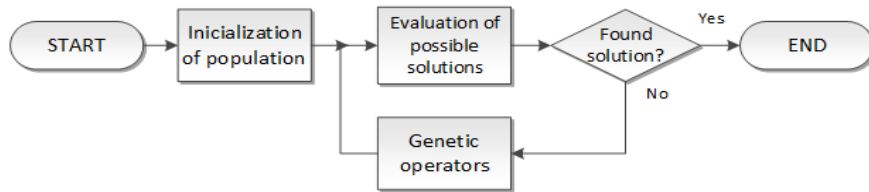


Figure 2

Fundamental evolutionary algorithm scheme

In this part of paper, NSGA-II algorithm is presented as algorithm chosen for defining the set of non-dominated solutions. This genetic algorithm was developed as an improved version of the NSGA genetic algorithm. The algorithm, compared

to its ancestor, is characterized by lower computational demands, better convergence and diversity. These improvements are reached by non-dominant sorting, elitism and crowding distance operations. [30]

2.2.1 Non-dominated Sorting

Non-dominated sorting is an operation sorting the chromosomes from the population into non-dominant fronts. The non-dominant front is a set of chromosomes that do not dominate each other. The dominance of the chromosome x above the chromosome y occurs when the value of all evaluation functions for the chromosome x is better than for the chromosome y . In the original NSGA algorithm, the sorting method was implemented in a way that all possible pairs of chromosomes were compared and the first non-dominant queue was found. These chromosomes were excluded from the population and the whole process was repeated without them. However, this method is computationally demanding. In the NSGA-II algorithm, queuing is accomplished by fast, non-dominant sorting - FNDS (closer description of the iterational process of FNDS can be found in [30]). Result of the process of FNDS is shown on Fig. 3.

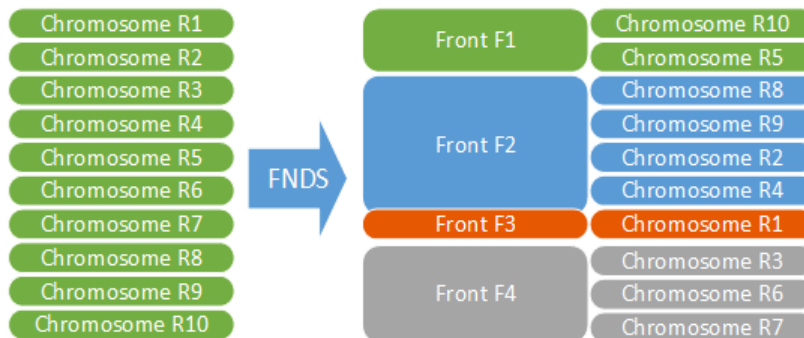


Figure 3

Diagram showing the results of fast non-dominated sorting

2.2.2 Crowding Distance

In the NSGA-II algorithm, the crowding distance is used to compare the chromosomes within one front. Crowding distance sorts the chromosomes according to their diversity (the chromosome most different from the others is considered the best). Procedure for implementing this part of the algorithm:

For each queue with the number of individuals n , individuals of every front are sorted according to the value of the m^{th} objective function

$$I = \text{sort}(F_i, m) \quad (14)$$

An infinite distance is assigned to the boundary chromosomes (first and last chromosome according to the sorting):

$$I(d_1) = \infty; I(d_n) = \infty \tag{15}$$

For other individuals ($k = 2, 3, \dots, n-1$) the following formula is used:

$$I(d_k) = I(d_k) + \frac{I(k+1)m - I(k-1)m}{f_m^{max} - f_m^{min}} \tag{16}$$

, where $I(k)m$ is the value of the m^{th} objective function of the individuals in sorting I. The metric by which chromosomes are organized, is defined as the sum of the chromosome's distances from the next chromosomes within the queue. Crowding distance is used in selecting chromosomes into a new generation, preferring chromosomes with the highest value of crowding distance. Results of applying the crowding distance are shown in Fig. 4.

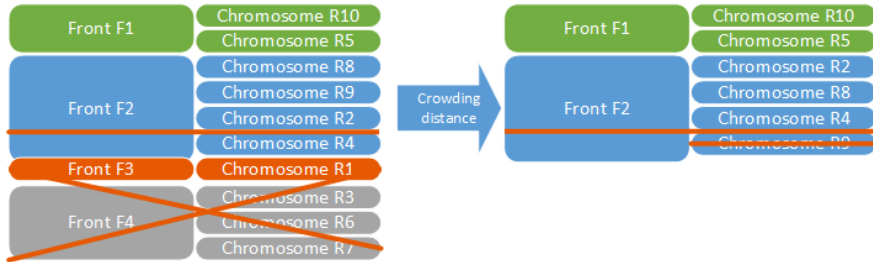


Figure 4

Diagram showing the results of rowding distance

2.2.3 Elitism

The principle of elitism keeps the chromosomes with the best results in the iteration process. The new generation is created by operations of crossing and mutation. Formulas used within the process of crossing and mutation are closely described in [6] and [26].

2.2.4 Iterative Process

The iterative process of the NSGA-II genetic algorithm can be described in the following steps:

1. Half of the population from the first iteration is generated with random genes, the other half is generated from the first iteration using crossing and mutation.
2. Chromosomes from the new population are sorted into non-dominant fronts by fast non-dominated sorting.

3. For the next iteration, half of the chromosomes with the best results are selected.
4. The second half of the population for the next iteration is generated in crossover and mutation operations.

The population is then again ranked and sorted etc. [12]

2.2.5 Modifications Realized in NSGA-II Algorithm

Fig. 5 shows the computational process of the modified NSGA-II algorithm (blue blocks represent the modified parts in comparison to the original NSGA-II computational process).

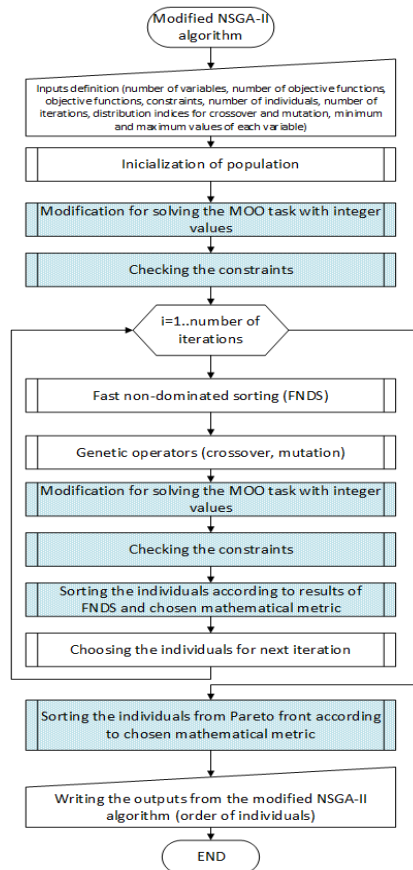


Figure 5
Algorithm of modified NSGA-II

For the proper functionality of the algorithm, several modifications were made to the computational process described in [13]. Modifications were made in order to modify the computational process of the NSGA-II algorithm for requirements of the resolved task:

- the algorithm considers the values of selected mathematical method as a secondary sorting criterion, instead of original criterion – crowding distance;
- it is necessary for the algorithm to work with integer values, since we are looking for number of products;
- the algorithm must be able to control the fulfillment of all defined constraints.

3 Solving MOO Problem of Assembly Line

This part of the paper is focused on solving the task of defining the optimal production process of one of the assembly line models at the Department of Cybernetics and Artificial Intelligence (DCAI) FEEI TUKE. Schematic view of the assembly line model is shown in Fig. 1.

3.1 Definition of MOO Task

The production line from Fig. 1 (closer description in [8]), is going to produce 4 different product types (mosaic) made from 4 different types of colored squared pieces: blue, white, green and black (Fig. 1).

The number of individual types of square pieces needed to manufacture the product is shown in Table 1, as well as the capacity of particular parts for one production cycle of this production line.

Table 1
Number of square pieces needed for manufacturing the products and their capacity

Part/Product	A	B	C	D	Capacity
Blue	5	7	7	3	100
White	3	4	2	4	80
Green	4	6	3	2	90
Black	5	5	6	6	120

The profit obtained from each blue part contained in the mosaic is € 3, of a white cube it is € 5, profit of using every green part is a € 4 and profit from every black part is € 2. Production time also depends on the number of parts included in the mosaic (placing one part of the product lasts 1,6 seconds). In a single production cycle, a maximum of 24 products can be produced, because only 24 products can

be stored simultaneously. The purpose of this MOO task is to define the number of products manufactured during the production process, in order to fulfill all constraints and to maximize both of the objective functions (profit from the production process as well as the saved time during the production process).

3.2 Definition of Objective Functions

As mentioned in the MOO task, the goal is to maximize profit as well as to maximize time savings. For the purpose of calculating the profit function, it is necessary to calculate the profit for each product (formula (17)).

$$\sum_{j=1}^{pv} z_i p k_{ij}, \text{ for } i = 1, 2, 3, 4. \quad (17)$$

where z_i is the profit from i^{th} part, $p k_{ij}$ is the number of parts of i^{th} type in j^{th} product and pv is the number of products. Using this formula, the profit from each type of product is obtained:

Table 2
Profit from manufacturing products

Product	A	B	C	D
Profit	56 €	75 €	55 €	49 €

From these values we can then define the objective function to maximize profit as

$$U_1(\mathbf{x}) = 56x_1 + 75x_2 + 55x_3 + 49x_4 \rightarrow \max \quad (18)$$

For the second objective function, we need to know the value of the time that is saved by producing this product, compared to producing the product with the maximum number of parts. It is not possible to define this objective function as a minimization of production time, since the ideal value would be 0 (doing nothing), which would affect the results in an undesirable manner. Since the templates for mosaic production have a size of 5 rows with 5 columns, one product can contain a maximum of 25 parts

$$\sum_{j=1}^{pv} p k_{ij}, \text{ for } i = 1, 2, 3, 4. \quad (19)$$

In (30), $p k_{ij}$ the number of parts of the i^{th} type in the j^{th} product and pv is the number of products, we calculate the total number of parts used for each type of product. These values are listed in Table 3.

Table 3
Number of parts used in manufacturing products

Product	A	B	C	D
Parts	17	22	18	15

The time savings obtained from the production of the product (co_j) when compared to the product consisting of the maximum number of parts (25) can be defined by formula (20). The obtained values are written in Table 4:

$$co_j = 1,6 (25 - pk_j) \quad (20)$$

Table 4
Amount of saved time by manufacturing products

Product	A	B	C	D
Saved time	12,8 s	4,8 s	11,2 s	16 s

Based on these values, we can define a second objective function as:

$$U_2(\mathbf{x}) = 12,8x_1 + 4,8x_2 + 11,2x_3 + 16x_4 \rightarrow \max \quad (21)$$

3.3 Definition of Constraints

To define the constraints, we start from the Table 1, which lists the number of parts needed to produce each type of product, as well their capacity. Based on this table, we can define the following constraints for this task:

$$5x_1 + 7x_2 + 7x_3 + 3x_4 \leq 100 \quad (22)$$

$$3x_1 + 4x_2 + 2x_3 + 4x_4 \leq 80 \quad (23)$$

$$4x_1 + 6x_2 + 3x_3 + 2x_4 \leq 90 \quad (24)$$

$$5x_1 + 5x_2 + 6x_3 + 6x_4 \leq 120 \quad (25)$$

Since the task is focused on one production cycle of the production line and the number of storage spaces is limited to 24, the number of products produced must not exceed this value:

$$x_1 + x_2 + x_3 + x_4 \leq 24 \quad (26)$$

The last constraint results from the logical assumption that the number of each of produced products can not be negative:

$$x_1, x_2, x_3, x_4 \geq 0 \quad (27)$$

3.4 Definition of Parameters for Iteration Process

To identify the Pareto front, we chose the NSGA-II algorithm, which was modified in order to deal with this MOO task. After defining of the Pareto front, the results will be sorted according to some of the mathematical methods in order to find the solution of the MOO task. Different mathematical metrics were used to

resolve the task and compare results, namely quadratic metric in a dimensionless form (metric 1), quadratic metric (metric 2 – chapter 2.1.1), weighted quadratic metric ($w=[0.8;0.2]$) (metric 3 – chapter 2.1.2), weighted linear metric ($w=[0.2;0.8]$) (metric 4 - chapter 2.1.2), linear metric (metric 5 - chapter 2.1.1) and percentual fulfillment of each objective function (metric 6 – chapter 3.5.2).

The NSGA - II algorithm was configured to process 2 objective functions with 4 variables, every population consisted of 200 individuals. 50 iterations were run with the crossing and mutation distribution parameter equaling 0. Vector of minimum parameter values was defined as $[0,0,0,0]$ (minimum number of products) and vector of maximum parameter values was set as $[24,24,24,24]$ (maximum number of products from each type).

3.5 Solving the MOO Task

3.5.1 Searching the Pareto Front Solutions

After the computational process of the modified NSGA – II algorithm was implemented in MATLAB, all possible MOO solutions were found, sorted according to their membership to front. To find the solution, the first (Pareto) front is important. The Pareto front contains non-dominated solutions (solutions that are not inferior in both objective functions than any other solution). Therefore, we will choose the solutions from the Pareto front (Table 6). On the Fig. 6 ,objective values are negative because the algorithms was built to minimize the objective functions. This is why the functions were multiplied by -1. Pareto front members are shown by red dots, chromosomes from the second front are represented as green dots, third front has blue dots and other fronts are displayed by black dots.

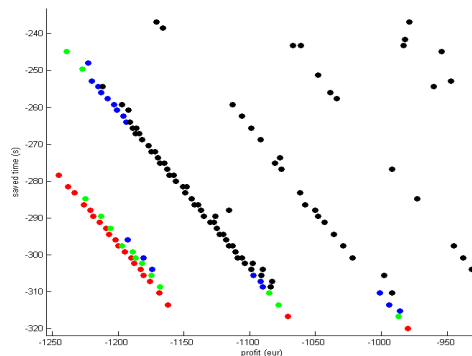


Figure 6

Graph showing the individuals from different non-dominant fronts

3.5.2 Application of Mathematical Metrics

Out of the individuals belonging to the Pareto front (listed in Table 6), we looked for the best possible solution of the MOO task. The solution using the percentual fulfillment of every objective function is shown closely. To calculate the percentual fulfillment of every objective function, we needed to know the maximum value of each of the objective functions. Values were calculated in the iterative process of the modified NSGA-II algorithm.

Table 5
Extreme values of objective functions

extr $U_1(x)$	extr $U_2(x)$
-1245	-320

For each individual from the Pareto front, the value of the percentual deviation was calculated from the ideal values and was realized using the formula

$$\delta U_i(\mathbf{x}) = \frac{\left| \min U_i(\mathbf{x}) - |U_i(\mathbf{x})| \right|}{\left| \min U_i(\mathbf{x}) \right|} \quad (28)$$

The sum of these deviations was then calculated according to (p is the number of objective functions):

$$\sum \delta U_i(\mathbf{x}) = \sum_{i=1}^p \frac{\left| \min U_i(\mathbf{x}) - |U_i(\mathbf{x})| \right|}{\left| \min U_i(\mathbf{x}) \right|} \quad (29)$$

The individual belonging to the Pareto front with the lowest value of the parameter $\sum \delta U_i(\mathbf{x})$ was chosen as the solution of the MOO task. In Table 6, Pareto front members are listed according to the parameter $\sum \delta U_i(\mathbf{x})$.

3.5.3 Interpretation of Results

The solution of the presented MOO task is represented by vector $\mathbf{x} = [12,0,0,10]$. This means that, according to the percentual fulfillment of each of the objective functions, the production line would have to produce 12 products of type A and 10 products of type D. The profit from one production cycle would be € 1162 and a time saved compared to the production of products with 25 parts would be 313,6 seconds. The deviation from the extreme values represents 6.67% from the maximum profit amount and 2% of the maximum saved time. Therefore, the deviation from the maximum values of the objective functions is 8.67%.

Table 6 shows that vector $[12,0,0,10]$ has the lowest value of deciding parameter. Therefore, it represents an optimal solution according to the chosen metric.

Table 6
Pareto optimal solutions ordered by percental fulfillment of objective functions

x ₁	x ₂	x ₃	x ₄	U ₁ (x)	U ₂ (x)	δU ₁ (x)	δU ₂ (x)	∑δU _i (x)
12	0	0	10	1162	313,6	0,066667	0,02	0,086667
13	0	0	9	1169	310,4	0,061044	0,03	0,091044
14	0	0	8	1176	307,2	0,055422	0,04	0,095422
11	1	0	10	1181	305,6	0,051406	0,045	0,096406
15	0	0	7	1183	304	0,049799	0,05	0,099799
12	1	0	9	1188	302,4	0,045783	0,055	0,100783
16	0	0	6	1190	300,8	0,044177	0,06	0,104177
13	1	0	8	1195	299,2	0,040161	0,065	0,105161
10	2	0	10	1200	297,6	0,036145	0,07	0,106145
14	1	0	7	1202	296	0,034538	0,075	0,109538
11	2	0	9	1207	294,4	0,030522	0,08	0,110522
15	1	0	6	1209	292,8	0,028916	0,085	0,113916
12	2	0	8	1214	291,2	0,0249	0,09	0,1149
9	3	0	10	1219	289,6	0,020884	0,095	0,115884
13	2	0	7	1221	288	0,019277	0,1	0,119277
10	3	0	9	1226	286,4	0,015261	0,105	0,120261
11	3	0	8	1233	283,2	0,009639	0,115	0,124639
8	4	0	10	1238	281,6	0,005622	0,12	0,125622
9	4	0	9	1245	278,4	0	0,13	0,13
6	0	0	15	1071	316,8	0,139759	0,01	0,149759
0	0	0	20	980	320	0,212851	0	0,212851

3.5.4 Synthesis of Results Obtained by Using other Mathematical Metrics

In Table 7 it can be seen that the choice of the best alternative depends on the chosen metric. Only the best solution for a particular MOO metric is displayed (M stands for metric and numbers corresponds with metrics mentioned in 3.4). It can be seen that the choice of the best alternative depends on the chosen metric.

Table 7
Best solutions using various mathematical metrics

M	x ₁	x ₂	x ₃	x ₄	U ₁ (x)	U ₂ (x)	δU ₁ (x)	δU ₂ (x)	∑δU _i (x)
1	13	0	0	9	1169	310,4	0,0037	0,0009	0,0046
2	13	2	0	7	1221	288	576	1024	1600
3	11	2	0	9	1207	294,4	0,0007	0,0012	0,0019
4	12	0	0	10	1162	313,6	16,6	5,12	21,72
5	9	4	0	9	1245	278,4	0	41,6	41,6
6	12	0	0	10	1162	313,6	0,066667	0,02	0,086667

One way to realize the synthesis of the results of different MOO metrics is to sort out the alternatives according to their standings in the optimization process

realized by every one of the metrics (the best alternative for each of the metrics obtains 1 point, the worst obtains pv points) and realize the subsequent synthesis of this score by formula

$$pb_i = \sum_{j=1}^{pn} b_{ij}, \text{ for } i = 1, 2, \dots, pv \quad (30)$$

where pb_i is the result of alternative I , b_{ij} is the score of alternative I using the j^{th} metric, pn is the number of metrics and pv is the number of alternatives. The results of Pareto front solutions according to this synthesis of results is in Table 8:

Table 8
Synthesis of solutions using various mathematical metrics

i	x ₁	x ₂	x ₃	x ₄	b _{i1}	b _{i2}	b _{i3}	b _{i4}	b _{i5}	b _{i6}	pb _i
1	10	2	0	10	9	11	1	9	11	9	50
2	11	2	0	9	11	9	2	11	9	11	53
3	14	1	0	7	10	10	3	10	10	10	53
4	13	1	0	8	8	12	6	8	12	8	54
5	16	0	0	6	7	13	8	7	13	7	55
6	12	1	0	9	6	14	9	6	14	6	55
7	11	1	0	10	2	16	13	4	16	4	55
8	15	1	0	6	12	8	4	12	8	12	56
9	15	0	0	7	5	15	12	5	15	5	57
10	12	2	0	8	13	7	5	13	7	13	58
11	14	0	0	8	3	17	15	3	17	3	58
12	13	0	0	9	1	18	17	2	18	2	58
13	9	3	0	10	14	5	7	14	6	14	60
14	12	0	0	10	4	19	19	1	19	1	63
15	10	3	0	9	16	1	11	16	4	16	64
16	13	2	0	7	15	4	10	15	5	15	64
17	11	3	0	8	17	2	14	17	3	17	70
18	8	4	0	10	18	3	16	18	2	18	75
19	9	4	0	9	19	6	18	19	1	19	82
20	6	0	0	15	20	20	20	20	20	20	120
21	0	0	0	20	21	21	21	21	21	21	126

As can be seen in the Table 8 and Fig. 7, according to synthesis of the results, the option $\mathbf{x}=[10,2,0,10]$ seems to be the best solution, followed by vectors $\mathbf{x}=[11,2,0,9]$ and $\mathbf{x}=[14,1,0,7]$. Winning solution from the percentual fulfillment of the objective functions (metric 6), $\mathbf{x}=[12,0,0,10]$ is only the 14th best option according to the synthesis of metrics. This fact can be considered as the proof that using more than one MOO method can result in defining solution, which is more complex when compared to the solution found using only one method.

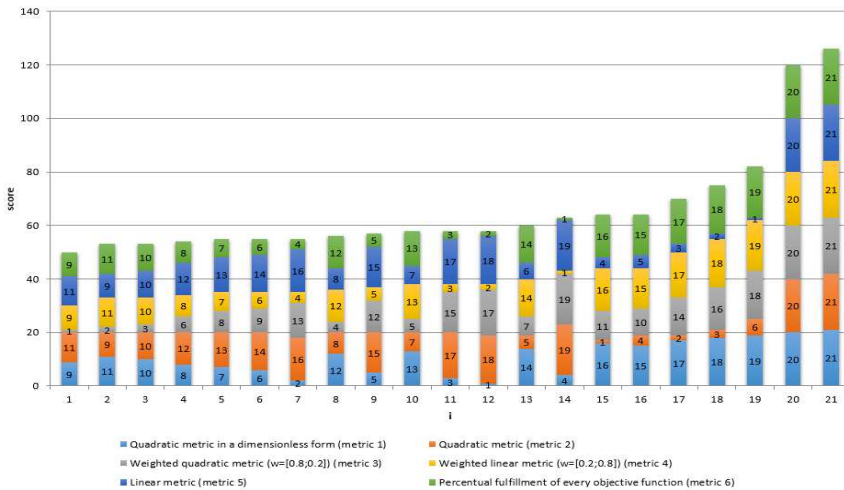


Figure 7

Graph of final score of alternatives using the synthesis of various mathematical metrics

On Fig. 8, user interface developed within our research for resolving multiobjective optimization tasks using combination of modified NSGA – II algorithm and various mathematical methods, is presented.

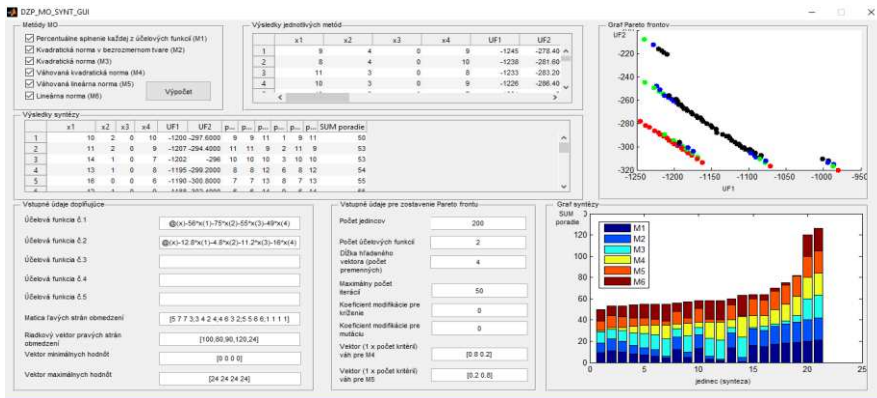


Figure 8

User interface for solving MOO tasks

Conclusions

In the presented paper, multi objective optimization task of definition of the optimal production process of the assembly line model within Center of Modern Control Techniques and Industrial Informatics (CMCT&II) within the Department of Cybernetics and Artificial Intelligence of FEEI TUKE. For resolving the task of choosing the optimal production strategy of the automated assembly line,

combination of modified evolutionary algorithm NSGA-II and various mathematical metrics was used. In defining the set of Pareto optimal solutions, some modifications had to be realized in order to improve the computational process. From the Pareto optimal solutions, the best option for production process was chosen by the percentual fulfilment of every objective function. Another presented option involved the synthesis of the solutions from different mathematical metrics.

In conclusion, the decision for choosing the metric used to define the order of the alternatives from the Pareto set should be realized with respect to the preferences of the decision-maker. Moreover, not all possible approaches can be used to solve a particular assembly line balancing problem. A survey of problems and applicable methods in this area can be found in [4]. Approaches focused on dealing with mixed-model assembly lines, which was also the model described in this paper, are available in [5]. Weighted objective functions can be used, if the decision-maker prefers one of the objectives over the others. Some of the methods for objectivization of the defined weights of objectives can be found in [9].

During the research in this area, we were focused on the optimization of the assembly lines, particularly on creating the simulation models of assembly lines with a focus on their time optimization [10], as well as solving the task of optimal assembly line configuration using the methods of the multi-criterial decision-making [9]. Results obtained within the research are described in [6]. The MOO of the production process of the assembly line, which is closely described within this paper, is another task resolved in the assembly line optimization area, which contributes to the portfolio of problems resolved in this area within our department.

Acknowledgement

This work has been supported by grant KEGA Implementation of research results in the area of modelling and simulation of cyber-physical systems into the teaching process - development of modern university textbooks – 072TUKE-4/2018 (80%). It was supported as well by the Research and Development Operational Program for project: University Science Park Technicom for innovative applications with knowledge technology support – 2nd phase (20%), ITMS code 313011D232.

References

- [1] A. Abraham and L. Jain. Evolutionary multiobjective optimization, Springer, London, 2005
- [2] J. Bautista, and J. Pereira. Ant algorithms for a time and space constrained assembly line balancing problem. European journal of operational research, 177.3, 2016-2032, 2007

-
- [3] N. Boysen, M. Fliedner and A. Scholl. A classification of assembly line balancing problems. *European journal of operational research*, 183.2, 674-693, 2007
- [4] N. Boysen, M. Fliedner and A. Scholl. Assembly line balancing: Which model to use when?. *International Journal of Production Economics*, 111.2, 509-528, 2008
- [5] N. Boysen, M. Fliedner and A. Scholl. Sequencing mixed-model assembly lines: Survey, classification and model critique. *European Journal of Operational Research*, 192.2, 349-373, 2009
- [6] J. Čabala. Creation of Methodology of Multicriterial Assembly Lines Optimization, Dissertation Thesis. CMCT&II DCAI FEEI TU Košice, 163 p., 2018 (in Slovak), supervisor: doc.Ing. J.Jadlovský, CSc.
- [7] J. Čabala and J. Jadlovský. Solving vector optimization problems using Optimization Toolbox. 22nd Annual Conference Proceedings of the International Scientific Conference - Technical Computing Bratislava 2014, published online, November 2014
- [8] J. Čabala, J. Jadlovský, and K. Dujavová. Realization of production process information system on RDBS Oracle base, *Electrical Engineering and Informatics: proceedings of the FEI of Technical University of Košice*, 6, 791-796, 2015
- [9] J. Čabala and J. Jadlovský. Solving optimal assembly line configuration task by multi-objective decision making methods, *Acta Electrotechnica et Informatica*, 2, 53-60, 2017
- [10] J. Čabala and J. Jadlovský. Application of Stateflow Diagrams in Production Line Modeling Danvers : IEEE, SAMI 2016 (Herľany, Slovakia), 125-130, 2016
- [11] Y. K. Choi, D. M. Lee and Y. B. Cho. An approach to multi-criteria assembly sequence planning using genetic algorithms. *The International Journal of Advanced Manufacturing Technology* 42. 1-2, 180-188, 2009
- [12] K. Deb, and S. Karthik. Dynamic multi-objective optimization and decision-making using modified NSGA-II: a case study on hydro-thermal power scheduling." *International conference on evolutionary multi-criterion optimization*. Springer, Berlin, Heidelberg, 803-817, 2007
- [13] K. Deb, S. Agarwal, A. Pratap, T. Meyarivan. A fast elitist nondominated sorting genetic algorithm for multi-objective optimization: NSGA-II. In: *Proceedings of the parallel problem solving from nature VI conference*, Paris, France, 849-858, 2000
- [14] M. Farina, K. Deb, and P. Amato. Dynamic multiobjective optimization problems: test cases, approximations, and applications. *IEEE Transactions on evolutionary computation* 8.5, 425-442, 2004
- [15] M. Fonseca, and P. J. Fleming. Genetic Algorithms for Multiobjective Optimization: Formulation Discussion and Generalization. *Icga*, 93, 416-423, 1993

- [16] K. Hrubina, A. Jadlovská and S. Hrehová: Algorithms of optimization methods with using programming systems. Prešov – Košice, Vol. 1, 393 p., 2005
- [17] S. D. Lapierre, A. Ruiz, and P. Soriano. Balancing assembly lines with tabu search. *European Journal of Operational Research*, 168.3, 826-837, 2006
- [18] H. Li, and Q. Zhang. Multiobjective optimization problems with complicated Pareto sets, MOEA/D and NSGA-II. *IEEE Transactions on evolutionary computation*, 13.2, 284-302, 2009
- [19] S. A. Mansouri. A multi-objective genetic algorithm for mixed-model sequencing on JIT assembly lines. *European Journal of Operational Research* 167.3, 696-716, 2005
- [20] R. T. Marler and J. S. Arora. Survey of multi-objective optimization methods for engineering. *Structural and multidisciplinary optimization* 26.6, 369-395, 2004
- [21] M. Pelikan. Evolutionary algorithms. *Artificial intelligence and cognitive science I*, 335-353, 2009 (in Czech)
- [22] R. E. Precup, and R. C. David. *Nature-Inspired Optimization Algorithms for Fuzzy Controlled Servo Systems*. Butterworth-Heinemann, 2019
- [23] C. Purcaru, et al. Optimal robot path planning using gravitational search algorithm. *International Journal of Artificial Intelligence* 10, S13, 1-20, 2013
- [24] D. Rosinová, and M. Dúbravská. *Optimization*. Bratislava: STU, 1st ed., 190 p., 2008 (in Slovak)
- [25] I. Sabuncuoglu, E. Erdal and A. Arda. Ant colony optimization for the single model U-type assembly line balancing problem. *International Journal of Production Economics* 120.2, 287-300, 2009
- [26] A. Seshadri. A fast elitist multiobjective genetic algorithm: NSGA-II, *Matlab Central*, file exchange, mathworks, 2007
- [27] M. Shams, et al. Ideal gas optimization algorithm. *International Journal of Artificial Intelligence* 15.2, 116-130, 2007
- [28] H. A. Taboada, F. Baheranwala, D. W. Coit, and N. Wattanapongsakorn. Practical solutions for multi-objective optimization: An application to system reliability design problems. *Reliability Engineering & System Safety*, 92(3), 314-322, 2007
- [29] J. Vaščák. Adaptation of fuzzy cognitive maps by migration algorithms. *Kybernetes* 41.3/4, 429-443, 2012
- [30] T. Weise. *Global optimization algorithms-theory and Application*. Self-Published, 2009
- [31] E. Zitzler. Evolutionary algorithms for multiobjective optimization, *CIMNE*, 19-26, 2002

Decentralized nonlinear robust control for multi-variable systems: Application to a 2 DoF laboratory helicopter

Marwa Yousfi^{1,*}, Chakib Ben Njima^{1,2}, Tarek Garna^{1,3}

¹ Laboratory of Automatic, Signal and Image Processing, National Engineering School of Monastir, University of Monastir, Ibn El Jassar Street, 5019 Monastir, Tunisia

² Higher Institute of Transport and Logistics of Sousse, University of Sousse, Erriadh city BP 247, 4023 Sousse, Tunisia

³ Higher Institute of Applied Science and Technology of Sousse, University of Sousse, Ibn Khaldoun city, 4003 Sousse, Tunisia

* Corresponding author, marwa.yousfi@enim.rnu.tn

Abstract: In this paper a decentralized nonlinear robust control (DNRC) using loop shaping design procedure (LSDP) and gain scheduling (GS) technique is developed for MIMO (multiple-input/multiple-output) systems. The nonlinear system is linearized in several equilibrium points and for each of these latter a decentralized robust controller is calculated, using a proposed LSDP based on RGA (Relative Gain Array) theory, to regulate the system around the equilibrium point. To do this. The use of RGA theory is exploited to define the structure of the weighting controller of the LSDP with the most effective input/output pairing. Then, for each equilibrium point a full-order robust controller is calculated using LSDP, which configuration is simplified exploiting the RGA theory by proposing a selection matrix to deduce a simplified final robust controller. The overall control system is obtained by GS technique from switching between local simplified final robust controllers according to the scheduling parameter's (SP) value. The proposed algorithm of control is validated on the AERO system of Quanser.

Keywords: Quanser's AERO; MIMO nonlinear systems; RGA theory; robustness; decentralized control; gain scheduling

1 Introduction

MIMO control systems has been always a rich material of research. Due to multi-variable system's loop interactions, this area of research challenged many researchers who have proposed many solutions to deal with loop interactions. Decen-

tralized control and decoupling have been used widely to minimize or compensate loop interactions in MIMO processes and many studies used these two solutions and combined them with other approaches to come up with good control systems for MIMO processes for example in [1], the authors proposed a novel inverted fuzzy decoupling scheme for MIMO systems with disturbance and the case of binary distillation column has been studied. In [2] an adaptive fuzzy decentralized control for a class of large-scale MIMO nonlinear state delay systems with unmodeled dynamics subject to unknown input saturation and infinite number of actuator failures was proposed. A review of the most extensively applied coupling interaction analysis and decoupler design methods for industrial processes is carried out in [3]. In [4], the authors reviewed and proposed a classification of a number of decentralized, distributed and hierarchical control architectures for large scale systems. An analysis and design of robust multivariable control systems focusing on practical feedback control and not on system theory in general is presented in [5]. [6] offers a novel take on advanced control engineering design techniques for wind turbine applications. In [7] a nonlinear intelligent decoupling controller is developed to stabilize the levitation system. The control architecture consists of three components: (1) fuzzy sliding mode technique for the uncertainty in the system parameter; (2) force distribution for decoupling; (3) extended state observer for compensating the system disturbance. However, to manage loop interactions one must quantify them first. In this context, many tools have been proposed in the literature to solve this issue [8, 9]. The RGA theory [10] is one of these tools that offers a simple way of calculating loop interactions and many extensions of this theory have been developed [11, 12, 13].

Recently, considerable attention has been paid to the control design of robots and helicopters specifically due to their potential military and civil applications see for instance [14, 15, 16]. The challenges in controller design for those type of systems originates from their particular characteristics namely nonlinearity, loop interactions and uncertainties. In the last two decades, many works have been reported in the area of control design for flying vehicles. A 2 DoF Helicopter is a typical MIMO nonlinear system with loop interactions. Hence, it is an ideal test bed to verify the effectiveness of various control schemes. In [17], LQR and LQR-I controllers are designed and have been turned out to be powerful in stabilization and also in tracking desired command input. However, controllers in [17] are not able to handle few uncertainties like, unmodeled elements and external disturbances. This requires the design of a robust controller which can handle above difficulties. In [18], the H_∞ loop shaping framework has been extended by applying two methods of compensator synthesis approach for tracking desired pitch and yaw angles of helicopter. The decentralized discrete-time neural control strategy has been presented in [19] to control pitch and yaw angles. A backstepping controller synthesis methodology has been presented in [20]. By suitably combining adaptive control and LQR-I control, a new robust control scheme has been presented in [21]. Furthermore, a multivariable adaptive sliding mode observer based robust control strategy is presented in [22]. From [23], an intelligent proportional–integral (iPI) is proposed using Takagi-Sugeno Fuzzy (TSF) logic for twin rotor aerodynamic systems. In [24] an hybrid PID controller was implemented using FPGA for a real time TRMS

control. Zeghlache and Amardjia proposed in [25] Real time implementation of non linear observer-based fuzzy sliding mode controller for a twin rotor MIMO system (TRMS).

In this paper, we use Quanser 2 DoF laboratory helicopter to investigate the robust stability and tracking control performances of the proposed decentralized nonlinear robust control. A 2 DoF Helicopter is a typical MIMO nonlinear system with cross couplings or process interactions and unmodeled dynamics. Hence, it is an ideal test bed to verify the effectiveness of various control schemes.

Otherwise, LSDP approach [26] is considered as one powerful tool for robust control system design, for handling model uncertainties and bounded external perturbations, that has been proven to be effective in industrial design. This approach involves the robust stabilization of additive perturbations of normalized coprime factors of a shaped plant. Prior to robust stabilization, the open-loop singular values are shaped using a weighting controller to give a desired open-loop shape which corresponds to a good closed-loop performance. The LSDP has attracted many researchers since 19th century, thanks to its simplicity and robustness as a result many theoretical researches and applications has been done [5, 27, 28, 29, 30]. For instance, in [31] the authors proposed a robust loop-shaping control for a nano-positioning stage. A multi-objective differential evolution (MODE)-based extended H-infinity controller for autonomous helicopter has been developed in [32]. A new Suggested Model Reference Adaptive Controller for the Divided Wall Distillation Column is suggested in [33].

However, a successful design using LSDP depends on the appropriate choice of weighting controllers. The selection of these latter is usually done by a trial-and-error method and is based on the designer's experience. Motivated by this fact, we propose the use of RGA theory to decide the structure of the weighting controller to yield a decentralized control structure which minimise loop interaction in a multi-loop context. The obtained LSDP controller will be a full-order matrix that we propose to simplify their structure using the RGA theory again.

In the other hand, most engineering system are non linear. Synthesis of nonlinear control systems interested many researchers. For instance, in [34] an approach to the design of nonlinear state-space control systems is presented. The approach is supported by a geometrical illustration of systems evolution in the state space. In our case, to move to the nonlinear case, we will be using GS technique. The basic idea is to divide the synthesis of a control system to two steps. The first step is the linearization on equilibrium points, which is based on the approximation of the nonlinear system with a set of linear local models computed for a family of fixed values of the SP ρ . Then an offline calculation of a controller using linear control strategies is applied to the linearized model at each equilibrium point. The second step, is accomplished by switching or interpolating the local controllers obtained for each operating point. The interpolation/switching is made from a set of SP ρ that capture the change in the system's equilibrium point. Thus, the dynamic behavior of a control system changes with the operating point. The GS technique is widely used to control nonlinear system [35, 36, 37, 38].

1.1 Main contribution

In literature, we precise that to guarantee MIMO process regulation, a several MIMO control approaches were proposed namely the sliding mode control [39, 40] and the adaptive predictive control [41, 42]. Adaptive predictive control is used to deal with some critical parameters in the system structure. In the other hand, sliding mode control deals with uncertainties in rapidly changing parameters and unstructured uncertainties. Then the adaptive predictive control and sliding mode control algorithms allow handling changes in the system's dynamics with respect to parametric uncertainties. Nevertheless, these algorithms don't deal with the input/output interactions problem using multiloop control structure design by exploiting a set of controllers. Consequently, we place ourselves in the so-called decentralized control which have proven its effectiveness compared to the centralized control dealing with the process interactions. Furthermore, because of the process interactions a change in a manipulated variable affects all the controlled variables and it is not always clear which input should be "paired" with which output to synthesize an effective control system. In this regard, we have studied the RGA theory and the LSDP approach which offers the following advantages. The RGA theory is used to quantify the loop interaction in MIMO systems. Thus, it could be made use of to decide the best control structure in a decentralized configuration framework. The LSDP controller tracks desired response quickly with minimum overshoot in presence of parametric uncertainties. However for MIMO systems a full order MIMO controller is obtained and things can gets complicated if the system has many inputs/outputs or important loop interactions. If LSDP approach and RGA theory are combined and a new algorithm is proposed, we can have all the advantages in one algorithm. This thought has motivated us to develop a new robust control algorithm. Thus, we propose the use of RGA theory to decide the structure of the weighting and the final robust controllers of the LSDP approach. To apply the proposed algorithm to nonlinear systems we used GS technique. Therefore, a set LSDP controller is calculated for a predefined number of equilibrium points. The overall controller is obtained by switching between these controllers. To demonstrate the superiority of the proposed controller, experimental results are obtained on a 2 DoF helicopter which is fourth order, two-input/two-output, nonlinear coupled system. The obtained results are quite satisfactory and support the validity of the analysis developed.

1.2 Structure of the paper

This paper is structured as follows: the first section is an introduction, where we present the essential of our work and the main contribution. The second section: 'background' we briefly review the notion of decentralized control and we introduce the RGA theory, then a brief introduction to the LSDP approach. In the third section 'Main results' we propose the use of the RGA theory to decide on the structure of the weighting controller matrix's configuration. Then, the LSDP approach is used to calculate for each equilibrium point a final robust controller. These latter are simplified using RGA theory and a global robust controller is synthesized by exploiting the GS technique. In the fourth section 'Experimental validation: AERO system' the proposed algorithm is tested on a 2 DoF helicopter.

2 Background

In this section we present the notions of decentralized control and RGA theory along with LSDP approach.

2.1 Decentralized control and RGA theory

The decentralized control [43, 44, 45], is based on a multiloop control structure i.e. the use of n SISO controllers to control a multivariable process with n inputs/outputs. Each loop is defined by an input u_j and its associated output y_k . The selection of input/output pairing can be decided using the RGA theory [10]. In fact, for most MIMO systems, each input affects all measured outputs, and it is not always clear which input should be "paired" with which output to calculate the most efficient control. Therefore the RGA theory is a one tool that allows to fix the most effective input/output pairing that allows to minimize loop interactions. Therefore, to minimize undesired interactions, pairings corresponding to a RGA element as close to one as possible should be selected, see for instance [11]. The RGA metric is given by:

$$\mathbf{\Lambda} = \mathbf{G}(s=0) \odot \mathbf{G}^{-T}(s=0) = [\lambda_{jk}]_{1 \leq j,k \leq n} \quad (1)$$

such that $\mathbf{G}(s=0)$ is the system transfer matrix and " \odot " is the Hadamard product (product element by element). Consequently, based on values of λ_{jk} , the configuration of the decentralized controller $\mathbf{K}_d(s)$ is decided as follows:

$$\mathbf{K}_d(s) : \begin{cases} K_{kj}(s) \neq 0 & \text{if } \lambda_{jk} \text{ is the closest to } 1 \\ K_{kj}(s) = 0 & \text{else} \end{cases} \quad (2)$$

2.2 LSDP approach

Many industrial systems are characterized by parametric uncertainties that may occur during their functioning and affect their dynamics. This phenomenon may cause problems specially for systems where parameter's precision is important namely the aeronautical and chemical systems (missiles, planes, batch reactors, CSTR, etc ...) where parameters uncertainties affect adversely the system's functioning. Calculating a controller for this type of systems is not an easy task because these uncertainties must be taken into account in order to obtain efficient control systems, which called robust control. The LSDP developed by [26] is one of these robust control approaches.

The LSDP is based on the exploitation of a filter called weighting controller $\mathbf{K}(s)$ to shape the singular values of open loop's transfer matrix $\mathbf{G}(s)$. The weighting controller $\mathbf{K}(s)$ serves to ameliorate the open loop performances. Typically, it aims to ensure high singular values at low frequencies (to ensure a zero static error in the case of a tracking reference) and low singular values at high frequencies (to ensure robustness against disturbance rejection). In this case, we get the shaped system $\mathbf{G}_{sh}(s) = \mathbf{G}(s)\mathbf{K}(s)$, which can be written in a state space representation [29]:

$$\begin{cases} \dot{\mathbf{x}}(t) = \mathbf{A}_{sh} \mathbf{x}(t) + \mathbf{B}_{sh} \mathbf{u}(t) \\ \mathbf{y}(t) = \mathbf{C}_{sh} \mathbf{x}(t) + \mathbf{D}_{sh} \mathbf{u}(t) \end{cases} \quad (3)$$

with $\mathbf{x}(t) \in \mathbb{R}^{m \times 1}$, $\mathbf{u}(t) \in \mathbb{R}^{n \times 1}$, $\mathbf{y}(t) \in \mathbb{R}^{p \times 1}$ are the states, inputs and outputs vectors, $\mathbf{A}_{sh} \in \mathbb{R}^{m \times m}$, $\mathbf{B}_{sh} \in \mathbb{R}^{m \times n}$, $\mathbf{C}_{sh} \in \mathbb{R}^{n \times m}$ and $\mathbf{D}_{sh} \in \mathbb{R}^{n \times n}$ are the state matrices such that pairs of state space matrices $(\mathbf{A}_{sh}, \mathbf{B}_{sh})$ and $(\mathbf{A}_{sh}, \mathbf{D}_{sh})$ are respectively controllable and observable with $m \in \mathbb{N}^+$ is the order of the system.

Thereafter, [26] proposed the computation of a robust controller $\mathbf{K}_\infty(s)$ guaranteeing robust stability against parametric uncertainties. The robust controller is defined as:

$$\mathbf{K}_\infty(s) := \left(\begin{array}{c|c} \mathbf{A}_{sh} + \mathbf{B}_{sh}\mathbf{F} + \varepsilon_{max}^{-2}(\mathbf{L}^T)^{-1}\mathbf{Y}\mathbf{C}_{sh}^T(\mathbf{C}_{sh} + \mathbf{D}_{sh}\mathbf{F}) & \varepsilon_{max}^{-2}(\mathbf{L}^T)^{-1}\mathbf{Y}\mathbf{C}_{sh}^T \\ \hline \mathbf{B}_{sh}^T\mathbf{X} & -\mathbf{D}_{sh}^T \end{array} \right) \quad (4)$$

with a maximum stability margin given as :

$$\varepsilon_{max} = (1 + \beta_{max}(\mathbf{X}\mathbf{Y}))^{-\frac{1}{2}} \quad (5)$$

where the parameters \mathbf{F} , \mathbf{L} , \mathbf{Y} and \mathbf{X} are calculated matrices given in [15]. The final robust Controller $\mathbf{K}_f(s)$ is Computed as:

$$\mathbf{K}_f(s) = \mathbf{K}(s)\mathbf{K}_\infty(s) \quad (6)$$

In order to ensure the robust stability of the closed loop system with respect to parameter uncertainties, the following theorems are proposed in the literature:

Theorem 1. [26]

Consider a shaped plant $\mathbf{G}_{sh}(s)$ and the stability margin ε_{max} . A robust controller $\mathbf{K}_\infty(s)$ stabilizes the uncertain system $\mathbf{G}_{sh,\Delta}(s)$:

i). $\mathbf{K}_\infty(s)$ stabilizes $\mathbf{G}_{sh}(s)$.

ii). $\left\| \left[\begin{array}{c} \mathbf{K}_\infty \\ \mathbf{I} \end{array} \right] (\mathbf{I} - \mathbf{G}_{sh}\mathbf{K}_\infty)^{-1} \tilde{\mathbf{K}}_{sh}^{-1} \right\|_\infty \leq \varepsilon^{-1}$ for all $\varepsilon \leq \varepsilon_{max}$

■

Theorem 2. [27]

Consider a shaped plant $\mathbf{G}_{sh}(s)$ and its robust controller $\mathbf{K}_\infty(s)$ calculated for the stability margin ε_{max} . Then the following properties are equivalent:

a). The robust controller $\mathbf{K}_\infty(s)$ guarantees the closed loop stability of all uncertain systems $\mathbf{G}_{sh,\Delta}(s)$ with a stability margin ε_{max} .

b). The robust controller $\mathbf{K}_\infty(s)$ stabilizes the uncertain systems $\mathbf{G}_{sh,\Delta}(s)$ such as $\delta_g(\mathbf{G}_{sh}, \mathbf{G}_{sh,\Delta}) \leq \varepsilon_{max}$ where δ_g is the gap metric.

■

From Theorems 1 and 2, we note that the robust controller $\mathbf{K}_\infty(s)$ obtained by LSDP approach for the shaped system $\mathbf{G}_{sh}(s)$ with maximum stability margin ε_{max} , ensures the stabilization of all uncertain systems $\mathbf{G}_{sh,\Delta}(s)$. Also, we note a fundamental link between the stability margin ε_{max} and the effect of the stabilization of the robust controller $\mathbf{K}_\infty(s)$.

3 Main results

In this section we present the essential of our work: The DNRC.

3.1 LSDP based on RGA theory

At this point, we propose the exploitation of RGA theory with the LSDP approach to develop an algorithm to control nonlinear multivariable uncertain systems guaranteeing both robust stability and reference tracking. The combination of RGA theory with the LSDP approach allows to adjust:

- The weighting controller matrix's configuration.
- The final robust controller matrix's configuration.

The RGA has been selected because it provides a quite simple way of choosing the best input/output pairing configuration to minimize loop interactions. The LSDP controller's configuration must preserve the decentralized control structure defined from RGA theory. Therefore, the LSDP approach can be reformulated as follows:

Step 1 - RGA calculation: given the open loop plant's transfer matrix $\mathbf{G}(s)$, calculate $\mathbf{\Lambda}$ from (1).

Step 2 - Loop Shaping technique based on RGA theory: to accentuate the most effective input/output pairing based on the RGA theory, we propose to fix the configuration of the weighting controller or the filter of the LSDP as $\mathbf{K}_d(s)$ defined in (2). This configuration results from the RGA elements of $\mathbf{\Lambda}$ pointed in step 1.

The LS technique provides the shaped system given by:

$$\mathbf{G}_{sh}(s) = \mathbf{G}(s)\mathbf{K}_d(s) \quad (7)$$

Step 3 - Value of $\mathbf{K}_d(s)$: typically the designer chooses the elements $K_{kj}(s)$, $j, k = 1, \dots, n$ as low pass filters in order to have a sufficiently small open-loop singular values in high frequencies in order to assure a good tracking performance with high open-loop singular values in low frequencies to improve noise rejection.

Our next proposition is to exploit the RGA again to simplify the final robust controller $\mathbf{K}_f(s)$ calculated using LSDP approach. The proposed simplified final robust controller $\tilde{\mathbf{K}}_f(s)$ is determined to emphasize the interaction (u_k/y_j) approved by the RGA theory. Therefore, the simplified final robust controller is calculated:

$$\tilde{\mathbf{K}}_f(s) = \mathbf{P} \odot \mathbf{K}_f(s) \quad (8)$$

where $\mathbf{K}_f(s)$ is the final robust controller:

$$\mathbf{K}_f(s) = \mathbf{K}_d(s)\mathbf{K}_\infty(s) = [K_{f,kj}(s)]_{1 \leq j, k \leq n} \quad (9)$$

and $\mathbf{P} \in R^{n \times n}$ is a selection matrix determined based on the RGA theory as:

$$\begin{cases} P_{kj} = 1 & \text{if } \lambda_{jk} \text{ is the closest to } 1 \\ P_{kj} = 0 & \text{else} \end{cases} \quad (10)$$

3.2 DNRC

We consider a linearization of the system in a set of L equilibrium points, where for each equilibrium point a simplified final robust controller is calculated using LSDP approach. All resulting simplified final robust controllers are interpolated using the GS technique to regulate the nonlinear MIMO system.

Considering a nonlinear continuous-time system described by its ordinary differential equation (ODE) [45, 46]

$$\Sigma : \begin{cases} \dot{\mathbf{x}}(t) = \mathbf{f}(\mathbf{x}(t), \mathbf{u}(t)) \\ \mathbf{y}(t) = \mathbf{g}(\mathbf{x}(t), \mathbf{u}(t)) \end{cases} \quad (11)$$

We note that each equilibrium point $(\mathbf{x}_{eq}, \mathbf{u}_{eq})$ can be defined function of the SP $\boldsymbol{\rho}$ [47, 48]. This latter is fixed as the output vector $\boldsymbol{\rho} = \mathbf{y}(t)$. For an equilibrium point $(\mathbf{x}_{eq}(\boldsymbol{\rho}), \mathbf{u}_{eq}(\boldsymbol{\rho}))$, the functions \mathbf{f} and \mathbf{g} are approximated to provide the following linear representation:

$$\mathbf{G}_{eq}(s) : \begin{cases} \dot{\mathbf{x}}(t) = \mathbf{A}_{eq}(\boldsymbol{\rho}) \mathbf{x}(t) + \mathbf{B}_{eq}(\boldsymbol{\rho}) \mathbf{u}(t) \\ \mathbf{y}(t) = \mathbf{C}_{eq}(\boldsymbol{\rho}) \mathbf{x}(t) + \mathbf{D}_{eq}(\boldsymbol{\rho}) \mathbf{u}(t) \end{cases} \quad (12)$$

where $\mathbf{A}_{eq}(\boldsymbol{\rho})$, $\mathbf{B}_{eq}(\boldsymbol{\rho})$, $\mathbf{C}_{eq}(\boldsymbol{\rho})$ and $\mathbf{D}_{eq}(\boldsymbol{\rho})$ are obtained by linearization (or first-order Taylor expansion) of the functions \mathbf{f} , \mathbf{g} at the equilibrium point $(\mathbf{x}_{eq}(\boldsymbol{\rho}), \mathbf{u}_{eq}(\boldsymbol{\rho}))$ [13].

We precise that we will obtain a set of L simplified final robust controller based on the LSDP approach applied for each equilibrium point. In fact, for each linear transfer matrix $\mathbf{G}_{eq}^i(s)$ associated to the i^{th} equilibrium point characterized by the SP $\boldsymbol{\rho}^i$, we compute the shaped system $\mathbf{G}_{sh}^i(s)$ using (7), the maximum stability margin ε_{max}^i using (5), the robust controller $\mathbf{K}_{\infty}^i(s)$ using (4), the final robust controller $\mathbf{K}_f^i(s)$ from (9) and the simplified final robust controller $\tilde{\mathbf{K}}_f^i(s)$ by (8) and (10).

The L simplified final robust controllers $\tilde{\mathbf{K}}_f^i(s)$, $i = 1, \dots, L$ are used to design a global robust controller $\mathbf{K}_{global}(s)$ for the nonlinear system by exploiting the GS technique by switching between the different simplified final robust controllers $\tilde{\mathbf{K}}_f^i(s)$ depending on the value of the SP $\boldsymbol{\rho}$ as follows:

$$\mathbf{K}_{global}(s) = \begin{cases} \tilde{\mathbf{K}}_f^i(s) \text{ if } \boldsymbol{\rho}^i \leq \boldsymbol{\rho} < \boldsymbol{\rho}^{i+1}, i = 1, \dots, L-1 \\ \tilde{\mathbf{K}}_f^L(s) \text{ if } \boldsymbol{\rho}^L \leq \boldsymbol{\rho} < \boldsymbol{\rho}^f \end{cases} \quad (13)$$

The proposed DNRC is detailed in algorithm 1.

Algorithm 1 algorithm of synthesis of DNRC system

1. Given a nonlinear system described by its ODE (11), fix the SP $\boldsymbol{\rho}$ as the output vector.
2. Based on the dynamics of the system, fix the equilibrium points $(\mathbf{x}_{eq}^i(\boldsymbol{\rho}^i), \mathbf{u}_{eq}^i(\boldsymbol{\rho}^i))$, $i = 1, \dots, L$.
3. Using linearization, calculate the state matrices \mathbf{A}_{eq}^i , \mathbf{B}_{eq}^i , \mathbf{C}_{eq}^i and \mathbf{D}_{eq}^i function of SP $\boldsymbol{\rho}$ for each equilibrium point.
4. Based on the RGA metric $\boldsymbol{\Lambda}$, fix the configuration for the future weighting controller matrices $\mathbf{K}_d^i(s) = [K_{kj}^i(s)]$; $j, k = 1 \dots, n$ associated to the i^{th} equilibrium point and calculate the transfer matrices $\mathbf{G}_{eq}^i(s)$ and the shaped transfer matrices $\mathbf{G}_{sh}^i(s)$ using (7).
5. Exploit the LSDP approach combined with RGA theory to calculate a robust \mathbf{K}_∞^i using (4) for each equilibrium point.
6. Calculate the final controllers $\mathbf{K}_f^i(s)$, $i = 1, \dots, L$ stabilizing $\mathbf{G}_{sh}^i(s)$ using (9) for each equilibrium point.
7. Calculate the simplified final robust controller $\tilde{\mathbf{K}}_f^i(s)$, $i = 1, \dots, L$ using (8) and (10).
8. Interpolate the L simplified final robust controllers $\tilde{\mathbf{K}}_f^i(s)$, $i = 1, \dots, L$, to yield the global robust controller $\mathbf{K}_{global}(s)$ by switching between $\tilde{\mathbf{K}}_f^i(s)$, $i = 1, \dots, L$ according to the value of SP $\boldsymbol{\rho}$ as described in (13).

Clearly from theorems 1 and 2, at each equilibrium point the robust controller \mathbf{K}_∞^i stabilizes the associated shaped plant \mathbf{G}_{sh}^i and we have the performance of the LSDP approach which guarantees the robust stability of the uncertain systems resulting from parameter uncertainties or external perturbation. This robustness property will therefore be reflected in the global robust controller \mathbf{K}_{global} .

4 Experimental validation: AERO system

The proposed DNRC is practically tested on a TITO system namely the 2 DoF laboratory helicopter: AERO system of Quanser.

4.1 System's description and modeling

The Quanser's AERO, is a fully integrated 2 DoF dual-motor laboratory test platform, designed for control experiments and research for aerospace application. The workstation, consists of an helicopter model mounted on a fixed base with two propellers that are driven by DC motors. The front propeller controls the elevation of the helicopter nose about the pitch axis and the back propeller controls the side to side motions of the helicopter about the yaw axis. The pitch and yaw angles are measured using high resolution encoders. The pitch and yaw encoder and motor

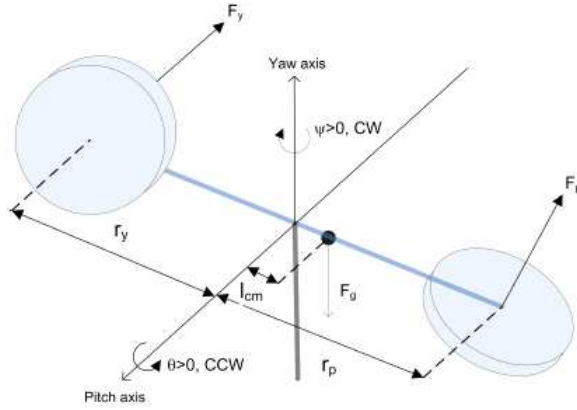


Figure 1
Free-body diagram of the 2 DOF laboratory helicopter

signals are transmitted via a slip ring. This eliminates the possibility of wires tangling on the yaw axis and allows the yaw angle to rotate freely about 360 degrees. However, due to physical limitations, the pitch body is limited to ± 60 degrees. The helicopter setup consists of two degrees of freedom as shown in Figure 1: a motion around the Z axis (yaw), represented by angle ψ , and the rotation around the Y axis (pitch), represented by the angle θ . The input voltages to the DC motors are the control variables and the objective is to control the pitch and yaw angles so as to make the system to track the reference trajectory.

The nonlinear equations of motion of the helicopter system derived using the Euler-Lagrange formula, are as follows :

$$\begin{cases} (J_p + ml^2)\ddot{\theta}(t) = K_{pp}V_{mp}(t) + K_{py}V_{my}(t) + mgl\cos\theta - B_p\dot{\theta}(t) + ml^2\sin\theta\cos\theta\dot{\psi}(t)^2 \\ (J_y + ml^2\cos^2\theta)\ddot{\psi}(t) = K_{yp}V_{mp}(t) + K_{yy}V_{my}(t) - B_y\dot{\psi}(t) + 2ml^2\sin\theta\cos\theta\dot{\psi}(t)\dot{\theta}(t) \end{cases} \quad (14)$$

where $\theta(t)$, $\dot{\theta}(t)$, $\psi(t)$, $\dot{\psi}(t)$, F_p , F_y , V_{mp} , V_{my} are respectively the pitch angle, pitch velocity, yaw angle, yaw velocity, pitch thrust force, yaw thrust force, control input voltage to pitch and yaw motor. The specifications of various parameters of the system are given in Table 1.

Table 1
AERO Parameters.

Symbol	Description	Value	Unit
J_p	Total moment of inertia about pitch axis	0.0384	$Kg.m^2$
J_y	Total moment of inertia about yaw axis	0.0432	$Kg.m^2$
B_p	Equivalent viscous damping about pitch axis	0.8	N/V
B_y	Equivalent viscous damping about yaw axis	0.318	N/V
K_{pp}	Thrust force constant of yaw motor	0.204	$N.m/V$
K_{yy}	Thrust torque constant of yaw axis from yaw motor	0.072	$N.m/V$
K_{py}	Thrust torque constant acting on pitch axis from yaw motor	0.0068	$N.m/V$
K_{yp}	Thrust torque constant acting on yaw axis from pitch motor	0.0219	$N.m/V$
m	Total moving mass of the helicopter	1.3872	Kg
l	Center of mass length along helicopter body from pitch axis	0.186	m
g	Gravitational acceleration	9.81	m/s^2

The nonlinear equations (14) of the AERO takes the form of (11) with:

$$\begin{aligned}
 \mathbf{x}(t) &= \begin{pmatrix} \theta(t) \\ \psi(t) \\ \dot{\theta}(t) \\ \dot{\psi}(t) \end{pmatrix}; \quad \mathbf{u}(t) = \begin{pmatrix} V_{mp}(t) \\ V_{my}(t) \end{pmatrix}; \quad \mathbf{y}(t) = \begin{pmatrix} \theta(t) \\ \psi(t) \end{pmatrix} \\
 \mathbf{f}(\mathbf{x}(t), \mathbf{u}(t)) &= \begin{pmatrix} \dot{\theta}(t) \\ \dot{\psi}(t) \\ K_{pp}V_{mp} + K_{py}V_{my} + mgl\cos\theta - B_p\dot{\theta}(t) + ml^2\sin\theta\cos\theta(\dot{\psi}(t))^2 \\ K_{yp}V_{mp} + K_{yy}V_{my} - B_y\dot{\psi}(t) + 2ml^2\sin\theta\cos\theta\dot{\psi}(t)\dot{\theta}(t) \end{pmatrix} \\
 \mathbf{g}(\mathbf{x}(t), \mathbf{u}(t)) &= \begin{pmatrix} \theta(t) & 0 & 0 & 0 \\ 0 & \psi(t) & 0 & 0 \end{pmatrix}
 \end{aligned} \tag{15}$$

The first step of algorithm 1 is the fixing of the SP $\boldsymbol{\rho}$. We will consider the output vector $\mathbf{y}(t)$ as SP:

$$\boldsymbol{\rho} = \begin{pmatrix} \theta_{eq} \\ \psi_{eq} \end{pmatrix} \tag{16}$$

The SP $\boldsymbol{\rho}$ define the equilibrium point $(\mathbf{x}_{eq}, \mathbf{u}_{eq})$ of the nonlinear system (14) and verify:

$$\mathbf{f}(\mathbf{x}_{eq}(\boldsymbol{\rho}), \mathbf{u}_{eq}(\boldsymbol{\rho})) = 0 \tag{17}$$

where :

$$\mathbf{x}_{eq} = \boldsymbol{\rho} \quad ; \quad \mathbf{u}_{eq} = \begin{pmatrix} V_{mp,eq} \\ V_{my,eq} \end{pmatrix} \tag{18}$$

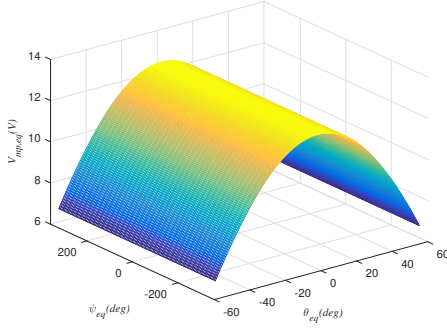


Figure 2
Pitch input voltage function of outputs angles

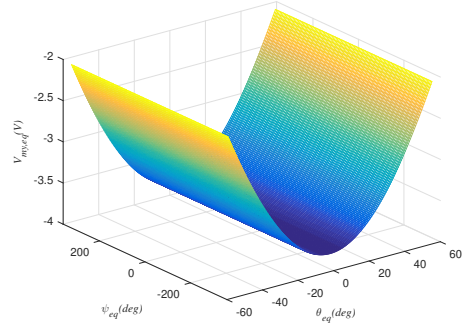


Figure 3
Yaw input voltage function of outputs angles

From (15) and (17) and after calculation, we get:

$$V_{mp,eq} = mgl \cos \theta_{eq} \frac{K_{yy}}{K_{pp}K_{yy} - K_{py}K_{yp}} \quad (19)$$

$$V_{my,eq} = -\frac{K_{yp}}{K_{yy}} V_{mp,eq}$$

The dynamics of the AERO is presented in Figures 2 and 3 where the yaw rotates freely about 360 degrees however the pitch rotation is delimited to ± 60 degrees due to physical constraints so the the operational domain is limited to:

$$\begin{aligned} -60^\circ &\leq \theta_{eq} \leq 60^\circ \\ -360^\circ &\leq \psi_{eq} \leq 360^\circ \end{aligned} \quad (20)$$

Based on Figures 2 and 3, we notice that the system's dynamics is rather linear for $\theta_{eq} \leq 0$ and $\theta_{eq} > 0$ so we will fix the equilibrium points based on this ascertainment as follows:

$$(\mathbf{x}_{eq}^1(\boldsymbol{\rho}^1), \mathbf{u}_{eq}^1(\boldsymbol{\rho}^1)) : \begin{cases} \theta_{eq}^1 = -60^\circ \\ \psi_{eq}^1 = -360^\circ \\ V_{mp,eq}^1 = 6.7726 \text{ V} \\ V_{my,eq}^1 = -2.06 \text{ V} \end{cases} ; (\mathbf{x}_{eq}^2(\boldsymbol{\rho}^2), \mathbf{u}_{eq}^2(\boldsymbol{\rho}^2)) : \begin{cases} \theta_{eq}^2 = 60^\circ \\ \psi_{eq}^2 = -360^\circ \\ V_{mp,eq}^2 = 6.7726 \text{ V} \\ V_{my,eq}^2 = -2.06 \text{ V} \end{cases} \quad (21)$$

which constitutes step 2 of algorithm 1 for $L = 2$.

Taking into account (15), the linearization of (14) around an equilibrium point

$(\mathbf{x}_{eq}(\boldsymbol{\rho}), \mathbf{u}_{eq}(\boldsymbol{\rho}))$ using first-order Taylor expansion is given:

$$\mathbf{A}_{eq}(\boldsymbol{\rho}) = \begin{pmatrix} 0 & 0 & 1 & 0 \\ 0 & 0 & 0 & 1 \\ \frac{mgl}{J_p + ml^2} \sin\theta_{eq} & 0 & -\frac{B_p}{J_p + ml^2} & 0 \\ \frac{(K_{yp}V_{mp,eq} + K_{yy}V_{my,eq})}{J_y + ml^2 \cos^2\theta_{eq}} 2ml^2 \sin\theta_{eq} \cos\theta_{eq} & 0 & 0 & -\frac{B_y}{J_y + ml^2 \cos^2\theta_{eq}} \end{pmatrix}$$

$$\mathbf{B}_{eq}(\boldsymbol{\rho}) = \begin{pmatrix} 0 & 0 \\ 0 & 0 \\ \frac{K_{pp}}{J_p + ml^2} & \frac{K_{py}}{J_p + ml^2} \\ \frac{K_{yp}}{J_y + ml^2 \cos^2\theta_{eq}} & \frac{K_{yy}}{J_y + ml^2 \cos^2\theta_{eq}} \end{pmatrix}; \quad \mathbf{C}_{eq}(\boldsymbol{\rho}) = \begin{pmatrix} 1 & 0 & 0 & 0 \\ 0 & 1 & 0 & 0 \end{pmatrix};$$

$$\mathbf{D}_{eq}(\boldsymbol{\rho}) = \begin{pmatrix} 0 & 0 \\ 0 & 0 \end{pmatrix} \quad (22)$$

which constitutes step 3 of algorithm 1.

4.2 DNR controller

The next step is the decision on the weighting controllers configuration, to do so it is necessary to discuss input/output pairing of the studied AERO. Thus, we calculated the RGA $\boldsymbol{\Lambda}$ of the system using (1). After variation of the SP $\boldsymbol{\rho} = (\theta_{eq} \ \psi_{eq})^T$, we notice that $\boldsymbol{\Lambda}$ in all equilibrium points is constant and given as:

$$\boldsymbol{\Lambda} = \begin{pmatrix} 1.0102 & -0.0102 \\ -0.0102 & 1.0102 \end{pmatrix} \quad (23)$$

Therefore, the pairing $(V_{mp}/\theta, V_{my}/\psi)$ is fixed, which means we will amplify the interaction between the voltage V_{mp} and the pitch rotation θ on one hand and the voltage V_{my} and the yaw rotation ψ on the other hand. In this way, based on (2), the weighting controllers $\mathbf{K}_d^i(s)$ will take the following form :

$$\mathbf{K}_d^i(s) = \begin{pmatrix} K_1^i(s) & 0 \\ 0 & K_2^i(s) \end{pmatrix} \quad \text{for } i = 1, 2 \quad (24)$$

with :

$$K_1^i(s) = \frac{250s^2 + 15040s + 4000}{s^2 + 100s}$$

$$K_2^i(s) = \frac{101s^2 + 105s + 500}{s^2 + 100s} \quad (25)$$

As stated in step 4 of algorithm 1, we calculate for each equilibrium point the transfer matrices $\mathbf{G}_{eq}^i(s)$. The results are presented in Table 2 along with the local sub-models parameters. Afterwards, the shaped systems $\mathbf{G}_{sh,eq}^i(s) = \mathbf{G}_{eq}^i(s) \mathbf{K}_d^i(s)$, $i = 1, 2$ are calculated.

Table 2
Equilibrium points $(\mathbf{x}_{eq}^i, \mathbf{u}_{eq}^i)$ and their corresponding transfer matrices \mathbf{G}_{eq}^i .

i	$\begin{pmatrix} \theta_{eq}^i \\ \psi_{eq}^i \end{pmatrix}$	$\begin{pmatrix} V_{mp,eq}^i \\ V_{my,eq}^i \end{pmatrix}$	\mathbf{G}_{eq}^i	ϵ_{max}^i
1	$\begin{pmatrix} -60 \\ -360 \end{pmatrix}$	$\begin{pmatrix} 6.7726 \\ -2.06 \end{pmatrix}$	$\begin{pmatrix} \frac{-2.06}{s^2 + 9.26s + 24.65} & \frac{0.07871}{s^2 + 9.26s + 24.65} \\ \frac{0.3828}{s^2 + 5.558s} & \frac{1.259}{s^2 + 5.558s} \end{pmatrix}$	0.4669
2	$\begin{pmatrix} 60 \\ -360 \end{pmatrix}$	$\begin{pmatrix} 6.7726 \\ -2.06 \end{pmatrix}$	$\begin{pmatrix} \frac{2.361}{s^2 + 9.26s - 24.65} & \frac{0.07871}{s^2 + 9.26s - 24.65} \\ \frac{0.3828}{s^2 + 5.558s} & \frac{1.259}{s^2 + 5.558s} \end{pmatrix}$	0.4103

Therefore, the nonlinear behavior of the system Σ is described by switching between local models \mathbf{G}_{eq}^i ; $i = 1, 2$ according to the SP $\boldsymbol{\rho} = (\theta_{eq} \ \psi_{eq})^T$.

$$\Sigma := \begin{cases} \mathbf{G}_{eq}^1 \text{ if } -60^\circ \leq \theta(t) \leq 0^\circ \text{ and } -360^\circ \leq \psi(t) \leq 360^\circ \\ \mathbf{G}_{eq}^2 \text{ if } 0 < \theta(t) \leq 60^\circ \text{ and } -360^\circ \leq \psi(t) \leq 360^\circ \end{cases} \quad (26)$$

Taking into account steps 5, 6 and 7 of algorithm 1, the resulting simplified final robust controllers $\tilde{\mathbf{K}}_f^i(s) = \mathbf{P} \odot \mathbf{K}_f^i(s)$ calculated using (8)-(10) are given by:

$$\tilde{\mathbf{K}}_f^i(s) = \begin{pmatrix} K_{f12}^i(s) & 0 \\ 0 & K_{f21}^i(s) \end{pmatrix}; \quad i = 1, 2 \quad (27)$$

where $K_{f12}^i(s)$ and $K_{f21}^i(s)$ are calculated and presented in Appendix A using (4) and (6) with \mathbf{P} is the selection matrix determined from RGA theory, as detailed in (10):

$$\mathbf{P} = \begin{pmatrix} 1 & 0 \\ 0 & 1 \end{pmatrix} \quad (28)$$

Then, as stated in (13) the global robust controller K_{global} of the AERO is constructed by switching between simplified final robust controllers $\tilde{\mathbf{K}}_f^i$, $i = 1, 2$. According to step 8 of algorithm 1, the switching between the simplified final robust controllers depends on the selection signal I_s which determines the position of the switcher according to the value of SP $\boldsymbol{\rho}$ as detailed as follows:

$$\begin{cases} I_s = 1 \text{ and } \mathbf{K}_{global} = \tilde{\mathbf{K}}_f^1 \text{ if } -60^\circ \leq \theta(t) \leq 0^\circ \text{ and } -360^\circ \leq \psi(t) \leq 360^\circ \\ I_s = 2 \text{ and } \mathbf{K}_{global} = \tilde{\mathbf{K}}_f^2 \text{ if } 0 < \theta(t) \leq 60^\circ \text{ and } -360^\circ \leq \psi(t) \leq 360^\circ \end{cases} \quad (29)$$

The experimental validation was assured thanks Quanser AERO USB experiment. This latter interfaces with Quanser control software QUARC running on a laboratory PC via a standard USB 2.0 connection. The Quanser AERO USB can be used with MATLAB/Simulink and Quanser QUARC software. With the USB version of the experiment, the experimental scheme control represented in Figure 4 is characterized by:

- Quanser Control Software (required for Quanser AERO USB experiment): QUARC for MATLAB/Simulink transfers the control signals V_{mp} and V_{my} generated by the controller and it also allows the acquisition of pitch and yaw angles measured through optical encoders.
- A PC with MATLAB/Simulink and QUARC installed.
- QFLEX 2 USB panel for real time communication with PC.
- Quanser's 2 DoF helicopter: AERO system.

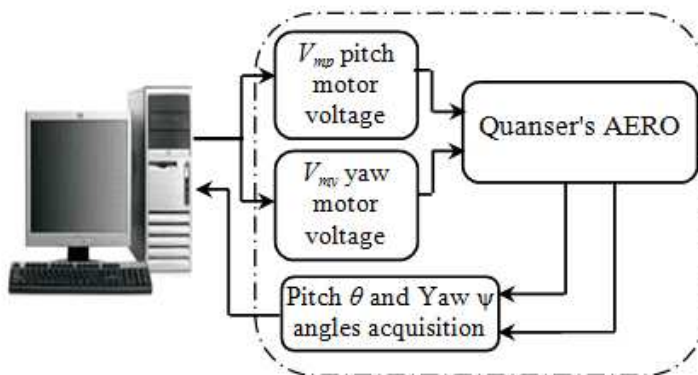


Figure 4
Experimental scheme

Figure 5 shows the the experimental setup. For more informations about the QUARC and the helicopter AERO of QUANSER one can refers to their data-sheets [49, 50]. We precise that, in our case, the sampling time was fixed as $T_e = 0.02s$.

Figures 6, 8 and 10 includes evolution of output and reference signals, control signals and selection indicator I_s respectively.

On examining Figure 6, output signals $\theta(t)$ and $\psi(t)$ are observed to follow the reference signals r_θ and r_ψ respectively. This highlights the good performance of the global controller \mathbf{K}_{global} according to the switching between the two simplified final robust controllers $\tilde{\mathbf{K}}_f^i(s)$; $i = 1, 2$. These controllers come into play by applying the control by GS technique as a function of the variation scheduling vector $\boldsymbol{\rho}$ controlling the switching from one controller to another. This is illustrated in Figure



Figure 5
Quanser's AERO System

10 where the selection indicator I_s shows the switching between the simplified final robust controllers which is essential to produce the control signal $\mathbf{u}(t)$ presented in Figure 8 guaranteeing the regulation of the AERO system.

Processes are subject to uncertainties in their parameters and perturbations that may affect their dynamics during operation. Therefore, it is worth to investigate the effectiveness of the synthesized controller with such circumstances. To test the robustness of the global controller K_{global} , a manual perturbation is applied to the process to the rotation of the pitch θ while operating to test the reaction of the control. Figures 7, 9 and 11 present the same previous signals with the applied perturbation.

Figure 7 shows that at the moment of the application of the perturbation due to loop interactions, the yaw angle ψ loosed its trajectory but quickly returned to the desired trajectory. This can be seen at Figure 11, such that at the time of the disturbance, we have a variation of the selection indicator I_s in order to switch between the 2 robust controllers $\tilde{\mathbf{K}}_f^1(s)$ and $\tilde{\mathbf{K}}_f^2(s)$. Therefore, from this switching, we observe from Figure 9 the calculation of new values of control signals V_{mp} and V_{my} in order to compensate and to cope with the manual disturbance. Finally, these Figures shows the robustness of the proposed global robust controller.

5 Conclusion

A DNRC algorithm of control of nonlinear MIMO systems was proposed using LSDP approach combined with RGA theory and GS technique which has been experimentally validated and proved to be a highly effective control strategy for handling model uncertainties and bounded external perturbations. This was clearly demonstrated through the case study using the 2 DoF laboratory helicopter. The

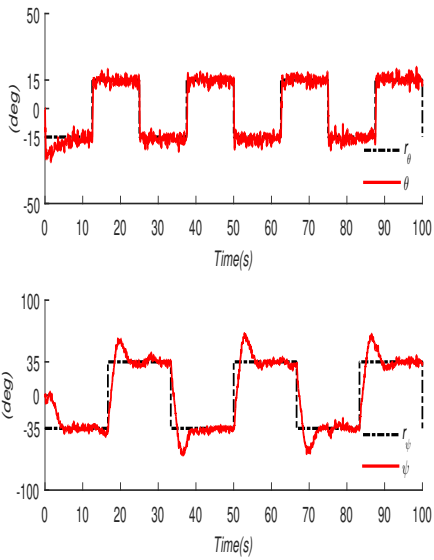


Figure 6
Evolution of output and reference signals without perturbation

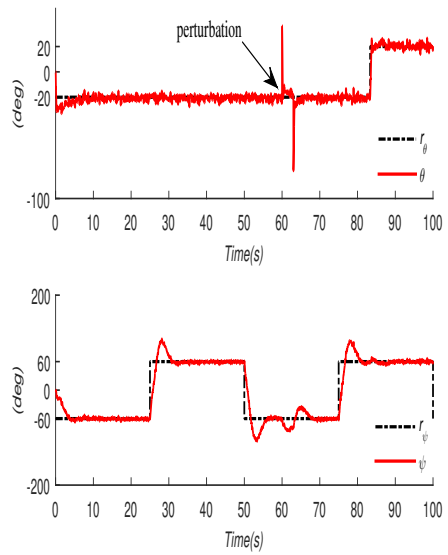


Figure 7
Evolution of output and reference signals with perturbation

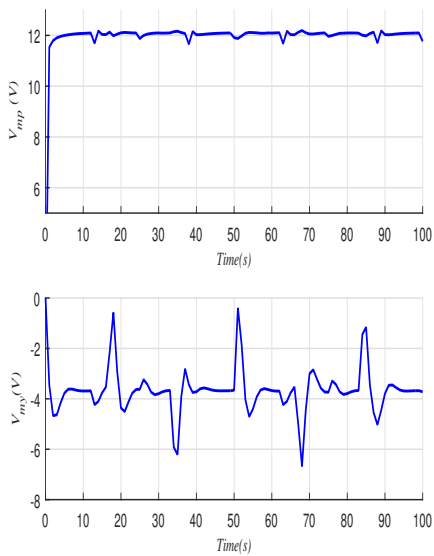


Figure 8
Evolution of control signals without perturbation

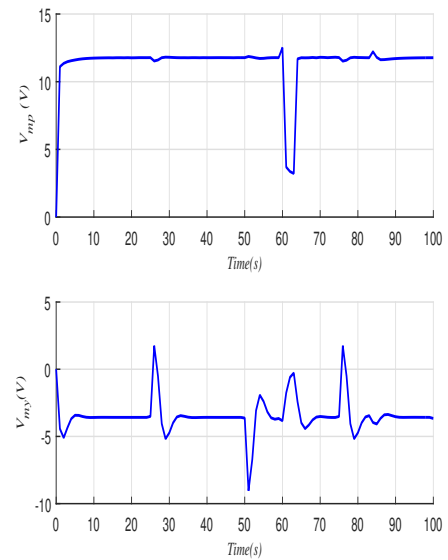


Figure 9
Evolution of control signals with perturbation

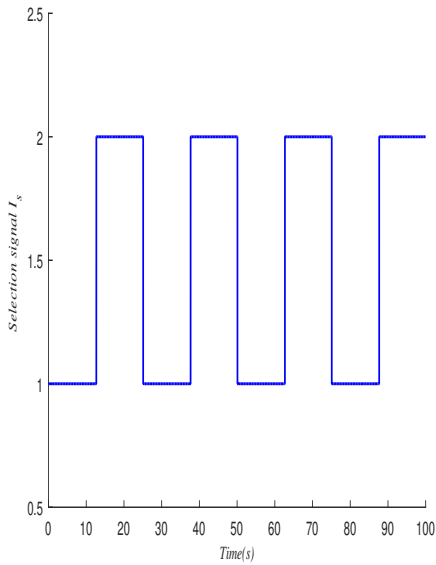


Figure 10
Evolution of the selection indicator I_s without perturbation

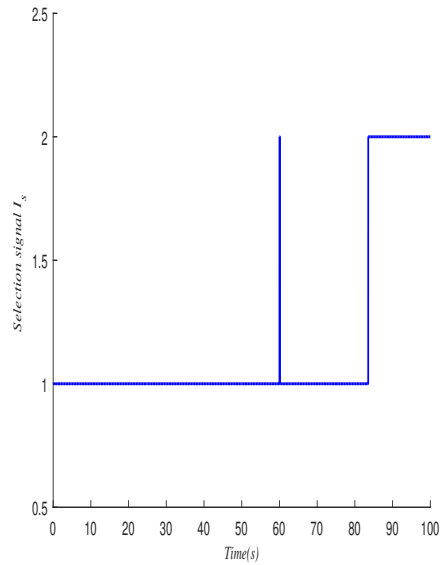


Figure 11
Evolution of the selection indicator I_s with perturbation

results show that the developed control strategy offers good performances in terms of robust stability, reference tracking and perturbation's rejection.

References

- [1] Hamdy, M., Ramadan, A. and Abozalam, B. (2018). A novel inverted fuzzy decoupling scheme for MIMO systems with disturbance: a case study of binary distillation column. *Journal of Intelligent Manufacturing*, 29(8), 1859-1871.
- [2] Moradvandi, A., Shahrokhi, M. and Malek, S. A. (2019). Adaptive fuzzy decentralized control for a class of MIMO large-scale nonlinear state delay systems with unmodeled dynamics subject to unknown input saturation and infinite number of actuator failures. *Information Sciences*, 475, 121-141.
- [3] Liu, L., Tian, S., Xue, D., Zhang, T., Chen, Y. and Zhang, S. (2019). A Review of Industrial MIMO Decoupling Control. *International Journal of Control, Automation and Systems*, 17(5), 1246-1254.
- [4] Scattolini, R. (2009). Architectures for distributed and hierarchical model predictive control—a review. *Journal of process control*, 19(5), 723-731.
- [5] Skogstad S and Postlethwaite I (2005) *Multivariable feedback control, Analysis and design*. John Wiley and sons, England.
- [6] Houppis, Constantine H, and Garcia-Sanz M (2012). *Wind energy systems: control engineering design*. CRC press.

- [7] Zhang J, Mei X, Zhang D, Jiang G and Liu Q (2013). Application of decoupling fuzzy sliding mode control with active disturbance rejection for MIMO magnetic levitation system. *Proceedings of the Institution of Mechanical Engineers, Part C: Journal of Mechanical Engineering Science*, 227(2), 213-229.
- [8] Kinnaert M (1995) *Interaction measures and pairing of controlled and manipulated variables for multiple-input-multiple-output systems: a survey*. *Journal A*, 36(4), 15-23.
- [9] van de Wal M and de Jager B (1995) *Control structure design: A survey*. In *American Control Conference, Proceedings* (Vol. 1, pp. 225-229). IEEE.
- [10] Bristol E (1966) *On a new measure of interaction for multivariable process control*. *IEEE transactions on automatic control*, 11(1), 133-134.
- [11] Khaki-Sedigh A and Moaveni B (2009) *Control configuration selection for multivariable plants* (Vol. 391). Springer.
- [12] Halvarsson B (2010). *Interaction Analysis in Multivariable Control Systems: Applications to Bioreactors for Nitrogen Removal* Acta Universitatis Upsaliensis. Uppsala Dissertations from the Faculty of Science and Technology 92. 162 pp. Uppsala. ISBN 978-91-554-7781-3.
- [13] Bequette, B. W. (2003). *Process control: modeling, design, and simulation*. Prentice Hall Professional.
- [14] Boza A S, Guerra R H and Gajate A (2011). Artificial cognitive control system based on the shared circuits model of sociocognitive capacities. A first approach. *Engineering Applications of Artificial Intelligence*, 24(2), 209-219.
- [15] Blažič S (2013). On periodic control laws for mobile robots. *IEEE transactions on industrial electronics*, 61(7), 3660-3670.
- [16] Takács Á, Kovács L, Rudas I, Precup R E and Haidegger T (2015). Models for force control in telesurgical robot systems. *Acta Polytechnica Hungarica*, 12(8), 95-114.
- [17] Apkarian J, Levis M, Fulford C (2012). *Usermanual of 2-DOF helicopter experiment setup and configuration*. Ontario, Canada: Quanser.
- [18] Halsey K M and Glover K (2005). Analysis and synthesis of nested feedback systems. *IEEE transactions on automatic control*, 50(7), 984-996.
- [19] Hernandez-Gonzalez M, Alanis A Y and Hernandez-Vargas E A (2012). Decentralized discrete-time neural control for a Quanser 2-DOF helicopter. *Applied Soft Computing*, 12(8), 2462-2469.
- [20] Samadi B and Rodrigues L (2014). A sum of squares approach to backstepping controller synthesis for piecewise affine and polynomial systems. *International Journal of Robust and Nonlinear Control*, 24(16), 2365-2387.

-
- [21] Nuthi P and Subbarao K (2015). Experimental verification of linear and adaptive control techniques for a two degrees-of-freedom helicopter. *Journal of Dynamic Systems, Measurement, and Control*, 137(6), 064501.
- [22] Khayati K (2015). Multivariable adaptive sliding-mode observer-based control for mechanical systems. *Canadian Journal of Electrical and Computer Engineering*, 38(3), 253-265.
- [23] Roman R C, Precup R E and David R C (2018). Second order intelligent proportional-integral fuzzy control of twin rotor aerodynamic systems. *Procedia computer science*, 139, 372-380.
- [24] Chang C M and Juang J G (2014). Real time TRMS control using FPGA and hybrid PID controller. In 11th IEEE International Conference on Control & Automation (ICCA) (pp. 983-988). IEEE.
- [25] Zeghlache S and Amardjia N (2018). Real time implementation of non linear observer-based fuzzy sliding mode controller for a twin rotor multi-input multi-output system (TRMS). *Optik*, 156, 391-407.
- [26] McFarlane D and Glover K (1990) *Robust Controller Design Using Normalized Coprime Factor Plant Descriptions* (Lecture Notes in Control and Information Sciences).
- [27] Georgiou T T and Smith M (1990). Optimal Robustness in the Gap Metric, *IEEE Transactions on Automatic Control*, Vol. 35, 6, 673-686.
- [28] Haj Salah A A, Garna T, Ragot J and Messaoud H (2016) *Transition and control of nonlinear systems by combining the loop shaping design procedure and the gap metric theory*. *Transactions of the Institute of Measurement and Control*, 38(8), 1004-1020.
- [29] Pohl, L. and Vesely, I. (2016). Speed control of induction motor using H linear parameter varying controller. *IFAC-PapersOnLine*, 49(25), 74-79.
- [30] Chen, C. L. and Tsai, M. C. (2018). Dynamic Switching of Two Degree-of-Freedom Control for Belt-Driven Servomechanism. *IEEE Access*, 6, 77849-77858.
- [31] Wang F C, Chen L S, Tsai Y C, Hsieh C H and Yen J Y (2014). Robust loop-shaping control for a nano-positioning stage. *Journal of Vibration and Control*, 20(6), 885-900.
- [32] Tijani, I. B., Akmeliawati, R., Legowo, A. and Budiyo, A. (2015). Optimization of an extended H-infinity controller for unmanned helicopter control using Multiobjective Differential Evolution (MODE). *Aircraft Engineering and Aerospace Technology: An International Journal*, 87(4), 330-344.
- [33] El-Gendy, E. M., Saafan, M. M., Elksas, M. S., Saraya, S. F. and Areed, F. F. (2019). New Suggested Model Reference Adaptive Controller for the Divided Wall Distillation Column. *Industrial and Engineering Chemistry Research*, 58(17), 7247-7264.

- [34] Pozna C and Precup R E (2018). An Approach to the Design of Nonlinear State-Space Control Systems. *Studies in Informatics and Control*, 27(1), 5-14.
- [35] Rugh W J and Shamma J S (2000) *Research on gain scheduling*. *Automatica*, 36(10), 1401-1425.
- [36] Kwon H Y and Choi H L (2014). *Gain scheduling control of nonlinear systems based on approximate input-output linearization*. *International Journal of Control, Automation and Systems*, 12(5), 1131-1137.
- [37] Wang Q, Zhou B and Duan G R (2015). Robust gain scheduled control of spacecraft rendezvous system subject to input saturation. *Aerospace Science and Technology*, 42, 442-450.
- [38] Yang Y and Yan Y (2016). Attitude regulation for unmanned quadrotors using adaptive fuzzy gain-scheduling sliding mode control. *Aerospace Science and Technology*, 54, 208-217.
- [39] Ghrab S et al. (2017). Robust discrete-time sliding mode control for systems with time-varying state delay and uncertainties on state and control input. *Transactions of the Institute of Measurement and Control*, 39(9), 1293-1312. DOI: 10.1177/0142331216636954.
- [40] Aksu, I. O. and Coban, R. (2019). Sliding mode PI control with backstepping approach for MIMO nonlinear cross-coupled tank systems. *International Journal of Robust and Nonlinear Control*, 29(6), 1854-1871. DOI: 10.1002/rnc.4469.
- [41] Taieb, A., Soltani, M., and Chaari, A. (2017). Parameter Optimization of MIMO Fuzzy Optimal Model Predictive Control By APSO, *Hindawi Complexity*, Volume 2017, <https://doi.org/10.1155/2017/5813192>.
- [42] Abdelwahed, I. B., Mbarek, A., and Bouzrara, K. (2017). Adaptive MPC based on MIMO ARX-Laguerre model. *ISA transactions*, 67, 330-347. <http://dx.doi.org/10.1016/j.isatra.2016.11.017>.
- [43] Benhammou A (1988) *Contribution à l'étude de la commande adaptative décentralisée des systèmes interconnectés*. PhD dissertation, Toulouse 3.
- [44] Lunze J (1992) *Feedback control of large scale systems*. Prentice Hall International (UK) Ltd, Germany.
- [45] Gagnon E (1999) *Commande Algébrique Décentralisée et Multivariable*. Ph.D Thesis, Laval University, Quebec.
- [46] Seborg D E, Mellichamp D A, Edgar T F & Doyle III F J (2010). *Process dynamics and control*, third editon. John Wiley & Sons.
- [47] Stilwell D J and Rugh W J (2000) *Stability preserving interpolation methods for the synthesis of gain scheduled controllers*. *Automatica*, 36(5), 665-671.

- [48] Leith D J and Leithead W E (1998) *Gain-scheduled controller design: an analytic framework directly incorporating non-equilibrium plant dynamics*. International Journal of Control, 70(2), 249-269.
- [49] Quanser (2019). Quanser QUARC Data Sheet. <https://quanserinc.app.box.com/s/gvsu5i63ytchc7z2zf0xpnrc9yib1wjs>. Ontario, Canada: Quanser.
- [50] Quanser (2019). Quanser QUARC Data Sheet. <https://quanserinc.box.com/shared/static/bkcgcyo1sl02r1a2mnvhg0zn4cecc6m8j.pdf>. Ontario, Canada: Quanser.

A Robust Controllers

$$\begin{aligned}
 K_{f,11}^1(s) &= \frac{4.327e^7s^8 + 4.475e^9s^7 + 1.978e^{11}s^6 + 3.618e^{12}s^5 + 2.851e^{13}s^4}{731s^9 + 1.828e^5s^8 + 2.108e^7s^7 + 1.185e^9s^6 + 3.033e^{10}s^5 + 3.022e^{11}s^4} \\
 &\quad \frac{+9.087e^{13}s^3 + 1.42e^{14}s^2 + 6.264e^{13}s + 8.192e^{12}}{+9.913e^{11}s^3 + 1.85e^{12}s^2 + 4.293e^{11}s} \\
 K_{f,22}^1(s) &= \frac{3.404e^6s^8 + 3.668e^8s^7 + 1.813e^{10}s^6 + 3.978e^{11}s^5 + 2.279e^{12}s^4}{731s^9 + 1.828e^5s^8 + 2.108e^7s^7 + 1.185e^9s^6 + 3.033e^{10}s^5 + 3.022e^{11}s^4} \\
 &\quad \frac{+4.853e^{12}s^3 + 1.024e^{13}s^2 + 5.699e^{12}s + 8.733e^{11}}{+9.913e^{11}s^3 + 1.85e^{12}s^2 + 4.293e^{11}s}
 \end{aligned} \tag{30}$$

$$\begin{aligned}
 K_{f,11}^2(s) &= \frac{4.467e^7s^8 + 4.767e^9s^7 + 2.235e^{11}s^6 + 4.599e^{12}s^5 + 4.246e^{13}s^4}{660.4s^9 + 1.587e^5s^8 + 1.813e^7s^7 + 1.035e^9s^6 + 2.78e^{10}s^5 + 3.023e^{11}s^4} \\
 &\quad \frac{+1.595e^{14}s^3 + 2.425e^{14}s^2 + 9.24e^{13}s + 1.021e^{13}}{+1.05e^{12}s^3 + 2.143e^{12}s^2 + 5.033e^{11}s} \\
 K_{f,22}^2(s) &= \frac{2.68e^6s^8 + 3.447e^8s^7 + 2.002e^{10}s^6 + 4.725e^{11}s^5 + 2.745e^{12}s^4}{660.4s^9 + 1.587e^5s^8 + 1.813e^7s^7 + 1.035e^9s^6 + 2.78e^{10}s^5 + 3.023e^{11}s^4} \\
 &\quad \frac{+5.871e^{12}s^3 + 1.244e^{13}s^2 + 7.04e^{12}s + 1.092e^{12}}{+1.05e^{12}s^3 + 2.143e^{12}s^2 + 5.033e^{11}s}
 \end{aligned} \tag{31}$$

Performance Assessment of Phenolic-based Non-Asbestos Organic Brake Friction Composite Materials with Different Abrasives

Tej Singh¹, Amar Patnaik², Ranchan Chauhan³, István Bíró⁴,
Endre János¹, Gusztáv Fekete¹

¹Savaria Institute of Technology, Eötvös Loránd University, Károlyi Gáspár tér 4, H-9700 Szombathely, Hungary; sht@inf.elte.hu, je@inf.elte.hu, fg@inf.elte.hu

²Department of Mechanical Engineering, Malaviya National Institute of Technology Jaipur, Jawahar Lal Nehru Marg, Jhalana Gram, Malviya Nagar, Jaipur, Rajasthan-302017, India; apatnaik.mech@mnit.ac.in

³Department of Mechanical Engineering, Dr. B.R. Ambedkar National Institute of Technology Jalandhar, Grand Trunk Road, Bye pass, Jalandhar, Punjab-144011, India; chauhanr@nitj.ac.in

⁴Institute of Technology, University of Szeged, Mars tér 4, H-6724 Szeged, Hungary; biro-i@mk.u-szeged.hu

Abstract: This research article presents the effects of different abrasives (aluminium oxide, magnesium oxide, zinc oxide, iron oxide, silicon dioxide, titanium dioxide and zirconium dioxide) on tribological performance of non-asbestos brake friction materials. Therefore, friction composites with different abrasives were fabricated and characterized for various mechanical, chemical, and physical properties. The tribological properties of the friction composites were evaluated by running a European testing standard on a Krauss testing machine. It was seen that the different sorts of abrasives substantially affected the tribological performance of the friction composites. The highest values of friction coefficient (0.425), least friction fluctuations (0.252), highest stability coefficient (0.87) as well as the lowest fade (~ 23%) were obtained from the friction composites containing aluminum oxide as an abrasive. The recovery performance of all the friction composites was found to exceed 100% and the actual recovery level depends upon the type of abrasive. Contrary to the friction performance, the wear performance decreased for aluminum oxide and friction composite containing zinc oxide showed higher wear resistance.

Keywords: Polymer composites; Friction materials; Abrasive; Fade; Recovery; Wear

1 Introduction

Composite materials used for automotive/locomotive brake systems usually contain property modifiers to enhance friction performance and to improve their wear resistance [1-4]. Abrasives, classified as property modifiers, are hard particles used in friction composite materials to enhance the friction performance [5]. They make the composites stable at elevated temperatures, while during the abrasive process, they remove the pyrolyzed surface film from the counterface disc [6, 7]. A perfect selection of an abrasive along with its type, shape, amount, size, and its closeness with other components in the formulation contributes to the better execution of any friction composite [8]. During braking, abrasive particles work at the tribo-interface either as a two-body or three-body abrasion model, while having a significant effect on friction and wear performance [9, 10]. In addition, rotor wear or rotor thickness variation may also appear, which is produced by the rubbing of brake pads against the rotor during sliding. It must be mentioned that the main culprit of braking noise is most likely credited to this effect [11]. Therefore, a careful selection of abrasives for brake friction materials is vital as it is an essential ingredient for the enhancement of friction, controlling the wear of tribo-couple, friction fluctuation, and noise-related problems generated during braking [12].

The vast majority of the literature referenced the individual aspect of particular abrasives e.g. aluminium oxide [12], zircon [13], silicon carbide [14], quartz [15], silicon dioxide [16], while comparative features of abrasives were also reported [17]. V. Tomasek et al. [12] concluded that an abrasive (aluminium oxide, average size of 100 mesh) addition in friction formulation not only helps in minimizing the negative wear rate, but it also helps in upgrading the friction performance. While studying the size effect of zircon particles (1, 6, 75, and 150 μm , respectively), K. H. Cho et al. [13] concluded that fade and friction instability remained the most significant in the friction composite having the smallest sized zircon particles with large frictional fluctuations and considerable wear. Fade resistance improved when coarse zircon particles were used. The composites exhibited excellent friction stability, however, the counter-face wear increased significantly as well. V. Matejka et al. [14] reported dissimilar results for silicon carbide filled composites. The authors studied the effect of silicon carbide particle size (3, 10, and 40 μm , respectively) on the tribological attributes of non-asbestos brake materials. The authors observed that the presence of 3 μm silicon carbide particles is responsible for highest friction performance accompanied with lowest fade. Authors observed that the specific wear rate decreases with increasing silicon carbide particle size. In another investigation, E. J. Lee et al. [15] explored the tribological behaviour of zircon (13.7, 133.1 μm) and quartz (20.6, 277.8 μm) filled friction composites where the addition of the quartz proved to be best from the coefficient of friction point of view.

Moreover, they observed that smaller particles were proven effective in increasing the friction performance while large particles inclusion produced higher disc wear. In a recent study, W. Sun et al. [16] investigated the influence of different silicon dioxide abrasive particles, (10, 80, 180-700, 700-2000, and 2000-3000 μm , respectively) in non-commercial friction composite materials. They observed that silicon dioxide particle size has a considerable influence on the friction mechanism of such composites. Higher contact films were observed for 10 μm particle-based composites, which reported to stabilize the friction performance. Authors also suggested that 80 μm particles usually work according to the three-body abrasive mechanism, 180-2000 μm sized particles can work as mixed two-body and three-body abrasive mechanisms, while 3000 μm sized particles usually work according to two-body abrasive mechanism. In addition, Bijwe et al. [17] compared tribological performance of micro and nano-abrasives (aluminium oxide: 40-80 nm and 48-100 μm , silicon carbide: 50-60 nm and 3-100 μm , silicon dioxide: 15 nm and 3 μm) of tribological performance of friction composites. They claimed that the formation of friction film on nano-abrasive filled composite mainly contributed in increased performance. B. K. Satapathy and J. Bijwe [18] investigated the influence of working parameters (sliding speed and braking pressure) on wear performance of different abrasives (silicon carbide, silicon dioxide, zircon dioxide, and aluminium oxide) filled friction materials. They revealed that comparatively to zircon dioxide, aluminium oxide and silicon dioxide-based friction composites remained less sensitive to working parameters.

Despite the above-mentioned studies, it is still challenging to describe the role of abrasives on the fade, recovery, friction stability, and variability aspects of brake friction materials. Therefore, it highly important to conduct a study to compare the tribo-performance of abrasives filled brake friction materials. Consequently, the present work is conducted to investigate the role of abrasives on the tribo-execution of automotive brake materials. Tribo-execution of the brake materials was completely assessed utilizing ECR-90 run.

2 Materials and Methods

2.1 Materials and Composite Fabrication

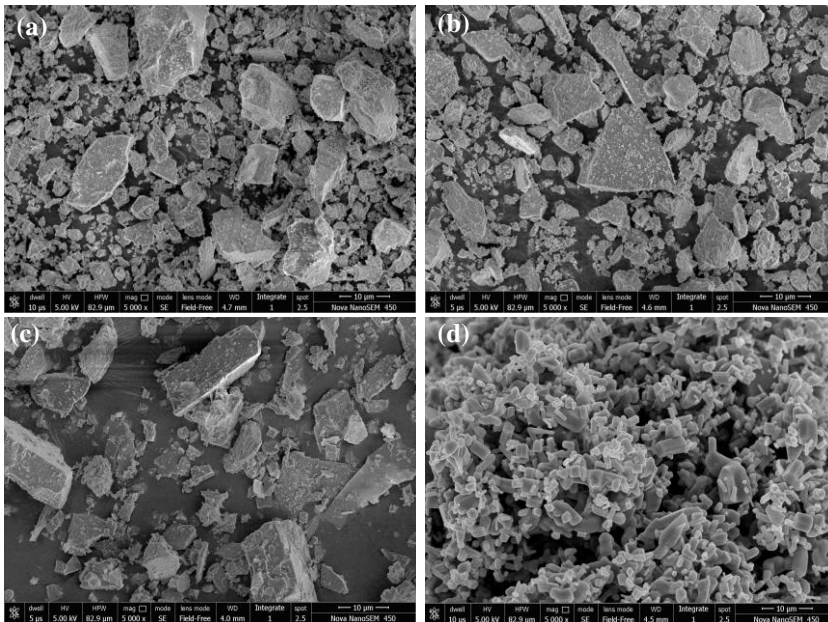
Ingredients such as Kevlar fiber, phenolic resin, graphite, barium sulphate, lapinus fiber, potassium titanate, vermiculite and abrasives (aluminium oxide, magnesium oxide, zinc oxide, iron oxide, silicon dioxide, titanium dioxide and zirconium dioxide) according to the compositional variations, as presented in Table 1, were used in the fabrication of brake composites. The ingredients were purchased from Starke International New Delhi, India.

The literature reveals that smaller sized abrasive particles develop a contact film, which stabilizes the friction performance and increase the wear resistance [14-17]. Hence, in this current study abrasives with an average size of 400 mesh were selected. The scanning electron micrographs of the selected abrasives are shown in Figure 1.

Table 1
Details of friction composites composition and nomenclature

Composition (wt.%)	Composite designation							
	MO-0	MO-1	MO-2	MO-3	MO-4	MO-5	MO-6	MO-7
*Parent composition	95	95	95	95	95	95	95	95
Barium sulphate	5	0	0	0	0	0	0	0
Aluminium oxide	0	5	0	0	0	0	0	0
Magnesium oxide	0	0	5	0	0	0	0	0
Zinc oxide	0	0	0	5	0	0	0	0
Iron oxide	0	0	0	0	5	0	0	0
Silicon dioxide	0	0	0	0	0	5	0	0
Titanium dioxide	0	0	0	0	0	0	5	0
Zirconium dioxide	0	0	0	0	0	0	0	5

*Parent composition: Barium sulphate-50 wt.%, graphite-5 wt.%, fibers (Kevlar, lapinus; 1:2)-15 wt.%, potassium titanate-5 wt.%, vermiculite-5 wt.% and phenolic resin-15 wt.%.



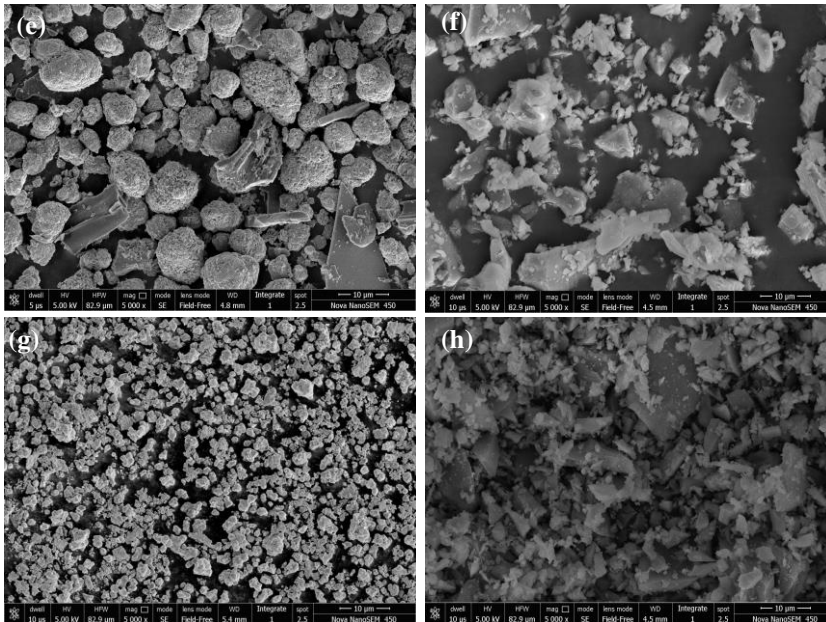


Figure 1

Scanning electron micrographs of (a) Barium sulphate (b) Aluminium oxide (c) Magnesium oxide (d) Zinc oxide (e) Iron oxide (f) Silicon dioxide (g) Titanium dioxide and (h) Zirconium oxide

The parent composition was always constant with 95 wt.% amount and 5 wt.% of abrasive was added to each composite. For comparison, an abrasive-free composite was also fabricated by adding 5 wt.% barium sulphate in the parent composition. To achieve mechanical isotropy, selected materials were blended in a mechanical mixer for 10 min [19]. The blend was put into a mold supported by the adhesive-coated steel back plates. The mold was then heat treated/cured at 155 °C of temperature for 10 min with 15 MPa pressure using a compression-molding machine [20]. After that, the brake pad composites were relieved in an oven at 170 °C for 4 h and used for different (mechanical, chemical, physical and tribological) characterizations.

2.2 Characterization of Mechanical, Chemical and Physical Properties

The density of the composites was determined with the help of the Archimedes principle, whereas a standard protocol JIS D 4418:1996 was used for porosity measurement [21]. The ash content was determined by scorching the composite specimen at ~800 °C of temperature. Soxhlet extraction was used for determining the acetone extraction (quantity of uncured resin) present in the composites.

Hardness investigation was done with the help of Rockwell hardness tester according to the ASTM D785 standards. Shear strength of the fabricated friction composite specimens was measured according to ISO 6312 whereas ISO 6310 was used for compressibility measurements.

2.3 Tribological Properties Evaluation

The tribological properties of the developed composites were assessed by running ECR (Economic Commission for Europe) R-90 procedure on Krauss machine. The detailed description of the machine and testing schedule is reported elsewhere [18-20]. The nominal braking pressure of 2 MPa and a speed of 660 rpm on the disc were applied following the regulation of the standard ECR R-90 test protocol which consists of seven cycles of ten brakes each for tribological properties assessment. The braking duration was 10 s and a 10 s interval was maintained between two successive brakes. Prior to seven test cycles, a bedding cycle of 30 brakes was initiated to ensure uniform contact between brake pad and disc. After the bedding cycle, the cold friction cycle began with 45 °C initial temperature while fans were employed to control the generated frictional heat of the disc. The cold cycle was trailed by five back-to-back fade cycles. At the beginning of each fade cycle, the disc temperature was kept under 100 °C and then permitted to rise progressively until the end of 10 brakes. Finally, after completion of the fifth fade cycle, the recovery cycle started by keeping up comparative conditions for fade cycles with air fan on. The wear of the friction composite was measured in terms of thickness and weight loss. For every composite specimen, three trials were conducted and the outcomes were inside 95% of certainty level.

3 Results and Discussion

3.1 Results of Mechanical, Physical and Chemical Properties

The evaluated properties of the composites specimens are presented in Table 2. It was observed that density ($\sim 2.26 \pm 0.04$ g/cm³) and porosity ($\sim 7.42 \pm 0.72\%$) of the tested composites remained broadly unaffected with compositional variations. On the other hand, the acetone extraction was found to be negligible and nearly equivalent ($\sim 0.32 \pm 0.09\%$) in all the tested composites and might be ascribed to the presence of an equal amount of organic content. Furthermore, the unchanged organic content in the composites resulted in almost equivalent ash content $\sim 72.18 \pm 1.96\%$. Hardness, compressibility and shear strength of the composites have been seen to stay in the range of $\sim 104 \pm 2.5$ in the L-scale, $\sim 0.90 \pm 0.12\%$ and $\sim 836 \pm 74$ kgf respectively.

Table 2
Physical, mechanical and chemical properties of friction composites

Properties	MO-0	MO-1	MO-2	MO-3	MO-4	MO-5	MO-6	MO-7
Density (g/cm ³)	2.28	2.27	2.24	2.30	2.29	2.22	2.23	2.30
Porosity (%)	7.56	7.78	7.44	6.70	8.14	7.84	7.16	7.18
Acetone extraction (%)	0.36	0.42	0.27	0.23	0.38	0.42	0.26	0.34
Ash content (%)	70.22	70.81	74.02	73.01	71.69	73.21	73.06	74.14
Shear strength (kgf)	762	875	890	795	910	825	900	835
Compressibility (%)	0.78	0.96	0.80	0.86	1.02	0.92	0.98	0.82
Hardness (HRL)	101.50	102.83	103.67	102.33	106.5	103.83	104.50	102.5

3.2 Braking Performance Response of the Composites

The coefficient friction (μ) and the corresponding temperature of the disc with respect to braking cycles (cold, fade and recovery) are depicted in Figure 2. It is clear that all the composites displaying the fluctuating/unsteady frictional response in cold cycle. As observed in Figure 2a for MO-0, the μ rose continuously until the third braking, and then it began diminishing until the 10th braking. This phenomenon was observed in the first three fade cycles, while some enhancement appeared later in two fade cycles. From Figure 2b, one can see that the first fade cycle behaviour of MO-1 and MO-0 is similar. However, in further fade cycles, the μ curve becomes flattered demonstrating good performance of MO-1. While for friction composite MO-2 (Figure 2c) appreciable fade was seen after the third braking onwards for the first two fade cycles, while the sharpness of the slope diminished and completely vanished during the fourth and the fifth fade cycles. For MO-3 and MO-4 (Figures 2d and 2e) composites, the friction performance remained wildly fluctuating.

Abrupt friction peaking with steeper friction-decay was observed in the first four fade cycles of MO-3 and MO-4 composites. However, in the fifth fade run, the μ response showed some signs of improvement. In the case of friction composite MO-5, as seen from Figure 2f, μ climbed continuously until the third braking and it began diminishing sharply until the 10th braking for the first three fade cycles and it demonstrated some enhancement in the last two fade cycles. Severe fade for MO-6 (Figure 2g) was seen in the first two fade runs after the third braking. From the third fade run, onwards a consistent friction build-up was observed with adequate friction-peaking effects without any substantial friction-decay. For MO-7 (Figure 2h), in the first fade cycle fade was observed after the third while for the next two fade cycles fade was seen after fourth braking. In the last two fade cycles of MO-7, the μ curve becomes flattered indicating improved fade performance.

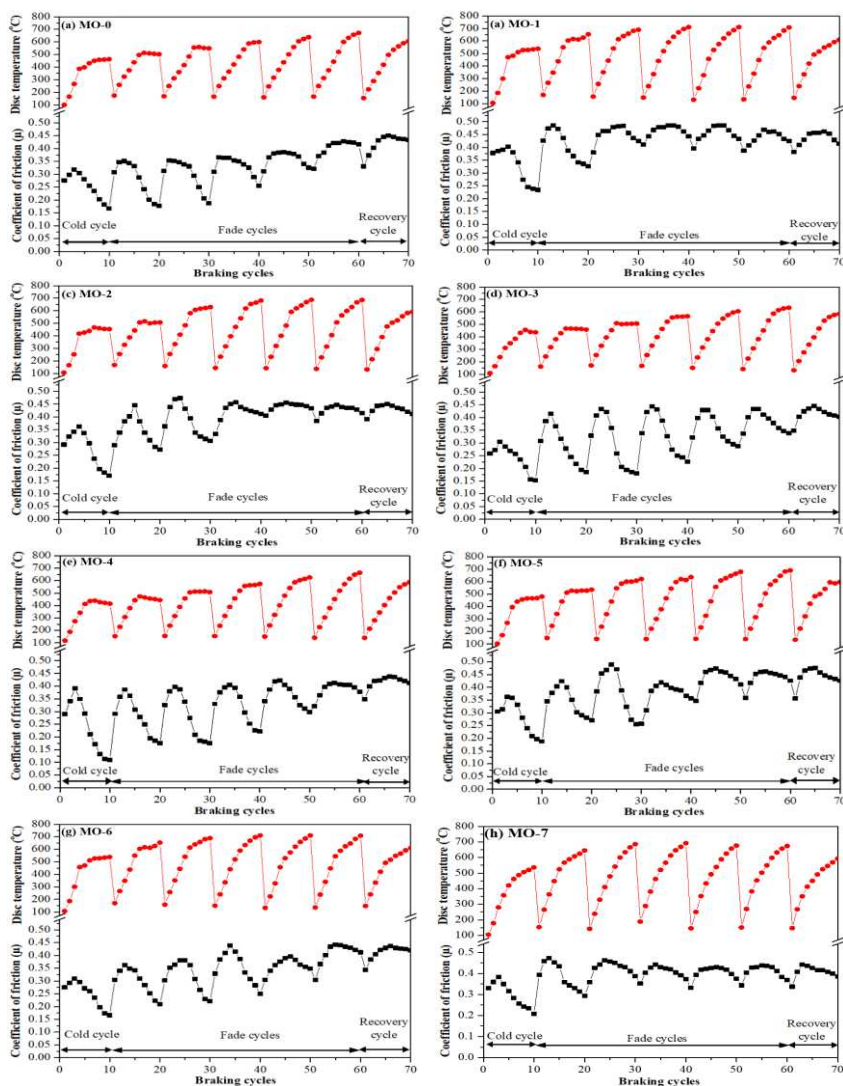


Figure 2

The coefficient of friction and disc temperature of the composites with respect to braking cycles

3.3 μ_P -performance (μ_P), μ_F -fade (μ_F), μ_R -recovery (μ_R) and Friction Fluctuations (μ_{\max} - μ_{\min})

The μ_P , μ_F and μ_R outcomes of the tested composites are depicted in Figure 3. μ_P is the average value of μ registered for seven cycles whereas, μ_F and μ_R are the minimum and maximum μ values registered for the fade and recovery cycles

respectively [22, 23]. In friction composite containing no abrasive i.e. MO-0, the frictional outputs (μ_P and μ_F) reflected at 0.335 and 0.178 respectively. However, the addition of abrasives has caused discrete changes in terms of their μ_P and μ_F outputs. It was observed that the inclusion of zinc oxide, iron oxide, and titanium dioxide resulted in almost similar μ_P (0.328-0.344) and μ_F (0.175-0.209) outputs. In addition, magnesium oxide, silicon dioxide and zirconium dioxide-based formulations resulted in higher μ_P (0.385-0.390) and μ_F (0.270-0.284) outputs while μ_P (0.425) and μ_F (0.326) were observed to be the highest for the aluminium oxide-based friction composites.

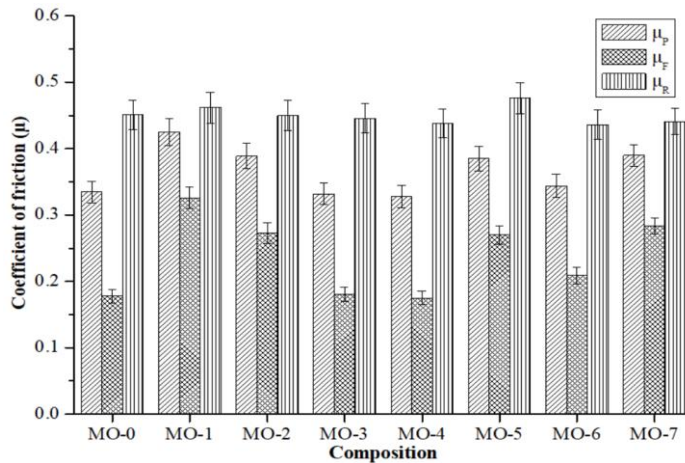


Figure 3

μ_P , μ_F and μ_R performance of the composites

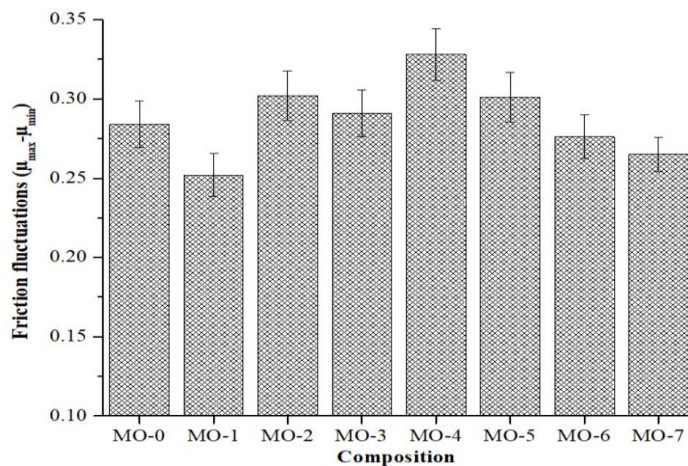


Figure 4

Friction fluctuations of the composites

Further, the μ_R was observed in the range of 0.436-0.476, which remained fairly comparable for all the friction composites irrespective of the abrasive. Such a performance theoretically suggests a similarity in the friction film creation/restoration process, which is initiated by organic ingredients and graphite having the same content in the friction formulations [24]. The frictional fluctuations as indicated by $\mu_{\max}-\mu_{\min}$ have been seen to be reliant upon the composition (Figure 4). It was seen that the composite that had the highest coefficient of friction (0.425) brought about the least friction fluctuations (0.252) as compared to the other investigated composites. The addition of aluminium oxide to friction material formulations not only helps in reducing the frictional fluctuations, i.e. $\mu_{\max}-\mu_{\min}$ but also resulted in enhanced μ_P and μ_F with a good recovery response.

3.4 Friction Stability and Variability

The stability and variability coefficients of the friction composite are presented in Figure 5. These two parameters were significant for the assessment of friction composite materials and calculated as follows [25, 26]:

$$\text{Stability coefficient} = \frac{\mu_P}{\mu_{\max}} \quad (1)$$

$$\text{Variability coefficient} = \frac{\mu_{\min}}{\mu_{\max}} \quad (2)$$

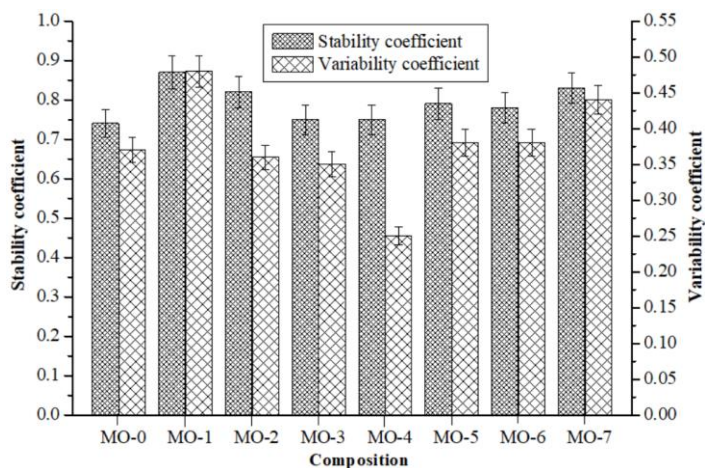


Figure 5

Stability and variability coefficients of the composites

A friction composite is rated superior for higher values of stability and variability coefficients. It was seen that the aluminium oxide-based composite, i.e. MO-1 demonstrating the highest friction performance also resulted in higher stability (0.87) and variability coefficients (0.48). The stability and variability coefficients were remaining lowest for MO-0 and MO-4 composites. The friction stability stayed nearly 0.74 for MO-0; however, the stability of various explored composites has appeared well above 0.75. This indicates that with the addition of abrasives the friction film stability/integrity is improved and the degree of heterogeneity in the friction layer will in general decline. It was observed that the friction composite MO-1 had the highest μ -performance resulting in the higher stability and variability coefficient with less fluctuation when compared to the other friction composites.

3.5 Fade, Recovery and Disc Temperature

The performance of investigated friction composites in terms of %-fade and %-recovery is presented in Figure 6. It is seen that the %-fade remains maximum (~47%) for the composition MO-0, whereas for MO-1, which has aluminium oxide as abrasive, it decreases drastically and the fade remains the lowest (~23%). The %-recovery of the investigated composites remains appreciably high (~108-135%) as prescribed by IS-2742 standard. Strikingly both the %-fade and %-recovery remained highest for MO-0 composite demonstrating that the fade-recovery characteristics were greatly affected by the nature of friction film formation. The abrasive particles in the composition try to grind down the film formed on the surface by the decomposition of the organic constituents.

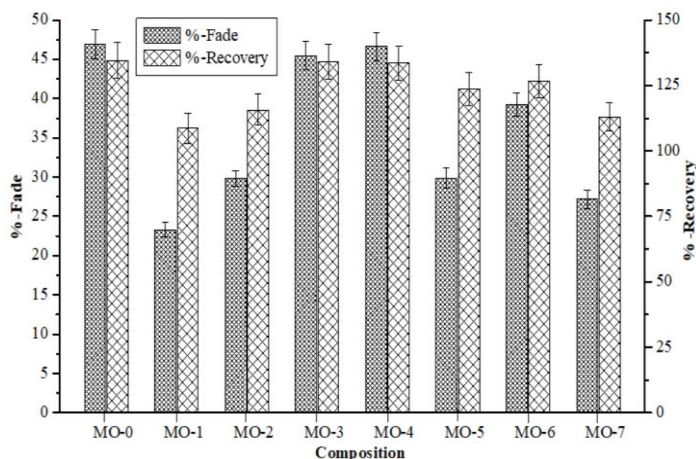


Figure 6

Variation of %-fade and %-recovery of the composites

The lowest %-fade (~23%) in spite of the highest disc temperature might be ascribed to the presence of hard aluminium oxide that minimizes/arrests the temperature-induced friction decay effect. The %-recovery performance of the studied friction composites specimens stayed in between 108-135%. The composite, MO-0 without any abrasive showing maximum fade (~47%), and it also exhibits the maximum recovery (~135%). The %-recovery performance mainly depends upon the friction/contact film deposited on the composite surface after the completion of the fifth fade cycle. Within the initial few brakings of the recovery cycle, this friction film will disintegrate into wear debris. With further brakings, these wear debris become entrapped between the composite and disc interface, which will enhance the friction performance according to the third body abrasion mechanism [27, 28]. Hence, the abrasive not only improves the μ -performance of the friction composites, but it also improves the μ -fade. The level of improvement depends upon the type of abrasive used in the composition. Moreover, the disc temperatures remained highest for MO-1 composite (710 °C), closely followed by MO-2, MO-5, and MO-7 (689.5 ± 2.5 °C, See Figure 7). The disc temperature remained lowest for the composite MO-3 (633 °C) whereas for composites MO-0, MO-4, and MO-6 the disc temperature remained between 668 ± 4 °C. This temperature (687 - 710 °C) build-up phenomenon in aluminium oxide (MO-1), magnesium oxide (MO-2), silicon dioxide (MO-5) and zirconium dioxide (MO-7) filled composites was sufficiently complemented by a higher μ -performance (0.385 - 0.425) response with reduced %-fade (~23-30%).

In addition, MO-0, MO-3, MO-4, and MO-5 composites have indicated higher degrees of %-fade (~40-47%), which additionally had an immediate association with lower disc temperature (633-672 °C). Thus, %-fade and %-recovery performance attributes were observed to be reliant on the utilized abrasives and they played a central role as performance determinants.

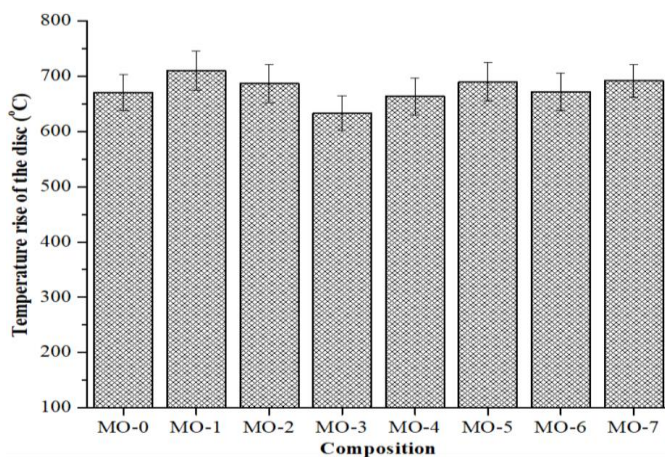


Figure 7

Disc temperature of the composites

3.6 Wear Performance of Composites

The wear performance (in terms of weight and thickness loss) is depicted in Figure 8. In general, component wear is obtained by normalizing the weight and thickness change of composite specimen before and after testing. The wear of composite MO-1 with aluminium oxide was the highest and that of composite MO-1 with zinc oxide was the lowest. The ingredients with high hardness such as aluminium oxide, magnesium oxide, silicon dioxide, and zirconium dioxide increase the wear of the friction composites due to their abrasive action against the sliding junction. The improved wear performance of MO-3 with zinc oxide may be due to its inherent wear resistance with a lower hardness that prevents the abrasion effect [29].

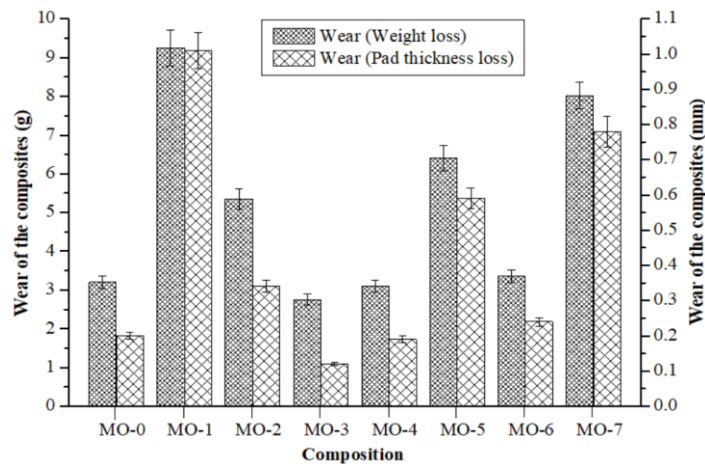


Figure 8

Wear of the composite

3.7 Worn Surface Morphology

The wear performance of the composite was further correlated with its worn surface as presented in Figure 9. It was reported in the literature that the extent of wear was mainly dependent upon the formation of contact plateaus (primary and secondary) on the composite surface [30-32]. The primary contact plateaus were originated by the embedment of hard ingredients in the composite surface. The secondary contact plateaus (generally the smooth glazy patches) were originated by the degradation of organic ingredients. The primary contact plateaus were reported to enhance the friction performance while secondary contact plateaus were reported to enhance wear performance of the composites [33-36].

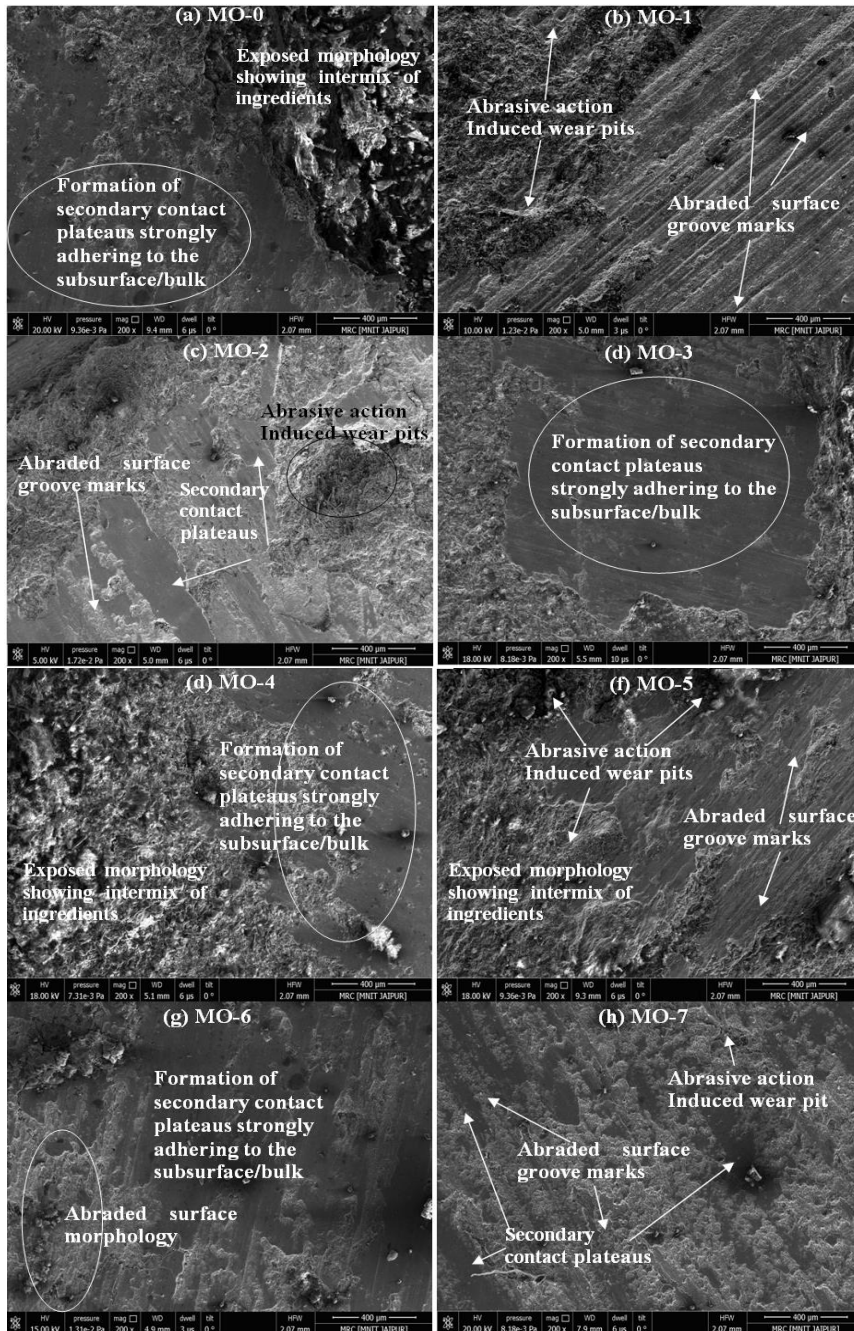


Figure 9
Worn surface morphology of the composites

It was observed that aluminium oxide (MO-1, Figure 9b), magnesium oxide (MO-2, Figure 9c), silicon dioxide (MO-5, Figure 9f) and zirconium dioxide (MO-7, Figure 9h) inclusion in friction composites resulted in a deterioration in the topography of surfaces. The abrasive action led to the formation of wear pits in these composites indicating that harder constituents encountered during braking result in a higher friction level ($\sim 0.405 \pm 0.020$) with lower wear performance ($\sim 7.83 \pm 1.42$ g). The worn surface of the composite MO-1 (Figure 9b) demonstrated harsh surface topography with considerably less degree of secondary contact plateaus suggesting a higher wear rate. Furthermore, with magnesium oxide (MO-2, Figure 9c), silicon dioxide (MO-5, Figure 9f), and zirconium dioxide (MO-7, Figure 9h) the worn surface topography remains rough. It must be mentioned, that the extent of secondary plateaus increased while the deterioration of primary ingredients decreased, resulting in their increased wear performance to that of an aluminium oxide-based composite. It can be seen that there were no significant differences in the worn surface topographies of the friction composites MO-0 (Figure 9a), MO-4 (Figure 9e) and MO-6 (Figure 9g). The worn surfaces of these composites showed smooth surface topography and higher secondary contact plateaus compared with the friction composites MO-1, MO-2, MO-5, and MO-7 resulting in their moderate wear rate. The worn surface of the friction composite MO-3 (Figure 9d) was covered extensively with the secondary contact plateaus. These secondary plateaus covered the composite surface to a larger amount, which minimizes the loss of the ingredients during sliding resulting in the lowest wear and the second-lowest friction performance.

Conclusions

The physical, mechanical, chemical, and tribological properties of brake friction composites containing different types of abrasives have been evaluated as per industrial norms. The following conclusions were achieved from the above investigations:

- The investigated physical, chemical, and mechanical properties broadly remain unaffected and do not follow any specific trend.
- The developed composites showed a coefficient of friction in the range of 0.30-0.45, which is in the desired range of industrial practice. The highest performance for the coefficient of friction, best fade performance, least friction fluctuations with the best stability and variability coefficient values were obtained in the composite containing aluminium oxide as abrasive.
- Parent composition suffered highest the fade and exhibits the highest recovery, which was reduced to their lowest level by the inclusion of aluminium oxide. Interestingly zinc oxide and iron oxide did not influence the fade and recovery properties of the parent composition appreciably. Whereas magnesium oxide, silicon dioxide, and zirconium dioxide-based composites exhibit fade and recovery performance next to aluminium oxide based

composites. All the composites irrespective of the abrasives have shown more than 100% recovery.

- The inclusion of zinc oxide and iron oxide helped improve the wear performance of the parent composition. Zinc oxide performed to be the best in this respect, while the incorporation of aluminium oxide proved detrimental.

Overall, it was concluded that the type of abrasive in brake friction composite materials influences the tribological properties drastically. Aluminium oxide appeared to be the best performing abrasive followed by zirconium dioxide, magnesium oxide and silicon dioxide.

Acknowledgment

This paper was supported by: Eötvös Loránd University, Malaviya National Institute of Technology Jaipur, Dr. B. R. Ambedkar National Institute of Technology Jalandhar, and the University of Szeged.

References

- [1] J. Bijwe: Composites as friction materials: Recent developments in non-asbestos fibre reinforced friction materials- a review, *Polymer Composites*, Vol. 18, No. 3, 1997, pp. 378-396
- [2] W. Zhen-yu, W. Jie, C. Feng-hong, M. Yun-hai, T. Singh, G. Fekete: Influence of banana fiber on physicochemical and tribological properties of phenolic based friction composites, *Materials Research Express*, Vol. 6, 2019, 075103
- [3] P. Wasilewski: Experimental study on the effect of formulation modification on the properties of organic composite railway brake shoe, *Wear*, Vol. 390-391, 2017, pp. 283-294
- [4] L. Lendvai, D. Brenn: Mechanical, Morphological and Thermal Characterization of Compatibilized Poly(lactic acid)/Thermoplastic Starch Blends, *Acta Technica Jaurinensis*, Vol. 13, No. 1, 2020, pp. 1-13
- [5] T. Singh: Tribo-performance evaluation of fibre reinforced and nano-filled composite friction materials, PhD Thesis, N.I.T. Hamirpur, 2013
- [6] M. Vlastimil, S. M. Grażyna, Y. Ma, Y. Lu: Semimetallic brake friction materials containing ZrSiO₄: friction performance and friction layers evaluation, *Journal of Composite Materials*, Vol. 43, No. 13, 2009, pp. 1421-1434
- [7] I. Sugozy, I. Mutlu, K. B. Sugozy: The effect of ulexite to the tribological properties of brake lining materials, *Polymer Composites*, Vol. 39, No. 1, 2018, pp. 55-62
- [8] R. Yun, G. M. Simha, L. Yafei: Performance and evaluation of nonasbestos organic brake friction composites with SiC particles as an abrasive, *Journal of Composite Materials*, Vol. 45, No. 15, 2011, pp. 1585-1593

-
- [9] T. Sasada, M. Oike, N. Emori: The effect of abrasive grain size on the transition between abrasive and adhesive wear, *Wear*, Vol. 97, 1984, pp. 291-302
- [10] T. Singh, R. Chauhan, A. Patnaik, B. Gangil, R. Nain, A. Kumar: Parametric study and optimization of multiwalled carbon nanotube filled friction composite materials using taguchi method, *Polymer Composites*, Vol. 39, No. S2, 2018, pp. E1109-E1117
- [11] Y. Ma, G. S. Martynkova, M. Valaskova, M. Vlastimil, L. Yafei: Effects of $ZrSiO_4$ in non-metallic brake friction materials on friction performance, *Tribology International*, Vol. 41, 2008, pp. 166-174
- [12] V. Tomasek, G. Kratosova, R. Yun, F. Yanli, L. Yafei: Effects of alumina in non-metallic brake friction materials on friction performance, *Journal of Materials Science*, Vol. 44, 2009, pp. 266-273
- [13] K. H. Cho, H. Jang, Y. S. Hong, S. J. Kim, R. H. Basch, J. W. Fash: The size effect of zircon particles on the friction characteristics of brake lining materials, *Wear*, Vol. 264, 2008, pp. 291-297
- [14] V. Matejka, Y. Lu, L. Jiao, H. Li, S. M. Grażyna, T. Vladimír: Effects of silicon carbide particle sizes on friction-wear properties of friction composites designed for car brake lining applications, *Tribology International*, Vol. 43, 2010, pp. 144-151
- [15] E. J. Lee, H. J. Hwang, W. G. Lee, K. H. Cho, H. Jang: Morphology and toughness of abrasive particles and their effects on the friction and wear of friction materials: a case study with zircon and quartz, *Tribology Letters*, Vol. 37, No. 3, 2009, pp. 637-644
- [16] W. Sun, W. Zhou, J. Liu, F. Xuesong, C. Guoqing, Y. Shan: The size effect of SiO_2 particles on friction mechanisms of a composite friction material, *Tribology Letters*, Vol. 66, 2018, p. 35
- [17] J. Bijwe, N. Aranganathan, S. Sharma, N. Dureja, R. Kumar: Nano-abrasives in friction materials-influence on tribological properties, *Wear*, Vol. 296, 2012, pp. 693-701
- [18] B. K. Satapathy, J. Bijwe: Wear data analysis of friction materials to investigate the simultaneous influence of operating parameters and compositions, *Wear*, Vol. 256, 2004, pp. 797-804
- [19] T. Singh, A. Tiwari, A. Patnaik, R. Chauhan, S. Ali: Influence of wollastonite shape and amount on tribo-performance of non-asbestos organic brake friction composites, *Wear*, Vol. 386-387, 2017, pp. 157-164
- [20] T. Singh, A. Patnaik, R. Chauhan, P. Chauhan: Selection of brake friction materials using hybrid analytical hierarchy process and vise Kriterijumska Optimizacija Kompromisno Resenje approach, *Polymer Composites*, Vol. 39, 2018, pp. 1655-1662

-
- [21] T. Singh, A. Patnaik: Thermo-mechanical and tribological properties of multi-walled carbon nanotubes filled friction composite materials, *Polymer Composites*, Vol. 38, 2017, pp. 1183-1193
- [22] J. Bijwe, M. Kumar: Optimization of steel wool contents in non-asbestos organic (NAO) friction composites for best combination of thermal conductivity and tribo-performance, *Wear*, Vol. 263, 2007, pp. 1243-1248
- [23] N. Kumar, T. Singh, J. S. Grewal, A. Patnaik, G. Fekete: Experimental investigation on the physical, mechanical and tribological properties of hemp fiber-based non-asbestos organic brake friction composites, *Materials Research Express*, Vol. 6, 2019, 085710
- [24] N. Dadkar, B. S. Tomar, B. K. Satapathy: Evaluation of flyash-filled and aramid fibre reinforced hybrid polymer matrix composites (PMC) for friction braking applications, *Materials and Design*, Vol. 30, 2009, pp. 4369-4376
- [25] N. Kumar, T. Singh, J. S. Grewal, A. Patnaik, G. Fekete: A novel hybrid AHP-SAW approach for optimal selection of natural fiber reinforced non-asbestos organic brake friction composites, *Materials Research Express*, Vol. 6, 2019, p. 065701
- [26] T. Singh, A. Patnaik, G. Fekete, R. Chauhan, B. Gangil: Application of hybrid analytical hierarchy process and complex proportional assessment approach for optimal design of brake friction materials, *Polymer Composites*, Vol. 40, 2019, pp. 1602-1608
- [27] A. Tiwari, H. S. Jaggi, R. K. Kachhap, B. K. Satapathy, S. N. Maiti, B. S. Tomar: Comparative performance assessment of cenosphere and barium sulphate based friction composites, *Wear*, Vol. 309, 2014, pp. 259-268
- [28] Y. Liu, Y. Ma, J. Che, L. Duanmu, J. Zhuang, J. Tong: Natural fibre reinforced non-asbestos organic non-metallic friction composites: effect of abaca fibre on mechanical and tribological behaviour. *Materials Research Express*, Vol. 5, 2018, 055101
- [29] K. S. Akant, Siddhartha, S. Yadav, P. K. Singh, Repercussion of manufacturing techniques on mechanical and wear peculiarity of ZnO particulate-filled polyester composites, *Polyester Composites*, Vol. 39, No. 3, 2018, pp. 654-667
- [30] Nidhi, J. Bijwe: NBR-modified resin in fade and recovery module in non-asbestos organic (NAO) friction materials, *Tribology Letters*, Vol. 27, 2007, pp. 189-196
- [31] P. D. Neis, N. F. Ferreira, G. Fekete, L. T. Matozo, D. Masotti: Towards a better understanding of the structures existing on the surface of brake pads, *Tribology International*, Vol. 105, 2017, pp. 135-147

-
- [32] I. Hatos, I. Fekete, T. Ibriksz, G. J. Kovács, B. M. Maros, H. Hajnalka: Surface modification and wear properties of direct metal laser sintered hybrid tools used in moulds. *Strojnicki Vestnik – Journal of Mechanical Engineering*, Vol. 64, 2018, pp. 121-129
- [33] Y. Liu, J. Xie, N. Wu, L. Wang, Y. Ma, J. Tong: Influence of silane treatment on the mechanical, tribological and morphological properties of corn stalk fiber reinforced polymer composites. *Tribology International*, Vol. 131, 2019, pp. 398-405
- [34] T. Singh, M. K. Rathi, A. Patnaik, R. Chauhan, S. Ali, G. Fekete: Application of waste tire rubber particles in non-asbestos organic brake friction composite materials, *Materials Research Express*, Vol. 6, 2019, 035703
- [35] P. C. Verma, R. Ciudin, A. Bonfanti, P. Aswath, G. Straffelini, S. Gialanella: Role of the friction layer in the high-temperature pin-on-disc study of a brake material, *Wear*, Vol. 346-347, 2016, pp. 56-65
- [36] T. Singh, C. I. Pruncu, B. Gangil, V. Singh, G. Fekete: Comparative performance assessment of pineapple and Kevlar fibers based friction composites, *Journal of Materials Research and Technology*, 2019, <https://doi.org/10.1016/j.jmrt.2019.11.074>

Actuator Fault Diagnosis System Design and Verification for Ball on Plate System

Matej Oravec, Anna Jadlovská

Department of the Cybernetics and Artificial Intelligence, Faculty of Electrical Engineering and Informatics, Technical University of Košice
Letná 9, Košice, Slovak Republic
matej.oravec@tuke.sk, anna.jadlovaska@tuke.sk

Abstract: The paper deals with the fault diagnosis methodology design for fault detection, localization, estimation and accommodation in a predictive control algorithm. The result of the proposed methodology realization is control and fault diagnosis system, which has a capability of actuators fault tolerance. The fault diagnosis system design is based on the group of unknown input observers. The fault diagnosis system and predictive control algorithm with fault accommodation are implemented in MATLAB. The designed algorithms, which are presented in this paper, are verified by simulations using the simulation model of the Ball on Plate system.

Keywords: fault diagnosis; fault-tolerant system; modeling; predictive control

1 Introduction

In recent years, control systems must ensure a very good steady-state and dynamic performance of controlled dynamic systems [1]. For these purposes, various types of control algorithms are designed using different approaches.

At present, the optimal control is very popular in various applications. In [2] is an optimal approach used for traffic lights optimization. In [1], authors present servo motor control system based on iterative feedback tuning that minimizes an objective function. Also, in [3], the iterative procedure is used for optimal control design of permanent magnet linear motor. Authors in [3] present speed controllers design for a class of small turbojet engines, which can be applied in a discrete digital control environment. In [18], the predictive control algorithms are listed which are based on the technique that solves the optimization problem at each sampling period. In this paper, the main focus is on the predictive control algorithm design using the discrete transfer function of the dynamic system.

Also, the risk of the dynamic system faults increases with its growing complexity means an undesirable influence on dynamic system control. The actuators and sensors are the most affected parts by faults. The fault tolerance capability of control algorithms is usually used to fulfil the given control goal, despite the actuator or sensor faults occurrence. The important assumption for control with fault tolerance is the Fault Detection and Diagnosis (FDD) system design, which is used for fault detection, localization, and estimation. The effectiveness of the diagnosis systems depends on the quality of used mathematical models [8].

In this paper, the predictive control algorithm is enhanced by the ability of fault tolerance [11], [12]. The information about faults is obtained from FDD system, which is based on the group of Unknown Inputs Observers (UIO) [9]. Also, the design of algorithms for the faults detection, localization, and estimation are shortly listed.

The Ball on Plate system has been widely used for the control algorithms design and verification of their performance because it is an unstable, nonlinear system [5], [6], [7], [18]. Application of the fault-tolerant control to Ball on Plate system is not common, but in [13] stress is put to solve this task. Also, this paper is dedicated to verification of the fault-tolerant control of Ball on Plate laboratory model, which is situated in the *Laboratory of Modern Control Techniques of Physical Systems* of the DCAI, FEEI at the Technical university of Košice. The paper follows previous research activities of the *Center of Modern Control Techniques and Industrial Informatics (CMCTII, web: <http://kyb.fei.tuke.sk>)* [21].

The main goal of this paper is to design of methodology that connects partial tasks as modelling, control or faults diagnosis algorithms design leading to creation of the complex control and FDD system. All steps of proposed methodology are described in next sections with their application to Ball on Plate system [22].

2 Design of Actuators Faults Diagnosis System

In general, faults detection and diagnosis system design consists of some steps, which are common for each dynamic system [9]. In this article, the methodology of the FDD system design for the actuators faults diagnosis is stated and implemented using the Ball on Plate model [22]. The presented methodology consists of these steps:

- 1) nominal system modeling,
- 2) design of nominal system control algorithm,
- 3) faulty system modeling and design of algorithms for actuator faults detection, localization and estimation,
- 4) fault-tolerant capability implementation to control algorithm.

Nominal model of Ball on Plate system is designed according to system analysis of laboratory model (<http://kyb.fei.tuke.sk/laben/modely/gnk.php>).

Model can be divided into the two subsystems, as the Servomotors subsystem and the B&P subsystem (Figure 1). The description of physical variables and parameters of the model are stated in Table 1.

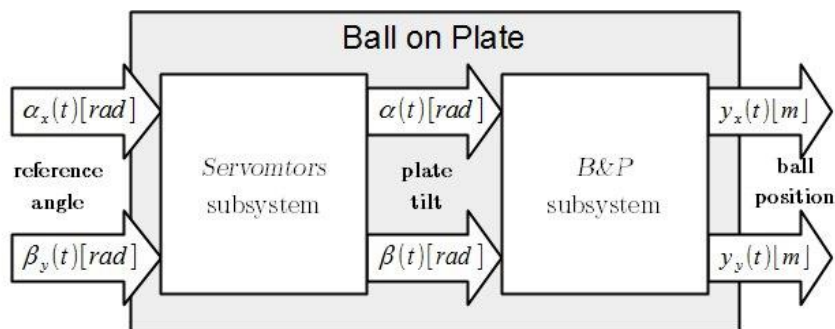


Figure 1

System decomposition of the Ball on Plate system

In the past, the Ball on Plate laboratory model was used for various control algorithms verification in CMCTII [13], [14], [15]. Also, the predictive control verification, which was designed using pseudo-state space form, was presented in [16].

Table 1

Variables and parameters of the Ball on Plate system

Description	Label	Units
ball position – axis x	$y_x(t)$	[m]
ball position – axis y	$y_y(t)$	[m]
plate tilt – axis x	$\alpha(t)$	[rad]
reference angle – axis x	$\alpha_x(t)$	[rad]
plate tilt – axis y	$\beta(t)$	[rad]
reference angle – axis y	$\beta_y(t)$	[rad]
servomotor gain – axis x	K_x	-
time constant of servomotor – axis x	T_x	[s]
servomotor gain – axis y	K_y	-
time constant of servomotor – axis y	T_y	[s]

This section shortly presents the algorithm design of the mentioned predictive control with actuator fault tolerant capability. However, early actuators fault detection, localization and estimation is very important for successful functionality of the control system. The Fault Detection and Diagnosis system (FDD) is implemented for this purpose, which is based on the group of the unknown inputs observers using Kalman filtration principles. The information from the FDD is

used for fault accommodation in control law. All algorithms are used in structure with interconnections between control and FDD system. The general scheme of control and FDD system is illustrated in Figure 2.

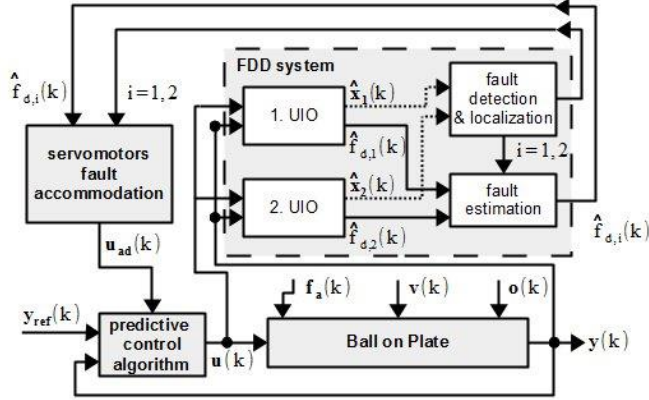


Figure 2

General scheme of the control & FDD system with fault accommodation in predictive control law

2.1 Ball and Plate System Modeling

As it was mentioned, the Ball on Plate system can be divided into two subsystems (Figure 1, Table 1). Mathematical model of the B&P subsystem can be designed as the two nonlinear differential equations:

$$\ddot{y}_x(t) = \frac{5}{7} g \sin \alpha(t) \quad (1)$$

$$\ddot{y}_y(t) = \frac{5}{7} g \sin \beta(t) \quad (2)$$

The subsystem of Servomotors can be expressed using two 1st order linear differential equations:

$$\dot{\alpha}(t) = \frac{K_x}{T_x} \cdot (\alpha_x(t) - \alpha(t)) \quad (3)$$

$$\dot{\beta}(t) = \frac{K_y}{T_y} \cdot (\beta_y(t) - \beta(t)) \quad (4)$$

where coefficients K_x , K_y , T_x , T_y are obtained by experimental identification [13].

The mathematical model of the system expressed by the differential equations (1) – (4) can be arranged into the canonical form using substitution:

- for axis x , where $y_x(t) = x_1(t)$, $\dot{y}_x(t) = x_2(t)$, $\alpha(t) = x_3(t)$, $\alpha_x(t) = u_x(t)$:

$$\dot{x}_1(t) = x_2(t) \quad (5)$$

$$\dot{x}_2(t) = \frac{5}{7}g \sin x_3(t) \quad (6)$$

$$\dot{x}_3(t) = \frac{1}{T_x}(K_x u_x(t) - x_3(t)) \quad (7)$$

- for axis y, where $y_y(t) = x_4(t)$, $\dot{y}_y(t) = x_5(t)$, $\beta(t) = x_6(t)$, $\beta_y(t) = u_y(t)$:

$$\dot{x}_4(t) = x_5(t) \quad (8)$$

$$\dot{x}_5(t) = \frac{5}{7}g \sin x_6(t) \quad (9)$$

$$\dot{x}_6(t) = \frac{1}{T_y}(K_y u_y(t) - x_6(t)) \quad (10)$$

The mathematical model in canonical state form (5) - (10) is used for the implementation as a simulation model in a *Matlab* environment. The simulation model was verified with the real laboratory model and the results [13], [14].

The nonlinear differential equations of the mathematical model in canonical form are linearized around the operating point:

$$x_x^{op} = [x_1^{op} \quad x_2^{op} \quad x_3^{op}], \quad x_y^{op} = [x_4^{op} \quad x_5^{op} \quad x_6^{op}] \quad (11)$$

The result of the linearization can be arranged into the two linear mathematical models in state-space form:

$$\underbrace{\begin{bmatrix} \dot{x}_1(t) \\ \dot{x}_2(t) \\ \dot{x}_3(t) \end{bmatrix}}_{\dot{x}_x(t)} = \underbrace{\begin{bmatrix} 0 & 1 & 0 \\ 0 & 0 & \frac{5}{7}g \\ 0 & 0 & -\frac{1}{T_x} \end{bmatrix}}_{A_x} \underbrace{\begin{bmatrix} x_1(t) \\ x_2(t) \\ x_3(t) \end{bmatrix}}_{x_x(t)} + \underbrace{\begin{bmatrix} 0 \\ 0 \\ \frac{K_x}{T_x} \end{bmatrix}}_{B_x} u_x(t) \quad (12)$$

$$y_x(t) = \underbrace{\begin{bmatrix} 1 & 0 & 0 \end{bmatrix}}_{C_x} \underbrace{\begin{bmatrix} x_1(t) \\ x_2(t) \\ x_3(t) \end{bmatrix}}_{x_x(t)} \quad (13)$$

$$\underbrace{\begin{bmatrix} \dot{x}_4(t) \\ \dot{x}_5(t) \\ \dot{x}_6(t) \end{bmatrix}}_{\dot{x}_y(t)} = \underbrace{\begin{bmatrix} 0 & 1 & 0 \\ 0 & 0 & \frac{5}{7}g \\ 0 & 0 & -\frac{1}{T_y} \end{bmatrix}}_{A_y} \underbrace{\begin{bmatrix} x_4(t) \\ x_5(t) \\ x_6(t) \end{bmatrix}}_{x_y(t)} + \underbrace{\begin{bmatrix} 0 \\ 0 \\ \frac{K_y}{T_y} \end{bmatrix}}_{B_y} u_y(t) \quad (14)$$

$$y_y(t) = \underbrace{\begin{bmatrix} 1 & 0 & 0 \end{bmatrix}}_{c_y^T} \underbrace{\begin{bmatrix} x_4(t) \\ x_5(t) \\ x_6(t) \end{bmatrix}}_{x_y(t)} \quad (15)$$

The state-space form (12)-(15) of the mathematical model is discretized using *c2d* function in *Matlab* environment and using a *ss2tf* function it can be expressed as the two transfer function:

$$F_x(z^{-1}) = \frac{B_x(z^{-1})}{A_x(z^{-1})} = \frac{b_{x,1}z^{-1} + b_{x,2}z^{-2} + b_{x,3}z^{-3}}{1 + a_{x,1}z^{-1} + a_{x,2}z^{-2} + a_{x,3}z^{-3}} \quad (16)$$

$$F_y(z^{-1}) = \frac{B_y(z^{-1})}{A_y(z^{-1})} = \frac{b_{y,1}z^{-1} + b_{y,2}z^{-2} + b_{y,3}z^{-3}}{1 + a_{y,1}z^{-1} + a_{y,2}z^{-2} + a_{y,3}z^{-3}} \quad (17)$$

where sampling period $T_s = 0.05$ s.

The mathematical model in the transfer functions form (16), (17) is used in the next subsection for the predictive control algorithm design. Also the state space form equations (12)-(15) are used for the faulty model derivation in Subsection 2.3.

2.2 Predictive Control Algorithm Design

For control of the Ball on Plate system a predictive control algorithm is used, which minimizes the cost function:

$$J_{PC} = \sum_{i=1}^{N_p} \mathbf{Q}[\hat{\mathbf{y}}(k+i) - \mathbf{y}_{ref}(k+i)]^2 + \sum_{i=1}^{N_u} \mathbf{R}[\mathbf{u}(k+i-1)]^2 \quad (18)$$

where N_p , N_u represents prediction horizon and control horizon, $\hat{\mathbf{y}}(k)$ is the vector of predicted values of the system output, $\mathbf{y}_{ref}(k)$ represents reference trajectory, $\mathbf{u}(k)$ is control input and \mathbf{Q} , \mathbf{R} are weight matrices [17], [19].

The predicted values $\hat{\mathbf{y}}(k)$ are obtained using pseudo-state space form:

$$\begin{aligned} \mathbf{X}(k+1) &= \mathbf{A}_0 \mathbf{X}(k) + \mathbf{B}_0 \mathbf{U}_0(k), \\ y(k) &= \mathbf{C}_0 \mathbf{X}(k), \end{aligned} \quad (19)$$

which can be derived from the system discrete transfer function (16) or (17) as follow:

$$\underbrace{\begin{pmatrix} \mathbf{X}(k+1) \\ y(k-n+2) \\ \vdots \\ y(k) \\ y(k+1) \end{pmatrix}}_{\mathbf{X}(k+1)} = \underbrace{\begin{pmatrix} 0 & 1 & \cdots & 0 \\ \vdots & & \ddots & \vdots \\ 0 & & \cdots & 1 \\ -a_n & -a_{n-1} & \cdots & -a_1 \end{pmatrix}}_{\mathbf{A}_0} \underbrace{\begin{pmatrix} \mathbf{X}(k) \\ y(k-n+1) \\ \vdots \\ y(k-1) \\ y(k) \end{pmatrix}}_{\mathbf{X}(k)} + \underbrace{\begin{pmatrix} 0 & 0 & \cdots & 0 \\ \vdots & & \ddots & \vdots \\ 0 & & \cdots & 0 \\ b_n & b_{n-1} & \cdots & b_1 \end{pmatrix}}_{\mathbf{B}_0} \underbrace{\begin{pmatrix} u(k-g+1) \\ \vdots \\ u(k-1) \\ u(k) \end{pmatrix}}_{\mathbf{U}_0(k)} \quad (20)$$

$$y(k) = \underbrace{(0 \dots 0 \ 1)}_{\mathbf{C}_0} \underbrace{\begin{pmatrix} y(k-n+1) \\ \vdots \\ y(k) \end{pmatrix}}_{\mathbf{x}(k)} \quad (21)$$

The system output prediction $\hat{\mathbf{y}}(k) = [y(k+1), \dots, y(k+N_p)]$ can be computed using pseudo-state space (13) in form:

$$\begin{pmatrix} y(k+1) \\ \vdots \\ y(k+N_p) \end{pmatrix} = \begin{pmatrix} \mathbf{C}_0 \mathbf{A}_0 \\ \vdots \\ \mathbf{C}_0 \mathbf{A}_0^{N_p} \end{pmatrix} \begin{pmatrix} y(k-n+1) \\ \vdots \\ y(k) \end{pmatrix} + \bar{\mathbf{G}} \begin{pmatrix} u(k-q+1) \\ \vdots \\ u(k+N_p-1) \end{pmatrix} \quad (22)$$

where matrix $\bar{\mathbf{G}}$ consists of:

$$\bar{\mathbf{G}} = \begin{pmatrix} \mathbf{C}_0 \mathbf{B}_0 & \mathbf{0} \\ \vdots & \vdots \\ \mathbf{C}_0 \mathbf{B}_i & \mathbf{0} \\ \vdots & \vdots \\ \mathbf{C}_0 \mathbf{B}_{N_p-1} & \mathbf{0} \end{pmatrix}, \mathbf{B}_0 = \begin{pmatrix} 0 & 0 & \dots & 0 \\ \vdots & & \ddots & \vdots \\ 0 & & & 0 \\ b_n & b_{n-1} & \dots & b_1 \end{pmatrix} \quad (23)$$

$$\mathbf{B}_i = (\mathbf{A}_0 \mathbf{B}_{i-1} \ 0 \dots 0) + (0 \dots 0 \ \mathbf{B}_0), \quad i = 1, \dots, N_p - 1 \quad (24)$$

Finally, the system output prediction $\hat{\mathbf{y}}(k)$, according to [18], can be expressed:

$$\hat{\mathbf{y}}(k) = \mathbf{y}_0(k) + \mathbf{G}\mathbf{u}(k) \quad (25)$$

where \mathbf{y}_0 represents system free response:

$$\mathbf{y}_0(k) = \begin{pmatrix} \mathbf{C}_0 \mathbf{A}_0 \\ \vdots \\ \mathbf{C}_0 \mathbf{A}_0^{N_p} \end{pmatrix} \begin{pmatrix} y(k-n+1) \\ \vdots \\ y(k) \end{pmatrix} + \bar{\mathbf{G}}_{(:,1:q-1)} \begin{pmatrix} u(k-q+1) \\ \vdots \\ u(k-1) \end{pmatrix} \quad (26)$$

and matrix $\bar{\mathbf{G}}_{(:,1:q-1)}$ consists of all rows and $q-1$ columns of the $\bar{\mathbf{G}}$ matrix (the convention “:” is used according to the *MATLAB* environment).

Next columns of matrix $\bar{\mathbf{G}}$ are used for the computation of the system forced response $\mathbf{G}\mathbf{u}(k)$, where:

$$\mathbf{G} = \bar{\mathbf{G}}_{(:,q:q+N_p-1)} \quad (27)$$

The matrices of the system output prediction can be arranged into the Hessian \mathbf{H} and gradient \mathbf{g} :

$$\mathbf{H} = (\mathbf{G}^T \mathbf{Q}^T \mathbf{Q} \mathbf{G} + \mathbf{R}^T \mathbf{R}) \quad (28)$$

$$\mathbf{g}^T = (\mathbf{y}_0 - \mathbf{y}_{ref}(k))^T \mathbf{Q}^T \mathbf{Q} \mathbf{G}$$

Control law has form:

$$\mathbf{u}_{opt}(k) = -\mathbf{H}^{-1} \mathbf{g} \quad (29)$$

where the optimal control sequence \mathbf{u}_{opt} is computed with respect to criteria:

$$\frac{\partial J_{pc}}{\partial \mathbf{u}(k)} \stackrel{!}{=} 0 \quad (30)$$

Also, physical constraints of the controlled system, which are composed to inequality $\mathbf{U}_{con}\mathbf{u}_{opt} \leq \mathbf{v}_{con}$, are assumed and they can be expressed in form:

$$\mathbf{U}_{con} = \begin{pmatrix} \mathbf{I}_D \\ -\mathbf{I}_D \end{pmatrix}, \mathbf{v}_{con} = \begin{pmatrix} \mathbf{1}u_{max} \\ -\mathbf{1}u_{min} \end{pmatrix} \quad (31)$$

and $\mathbf{1}$ is a unit vector and \mathbf{I}_D is a unit matrix [19].

The optimal control sequence $\mathbf{u}_{opt}(k)$ can be computed in *Matlab* environment using the *quadprog* function (function of *Optimization toolbox*) by formula:

$$\min_{\mathbf{u}} \left(\frac{1}{2} \mathbf{u} \mathbf{H} \mathbf{u} + \mathbf{g}^T \mathbf{u} \right) \quad (32)$$

The designed predictive control algorithm is implemented as *m-file* called *ioGPCcon* to the *Matlab* environment with respect to control structure, which is shown in Figure 3. The predictive control algorithm is illustrated as a flowchart in Figure 4.

For computation of the Hessian \mathbf{H} , matrices of the free response y_0 and matrix of the forced response \mathbf{G} is also a created function - $[H, y0_AC, y0_G, G, Ucon, vcon] = \text{paramGPCc}(Bx, Ax, Q, R, Np, Nu)$.

The predictive control algorithm is used twice for the control of the servo motors in x or y direction independently.

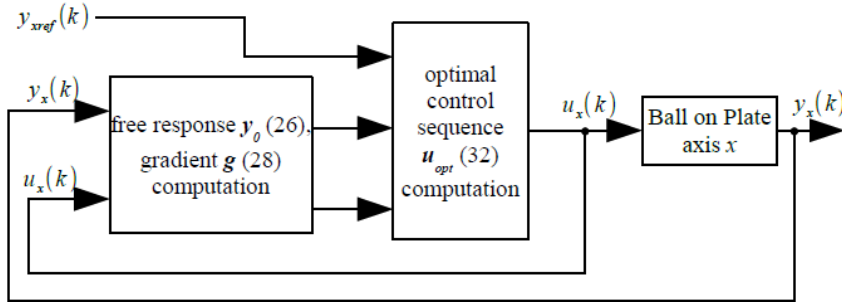


Figure 3

The predictive control of the dynamic system implemented to the control structure

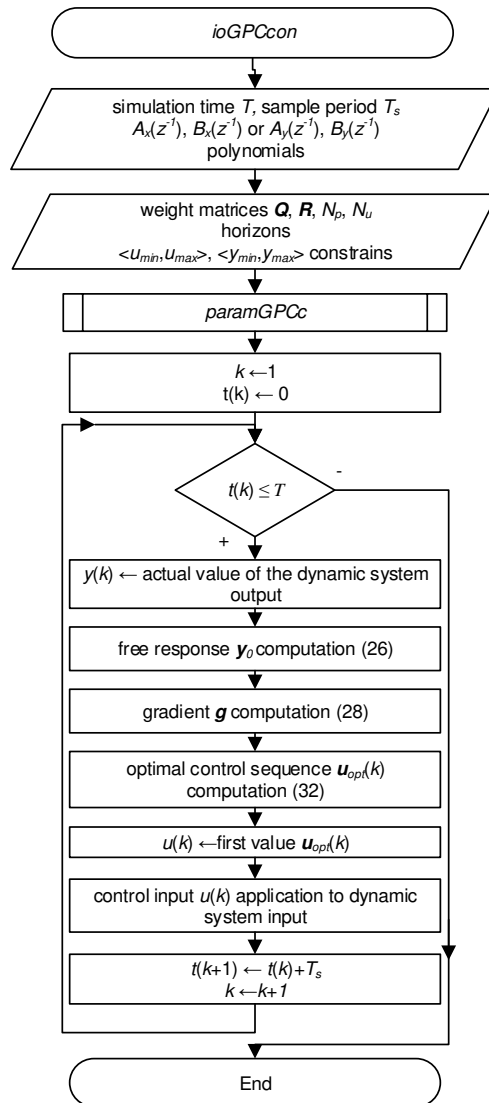


Figure 4

The predictive control of the dynamic system implemented to the control structure

The designed predictive control of the nominal system was verified by a simulation model of Ball on Plate for the circle trajectory tracking. The control inputs and ball position time responses are illustrated in Figure 5.

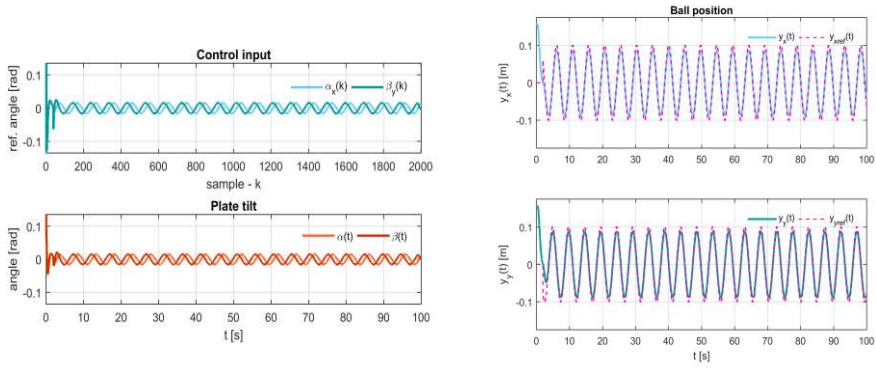


Figure 5

Time responses of nominal Ball on Plate system outputs and control inputs

After successful verification of the designed predictive control algorithm of the nominal system, the fault detection and diagnosis system design is the next step according to the presented methodology.

2.3 Actuators Fault Detection and Diagnosis System Design

The fault detection and diagnosis system is based on the group of observers with unknown inputs (UIO). For their design, it is important to rearrange the state space models (12) - (15) of the Ball on Plate system and also specify the faulty models of the system. The state space models (12) - (15) can be expressed as MIMO model of the system:

$$\underbrace{\begin{bmatrix} \dot{x}_1(t) \\ \dot{x}_2(t) \\ \dot{x}_3(t) \\ \dot{x}_4(t) \\ \dot{x}_5(t) \\ \dot{x}_6(t) \end{bmatrix}}_{\mathbf{x}(t)} = \underbrace{\begin{bmatrix} 0 & 1 & 0 & 0 & 0 & 0 \\ 0 & 0 & \frac{5}{7}g & 0 & 0 & 0 \\ 0 & 0 & -\frac{1}{T_x} & 0 & 0 & 0 \\ 0 & 0 & 0 & 0 & 1 & 0 \\ 0 & 0 & 0 & 0 & 0 & \frac{5}{7}g \\ 0 & 0 & 0 & 0 & 0 & -\frac{1}{T_y} \end{bmatrix}}_{\mathbf{A}} \underbrace{\begin{bmatrix} x_1(t) \\ x_2(t) \\ x_3(t) \\ x_4(t) \\ x_5(t) \\ x_6(t) \end{bmatrix}}_{\mathbf{x}(t)} + \underbrace{\begin{bmatrix} 0 & 0 \\ 0 & 0 \\ \frac{K_x}{T_x} & 0 \\ 0 & 0 \\ 0 & 0 \\ 0 & \frac{K_y}{T_y} \end{bmatrix}}_{\mathbf{B}} \mathbf{u}(t) \quad (29)$$

$$\underbrace{\begin{bmatrix} y_1(t) \\ y_2(t) \\ y_3(t) \\ y_4(t) \\ y_5(t) \\ y_6(t) \end{bmatrix}}_{\mathbf{y}(t)} = \underbrace{\begin{bmatrix} 1 & 0 & 0 & 0 & 0 & 0 \\ 0 & 0 & 1 & 0 & 0 & 0 \\ 0 & 0 & 0 & 1 & 0 & 0 \\ 0 & 0 & 0 & 0 & 0 & 1 \end{bmatrix}}_{\mathbf{C}^T} \mathbf{x}(t) \quad (30)$$

which can be also discretized using sampling period $T_s = 0.05$ s:

$$\mathbf{x}(k+1) = \underbrace{\begin{bmatrix} a_{11} & a_{12} & a_{13} & 0 & 0 & 0 \\ 0 & a_{22} & a_{23} & 0 & 0 & 0 \\ 0 & 0 & a_{33} & 0 & 0 & 0 \\ 0 & 0 & 0 & a_{44} & a_{45} & a_{46} \\ 0 & 0 & 0 & 0 & a_{55} & a_{56} \\ 0 & 0 & 0 & 0 & 0 & a_{66} \end{bmatrix}}_{\mathbf{A}_d} \mathbf{x}(k) + \underbrace{\begin{bmatrix} 0 & 0 \\ 0 & 0 \\ b_{31} & 0 \\ 0 & 0 \\ 0 & 0 \\ 0 & b_{62} \end{bmatrix}}_{\mathbf{B}_d} \mathbf{u}(k) \quad (31)$$

$$\mathbf{y}(k) = \mathbf{C}^T \mathbf{x}(k) \quad (32)$$

In the MIMO model of the system (33) - (36), the angle of the plate tilt should be possible to measure in real system by sensor (3-axis accelerometer or gyroscope).

The faulty model of the Ball on Plate system is assumed in general state space form:

$$\mathbf{x}(k+1) = \mathbf{A}_d \mathbf{x}(k) + \mathbf{B}_d \mathbf{u}(k) + \mathbf{F}_d \mathbf{f}_d(k) + \mathbf{v}(k) \quad (33)$$

$$\mathbf{y}(k) = \mathbf{C}^T \mathbf{x}(k) + \mathbf{o}(k)$$

where $\mathbf{f}_d(k)$ is vector of faults magnitudes, $\mathbf{v}(k)$, $\mathbf{o}(k)$ are system and measurement noise. Also, it is assumed that faulty matrix $\mathbf{F}_d = \mathbf{B}_d$.

The faulty model of the system can be expressed as follows:

$$\mathbf{x}(k+1) = \mathbf{A}_d \mathbf{x}(k) + \mathbf{B}_d \mathbf{u}(k) + \mathbf{F}_{d,i} f_{d,i}(k) + \mathbf{F}_d^* \mathbf{f}_d^*(k) + \mathbf{v}(k) \quad (34)$$

$$\mathbf{y}(k) = \mathbf{C}^T \mathbf{x}(k) + \mathbf{o}(k)$$

where $\mathbf{F}_{d,i}$ is the i -th column of faulty matrix \mathbf{F}_d , $f_{d,i}$ is the i -th actuator fault magnitude, \mathbf{F}_d^* , \mathbf{f}_d^* are composed from the faulty matrix \mathbf{F}_d and vector \mathbf{f}_d without i -th column [8].

In the FDD system two faulty models of Ball on Plate system are used.

2.3.1 Unknown Input Observer Design for Actuator Fault Detection, Localization and Estimation

For actuator faults detection, localization, and estimation of Ball on Plate system two UIO (Figure 2) are used. According to [9], these assumptions have to be satisfied for UIO design:

- number of estimated faults (rank of matrix $\mathbf{F}_{d,i}$) is lower than number of system outputs (rank of matrix \mathbf{C}^T)
- $\text{rank}(\mathbf{C}^T \mathbf{F}_{d,i}) = \text{rank}(\mathbf{F}_{d,i})$

In general, the UIO has form:

$$\mathbf{x}_e(k+1) = \mathbf{F}_e \mathbf{x}_e(k) + \mathbf{T}_e \mathbf{B}_d \mathbf{u}(k) + \mathbf{L}(k) \mathbf{C}^* \mathbf{x}(k) \quad (35)$$

$$\hat{\mathbf{x}}(k) = \mathbf{x}_e(k) + \mathbf{C}^* \mathbf{H}_e \mathbf{x}(k)$$

where \mathbf{x}_e is extended state vector of the UIO and \mathbf{F}_e , \mathbf{T}_e , \mathbf{H}_e matrices are expressed:

$$\mathbf{H}_e = \mathbf{F}_{d,i} \left(\mathbf{C}^* \mathbf{F}_{d,i} \right)^+ \quad (36)$$

$$\mathbf{T}_e = \mathbf{I} - \mathbf{H}_e \mathbf{C}^* \quad (37)$$

$$\mathbf{A}_1 = \mathbf{T}_e \mathbf{A}_d \quad (38)$$

and $\mathbf{C}^* = \mathbf{C}^T$ in case of actuator fault.

The gain \mathbf{L} of UIO is iterative computed using Kalman principles as follow:

$$\mathbf{L}(k) = \mathbf{L}_1(k) + \mathbf{L}_2(k) \quad (39)$$

$$\mathbf{L}_1(k) = \mathbf{A}_1 \mathbf{P}_1(k | k-1) \mathbf{C}^{*T} \left(\mathbf{C}^* \mathbf{P}_1(k | k-1) \mathbf{C}^{*T} + \mathbf{R}_o \right)^{-1} \quad (40)$$

$$\mathbf{L}_2(k) = \mathbf{F}_e(k) \mathbf{H}_e \quad (41)$$

$$\mathbf{F}_e(k) = \mathbf{A}_1 - \mathbf{L}_1(k) \mathbf{C}^* \quad (42)$$

where the covariance matrix $\mathbf{P}_1(k|k-1)$ is computed:

$$\mathbf{P}_1(k | k-1) = \mathbf{P}_e(k | k-1) - \mathbf{L}_1(k-1) \mathbf{C}^* \mathbf{P}_e(k | k-1) \mathbf{A}_1^T \quad (43)$$

$$\mathbf{P}_e(k+1 | k) = \mathbf{A}_1 \mathbf{P}_1(k | k-1) \mathbf{A}_1^T + \mathbf{T}_e \mathbf{Q}_v \mathbf{T}_e^T + \mathbf{H}_e \mathbf{R}_o \mathbf{H}_e^T \quad (44)$$

where \mathbf{Q}_v , \mathbf{R}_o are system and measurement covariance matrices [10].

The algorithm of state estimation by UIO is expressed by in flowchart in Figure 6.

The estimated states are used for the residuals generation in form:

$$\mathbf{r}(k) = \mathbf{y}(k) - \mathbf{C}^T \hat{\mathbf{x}}(k) \quad (45)$$

Fault detection is based on GLR test using a residuals generator (49) and it can be expressed as follows:

$$J(k) = \max_{k-M_d+1 \leq i \leq k} \frac{1}{2} \left(\sum_{i=k-M_d+1}^k (\mathbf{r}(i) - \boldsymbol{\mu}_0) \right)^T \mathbf{Q}_z^{-1} \left(\sum_{i=k-M_d+1}^k (\mathbf{r}(i) - \boldsymbol{\mu}_0) \right) \quad (46)$$

where $\boldsymbol{\mu}_0$ is the mean value and \mathbf{Q}_z is matrix of variances, which are determined using the residuals obtained from the nominal system. The fault detection function $J(k)$ is used for the generation of the fault symptoms:

$$s = \begin{cases} 0, & \text{if } J(k) < J_{th} \\ 1, & \text{if } J(k) \geq J_{th} \end{cases} \quad (47)$$

where J_{th} is threshold value.

The generated symptoms s_l ($l=1,2$) are used for the fault localization (Table 2).

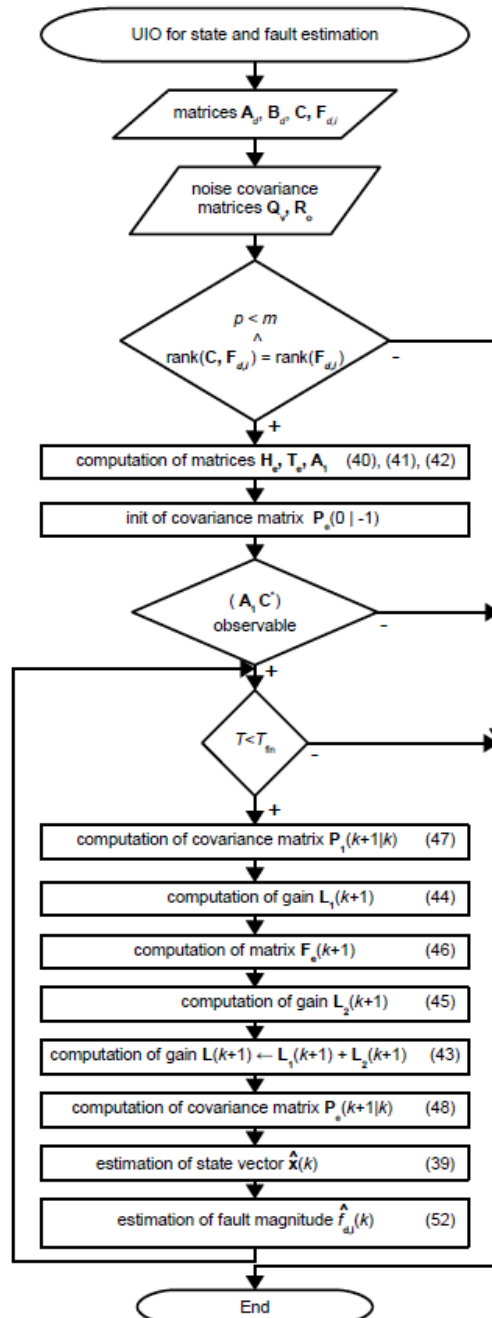


Figure 6
Flowchart of the UIO algorithm

Table 2
Localization of actuators faults using symptoms generation

	Fault free	Fault – servo of axis x	Fault – servo of axis y	Fault – both servos
s ₁	0	0	1	1
s ₂	0	1	0	1

After the successful fault detection and localization the fault magnitude can be estimated:

$$\hat{f}_{d,i}(k) = \mathbf{VS}^{-1}\mathbf{U}^T \hat{\mathbf{x}}(k) \quad (48)$$

where matrices \mathbf{U} , \mathbf{S} , \mathbf{V} are computed using SVD decomposition of matrix $\mathbf{F}_{d,i}$:

$$\mathbf{F}_{d,i} = \mathbf{U} \begin{bmatrix} \mathbf{S} \\ \mathbf{0} \end{bmatrix} \mathbf{V}^T \quad (49)$$

The results of the fault detection, localization and estimation are used in fault accommodation in the predictive control algorithm [9], [11].

2.3.2 Fault Accommodation in Predictive Control Algorithm

If the fault of the some actuator occurs during the control of the Ball on Plate system, the control inputs are affected. The influence of the fault can be eliminated using fault accommodation in control law [11].

According to [11], both control laws are extended by the additive inputs, which are determined using the results of fault detection and localization (Figure 2) [22]. Finally, the control laws in general have form:

$$\mathbf{u}(k) = \mathbf{u}_f(k) + \mathbf{u}_{ad}(k) \quad (50)$$

where:

$$\mathbf{u}(k) = \begin{bmatrix} u_x(k) \\ u_y(k) \end{bmatrix}, \quad \mathbf{u}_f = \begin{bmatrix} u_{x,f}(k) \\ u_{y,f}(k) \end{bmatrix}, \quad \mathbf{u}_{ad} = \begin{bmatrix} u_{x,ad}(k) \\ u_{y,ad}(k) \end{bmatrix} = \begin{bmatrix} -\hat{f}_{d,1}(k) \\ -\hat{f}_{d,2}(k) \end{bmatrix} \quad (51)$$

and also have to be updated constraints values:

$$\mathbf{U}_{con} = \begin{pmatrix} \mathbf{I} \\ -\mathbf{I} \end{pmatrix}, \quad \mathbf{v}_{con} = \begin{pmatrix} \mathbf{u}_{\max} + \mathbf{I}\hat{f}_{d,i}(k) \\ -\mathbf{u}_{\min} - \mathbf{I}\hat{f}_{d,i}(k) \end{pmatrix} \quad (52)$$

3 Simulation Verification of Actuators Faults Diagnosis System

According to FDD system design methodology presented in Section 2, it was implemented and tested in MATLAB environment using the nonlinear simulation model of the Ball on Plate system. Also, the effect of the fault accommodation in the predictive control algorithm was verified and evaluated by simulations, which are shortly introduced in this section. In the first case the multiplicative fault of the servomotor (loss of effectiveness) was assumed in a axis x direction, which occurred in $T_f = 25$ s. The effect was reflected mainly in time response of the ball position (Figure 7) and also in the second fault detection function J_2 (Figure 8). The estimated magnitude of the actuator fault (Figure 8) was used for fault accommodation in the control algorithm (Figure 9).

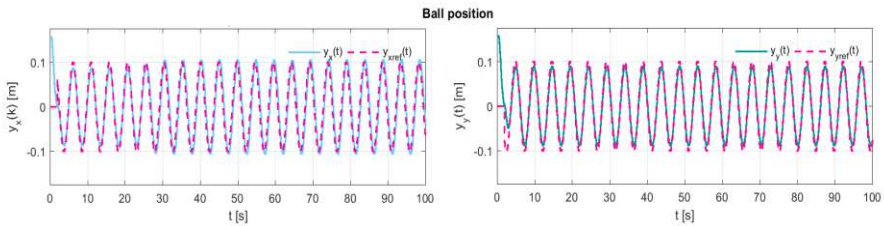


Figure 7

Time responses of B&P system outputs with servomotor multiplicative fault (axis x)

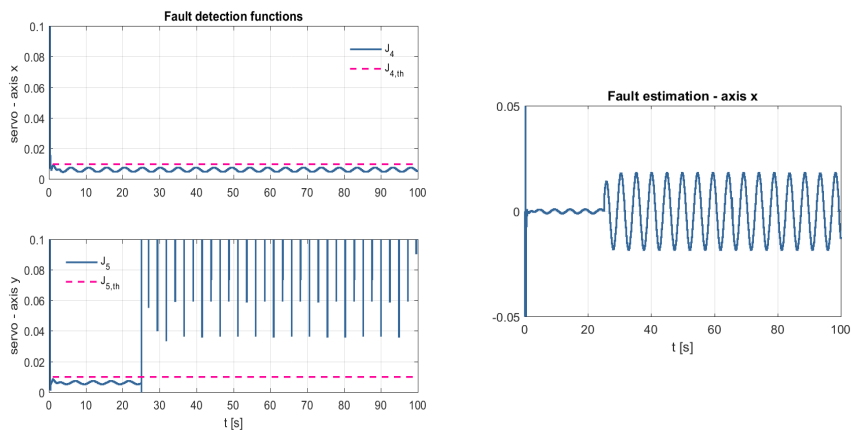


Figure 8

Detection functions and fault estimation generated by FDD system - servomotor fault (axis x)

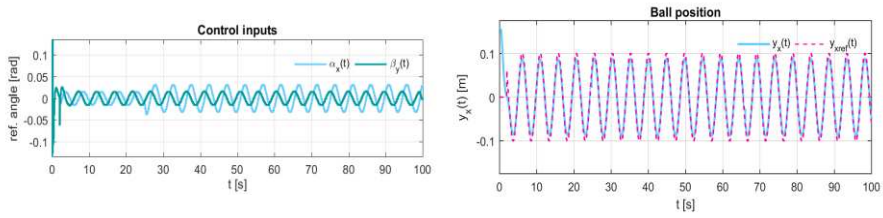


Figure 9

Time responses of Ball on Plate system output and control inputs with fault accommodation for servomotor of axis x

In the second case, the presence of multiplicative fault of the servomotor in a axis y direction (Figure 10, Figure 11) was simulated. The fault occurred in $T_f = 30$ s and its effect was eliminated by the fault accommodation using estimated magnitude (Figure 12).

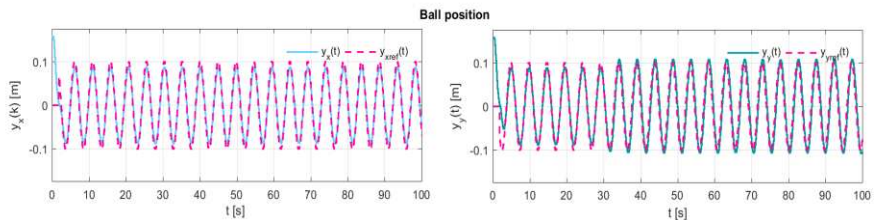


Figure 10

Time responses of B&P system outputs with servomotor multiplicative fault (axis y)

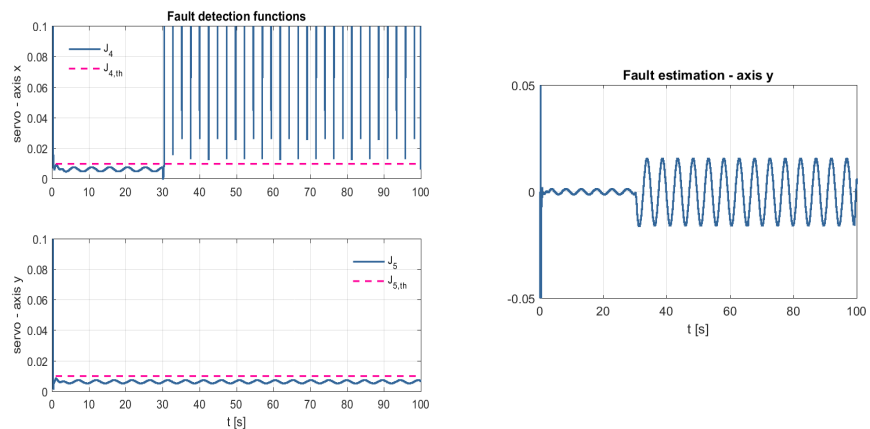


Figure 11

Detection functions and fault estimation generated by FDD system - servomotor fault (axis y)

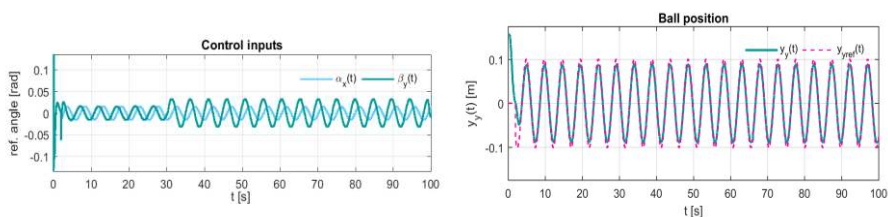


Figure 12

Time responses of Ball on Plate system output and control inputs with fault accommodation for servomotor of axis y

The results of simulations shows that the system output in both cases had higher amplitudes in axis x (Figure 7) or axis y (Figure 10) after faults occurring ($T_f=25$ s in case one or $T_f=30$ s in case two). When the fault tolerant capability was used in the predictive control algorithm, the system output responses (Figure 9, Figure 12) were very similar with no-fault case (Figure 5). The fault accommodation effect in the predictive control was also evaluated using the quantitative method. The norm of control errors in both directions were evaluated using formulas:

$$\|e_x\| = \sqrt{\sum_{k=0}^{T_{sim}/T_s} e_x^2(k)} = \sqrt{\sum_{k=0}^{T_{sim}/T_s} (y_{x,ref}(k) - y_x(k))} \quad (53)$$

$$\|e_y\| = \sqrt{\sum_{k=0}^{T_{sim}/T_s} e_y^2(k)} = \sqrt{\sum_{k=0}^{T_{sim}/T_s} (y_{y,ref}(k) - y_y(k))} \quad (54)$$

The results of the control errors computation are presented in the Table 3.

If the fault occurred, the fault tolerant predictive control of Ball on Plate system has better results than without this capability, this illustrated by laboratory model simulation outputs (Figure 7 - Figure 12) and also evaluated by norm of control error (Table 3).

Table 3
Norm of predictive control error

	nominal system	fault of servomotor - x axis		fault of servomotor - y axis	
		without fault accomodation	with fault accomodation	without fault accomodation	with fault accomodation
$\ e_x\ $	0,7942	1,1318	0,7738	0,7942	0,7942
$\ e_y\ $	0,8542	0,8542	0,8542	1,117	0,8398

The purpose of the the realized simulations was to confirm the accuracy of the proposed methodology and also capability of the designed predictive control algorithm to fault tolerant control.

Conclusions

The designed methodology for control and fault detection and diagnosis system design was presented in this paper. The steps of the presented methodology includes the modeling of the nominal system, the predictive control and the

diagnosis system design with capability of actuators faults tolerance. Finally, the results of the designed control and diagnosis systems according to the methodology were verified by simulation in the MATLAB environment. The time responses and quantitative evaluation of the simulations results shows that the FDD system is able to detect, localize, and estimate actuator fault magnitude. Also, the fault accommodation in the predictive control algorithm almost completely eliminates the effect of the actuator fault using the information about fault from the diagnosis system. The problem of the predictive control of Ball on Plate system with fault tolerance capability is not solved very often and this paper demonstrates it. In case of the Ball on Plate system, the fault accommodation is limited only to one actuator fault occurrence, but the faults of both servomotors concurrently is unlikely.

The issues mentioned in this article were also solved within the tasks of the project *University Science Park Technicom for innovative applications with knowledge technology support* (ITMS code 313011D232). The next step of the research should be oriented toward verification of the designed FDD system in a real laboratory model of Ball on Plate.

Acknowledgement

This work has been supported by grant KEGA Implementation of research results in the area of modeling and simulation of cyber-physical systems into the teaching process – development of modern university textbooks – 072TUKE - 4/2018 (100%).

References

- [1] S. Preitl *et. al.*, “Iterative feedback and learning control, servo systems applications,” IFAC Proceedings Volumes, Vol. 40, Issue 8, pp. 16-27, 2007, ISSN 1474-6670
- [2] R. G. Alvarez, Z. Johanyák, T. Kovács, “Surrogate model based optimization of traffic lights cycles and green period ratios using microscopic simulation and fuzzy rule interpolation,” *International Journal of Artificial Intelligence*, Vol. 16, Issue 1, pp. 20-40, 2018, ISSN 0974-0635
- [3] K. K. Tan, S. Zhao and J. Xu, “Online automatic tuning of a proportional integral derivative controller based on an iterative learning control approach,” *IET Control Theory & Applications*, Vol. 1, No. 1, pp. 90-96, 2007, ISSN 1751-8644
- [4] R. Andoga, L. Fozo, R. Kovács, K. Beneda, T. Moravec, M. Schreiner, “Robust Control of Small Turbojet Engines,” *Machines*, Vol. 7, Issue 1, 2019, ISSN 2075-1702

-
- [5] B. Heeseung, L. Young, "Embedded Model Predictive Control for Enhancing Tracking Performance of a Ball and Plate System," IEEE Access, Vol. 7, pp. 39652-39659, 2019, ISSN 2169-3536
- [6] B. Heeseung, L. Young, "Implementation of a Ball and Plate Control System Using Sliding Mode Control," IEEE Access, Vol. 6, pp. 32401-32408, 2018, ISSN 2169-3536
- [7] U. Musa et. al., "Position and Trajectory Tracking Control for the Ball and Plate System using Mixed Sensitivity Problem," Covenant Journal of Informatics & Communication Technology. Vol. 6, No. 1, 2018, ISSN 2354-3507
- [8] D. Theilliol, H. Noura, J.-C. Ponsart, "Fault diagnosis and accommodation of a three-tank system based on analytical redundancy," ISA transactions, Vol. 41, Issue 3, pp. 365-382, 2002, ISSN 0019-0578
- [9] P. F. Odgaard, J. Stoustrup, "Unknown input observer based scheme for detecting faults in a wind turbine converter," IFAC Proceedings Volumes, Vol. 42, Issue 8, pp. 161-166, 2009
- [10] E. F. Camacho, T. Alamo, D. Muñoz de la Peña, "Fault-tolerant model predictive control," Emerging Technologies and Factory Automation (ETFAs), IEEE Conference Bilbao, Spain, pp. 1-8, 2010, ISSN: 1946-0740
- [11] T. Miksch, A. Gambier, E. Badreddin, "Real-time implementation of fault-tolerant control using model predictive control," International Federation of Automatic Control Proceedings, Vol. 41, Issue 2, pp. 11136-11141, 2008, ISBN 978-3-902661-00-5
- [12] A. R. Kodakkadan, S. Olaru, V. Reppa, "Experimental fault tolerant control of a ball-on-plate system," 21st International Conference -System Theory, Control and Computing (ICSTCC), IEEE pp. 577-582, 2017, ISBN 978-1-5386-3843-9
- [13] M. Oravec, A. Jadlovská, "Optimal State Control of the Mechatronical Laboratory Model B&P_Kyb," Electrical Engineering and Informatics 5: Proceedings of the Faculty of Electrical Engineering and Informatics of the Technical University of Košice, TU, pp. 9-16, 2014, ISBN 978-80-553-1704-5
- [14] M. Oravec, A. Jadlovská, "Model predictive control of a ball and plate laboratory model," Symposium of Applied Machine Intelligence and Informatics (SAMII), IEEE 13th International Symposium, pp. 165-170, 2015, ISBN 978-1-4799-8220-2

- [15] M. Oravec, A. Jadlovská, “Intelligent positioning plate predictive control and concept of diagnosis system design,” *Journal of Manufacturing and Industrial Engineering*, Vol. 15, Issues 1-2, pp. 1-9, 2017, ISSN 1339-2972
- [16] A. W. Ordys, D. W. Clarke. “A state-space description for GPC controllers”, *International Journal of Systems Science*, Vol. 24, Issue 9, pp. 1727-1744, 1993, ISSN 1464-5319
- [17] K. Belda, J. Böhm, “Adaptive Generalized Predictive Control for Mechatronic Systems”, *WSEAS Transactions on Systems*, Athens, Greece, Vol. 5, Issue 8, pp. 1830-1837, 2006
- [18] Š. Jajčišin, A. Jadlovská, “Predictive Control Algorithms Verification on the Laboratory Helicopter Model,” *Acta Polytechnica Hungarica (Journal of Applied Sciences)*, Vol. 9, No. 4, 2012, ISSN 1785-8860
- [19] Š. Jajčišin, A. Jadlovská, “Design of predictive control algorithms using nonlinear models of physical systems,” (in Slovak), Košice: elfa, 2013, pp. 139, ISBN 978-80-8086-229-9
- [20] S. X. Ding, “Model-based fault diagnosis techniques: design schemes, algorithms and tools,” Springer Science & Business Media, 2008, ISBN 978-3-540-76303-1
- [21] J. Jadlovský, A. Jadlovská, S. Jadlovská, J. Čerkala, M. Kopčík, J. Čabala, M. Oravec, M. Varga, D. Vošček, “Research Activities of the Center of Modern Control Techniques and Industrial Informatics,” In: SAMI 2016: IEEE 14th International Symposium on Applied Machine Intelligence and Informatics: proceedings, 2016, pp. 279-285, ISBN 978-1-4673-8739-2
- [22] M. Oravec, “Methodology design for fault diagnosis of model of physical systems and its application into the distributed control system,” Dissertation Thesis. CMCT&II DCAI FEEI TU Košice, Slovakia, 2018, pp. 163 (in Slovak)

Study on the Deformability Characteristics of Steels for Seamless Tubes and Pipes destined for the Petrochemical Industry

Imre Kiss, Vasile Alexa

University Politehnica Timișoara, Faculty of Engineering Hunedoara, Department of Engineering & Management, 5, Revolutiei, Hunedoara, Romania
e-mails: imre.kiss@fih.upt.ro, vasile.alexu@fih.upt.ro

Abstract: The hot rolled seamless steel pipes and tubes are used successfully in areas such as the petrochemical industry (in oil and gas transport or in the extraction industry). This study includes results of the experimental hot torsion tests conducted to find the plasticity and deformability characteristics of two low alloyed medium carbon steel grades (EA < 2.5%) destined for seamless tubes and pipes manufacturing, used in the petrochemical industry (fluid transport, extraction industry): grade 43MoMn16 and grade 33MoCr11.

Keywords: low alloyed medium carbon steel grades (43MoMn16, 33MoCr11); seamless tubes and pipes; temperature; hot torsion tests; deformability; diagrams

1 Introduction

The major reason for the seamless steel pipe market is the rise in demand from the oil and gas industry, a sector that is expanding, and they are now being found at greater depths than before [1]. The hot rolled seamless steel pipes and tubes are used successfully in areas such as the petrochemical industry (fluid transport, extraction industry), in the construction industry (such as pipes for general use, or in installations as pipelines for gas or oil products), or in general mechanical constructions [1]. Seamless steel pipes are preferred over others due to their strength, durability and its nature to withstand extreme temperature, being used increasingly in industrial boiler applications and in the oil and gas sector [1].

The seamless pipes and tubes manufacturing process (Figure 1) involves the following two main technological processes: [2-4]

— transformation of raw materials into steel bars (electric arc furnace, ladle furnace, vacuum degassing and continuous casting processes) i.e. steel

- manufacturing (melting process, alloying, degassing, and continuous casting into bars or billets);
- transformation of steel bars into pipes or tubes, which are manufactured in different types of rolling mills, in uniformly heated in the rotary hearth heating furnace and then pierced by a piercer. In fact, the hot-rolled seamless steel pipes or tubes production base deformation process can basically be summarized as three stages:
 - ≡ stage of perforation process (piercing in cylindrical billets into a continuous rolling mill, named piercing mill);
 - ≡ stage of extension (elongation into a mandrel mill where the pipe or tube wall thickness is reduced by the mandrel bar and calibre rolls), and
 - ≡ stage of finishing (diameter reducing into a sizing/reducing mill).



Figure 1

The seamless pipes and tubes manufacturing process

Pipes and tubes shall have smooth exterior and interior surfaces, in accordance with the manufacturing process [2-4]. The outer and inner surfaces of the pipes shall be free from cracks, overlaps of material, non-metallic inclusions or other visible defects [2-4]. All these aspects are resolved at the stage of steel manufacturing stages, the steel's chemical composition being the main technological factor that influences the quality of the half-products (steel bars and billets). There will be no discussions to such aspects in this article. Therefore, in the laboratory determinations, we will use steels that are long documented by industrial practice.

The typical rolling process (the second step of the seamless pipes and tubes manufacturing process) is schematically shown in Figure 2 [2-5]. Depending on the number of rolls, the piercing mills (stage of perforation process) can be divided into:

- two-roll piercing mills with two working rolls and two guiding devices which hold the tube shell along the rolling axis (Figure 3a); [5]
- three-roll piercing mills with three working rolls that operate without any additional guiding devices for the metal (Figure 3b). [5]

During the second step, the steel bars or billets are subjected to large local deformations, so their deformation behaviour is very important [2-5]. In the piercing mill, deformation of the material, especially at the front end of the plug is large, and as the rolling operation progresses, the material at the centre of the plug front end is subject to an extremely large shear deformation along the plug surface [2-5].

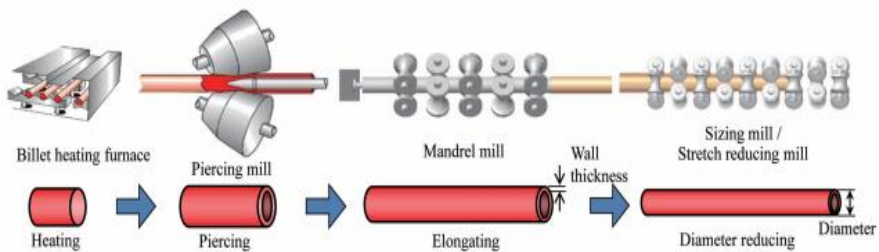


Figure 2

The typical rolling process of the seamless pipes and tubes manufacturing process – General view

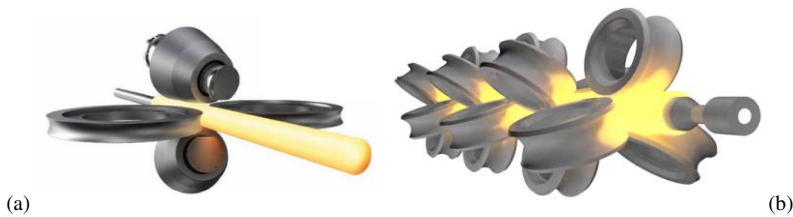


Figure 3

Typical piercing mills: (a) two-roll mills with two working rolls and two guiding devices; (b) three-roll mills with three working rolls, without any additional guiding devices

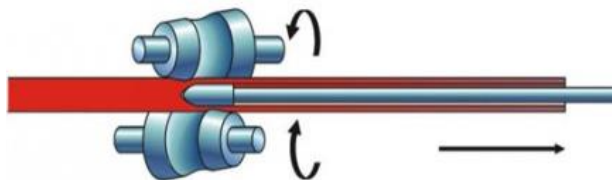


Figure 4

The two-roll piercing mills with two working rolls – General view

The first step (stage of perforation process) is usually a matter of poking a hole through a red-hot solid billet (Figure 4) [2-5]. In fact, during the primary piercing operation, the red-hot steel billet is rolled on the cross-roll piercing mill [2-5]. The quality of the piercing process has a major effect on the downstream processes and the finished product. At this stage of the process, the deformation plays a very important role.

In the two-roll-type mandrel mill (in stage of extension), which uses two rolls on each stand, the directions perpendicular to each other within the cross-section of a tube are alternately rolled by the odd-numbered and even-numbered stands (Figure 5) [2-5]. In the stage of finishing, the pipe diameter is reduced into a sizing/reducing mill (Figure 6) [2-5].

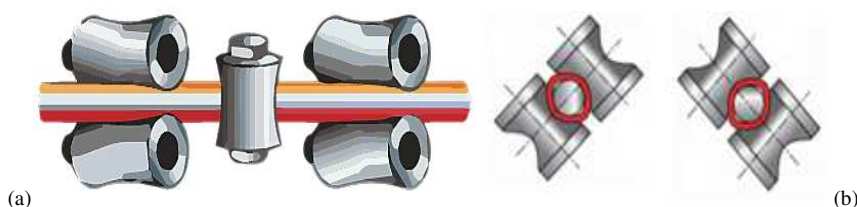


Figure 5

General view and cross-section of the mandrel mill (odd and even numbered stand)



Figure 6

General view of the sizing/reducing mill and the arrangement of rolls

Knowledge of the seamless pipe and tube steel's deformability characteristics (plasticity and deformation resistance) has for the hot rollers a great practical significance because they are important elements in establishing a proper technological process [6-9].

The ability to permanently deform without breaking the internal structural bonds is defined as deformability [6-9]. In fact, the deformability is the ability of a material to be plastically deformed without the occurrence of undesired conditions (cracking of material during the plastic deformation, inadequate quality of the surface, etc.) [6-9]. In this sense, the deformability of a material is expressed by the degree of deformation to which the first cracks appear [6-9].

The plastic deformation of steels is based on the property of plasticity, which defines their ability to acquire permanent deformations under the action of external forces [6-9]. Therefore, knowledge of the rolled steel's plasticity becomes the determining factor in the entire hot plastic deformation.

2 The Research Methodology

Besides the determination of deformability characteristics (plasticity and deformation resistance), several methods enable that to study the influence of the main deformation conditions (heating rate, holding time, heating temperature, deformation rate etc.) [7-9]. For determining the deformability of the steels are used methods like: [7, 8]

- based on the compression, rolling or forging, taking account of friction;
- based on the bending, tensile or torsion, without taking account of friction.

Among them, determination of the steel deformability by hot torsion method is the only one that allows obtaining large deformations along the length of the specimen [7, 8]. By this method, the hot deformability of the steel is determined by subjecting to torsion a cylindrical specimen maintained at the deformation temperature in a tubular oven [7, 8].

The deformability caused by hot torsion reflects quite accurately the steel behavior at hot plastic deformation, and due to the fact that the specimens can be maintained in the attached oven during deformation, we can ensure the stability of temperature [7, 8]. The size of the required moment for torsion the specimen expresses the resistance to plastic deformation, and the number of torsions up to breaking expresses the plasticity limit of that steel [7, 8].

The experimental equipment used to study the steel deformability by hot torsion belongs to the Faculty of Engineering Hunedoara [7, 8]. The equipment is provided with an electric oven which provides the sample heating in the range 20-1300°C. The experimental equipment is shown in Figure 7 [7, 8].



(a)



Figure 7

The experimental equipment built for determining the hot torsion tests of steels [7, 8]
a) the prepared experimental equipment; b) the central shaft (with the experimental samples),
without the heating oven; c) the inside of the heating oven

The test specimens are typically cylindrical, with a calibrated small-diameter central portion, having the ratio $l/d = 5$ in the point of deformation [7, 8]. The specimens for hot torsions were mechanically taken from $\Phi 20$ mm hot-rolled steel bars.

For the hot torsion test, we prepared 27 specimens-samples from each steel grade. They were subjected to torsional deformation by maintaining the deformation temperature in the experimental facility, from 50 to 50°C, within the range 800-1200°C [7, 8].

For the experimental tests, we used representative low alloyed medium carbon steel grades (43MoMn16 and 33MoCr11), destined for seamless tubes and pipes manufacturing. Typical chemical compositions of these steels are presented in Table 1 [10, 11]. We used several lots of low alloyed medium carbon steel grades (two lots for 43MoMn16 grade – lots 1 and 2, another two lots for 33MoCr11 – lots 3 and 4) (Table 2).



Figure 8

The steel specimens used in the hot torsion tests (experimental lots 1-4)

Table 1

Typical chemical compositions of low alloyed medium carbon steel grades (43MoMn16 and 33MoCr11), destined for seamless tubes and pipes manufacturing [10, 11]

Steel grades	The chemical composition, [%]						
	C	Mn	Si	P	S	Cr	Mo
43MoMn16	0.4-0.46	1.4-1.7	0.17-0.37	0.035	0.035	–	min. 0.16
33MoCr11	0.3-0.37	0.4-0.8	0.17-0.37	0.035	0.035	0.9-1.3	0.15-0.3

Table 2

The chemical compositions of the low alloyed medium carbon steel grades

No. lots	The chemical composition, [%]							
	C	Mn	Si	P	S	Cr	Mo	Al
1	0.50	1.90	0.33	0.01	0.009	–	0.26	0.056
2	0.42	1.53	0.38	0.04	0.008	–	0.26	0.024
3	0.36	0.84	0.31	0.007	0.041	0.93	0.13	0.050
4	0.40	1.00	0.32	0.007	0.018	1.16	0.23	0.069

3 The Experimental Results

Hot torsion testing is key in find the interdependence between hot plastic deformation process parameters and the steel's properties. This method has been useful to provide the existence of hot deformability as being dependent on elevated temperatures (between 800-1200°C). A versatile hot torsion testing machine (Figure 7) has been developed in the Faculty of Engineering Hunedoara, to simulate deformation schedules encountered in practical hot working operations such as rolling [7, 8].

The magnitude of the torque required to the specimen's torsion expresses the resistance to deformation [7, 8]. The number of torsions up to breaking expresses the plasticity limit of that steel at a given temperature and deformation rate [7, 8].

Table 3

The torque moment results of hot torsion tests: experimental lot 1 and experimental lot 2

No. of exp.	Testing temperature, [°C]	Torque moment [daN*cm]			
		Lot 1		Lot 2	
		Unitary value	Average value	Unitary value	Average value
1	800	212	207	242	243
2		209		242	
3		202		244	
4	850	210	191	168	165
5		200		165	
6		163		163	

7	900	179	171	163	154
8		170		149	
9		163		131	
10	950	134	133	134	136
11		133		138	
12		133		135	
13	1000	119	119	134	134
14		119		134	
15		119		134	
16	1050	104	102	106	107
17		96		108	
18		106		106	
19	1100	85	84	75	76
20		88		76	
21		78		76	
22	1150	79	74	72	72
23		71		72	
24		72		73	
25	1200	40	45	54	56
26		50		64	
27		45		50	

Table 4

The torque moment results of hot torsion tests: experimental lot 3 and experimental lot 4

No. of exp.	Testing temperature, [°C]	Torque moment [daN*cm]			
		Lot 3		Lot 4	
		Unitary value	Average value	Unitary value	Average value
1	800	258	257	242	249
2		251		253	
3		262		251	
4		165		163	
5	850	168	166	163	163
6		165		163	
7		150		150	
8	900	148	146	149	151
9		140		153	
10		130		125	
11	950	120	125	130	127
12		125		126	
13		100		110	
14	1000	108	102	118	115
15		100		116	
16		96		80	
17	1050	79	85	84	81
18		80		79	
19		70		88	
20	1100	77	74	76	79
21		75		72	
22		60		65	
23	1150	75	67	65	65
24		65		66	
25		50		50	
26	1200	57	54	52	53
27		54		58	

Table 5
The number of torsions up to breaking results of hot torsion tests: lots 1 and 2

No. of exp.	Testing temperature, [°C]	Number of torsions up to breaking [-]			
		Lot 1		Lot 2	
		Unitary value	Average value	Unitary value	Average value
1	800	36	37	33	33
2		39		33	
3		37		33	
4	850	39	44	35	38
5		45		38	
6		49		42	
7	900	41	45	45	47
8		50		47	
9		41		48	
10	950	48	46	46	47
11		44		47	
12		45		47	
13	1000	58	52	52	55
14		46		57	
15		52		57	
16	1050	57	59	68	67
17		58		66	
18		65		67	
19	1100	64	63	70	72
20		66		73	
21		59		72	
22	1150	63	64	71	73
23		64		74	
24		65		73	
25	1200	62	68	71	74
26		73		78	
27		68		74	

Table 6
The number of torsions up to breaking results of hot torsion tests: lots 3 and 4

No. of exp.	Testing temperature, [°C]	Number of torsions up to breaking [-]			
		Lot 3		Lot 4	
		Unitary value	Average value	Unitary value	Average value
1	800	41	41	36	29
2		42		27	
3		39		25	
4	850	45	43	40	37
5		42		32	
6		42		38	
7	900	47	47	47	45
8		49		48	
9		44		42	
10	950	48	45	39	46
11		45		50	
12		40		48	
13	1000	46	48	48	51
14		48		55	
15		50		50	
16	1050	50	58	54	52
17		65		50	
18		57		50	
19	1100	68	63	58	58
20		56		54	
21		65		60	
22	1150	53	65	53	61
23		65		60	
24		67		69	
25	1200	63	67	64	66
26		65		66	
27		72		68	

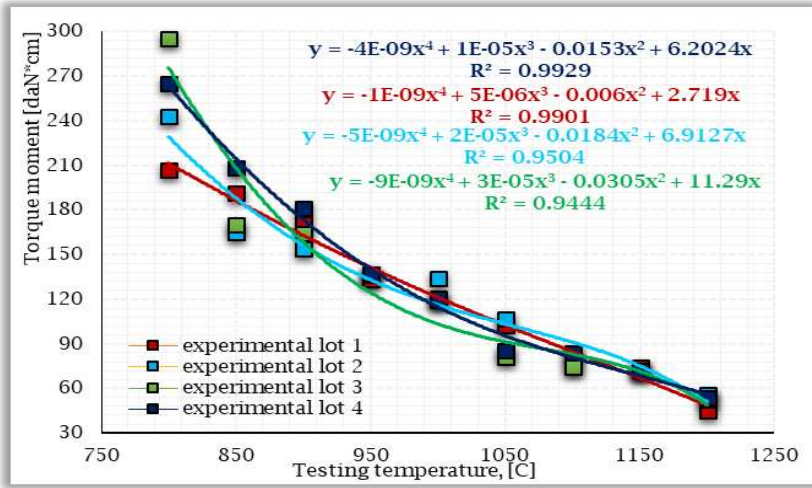


Figure 9

The variation of torque moment (variation of deformation resistance) in case of the 4 experimental lot of steels, at the experimental testing temperature (heating between 800-1200°C)

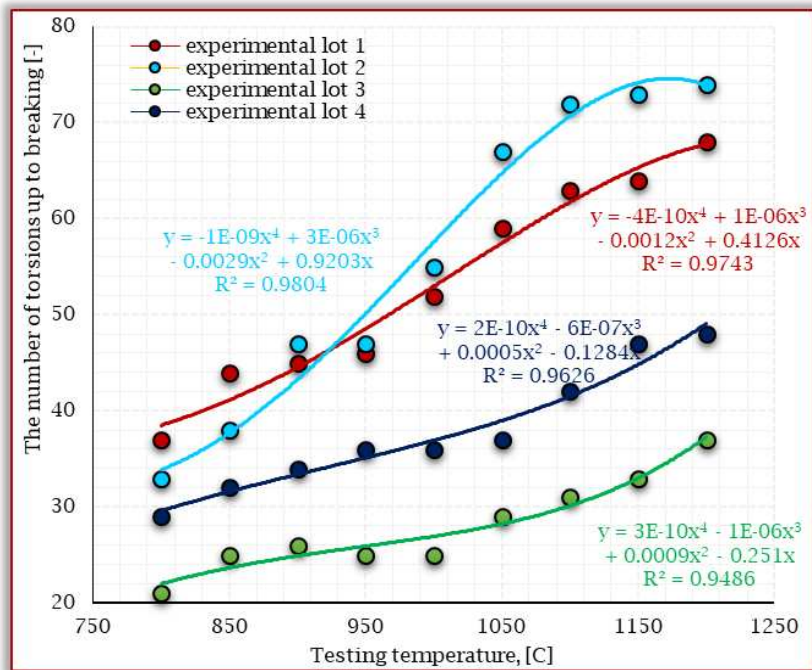


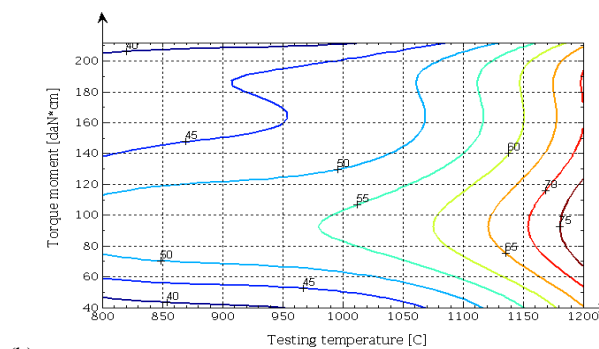
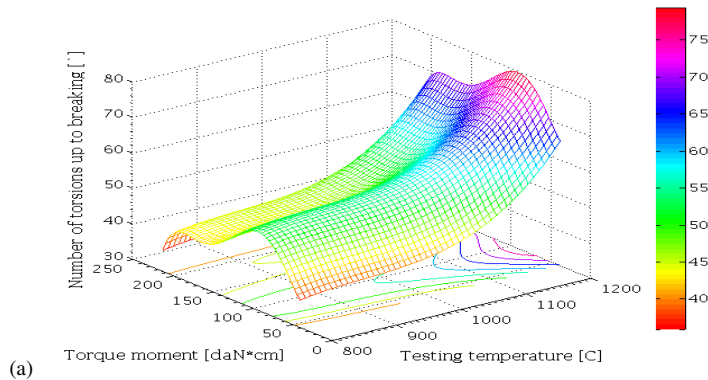
Figure 10

The number of torsions up to breaking (variations of plasticity) in case of the 4 experimental lot of steels, at the experimental testing temperature (heating between 800-1200°C)

4 The Statistical Modeling

Regarding the statistical modeling by the multiple linear regression, in order to understand the relationships between variables and their relevance to the problem being studied, have been established the following technical conditions:

- The used univariate and multivariate analyses were based on the statistical principle of multivariate statistics, which involves observation of the deformability characteristic's variations, in the experimental testing temperature range (heating between 800-1200°C).
- In the used statistical modeling, the regression analysis is a set of statistical processes for estimating the relationships among the deformability characteristics (plasticity, described by the number of torsions up to breaking and deformation resistance, described by the torque moment value) and the testing temperature.



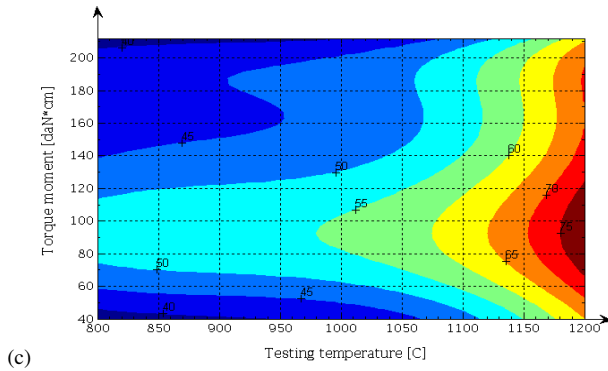
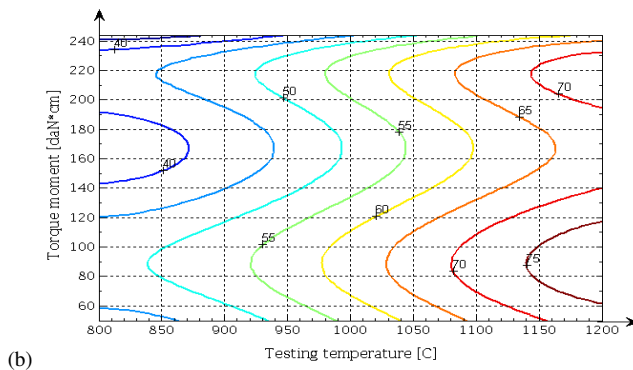
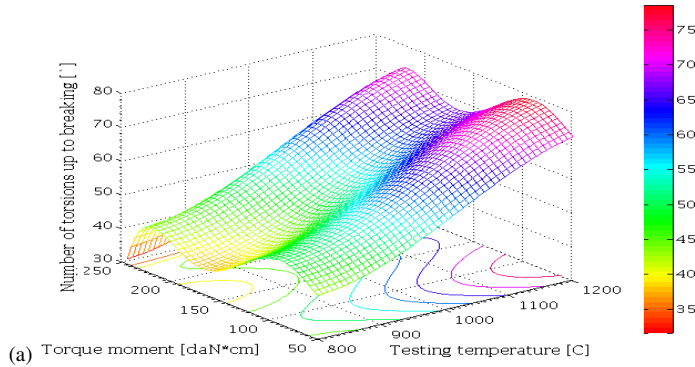


Figure 11

Diagrams for the steel specimens (lot 1), at the testing temperature (heating between 800-1200°C)

(a) the variation of deformation resistance, described by the torque moment value [equation type: $z = a_1 + a_2x + a_3x^2 + a_4x^3 + a_5y + a_6y^2 + a_7y^3 + a_8y^4 + a_9y^5$, standard deviation: $r^2 = 0.8870$, $a_1 = -545.8069$; $a_2 = 2.0159$; $a_3 = -0.0022$; $a_4 = 8.2793$; $a_5 = -2.2735$; $a_6 = 0.0652$; $a_7 = -0.0007$; $a_8 = 3.3254$; $a_9 = -5.6431$];

(b), (c) the technological domains area of the deformation resistance, described by the experimental torque moment value



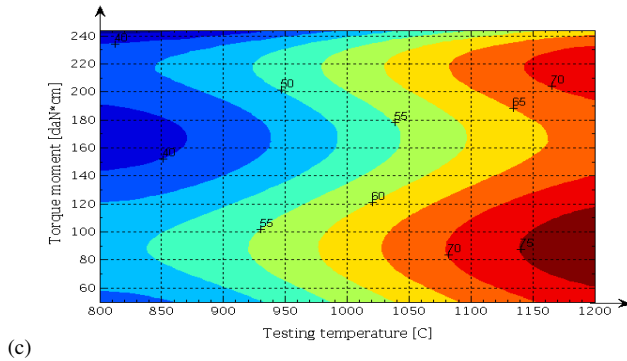
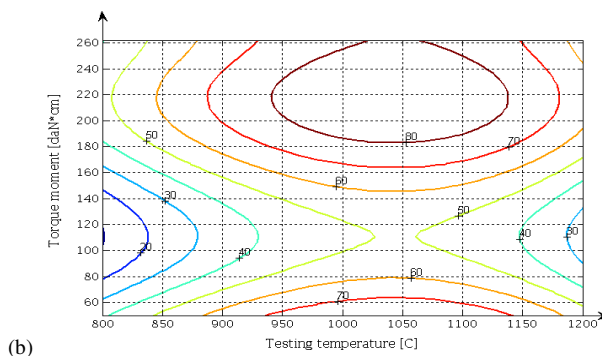
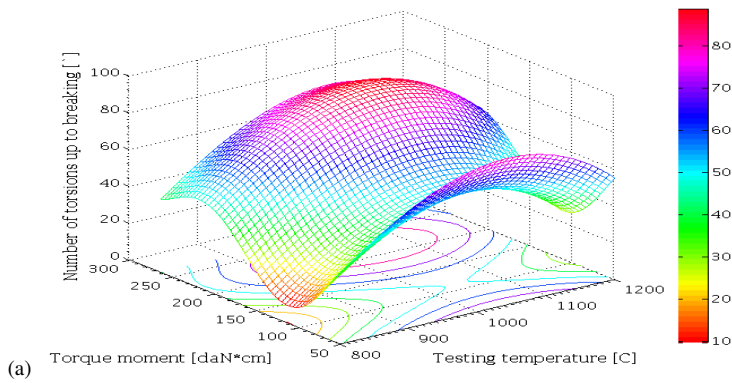


Figure 12

Diagrams for the steel specimens (lot 2), at the testing temperature (heating between 800-1200°C)

(a) the variation of deformation resistance, described by the torque moment value [equation type: $z = a_1 + a_2x + a_3x^2 + a_4x^3 + a_5y + a_6y^2 + a_7y^3 + a_8y^4 + a_9y^5$, standard deviation: $r^2 = 0.9764$, $a_1 = 631.8348$; $a_2 = -1.8157$; $a_3 = 0.0019$; $a_4 = -1.9134$; $a_5 = 0.0495$; $a_6 = 0.0652$; $a_7 = -0.0005$; $a_8 = 2.2429$; $a_9 = -3.5361$];

(b), (c) the technological domains area of the deformation resistance, described by the experimental torque moment value



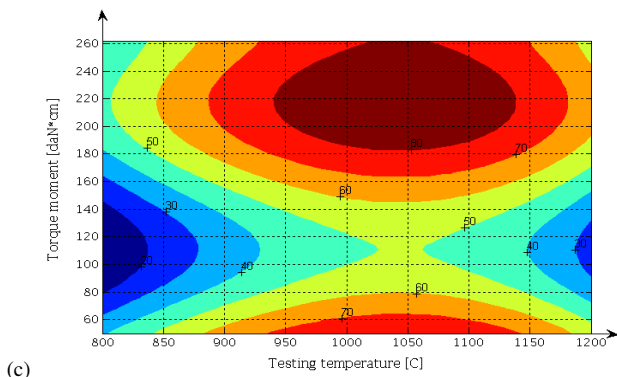
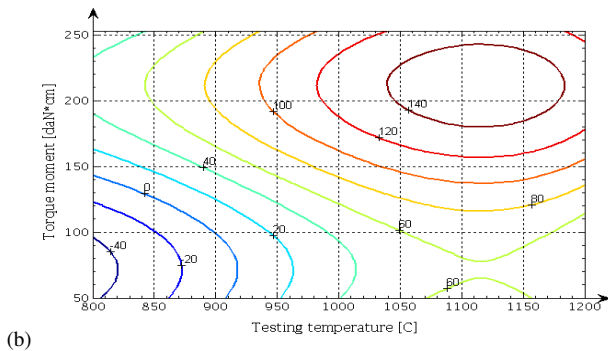
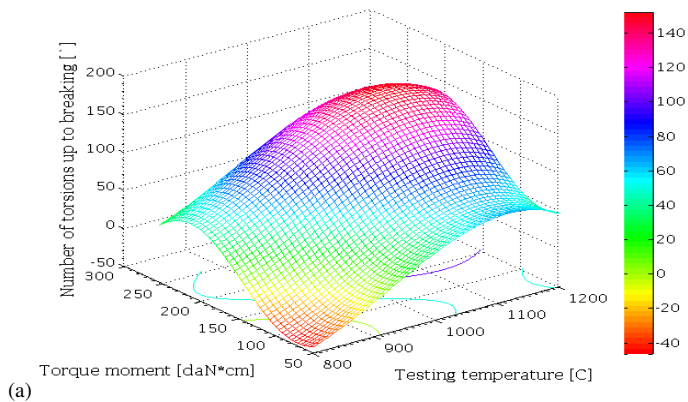


Figure 13

Diagrams for the steel specimens (lot 3), at the testing temperature (heating between 800-1200°C)

- (a) the variation of deformation resistance, described by the torque moment value [equation type: $z = a_1 + a_2x + a_3x^2 + a_4x^3 + a_5y + a_6y^2 + a_7y^3 + a_8y^4 + a_9y^5$, standard deviation: $r^2 = 0.8287$, $a_1 = 0.0002$; $a_2 = -0.7729$; $a_3 = 0.0016$; $a_4 = -7.9719$; $a_5 = 2.8268$; $a_6 = -0.0707$; $a_7 = 0.0006$; $a_8 = -2.2391$; $a_9 = 2.8577$];
- (b), (c) the technological domains area of deformation resistance, described by the experimental torque moment value



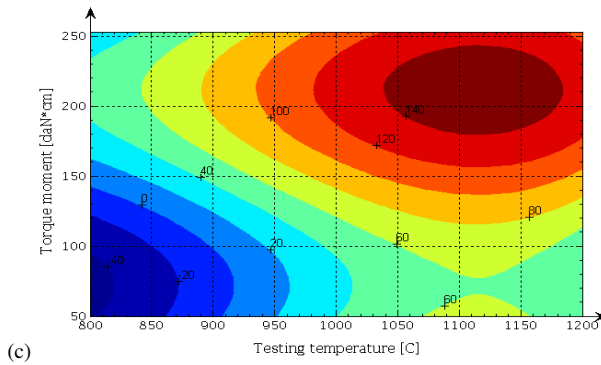
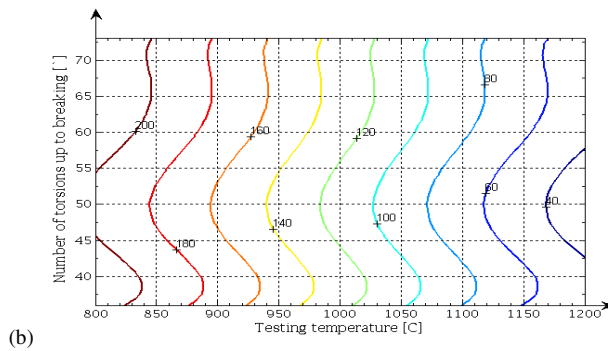
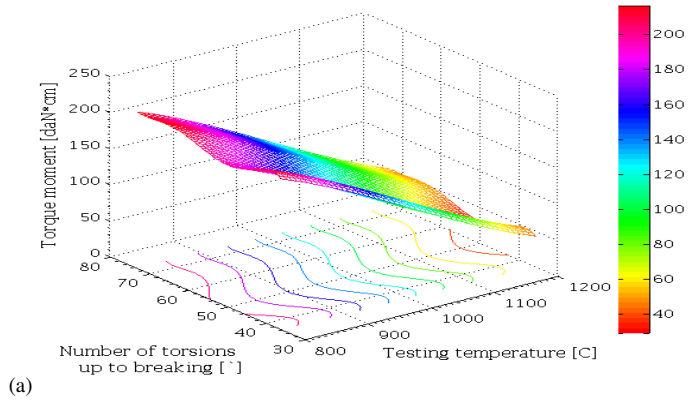


Figure 14

Diagrams for the steel specimens (lot 4), at the testing temperature (heating between 800-1200°C)

(a) the variation of deformation resistance, described by the torque moment value [equation type: $z = a_1 + a_2x + a_3x^2 + a_4x^3 + a_5y + a_6y^2 + a_7y^3 + a_8y^4 + a_9y^5$, standard deviation: $r^2 = 0.8511$, $a_1 = 2645.1552$; $a_2 = -9.4335$; $a_3 = 0.0107$; $a_4 = -3.8952$; $a_5 = -0.0935$; $a_6 = -0.0194$; $a_7 = 0.0003$; $a_8 = -1.2939$; $a_9 = 1.7628$];

(b), (c) the technological domains area of deformation resistance, described by the experimental torque moment value



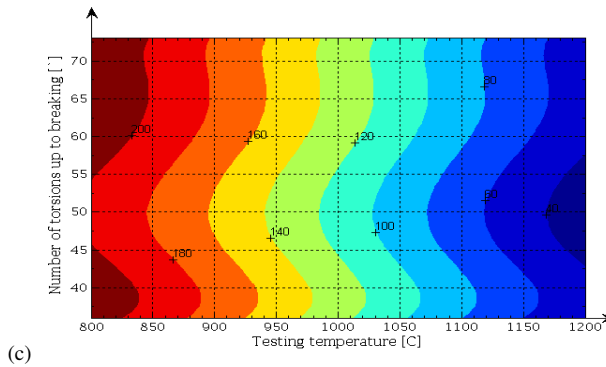
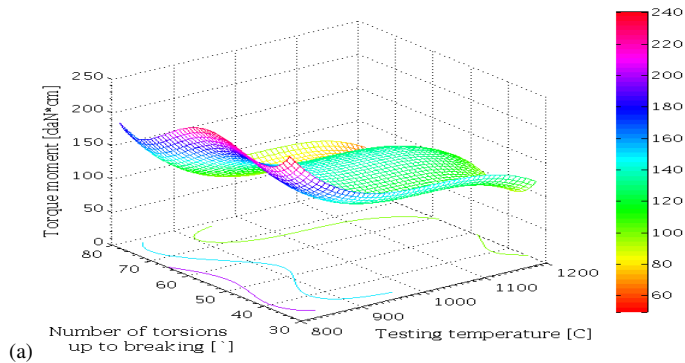


Figure 15

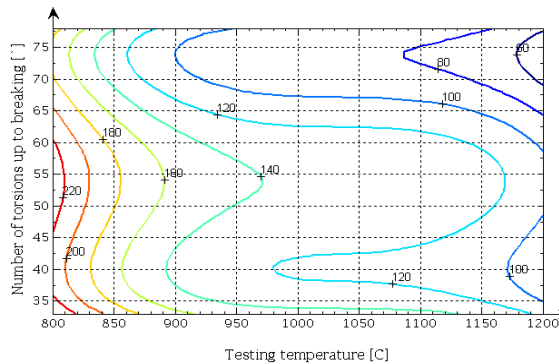
Diagrams for the steel specimens (lot 1), at the testing temperature (heating between 800-1200°C)

(a) the variations of plasticity, described by the number of torsions up to breaking [equation type: $z = a_1 + a_2x + a_3x^2 + a_4x^3 + a_5y + a_6y^2 + a_7y^3 + a_8y^4 + a_9y^5$, standard deviation: $r^2 = 0.9886$, $a_1 = -12388.9786$; $a_2 = 2.9529$; $a_3 = -0.0034$; $a_4 = 1.1348$; $a_5 = 1138.5959$; $a_6 = -42.8862$; $a_7 = 0.7911$; $a_8 = -0.0072$; $a_9 = 2.5444$];

(b), (c) the technological domains area of plasticity, described by the experimental number of torsions up to breaking



(a)



(b)

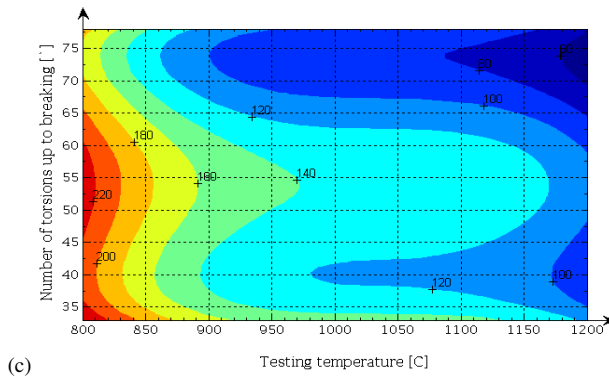
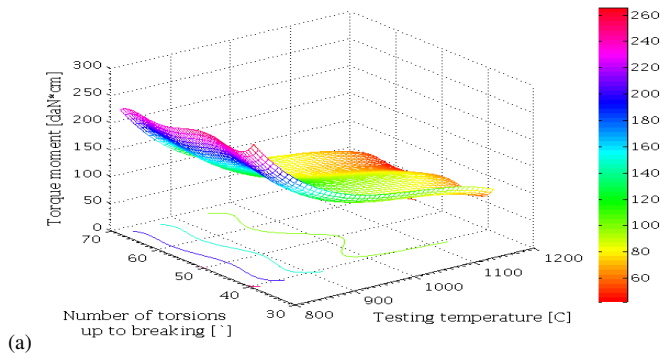


Figure 16

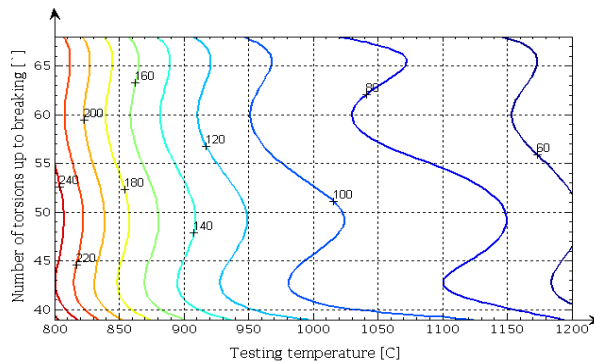
Diagrams for the steel specimens (lot 2), at the testing temperature (heating between 800-1200°C)

(a) the variations of plasticity, described by the number of torsions up to breaking [equation type: $z = a_1 + a_2x + a_3x^2 + a_4x^3 + a_5y + a_6y^2 + a_7y^3 + a_8y^4 + a_9y^5$, standard deviation: $r^2 = 0.9923$, $a_1 = 10758.4402$; $a_2 = -22.3451$; $a_3 = 0.0215$; $a_4 = -6.9343$; $a_5 = -217.5808$; $a_6 = 5.6907$; $a_7 = -0.0567$; $a_8 = 7.0028$; $a_9 = 1.2923$];

(b), (c) the technological domains area of plasticity, described by the experimental number of torsions up to breaking



(a)



(b)

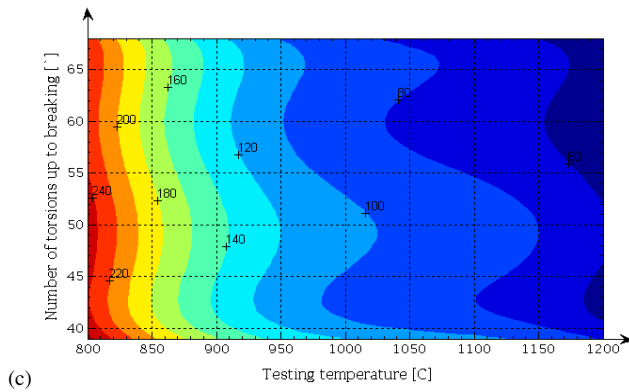
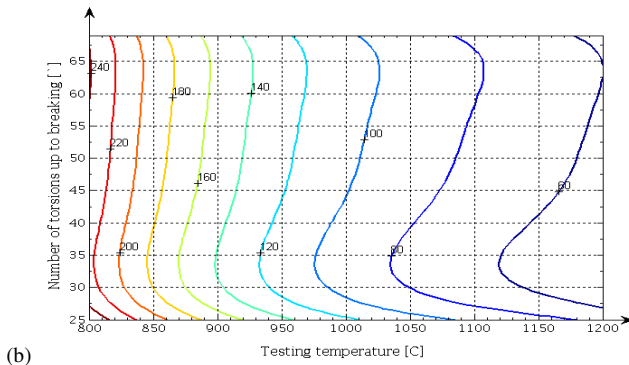
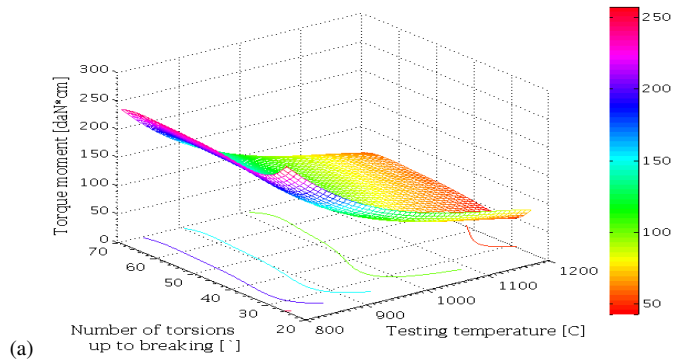


Figure 17

Diagrams for the steel specimens (lot 3), at the testing temperature (heating between 800-1200°C)

(a) the variations of plasticity, described by the number of torsions up to breaking [equation type: $z = a_1 + a_2x + a_3x^2 + a_4x^3 + a_5y + a_6y^2 + a_7y^3 + a_8y^4 + a_9y^5$, standard deviation: $r^2 = 0.9922$; $a_1 = 73428.8648$; $a_2 = -21.6111$; $a_3 = 0.0201$; $a_4 = -6.2614$; $a_5 = -6257.4592$; $a_6 = 236.7125$; $a_7 = -4.4353$; $a_8 = 0.0412$; $a_9 = -0.0002$];

(b), (c) the technological domains area of plasticity, described by the experimental number of torsions up to breaking



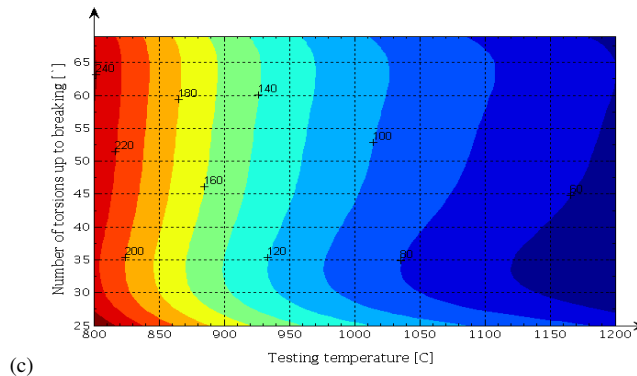


Figure 18

Diagrams for the steel specimens (lot 4), at the testing temperature (heating between 800-1200°C)

(a) the variations of plasticity, described by the number of torsions up to breaking [equation type: $z = a_1 + a_2x + a_3x^2 + a_4x^3 + a_5y + a_6y^2 + a_7y^3 + a_8y^4 + a_9y^5$, standard deviation: $r^2 = 0.9879$, $a_1 = 6295.2783$; $a_2 = -10.4354$; $a_3 = 0.0090$; $a_4 = -2.6546$; $a_5 = -227.7726$; $a_6 = 9.4815$; $a_7 = -0.1935$; $a_8 = 0.0019$; $a_9 = -7.7299$];

(b), (c) the technological domains area of plasticity, described by the experimental number of torsions up to breaking

5 Discussions

Regarding the hot torsion testing, we have the following remarks:

- As indicated in the research line, 4 lots of low alloyed medium carbon steel grades (grade 43MoMn16 and grade 33MoCr11) were developed, as shown in Table 2. From these steels the test samples were made, in order to determine the deformability characteristics (plasticity and deformation resistance);
- Thus, 108 specimen–samples belonging to the 4 lots were made and subjected to the hot torsion tests, in an own facility equipped with a tubular oven, at the testing temperature (heating being between 800-1200°C). Each determination has been repeated three times, and on the same number of test samples. The results are presented in Tables 3-6.

In the graphical representation of the hot torsion tests results, presented in Figures 9-10, we have the following comments and remarks:

- The cumulative variations presented in Figures 9-10 are shown as quantitative dependencies, based on the results shown in Tables 3-6;

-
- The variation of torque moment (variation of deformation resistance) in the case of the 4 experimental lots of steels, at the experimental testing temperature (heating between 800-1200°C) are presented cumulative in the Figure 9. The variations, as shown in the above mentioned figures, indicate that the deformation resistance decreases with increasing the heating temperature;
 - The number of torsions up to breaking (variations of plasticity) in the case of the 4 experimental lot of steels, at the experimental testing temperature (heating between 800-1200°C) are presented cumulative in Figure 10.
 - It is observed a clear similarity between the characteristics of the analyzed steels, being higher in cases of lots 3 and 4. This explanation consists in the fact that, by increasing the alloying degree, the crystallization speed decreases, which means that loss of plasticity, especially close to the 900°C. Although the steel in the lot 3 is allied with Chrome and Molybden, the level of the characteristics of plasticity is lower but constant, with a slight increase at temperature, in the range of 1100-1200°C compared to steels in lots 1 and 2.
 - We note that the analyzed steel grades show lower plasticity under 900°C, when the deformation resistance increases considerably, which is more evident in cases of lots 3 and 4. Between 900-1200°C, the plasticity is good and it increases with the temperature increases. The resistance at the deformation is not too high.
 - A higher amount of Sulphur is available for steel in lot 3, which deserves a specific analysis. As this quantity is much greater than lots 1 and 2 or even the lot 4, a comparative analysis of these should be performed, indicating the effect on the deformation of the Sulphur content which forms more or less complex inclusion. These results relate quite well to current trends in the steels destined to the seamless pipe manufacturing, and impose steels for these purposes a certain Sulphur content, in view to increasing the plasticity.

Regarding the regression analysis used for observation of the deformation resistance of the 4 lots of low alloyed medium carbon steel grades, we have the following comments:

- The variations of deformation resistance, described by the torque moment value, are presented in Figure 11-14 (a), determined by Matlab, using the regression analysis [equation type: $z = a_1 + a_2x + a_3x^2 + a_4x^3 + a_5y + a_6y^2 + a_7y^3 + a_8y^4 + a_9y^5$, with standard deviation r^2 between 0.8287–0.9764];
- The technological domains area of deformation resistance, described by the torque moment value represents the deformability diagrams for the steel specimens (lots 1-4), at the experimental testing temperature (heating between 800-1200°C). These diagrams are presented in Figure 11-14 (b)-(c).

— The relationships that determine the technological areas are useful because they can indicate a predictive relationship that can be exploited in practice.

Regarding the regression analysis used for observation of the plasticity of the 4 lots of low alloyed medium carbon steel grades, we have the following comments:

— The variations of plasticity, described by the number of torsions up to breaking, are presented in Figure 15-18 (a), determined by Matlab, using the regression analysis [equation type: $z = a_1 + a_2x + a_3x^2 + a_4x^3 + a_5y + a_6y^2 + a_7y^3 + a_8y^4 + a_9y^5$, with standard deviation r^2 between 0.9879-0.9986];

— The technological domains area of plasticity, described by the number of torsions up to breaking represents the deformability diagrams for the steel specimens (lots 1-4), at the experimental testing temperature (heating between 800-1200°C). These diagrams are presented in Figure 15-18 (b)-(c).

Having in view the experimental results described above, we can conclude the followings:

— The temperature range at which deformation is to be made must be determined first if an optimal heat condition is chosen. This temperature range is specific to each material and is dependent on the size of the degree of deformation that can be made without apparition of any cracks;

— The allowed temperature range is set so that the deformation resistance is low and the high deformation is achieved. In terms of resistance to deformation, the trend would be that the upper-temperature limit is as high as possible. For the purpose of deformations this limit is fixed at that temperature at which the deformability begins to fall;

— The technological temperature range shall be the interval for plastic deformation and shall be within the permissible temperature range. This range must be determined on the basis of correlation diagrams drawn follow the technological tests which determine the deformability of steel;

— The upper limit of the optimum value of heating temperatures applied for deforming both low alloyed medium carbon steel grades, results clearly from the correlation diagrams, is 950°C;

— Regarding the end heating temperature, for the hot deformation of the low alloyed medium carbon steel grades, we have the following experimental values (or ranges):

≡ 1150-1200°C, for grade 43MoMn16;

≡ 1150°C, for grade 33MoCr11;

— Thus, from the hot torsion tests carried out to determine the hot deformability, it results that the optimal plasticity of the analyzed steels is found within the temperature range 950-1200°C. The interpretation of the deformation diagrams

leads to the conclusion that the optimum plasticity for plastic deformation by hot rolling of the analyzed 4 lots is recommended in a range of 950-1200°C;

- Starting from the temperature of 900°C, both steel grades from the four lots have sufficient plasticity, but the value of the deformation resistance is still high up to the temperature of 950°C. The growth dynamic of the plasticity characteristics is continuous, reaching the maximum value at the temperature of 1200°C, while the resistance to deformation is reduced.

Conclusions

Hot-rolled seamless steel pipe is defined as a wrought steel tubular product made without a welded seam, manufactured by hot-rolling. It is used for conveying gas, water, and petroleum of both oil and natural gas industries. This study includes the results of the experimental tests conducted to find the plasticity and deformability characteristics of two low alloyed medium carbon steel grades (EA < 2.5%) destined for seamless tubes and pipes manufacturing and used in the petroleum industry: grade 43MoMn16 and grade 33MoCr11.

Existing standards in the oil and gas industry regulate the physico-mechanical characteristics and test patterns of steels from which the hot rolled seamless steel pipes and tubes are used, framing them in some classes of resistance. The composition of steels, their method of elaboration, and the thermal treatments corresponding to these classes are left at the discretion of the manufacturers. Therefore, the knowledge about the characteristics of deformability has for the technologist, as well as for the designer and researcher, a great practical significance, because they are important elements in establishing a correct technological process. The indications regarding the variation of plasticity with the temperature, using the hot torsion method, allowed for establishing the temperature range within which the steel plasticity is optimal and in which, in general, it is recommended to perform the entire hot plastic deformation.

The study of deformations according to the temperature (and the chemical composition too), on test lots, has established useful conclusions for the practice of rolling of these grades (43MoMn16 and 33MoCr11). The determination of hot plastic deformations values, correlated with the results of several structural research, may constitute the basic parameters for the rational development of the rolling processes.

Acknowledgement

The equipment destined to study the steels deformability by hot torsion (property of the Faculty of Engineering Hunedoara), is subject to a Romanian patent, entitled “Facility adapted for experimental determination of the resistance to thermal fatigue of samples placed tangentially on the generator of support discs,” registered in the Romanian State Office for Inventions and Trademarks (OSIM).

References

- [1] Reports and Data – Market News, 2019, <https://www.reportsanddata.com>
- [2] A. Yamane, H. Shitamoto, K. Yamane, Development of numerical analysis on seamless tube and pipe process, Nippon Steel & Sumitomo Metal Technical Report, 107 (2015), pp. 108-113
- [3] K. Masamura, Y. Nagahama, Manufacturing processes and products of steel pipes and tubes in JFE steel, JFE Technical Report, 7 (2006), pp. 1-6
- [4] D. Kuc, G. Niewielski, Technological plasticity and structure in stainless steels during hot-working, Journal of Achievements in Materials and Manufacturing Engineering, 32, 2 (2009), pp. 154-161
- [5] Z. Pater, J. Kazanecki, Complex numerical analysis of the tube forming process using diescher mill, Archives of Metallurgy and Materials, 58/3 (2013), pp. 717-724
- [6] J. Magaone, I. Ilca, Influence factors analysis and steels behavior within the high temperature operating, Știința și Inginerie, 16 (2009), pp. 629-636
- [7] V. Alexa, I. Kiss, Experimental tests on the plasticity and deformability characteristics of several stainless steel grades used for hydro-pneumatic equipment's manufacturing, Acta Polytechnica Hungarica, 15, 8 (2018), pp 121-139
- [8] V. Alexa, I. Kiss, Deformability of martensitic stainless steel (grade X46Cr13) by hot torsion, Annals of Faculty Engineering Hunedoara – International Journal of Engineering, XVII, 2 (2019), pp. 209-214
- [9] I. Ilca, I. Kiss, V. Alexa, S. Rațiu, Analysis of some steel behaviour at high operating temperatures, Annals of Faculty of Engineering Hunedoara–International Journal of Engineering, 14, 2 (2016), pp. 183-189
- [10] STAS 8185–88: Steels for seamless tubes for petroleum industry. Grades and technical requirements for quality
- [11] DIN EN 10297–1: Seamless circular steel tubes for mechanical and general engineering purposes; Non–alloy and alloy steel tubes

Security Risk Assessment-based Cloud Migration Methodology for Smart Grid OT Services

**Bojan Jelacic, Imre Lendak, Sebastijan Stoja,
Marina Stanojevic, Daniela Rosic**

Faculty of technical sciences, University of Novi Sad
Trg Dositeja Obradovica 6, 21000 Novi Sad, Serbia
E-mail: bojan.jelacic@uns.ac.rs; lendak@uns.ac.rs; sebastijan.stoja@uns.ac.rs;
marina.stanojevic@uns.ac.rs; drosic@uns.ac.rs;

Abstract: The primary goal of this paper is to present a security risk assessment-based methodology for migrating sensitive Smart grid operational technology (OT) services to the computing cloud, either on or off-premise. We created a baseline system architecture diagram for smart grid Industrial Control Systems (ICS) aligned with the IEC-62443 model of security zones. We identified potential threat sources and threats which might affect the confidentiality, integrity, and availability (CIA triad) of OT services. We defined a threat impact and likelihood assessment strategy tailored for use in smart grids. Based on the combined impact and likelihood of threats we present a risk matrix, a tabular risk assessment template, and a baseline cloud migration strategy. We test our methodology on two cloud migration case studies, namely a large distribution system operator (DSO) with a complex OT environment; and a small DSO with limited OT capabilities, budget, and IT staff. As there are no risk assessment-based studies which tackle the problem of migrating smart grid OT services to a cloud computing architecture in a systematic way, our method will be a valuable asset for any smart grid system owner/operator. Which will be able to guide them in choosing an optimal cloud migration strategy, both fitting their specific requirements and maintaining an adequate level of information security.

Keywords: Smart Grid; Cloud computing; control systems; information security; IT/OT systems; risk analysis; SCADA systems

1 Introduction

Industrial control systems (ICS) allow the operators of various systems, ranging from food processing plants to electric power systems, to remotely monitor and control the underlying physical processes. Modern ICS are complex and heterogeneous information systems, which can be regarded as a critical link connecting the cyber with the physical, i.e. connecting the hardware components

in the process environment with the software used to monitor and control the industrial processes, thereby gluing the system together into a true cyber-physical system. Modern smart grid ICS consist of a diverse range of software-intensive solutions and services, e.g. the Supervisory Control and Data Acquisition (SCADA) allows remote monitoring and control, the Outage Management System (OMS) allows operators to handle planned and unplanned outages, Geographic Information Systems (GIS) are used to manage a company's assets, and Meter Data Management (MDM) systems handle large volumes of data collected by myriads of smart meters installed. Although the list of services used is usually quite different for each smart grid system operator, there are common elements, which allow us to perform their comprehensive security analysis. There are specific cloud migration challenges in smart grids as they are critical infrastructures whose continuous operation is of utmost importance to their owners, customers and the Nation. Their dual information systems consist of the information technology (IT) and operational technology (OT) elements tasked with business and real-time operations. Although these systems (IT and OT) worked as separate entities traditionally, the latest trends show that the two 'silos' converge. This IT-OT integration is regarded as a vital steppingstone towards a successful smart grid.

Different actors consider the integration of cloud computing into their (control) systems as the cloud would allow them to outsource hardware acquisition and maintenance costs. Obviously, cybersecurity is a highly relevant aspect of any cloud migration strategy, as cyber-attacks might impact national security, the economy, and the safety of the general population. Therefore, the goal of this paper is to propose a risk assessment-based methodology which can be systematically used by smart grid system owners and/or operators to create a tailored cloud migration strategy for their OT services. Our method is aligned with the Federal Information Processing Standards (FIPS) 199 security categorization of information and services [1] and the IEC-62443 model of security zones [2].

Apart from this introduction, the paper consists of three sections. In section two we overview the state-of-the-art in smart grid security, cloud security, and risk assessment. In the third section we formalize the security risk assessment methodology for smart grid OT environments. In the fourth section we present two case studies in which significantly different smart grid OT systems are migrated to the (hybrid) computing cloud using the proposed methodology.

2 Related Work

In this section, we overview the state-of-the-art in the fields of smart grid security, cloud computing security, risk assessment, and the intersections of these three domains.

2.1 Smart Grid Security

While bringing along substantial benefits in automation, supervision, real-time monitoring, and control throughout the system, modern power systems introduce new vulnerabilities and security issues [3]. The threat to energy firms is likely to increase in the coming years as new developments, such as further extensions of smart grids and smart metering expose more of their infrastructure to the Internet [4]. The Stuxnet sabotage attack against nuclear facilities in Iran made clear what could be done through cyberattacks [5]. The Ukraine 2015 and 2016 cyberattacks against selected elements of the state's electric power system showed that such attacks against cyber-physical systems can have significant consequences in the form of power outages, which in 2015 lasted 1-6 hours and affected ~225,000 customers [6].

The importance of security and privacy in smart grids is explained through a systematic study of thirty-six publications on this topic [7]. In reference [8] the authors claim that cyberattacks on power grid could result in significant damages and they describe a cybersecurity protection approach to assist in the design and implementation of power grid protection systems. Others believe that cyberattacks on power grids are pushing threat and risk assessment to another complexity level [9]. The Security for Smart Electricity Grids (SEGRID) project was tasked with building on existing methods to address the inter-dependencies characteristic of a smart grid [10]. Reference [11] contains a vulnerability analysis of a simultaneous attack scenario, using a modified cascading failure simulator. The authors claim that their simulator can automatically find the strongest attack combinations for reaching maximum damage in terms of generation power loss and time to reach black-out. The authors of reference [12] claim that one way to ensure vital asset protection is to look for vulnerabilities from an attacker's viewpoint. High-priority and prescriptive compliance frameworks (e.g. the NERC CIP requirements [13]) require IT staff and OT staff to work together in new and innovative ways to share documentation and collaborate on risks and mitigation [14].

2.2 Cloud Computing Security

The National Institute of Standards and Technology (NIST) outlines four cloud delivery models [15] [16]: *public clouds* available to the public, *private clouds* operated solely by or for a single organization, *community clouds* shared by a specific community, as well as *hybrid clouds* which are compositions of two or more of the above three models. References [17] [18] assess the various technical aspects of cloud migration in different settings. One of the main challenges in the wider adoption of any of the above cloud computing delivery models is (information) security. This challenge is even higher when the migrated systems are involved in national security, disaster response, defense, or homeland security missions, where the criticality of service availability is elevated [19]. The authors of references [20] and [21] report a detailed analysis and categorization of various

security threats in a cloud computing environment. The Cloud Security Alliance (CSA) listed the “Treacherous 12,” the top 12 cloud computing threats organizations (both cloud customers and providers) faced in 2016 that can erase any gains made by the switch to cloud technology [22]. A survey conducted with IT managers found cost efficiency and data security the top two most sensitive aspects in cloud platform adoption [23]. The most important challenges to be solved before organizations and individuals will have the trust to deploy their systems in cloud environments are security, privacy, power efficiency, compliance, and integrity [24]. A recent study [25] indicated that the ideal ratio of a hybrid cloud environment is around 60 percent cloud and 40 percent physical servers.

In general, most studies about cloud computing applications in power systems are from the performance and/or cost perspectives. According to the authors of reference [26], cloud computing can significantly improve the operational performance of power systems. Reference [27] presents a methodology for deploying a monolithic Advanced Distribution Management System (ADMS) in the cloud without impacting its operational performance.

2.3 Risk Assessment and Threat Modeling

Information security risks arise from the loss of confidentiality, integrity, or availability (i.e. the CIA triad) of information or information systems and reflect the potential adverse impacts to (organizational) mission, functions, image, or reputation [28]. Risk assessment is the process of identifying, estimating, and prioritizing information security risks. The Federal Information Processing Standards (FIPS) 199 establishes three security categories for information and information systems [1], based on the potential impact on an organization if certain events occur: low, moderate, and high.

The European Network and Information Security Agency (ENISA) analyzes threats against smart grids and concludes that availability and integrity are of higher importance in time-critical industrial control systems, while confidentiality is important in enterprise services provided to end customers or businesses [29]. Threat modeling allows us to identify and rate the threats associated with a system. It might be implemented using one of the following three approaches: asset-centric, software-centric, and attacker-centric. The authors of [30] propose a software-centric threat analysis-based cloud migration strategy for smart grid ICS, based on Microsoft’s STRIDE methodology.

Based on the above state-of-the-art review, we conclude that there are no risk assessment-based studies that specifically tackle the problem of systematically migrating smart grid OT services to a system architecture utilizing the benefits of cloud computing. That is the gap we intend to fill by proposing a method that can be used by any smart grid owner/operator in need to devise an optimal cloud migration strategy.

3 Risk Assessment Methodology

In this section, we describe the vital elements of our risk assessment method. We list threat sources and (most likely) threats, domain-specific definitions of impact, and likelihoods. We define a risk matrix, a risk assessment template, and a baseline (risk assessment-based) migration strategy to a cloud computing environment.

3.1 Threat Sources and Threats

Most likely smart grid-specific threat sources are insiders, state-sponsored actors deploying advanced persistent threats (APT) or professional hacker groups executing attacks in hope of reaping some form of financial reward, e.g. through ransomware attacks. We grouped a non-definite list of most likely smart grid OT threats based on which element of the CIA triad might be most affected if they were realized. The resulting threat grouping is shown in the table below.

Table 1
CIA-based grouping of smart grid ICS threats

CIA	Threats
Confidentiality	Confidentiality loss of configuration data
	Confidentiality loss of operational data
Integrity	Unauthorized modification or deletion of configuration data
	Unauthorized modification or deletion of operational data
Availability	Denial of service attack on backend services
	Backend service failure due to bad data
	Denial of service attack on communication channels, e.g. mobile or network communications unavailable due to an attack
	Denial of service attack on the human-machine interface

As our analysis is mainly focused on the OT subsystem, we consider confidentiality and integrity of operational and/or configuration data. With availability, being a key security goal in OT systems, we identified four threats, which might affect the backend services, human-machine interface or the communication layer of the smart grid, caused by either the insertion of bad data or a Distributed DoS (DDoS) attack.

3.2 Likelihoods

Due to the relatively small number of publicized cyberattacks against smart grids, assessing the likelihood of such attacks is a considerable challenge. We hereby propose an industry-specific likelihood classification based on the following threat actor and smart grid characteristics:

- Existence of vulnerabilities in the smart grid services or infrastructure, ranging from serious to none.
- Known exploits and the level of difficulty to execute them remotely, via physical access and/or by gaining elevated privileges.
- Workforce loyalty and insider threat monitoring capabilities.
- Existence of capable threat sources and level of their motivation to execute attacks.
- Level of staff information security training, especially in the OT department(s).
- Level and quality of IT/OT system segmentation into security zones.

Table 2
Smart grid ICS threat likelihoods

Likelihood	Threat source/system characteristics
Very likely	Serious security flaws in the smart grid services or underlying infrastructure (e.g. operating systems)
	Known exploits can be launched from the Internet, semi-trusted or untrusted networks
	No insider threat monitoring, workforce loyalty issues
	Highly motivated and capable threat-source
	OT personnel without proper security training
	Highly integrated IT-OT systems exposing the OT environment
Moderate	Limited security flaws in smart grid services and infrastructure
	Known exploits can be launched only via physical access to the target system
	Loyal workforce and limited insider threat monitoring in place
	Limited threat source motivation, due to limited political or financial impact of potential attacks
	Limited security training for OT personnel
	Custom IT-OT system segmentation, limited OT system exposure
Low	No known security flaws in the smart grid services and infrastructure
	No known exploits, malicious users need physical access and elevated privileges in the target system
	Loyal workforce, advanced insider threat monitoring
	No threat source motivation due to minimum political or financial impact
	Well-trained OT workforce knowledgeable about the latest threats
	Excellent IT-OT system segmentation, no OT system exposure

Obviously, any occurrence of ‘very likely’ threats should be mitigated first by putting proper security controls in place. Possible threats in the ‘low’ likelihood class might be tackled last.

3.3 Impact

We propose the following three-level, smart grid-specific impact classification based on a theoretical attack's possible effect on (1) the correct operation of the smart grid and (2) the operating company's public image.

- **High-severity** impacts include loss of human lives or serious injuries of employees or customers, widespread power outages, severe infrastructure damage, and critical service malfunctions (e.g. prolonged SCADA outage).
- **Medium-severity** impacts include availability loss of non-critical services (e.g. GIS or EMS) or (limited) access to sensitive information (e.g. personally identifiable information or sensitive business data). These might cause reputation damage, significant client dissatisfaction, and possibly even penalties imposed by regulatory bodies and government agencies.
- **Low-severity** impacts do not lead directly to the failure of critical services or confidentiality loss of sensitive business or customer data. However, they cause delays in non-critical services or information disclosure that does not have a direct business impact, but may lead to exploitable vulnerabilities.

The above listed possible impacts are summarized in the table below.

Table 3
Smart grid ICS impact levels

Level	Impact description
High severity	Loss of human lives or serious injuries
	Widespread power outages
	Severe infrastructure damage (e.g. high voltage transformer damage)
	Prolonged critical service malfunctions (e.g. SCADA)
Medium severity	Exposure of personally identifiable information or sensitive business data
	Very limited power outages
	Limited infrastructure damage (e.g. single transformer)
Low severity	Prolonged non-critical service malfunction (e.g. GIS)
	Limited unavailability of non-critical services
	Information disclosure without direct financial impact or adverse impact on company image

3.4 Risk Matrix

Based on the above-presented likelihood and impact classifications we determined the risk rating matrix shown in Figure 1. Impact is on the horizontal axis, likelihood on the vertical axis, and the rounded rectangles in the center of Figure 1 represent risk levels.

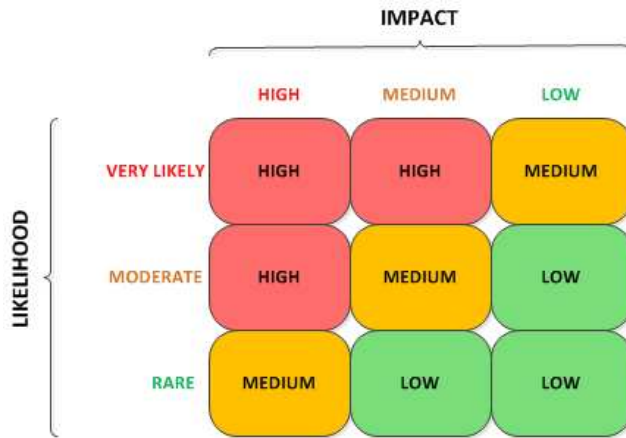


Figure 1
Risk rating matrix

We identified three risk levels: low, medium, and high. High risk is associated with those threats which are both likely and have a medium to high impact, e.g. a known vulnerability with an existing exploit in OT systems which might be used to cause a major power outage. The Ukraine 2015 attack falls into this category because the attack was very likely, due to weaknesses in personnel and IT systems security, as well as the geopolitical situation in 2015. Converged IT-OT privileged account management allowed the attackers to gain access to the OT system and execute commands which led to widespread power outages, i.e. had a high impact.

It is important to note that the threat sources, threats, impacts, likelihoods, and risk levels defined in this section are not definite and might be tailored for different OT environments based on their specific requirements. If the levels proposed in this paper are modified, then the migration strategies outlined in the following chapters might change as well.

3.5 Risk Assessment Template

Based on the above analysis of the possible threats, likelihoods and impacts, we created a risk assessment template, which can be used by smart grid owners/operators to document their risk assessments. For each identified threat we added one row, and each OT service should be entered as columns. After that, it is necessary to assess the impacts and likelihoods of the threats for each OT service (i.e. in each row) and to enter their ratings under column headers “I” and “L”. The cumulative risk is determined based on the risk rating matrix shown in Figure 1 and should be entered into the lower parts of the three-element cells with darker backgrounds in the risk assessment template below.

Table 4
Smart grid ICS risk-assessment template

Threat / Service	OT Service #1		OT Service #2		...		OT Service #N	
	I	L	I	L	I	L	I	L
Confidentiality loss of configuration data								
Confidentiality loss of operational data								
Configuration data integrity loss								
Operational data integrity loss								
Backend service failure due to bad data								
DoS against backend services								
DoS against the communication system								
DoS against the human-machine interface								

This risk assessment template can be generalized, as both the list of threats in the rows, as well as the list of IT/OT services in its columns can be tailored and aligned with specific smart grid system architectures. It can be tailored to other critical infrastructures or any industrial systems as well.

3.6 Baseline Cloud Migration Strategy

We propose the following baseline cloud migration strategy when deciding whether to keep an OT service on-premise (i.e. on physical servers or a private cloud), or deploy it in a community cloud:

- Keep services on-premise if they directly interface (i.e. connect to) physical equipment and do not have extremely high storage and/or processing requirements.
- Keep workstations in the control center so that the operators monitor and control the smart grid from a physically secured location.
- Move all low (L) and medium (M) risk services to the community cloud.

- Assess all high (H) risk services and move them to the community cloud if their storage or processing requirements are high¹.

Obviously, the above rules might be tailored according to the risk ‘appetite’ of smart grid owners/operators, i.e. aligned with their willingness to accept certain levels of risk.

4 Case Studies

We used the risk assessment method presented in the previous sections to analyze two significantly different case studies, in which different types of distribution system operators (DSO) migrate parts of their OT systems to the computing cloud. In the first case study, we performed a risk assessment based on which we proposed a hybrid cloud-based architecture for a large, multi-state and/or international DSO. In the second case study, we did the same for a (very) small DSO. We also present the most relevant characteristics of these two types of systems, document our risk analysis approach, and draw future, cloud-based system architecture diagrams. As a guide in any OT-to-cloud migration, we developed a somewhat simplified smart grid IT/OT control system architecture shown in Figure 2. In line with the IEC-62443 model [2], the building blocks of this system architecture are grouped into the following five security levels:

- **Level 1: Process Environment** - Contains the process subsystem, e.g. substations, remote terminal units (RTU), local SCADA (not shown in Figure 2).
- **Level 2: Operational Technology (OT)** – Consists of the services which allow system owners/operators to remotely monitor and control the smart grid from a control center. A subset of such services is shown in Figure 2: Supervisory Control and Data Acquisition (SCADA), Energy/Distribution Management System (EMS/DMS), Switching Management (SM), Outage Management System (OMS) and Meter Data Management (MDM) services. The MDM usually does not share its communication infrastructure with the SCADA.
- **Level 3: OT DMZ** – It is the main link between the OT and IT domains, allows data to flow in a tightly controlled manner between these two zones. In our, simplified smart grid system architecture it contains (only) the Historical and Security Information and Event Management (SIEM) services.

¹ The definition of ‘high’ will obviously vary between smart grids, and it will not be possible to exactly specify it here. Each system owner/operator will measure it based on its current and (planned) future capabilities.

- **Level 4: Information Technology (IT)** – The majority of IT services are hosted in this environment. We consider only the Geographic Information System (GIS), as it is often the master source of the network model, i.e. the asset information is exported from the GIS and imported into different OT services, e.g. SCADA, EMS, OMS, DMS, whose operation relies on having access to the up-to-date network model of the electric power system.
- **Level 5: IT DMZ** – Usually hosts services accessible from the Internet and/or interfacing information systems maintained by other smart grid actors, e.g. regulators, adjacent generation, transmission or distribution systems.

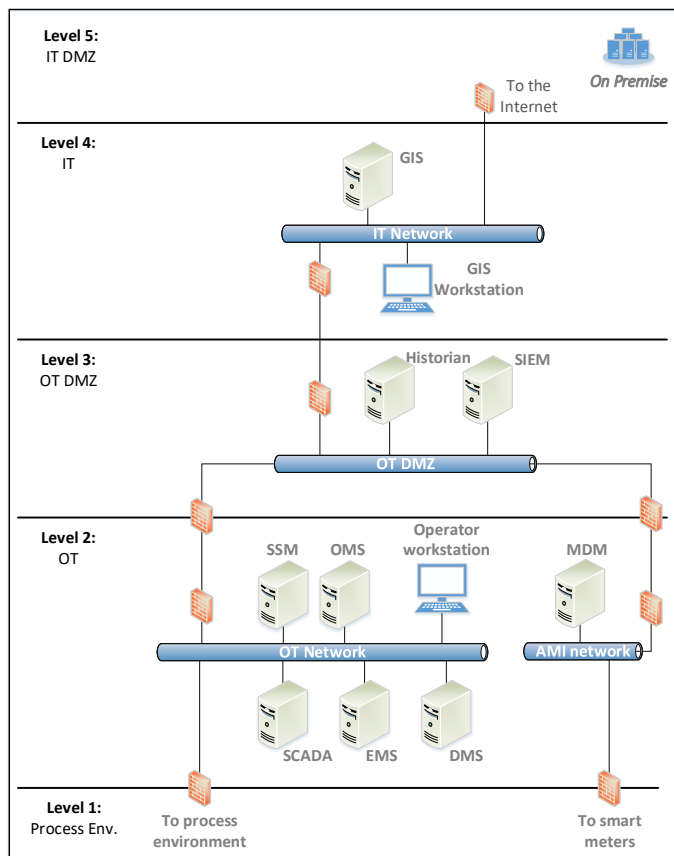


Figure 2

Original large DSO system architecture

Levels 1 and 2 correspond to the OT environment. Levels 4 and 5 are constituents of the IT environment. Level 3 is an IT/OT hybrid.

4.1 Large DSO Cloud-Based System Architecture

We define the large DSO as a system supplying at least one million customers either in a densely populated, urban area or in a larger geographic area. As additional inputs to the risk assessment, our theoretical DSO possesses the following specific characteristics:

- There is only one, primary data center. There is no disaster recovery (DR) center, but the DSO plans to invest in DR capabilities.
- There are no known vulnerabilities on the servers, workstations, and underlying communication infrastructure.
- There are no known exploits that can be launched from untrusted networks or via gaining physical access to the system or gaining elevated privileges.
- There are highly motivated state-sponsored and other threat sources.
- Loyal, tightly controlled, and security-aware workforce.
- Adequate IT budget and staff. A small but dedicated information security team.
- Clearly separated security zones aligned with IEC 62443 (see Figure 2).

4.1.1 Impact Assessment

In the above-described setting and by using the impact classification template in Table 3 we identified the following high impact threats, either leading to (1) loss of human lives or injury (e.g. field crew affected), (2) widespread outages, (3) severe infrastructure damage (e.g. critical power transformer failure), or (4) prolonged critical service malfunctions (e.g. SCADA failure):

- Integrity loss of SCADA operational data if it leads to infrastructure damage.
- Integrity loss of operational EMS/DMS data if it leads to service or power outages, which is likely if they operate in a closed-loop and automatically issue commands via the SCADA.
- Integrity loss of SM operational data if it leads to personnel injury.
- Any availability loss of SCADA (backend) services.

We identified the following groups of medium impact threats:

- Exposure of personally identifiable (operational) data in the MDM or OMS, which handles customer information.
- Any DoS attack against any of the (non-critical) backend services.
- Any operational data confidentiality loss, as all services handle sensitive business data.

4.1.2 Likelihood Assessment

We assessed likelihoods in line with the specific case study setting, in which there are no known vulnerabilities, but there are highly motivated threat sources that might exploit zero-day vulnerabilities. As we identified a loyal and well-monitored workforce, we will consider insider threats infiltrated by threat actors as unlikely. Threat sources might initiate attacks from untrusted networks (i.e. the Internet), the public switched telephone network, or the process environment by gaining physical access to the geographically dispersed assets of the DSO. In such a setting DoS attacks against the GIS backend services from the Internet or hacked assets in the IT network are very likely.

As far as the moderately likely threats are concerned, we identified the following:

- All threat types against the Historian and SIEM due to their more exposed position towards untrusted networks in the OT DMZ.
- All remaining threats against the systems which are more exposed to attacks from the process environment, i.e. SCADA, MDM.
- All threat types against the OMS/SM which might be carried out via the mobile devices of the field crew or the public switched telephone network.
- EMS/DMS service failure caused by operational or configuration data integrity loss, e.g. intentional insertion of bad data.

Denial of Service attacks against the OMS/SM backend services, initiated either from the public switched telephone network, or the mobile devices carried by field crews.

4.1.3 Risk Assessment Results

Based on the above impact and likelihood analysis, as well as the risk matrix in Figure 1 we populated the risk cells in the risk assessment template below.

Table 5
Large DSO's risk assessment

Threat / Service	SCADA		OMS \ SM		DMS \ EMS		GIS		MDM		HIS \ SIEM	
	I	L	I	L	I	L	I	L	I	L	I	L
Confidentiality	M	L	M	L	M	L	M	M	M	M	M	M
loss of configuration data	L		L		L		M		M		M	
Confidentiality	M	M	M	M	M	L	M	V	M	M	M	M

loss of operational data	H		M		L		H		H		M	
Configuration data integrity loss	M	L	M	L	M	L	M	M	M	M	M	M
	L		L		L		M		M		M	
Operational data integrity loss	H	M	H	M	H	L	M	V	M	M	M	M
	H		H		M		H		H		M	
Backend service failure due to bad data	H	M	M	L	M	M	M	M	M	M	M	M
	H		L		H		M		M		M	
DoS against backend services	H	M	M	M	M	L	M	V	M	M	M	M
	H		M		L		H		M		M	
DoS against the communication system	H	M	M	M	M	L	M	V	M	M	M	M
	H		M		L		H		M		M	
DoS against the human-machine interface	L	M	L	L	L	L	L	M	L	M	L	M
	L		L		L		L		L		L	

The baseline cloud migration strategy presented in section III/F was slightly adapted in the following manner to further distinguish high-risk services:

- Keep services on-premise if they directly interface (i.e. connect to) physical equipment.
- Keep all high (H) risk services on-premise if their impact rating is also high.
- Assess all (high risk, medium impact) and medium risk services. If their storage and/or processing requirements are high, then move them to a community cloud. The SIEM and the Historian usually fall into this category.
- Move all low (L) risk services to the community cloud.
- Move the disaster recovery center to a community cloud. The DR services physically interfacing equipment in the process environment (e.g. SCADA) need to be kept on-premise.

Based on the case study definition and our risk assessment, we propose that the large DSO migrates its OT services to the cloud-based system architecture shown in Figure 3.

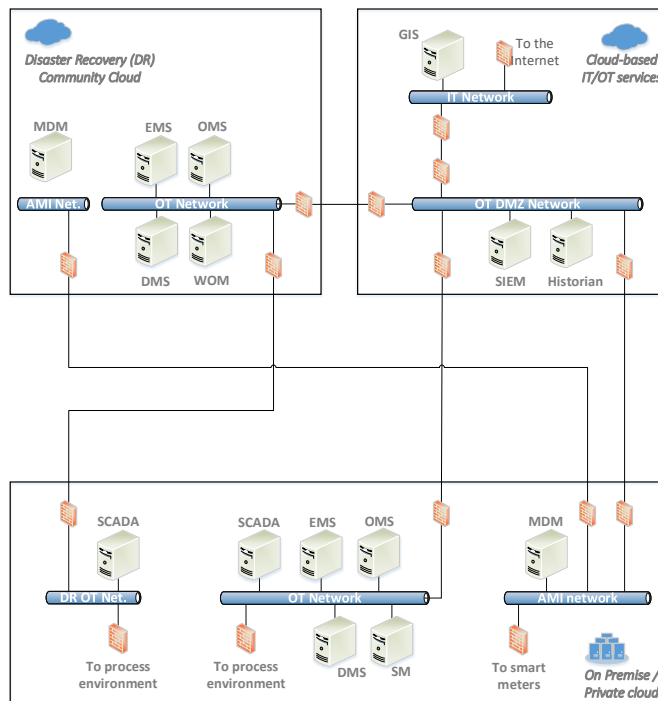


Figure 3
Large DSO's cloud-based OT system

The most notable advantages of this solution compared to the original solution (and to those operated by most modern, large DSOs) are the following:

- Potentially improved security monitoring and awareness capabilities via a community cloud-based SIEM, which might have insight into the security posture of multiple smart grid actors if they shared a Security Operations Center (SOC).
- Lowered disaster recovery costs².
- Seamless upgrades to new versions of the services utilized, as the community cloud service provider (CSP) might perform regular system upgrades as part of its service level agreement (SLA).

It must be noted that seamless upgrades to new versions for different large DSOs using a solution offered from the same computing cloud would be complex undertakings, as large DSOs tend to have different internal processes and (a plethora of) customer-specific requirements. It must be mentioned that a vital

² Costs can be lowered if the DR deployment is minimal.

precondition for the creation of such system architectures is the existence of community clouds for smart grids, which would be similar to the federal cloud in the USA.

4.2 Small DSO Cloud-based System Architecture

One possible criterion for identifying a small DSO is to check the number of customers and characterize it as ‘small’ if it has up to 100,000 (one hundred thousand) customers in a small or larger, but sparsely inhabited geographic region. Today such companies (usually) have limited IT budgets, which in turn means that their spending on computing hardware and information security capabilities is also limited. Regardless of the limited IT budgets, these companies still need at least asset and outage management (i.e. GIS and OMS) capabilities, which allow them to have insight into the up-to-date inventory of equipment owned, and timely outage management necessary for an acceptable level of customer satisfaction. Depending on their needs, they might invest into fully featured SCADA, MDM, DMS or SM solutions. Their day-to-day operations will most often be carried out without the benefits of having a SIEM and/or Historian. These systems usually do not fall under the jurisdiction of NERC CIP [13] or similar mandatory security requirements imposed by regulatory bodies. As additional inputs to the risk assessment, our theoretical (small) DSO possesses the following specific characteristics:

- There is only one, primary data center without a DR center or plans for setting it up in the future.
- There is an unknown number of vulnerabilities in the integrated IT/OT environment.
- There are known exploits that can be launched from untrusted networks or via physical access.
- There are no highly motivated state-sponsored and other, high-profile threat sources.
- Loyal, tightly controlled, but security-unaware workforce.
- No IT budget and staff. No information security team.
- Tightly coupled IT and OT zones.

In summary and based on the above introduction, we conclude that such systems possess limited capabilities in the following domains: No security monitoring and awareness without a SIEM; No analytical capabilities without a DMS/EMS; No audit capabilities without a Historian and/or a SIEM; Limited automation and remote-control capabilities without a SCADA; There is no disaster recovery center (DR).

We analyzed the above-described system and we classified operational data integrity loss in the OMS as high impact because such threats can lead to service personnel injury or extended power outages. We considered attacks against both the OMS and GIS more likely than in the large DSO scenario, as they are usually more exposed to untrusted networks in smaller systems (with lower IT and cybersecurity budgets).

We populated the risk assessment template presented in Table 4. The resulting risk assessment results are shown in Table 6.

Table 6
Small DSO's risk assessment

Threat / Service	OMS		GIS	
	I	L	I	L
Confidentiality loss of configuration data	M	L	M	L
	L		L	
Confidentiality loss of operational data	L	V	L	V
	M		M	
Configuration data integrity loss	M	L	M	L
	L		L	
Operational data integrity loss	H	V	L	V
	H		M	
Backend service failure due to bad data	M	L	M	L
	L		L	
DoS against backend services	M	L	M	L
	L		L	
DoS against the communication system	M	L	M	L
	L		L	
DoS against the human-machine interface	L	V	L	V
	M		M	

We identified the following high and medium risk threats: H: Integrity loss of OMS operational data; M: Confidentiality loss of OMS operational data; M: Confidentiality loss of GIS operational data; M: Availability loss of OMS clients; M: Availability loss of GIS clients.

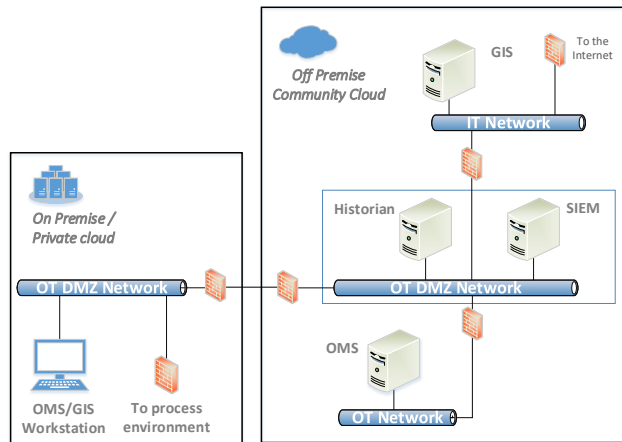


Figure 4
Small DSO's cloud-based OT system

Most of the above listed common disadvantages and risks identified can be mitigated if the small DSO switches to a hybrid cloud-based system architecture presented in Figure 4.

In this architecture, the DSO keeps in its control center only the operator workstations. The GIS and OMS are migrated to a remote community cloud data center. The high and medium risks identified during risk assessment are mitigated by the introduction of the SIEM and Historian, which are offered to all cloud customers by the cloud service provider (CSP). The most notable benefits of this system architecture compared to the original solution are the following:

- Information security is improved via segmenting the networks into OT, OT DMZ, and IT zones, aligned with IEC-62443.
- Security monitoring, awareness, monitoring, and audit capabilities via the SIEM and Historian in the cloud. These services reside in the OT DMZ and are differently shaded in Figure 4.
- Seamless upgrades to new versions of the OT services, i.e. the small DSO does not have to upgrade its sub-systems every 7-10 years as the community cloud provider will do that as part of its SLA.

A downside of this system architecture is that disaster recovery is not addressed. If the (small) DSO's budget permits, it might maintain a cold or warm start subsystem in a separate community cloud in a different (geographic) location as a DR solution.

Conclusions

Based on our state-of-the-art review we concluded that there are no risk assessment-based studies that specifically tackle the problem of migrating smart grid OT services to a cloud computing architecture in a systematic way. That is the gap that we filled with the research presented in this paper. We presented a method valuable to any smart grid system owner and/or operator, which can help them to choose an optimal cloud migration strategy, fitting their specific requirements and maintaining an adequate level of information security.

We presented a baseline smart grid OT system architecture aligned with the IEC-62443 model. We identified smart grid-specific threat sources, threats, likelihoods, and potential impacts. We performed a detailed risk analysis of the common OT services from the confidentiality, integrity and availability (CIA triad) perspective. Additionally, we defined a baseline cloud migration strategy for smart grid OT services. We applied our risk assessment methodology in two cloud migration case studies. Our first case study involved a large DSO with complex OT capabilities. We theorized that there were highly motivated and capable threat sources, numerous IT and OT services, and possible attack vectors from untrusted networks, via physical access to the equipment in the field or via the communication infrastructure. We applied the proposed method and presented a hybrid cloud-based smart grid ICS architecture with disaster recovery (DR) capabilities. In the second scenario, we analyzed the security risks in a small DSO with a limited budget and IT staff. We applied the method again and proposed a fitting, mostly (community) cloud-based system architecture.

This work focused on information security. Therefore, the proposed cloud migration strategy and the case studies analyzed did not include additional key metrics, e.g. personnel and cloud service costs, level of management support, compliance with relevant standards and specifications (e.g. NERC CIP), or the temporal aspect of threat sources and threats, i.e. the fact that threat sources and threats change in time. The authors intend to incorporate these measures as part of their future work. Also, as part of their future work, the authors plan to research the technical details of cloud architecture model and migration processes represented in [17] [18], and to implement and test the presented risk assessment methodology in practice. Additionally, this research can be expanded by exploring and proposing the implementation of various mitigations based on the risk assessment methodology presented.

References

- [1] New Standards for Security Categorization of Federal Information and Information Systems, NIST Federal Information Processing Standard (FIPS) 199, Feb. 2015
- [2] International Electrotechnical Commission. Industrial communication networks - Network and system security - Part 3-3: System security

- requirements and security levels. IEC 62443-3-3, Geneva, Switzerland, 2013
- [3] D. Rosic, I. Lendak, and S. Vukmirovic, "A Role-Based Access Control Supporting Regional Division in Smart Grid System", *Acta Polytechnica Hungarica*, Vol. 12, No. 7, pp. 237-250, 2015
- [4] D. Healey, S. Meckler, U. Antia, E. Cottle, "Cyber Security Strategy for the Energy Sector", ITRE Committee, Oct. 2016
- [5] D. Kushner, "The real story of Stuxnet", *IEEE Spectrum*, Vol. 3(50), 2014
- [6] R. M. Lee, M. J. Assante, and T. Conway, "Analysis of the Cyber Attack on the Ukrainian Power Grid", Defense Use Case, SANS ICS, Mar. 2016
- [7] R. Leszczyna, "Cybersecurity and privacy in standards for smart grids – A comprehensive survey", *Computer Standards & Interfaces*, Vol. 56, Feb. 2018
- [8] J. Jarmakiewicz, K. Parobczak, and K. Maślanka, "Cybersecurity protection for power grid control infrastructures", *International Journal of Critical Infrastructure Protection*, Vol. 18, pp. 20-33, Sep. 2017
- [9] J. E. Y. Rossebo, R. Wolthuis, F. Fransen, G. Björkman, and N. Medeiros, "An Enhanced Risk-Assessment Methodology for Smart Grids", *IEEE Computer*, Vol. 50, No. 4, pp. 62-71, Apr. 2017
- [10] "Security for smart Electricity GRIDs", SEGRID Whitepaper, Edited by F. Fransen, and R. Wolthuis, Jul. 2017 [Online] Available: <https://segrid.eu/wp-content/uploads/2017/07/Whitepaper-SEGRID.pdf>
- [11] S. Paul, and Z. Ni, "Vulnerability analysis for simultaneous attack in smart grid security," in Proc. 2017 IEEE Power & Energy Society Innovative Smart Grid Technologies Conference (ISGT), Washington, USA, 2017, pp. 1-5
- [12] S. Nazir, S. Patel, and D. Patel, "Assessing and augmenting SCADA cyber security: A survey of techniques", *Computers & Security*, Vol. 70, Sep. 2017
- [13] Critical Infrastructure Protection (CIP) Standards, Version 6, North American Electric Reliability Corporation (NERC), Jul. 2016
- [14] R. Paes, D. C. Mazur, B. K. Venné, and Jack Ostrzenski, "A guide to securing industrial control networks — (IT/OT) convergence", in Proc. 2017 Petroleum and Chemical Industry Technical Conference (PCIC), Calgary, Canada, Dec. 2017, pp. 89-96
- [15] Evaluation of Cloud Computing Services Based on NIST SP 800-145, NIST Special Publication 500-322, February 2018

-
- [16] US Government Cloud Computing Technology Roadmap Volume I, High-Priority Requirements to Further USG Agency Cloud Computing Adoption”, NIST Special Publication 500-293, Oct. 2014
- [17] Pooyan Jamshidi, Claus Pahl, Nabor C. Mendonça, Pattern-based multi-cloud architecture migration, 03. October 2016
- [18] Mahdi Fahmideh, Farhad Daneshgar, Fethi Rabhi, Ghassan Beydoun, A generic cloud migration process model, *European Journal of Information Systems*, Volume 28, 2019 - Issue 3
- [19] R. Garcia, and C. E. Chow, “Identity considerations for public sector hybrid cloud computing solutions”, presented at the *2015 International Conference Computer Communication and Informatics (ICCCI)*, India, 2015
- [20] P. Gayatri, M. Venunath, V. Subhashini, Syed Umar Securities and threats of cloud computing and solutions, Coimbatore, India, 2018
- [21] P. Deshpande, S. C. Sharma, and P. Sateesh Kumar, “Security threats in cloud computing”, in *Proc. 2015 International Conference Computing, Communication & Automation (ICCCA)*, Noida, India, 2015, pp. 632-636
- [22] R. Wynn, “The 2016 Dirty Dozen: 12 cloud security threats”, Cloud Security Alliance Southwest Chapter meeting, Cloud Security Alliance, Apr. 2016
- [23] J. Y. Kimm, and Y. Kim, “Benefits of cloud computing adoption for smart grid security from security perspective”, *The Journal of Supercomputing*, Vol. 72, No. 9, pp. 3522-3534, Sep. 2016
- [24] T. Radwan, M. A. Azer, and N. Abdelbaki, “Cloud computing security: challenges and future trends”, *International Journal of Computer Applications in Technology*, Vol. 55, No. 2, 2017
- [25] B. Fortna, “Securing the federal hybrid cloud”, Industry Insight, GCN, 2018
- [26] Z. Cao, J. Lin, C. Wan, Y. Song, Y. Zhang, and X. Wang, “Optimal Cloud Computing Resource Allocation for Demand Side Management”, *IEEE Transactions on Smart Grid*, Vol. 8, No. 99, pp. 1943-1955, Jul. 2017
- [27] N. Popovic, D. Popovic, and I. Seskar, “A novel cloud-based Advanced Distribution Management System solution”, *IEEE Transactions on Industrial Informatics*, Vol. 14, No. 8, pp. 3469-3476, Aug. 2018
- [28] Risk Management Framework for Information Systems and Organizations, NIST Special Publication 800-37, October 2018
- [29] Smart Grid Security: Recommendations for Europe and Member States, Annex II. Security Aspects of the Smart Grid, European Network and Information Security Agency (ENISA), 2012

- [30] B. Jelacic, D. Rosic, I. Lendak, M. Stanojevic, and S. Stoja “STRIDE to a secure Smart Grid in a hybrid cloud”, in Proc. European Symposium on Research in Computer Security, SECPRE 2017, CyberICPS 2017, Lecture Notes in Computer Science, Vol. 10683, Oslo, Norway, 2017, pp. 77-90

Biomimetic Middleware Design Principles for IoT Infrastructures

**Zenon Chaczko¹, Ryszard Klempous², Jerzy Rozenblit³,
Tosiron Adegbiya³, Christopher Chiu^{1,2*}, Konrad Kluwak²,
Czeslaw Smutnicki²**

¹ University of Technology, Sydney, 15 Broadway, Ultimo, NSW 2007, Australia
zenon.chaczko@uts.edu.au, christopher.chiu@uts.edu.au

² Faculty of Electronics, Wrocław University of Science and Technology,
Wybrzeże Wyspiańskiego 27 50-370 Wrocław, Poland
ryszard.klempous@pwr.edu.pl, konrad.kluwak@pwr.edu.pl,
czeslaw.smutnicki@pwr.edu.pl

³ The University of Arizona, Dept. of Electrical and Computer Engineering,
1230 East Speedway Blvd. P.O. Box 210104, Tucson, AZ 85721-0104, USA
jr@ece.arizona.edu, tosiron@email.arizona.edu

Abstract: The advancement of Internet of Things (IoT) has made it practical to discover, localize and pinpoint smart sensing devices based on the situational context, relevancy, and characteristics to query data intelligently, or conduct actions. Furthermore, the development of large-scale applications must deal with data collection and data sensing from a massive number of ubiquitous components, ultimately converging into 5G mobile networking. Additionally, IoT involves managing the expectations of Big Data sourced from many heterogeneous sources. This paper provides an overview of biomimetic methodologies, which represent a viable solution for large-scale data delivery through the aggregation of information with large-scale IoT technologies.

Keywords: 5G communications; big data; Internet of Things; machine-to-machine systems; massive-scale systems; middleware; ubiquitous systems; wireless sensor and actuator networks

1 Introduction to IoT-based Middleware

The Internet of Things (IoT) presents several potential research opportunities and raises development challenges in modern computing [7]. Technological advancements stimulate a new paradigm where sensors and actuators are managed

^{1,2*} On leave from University of Technology, Sydney

as common infrastructure, offering multiple concurrent services and intelligent data aggregation to many users [6], [12].

Advancements driving the massive-scale IoT infrastructure concept include:

- Autonomic Computing [1] and Middleware Design [3];
- Smart Wireless Sensor and Actuator Networks (WSANs);
- Artificial Intelligence (AI);
- Communication Protocols and Standards; and
- Fifth Generation Mobile Cellular Networks (5G).

Along with the deployment of 5G networking, the opportunity presented in the realm of IoT and multimedia sphere includes responsive connectivity for Machine-to-Machine systems (M2M), and possibilities into near real-time interactive services. It is also important to consider practical 5G rollout challenges when adopting multimedia interactivity such as latency and bandwidth constraints.

In addition, the significance that IoT places on 5G regarding future demand must be considered, using the experiences of current cellular utilization. Rapidly advancing services including Augmented Reality (AR), Virtual Reality (AR) and multi-user conferencing must be factored into the IoT middleware as part of the architectural framework.

The approach is different when compared to dedicated systems forming part of legacy telecommunications and computer infrastructures. Much research needs to be considered to adapt standard protocols, middleware model standards, data aggregation, and methods of sensor fusion as well as mechanisms of data delivery, to configure the approach IoT can integrally build into public infrastructures. The emergence of new communication technologies requires adaptable solutions that handle M2M connectivity while minimizing harmful downtime interruptions.

The solution is an architectural model for implementing the software-directed paradigm known as the Biomimetic Model of Middleware (BMM) [5]. The localization and topology of middleware components in the IoT software solution is shown in Figure 1. The components are IoT devices, local and, core middleware and Internet connectivity.

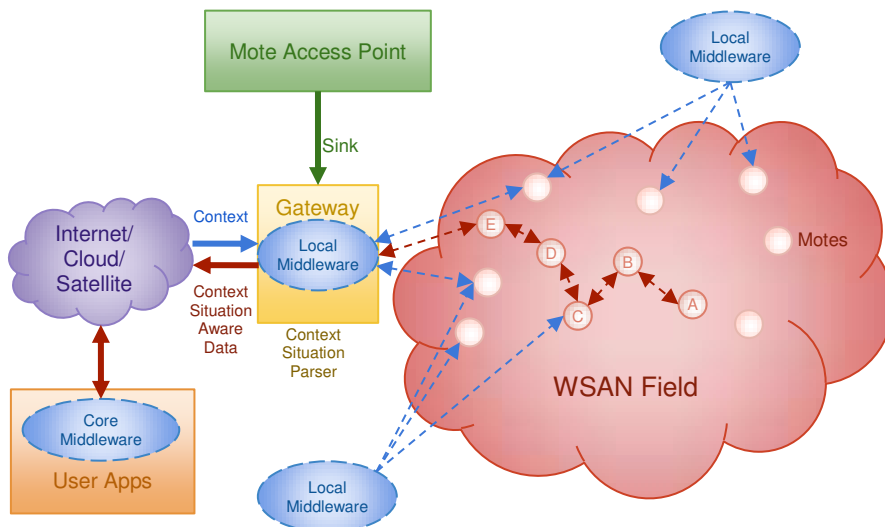


Figure 1

IoT Middleware Architecture featuring Biomimetic Principles

For IoT nodes, Mote Access Point (MAP) devices have two main responsibilities:

1. Manage IoT devices while also partitioning the core functions of different components and ensuring that every component runs effectively:
 - a. Sensors as data sinks, and
 - b. Actuators as control sinks;
2. Act as intelligent access points with router functionality at the sensor/control boundary of IoT devices, which are composed of context aware:
 - a. Data parsers, and
 - b. Gateway processors.

The research work reflects the innovative form of biomimetic middleware for IoT infrastructures, along with the complementary models for data aggregation. The biomimetic middleware enables the generation of adaptable WSANs and services that lead to practical viability [5].

By providing a discussion on the design concerns of IoT-based middleware, the potential innovations include the broader vision of large scale, advanced software-intensive IoT infrastructures for modern computation and connectivity facilitating smart M2M communications.

In this work, we propose a Biomimetic Model of Middleware (BMM), along with adaptive techniques for data aggregation. Next, we explore biomimetic middleware design aspects that enable the development and deployment of contextually aware, heterogeneous, secure, and massive-scale system solutions [8].

Finally, we provide a practical illustration to show the viability and feasibility of implementing BMM for IoT infrastructures, showing the possibilities to deploy the BMM approach from a broad-based perspective. This is important, given the role of software in the field of Software Defined Networking (SDN) solutions that plays a critical role in 5G cellular communications.

2 Biomimetic Middleware Models

Examples of technological advancements that can enable biomimetic solutions in various technical fields are shown in Table 1 [2]. Progress in modern technologies is driven by biomimetic forms in design in the areas of advanced manufacturing, cloud computing infrastructures and open-learning AI frameworks. These sectors will play a critical role in the design, implementation, and deployment of IoT infrastructures.

Table 1
Biomimetic Solutions in Modern Industrial Implementations

Field	Implementation	Biomimetic Solution
Advanced Manufacturing	Additive Manufacturing	3D, 4D, 5D Printing
	Kirigami Construction	Additive Lattice Structures
Cloud Computing	AI and Machine Learning	AIaaS, MLaaS Services
	Containers, Funtainers	CaaS, FaaS Services
Learning Frameworks	AI & Deep Learning	Intel AI Framework, BigDL
	Flow Graph Computation	CNTK, TensorFlow
	Image Classifier Processing	Caffe & Caffe2
	Natural Language Libraries	Gensim
	Neural Network Frameworks and Dynamic Parallelization	Apache Mxnet, Chainer, CMU Dynet, Keras, Paddle, Pytorch & Torch
	Statistical Data Processing	Gluon, H2O, RStudio

2.1 Advanced Manufacturing

2.1.1 Additive Manufacturing

Additive manufacturing has guided the design and construction of uniquely complex structures that would be impossible with traditional subtractive manufacturing. Technologies such as 5D printing can readily build sophisticated, multi-faceted designs that will propel innovative technical approaches within a short lead time.

By enabling the rise of rapid prototyping in IoT infrastructures, additive manufacturing allows designers and engineers to build IoT solutions while

minimizing construction and testing outlay. Thus, BMM infrastructure deployment is accomplished as IoT mote and gateway designs can be easily revised for a specific context while maintaining cost efficiency.

2.1.2 Kirigami Structures

Kirigami is the Japanese art of folding paper objects that can be unfurled into elaborate structures. The strategic fold points maximize the compressibility of the structure when compacted, but once unfolded reveals its true form. Thus, the unfolded form serves the genuine intention of the structure, operating its true functionality.

This approach is applicable for IoT, where the design and deployment can take place in confined environments, or in restricted domains where total space is at a premium. Thus, it is compressible into a stored manner when not used, or expandable as necessary such as maximizing signal strength during radio congestion.

2.2 Cloud Computing

2.2.1 Artificial Intelligence and Machine Learning Services

The adoption of AI cloud platforms by academia and industry is driven by the low-cost of entry and simplicity of provisioning resources. Corporate providers including Amazon Web Services, Google Cloud and Microsoft Azure offer on-demand turnkey services that include open source libraries with broad accessibility and technical support.

As AI and ML cloud services migrate to Systems on a Chip (SOC) and Application Specific Integrated Chipset (ASIC) solutions, this has led to highly optimized computing efficiency gains that lower the total cost of ownership for IoT-based platforms that cannot feasibly be achieved using general purpose computing infrastructure.

The net result of these industry trends means tailored big data solutions are deployable remotely from the IoT cloud, to reach optimum economies of scale for computing resources, and thus satisfy peak operational storage and processing efficiency.

2.2.2 Containers and Funtainers

In conjunction with container-based solutions in the cloud, these solutions provide a highly encapsulated environment where all functional libraries are included in the virtual computing space. Therefore, one can rapidly deploy functionally similar components experimentally that is less prone to configuration errors and other constraints.

By enabling rapid software prototyping, it is advantageous for designing IoT infrastructures where an adaptable BMM can be immediately deployed. The testing and results of the solution can be assessed and collated for further investigation, with the development of new AI and ML algorithms to evaluate using IoT infrastructure.

2.3 Learning Frameworks

Collaborations between industry and academic research sectors have resulted in the development of open-source frameworks for machine learning. These collaborations have enabled a wide variety of datasets and algorithms suitable for IoT middleware solutions, along with their combined experience of development skills and expertise. Examples of open-source frameworks contributed by the academic and industrial communities include Apache Mxnet, Caffe, Caffe2, Chainer, CMU DyNet, DSSTNE, Gensim, Gluon, H2O, Intel AI Framework, Intel BigDL, Keras, Microsoft CNTK, Paddle, Pytorch and Torch, RStudio and TensorFlow.

Machine Learning (ML) has been applied to various fields including medicine, precision agriculture, sports science, and entertainment. Thus, ML is applicable for IoT deployment where node routing and management must be achieved efficiently while preserving the energy constraints of mote batteries. Hence, IoT middleware design can be implemented to accomplish tailored tasks including recognition of patterns for industrial and government applications, or in surveillance, where security patrol can be augmented with AI recognizers that aid in repetitive operations such as feature identification.

Recognition of patterns within Computer Vision (CV) enhancement is feasible, especially where compute capability is limited due to energy constraints. This is because the trend of mobile multi-core processors has reached maturity, such that elementary AI tasks can be performed at the edge gateway. The development of a hierarchical middleware model breaks down computational tasks in an intelligent manner where low-demand operations are performed on-field, while computationally complex big data tasks are done in the cloud, as illustrated in Table 2 [10].

Table 2
AI Operations for an IoT-based Context

Operational Location	Compute Device	AI/ML Examples
On-field/site: Local Operations	IoT Devices: <ul style="list-style-type: none"> ● WSAN End Points ● Edge Gateway 	Unsupervised Learning: <ul style="list-style-type: none"> ● Self-Organized Maps ● Neural Networks
Off-field/site: Remote Operations	Cloud Infrastructures: <ul style="list-style-type: none"> ● AIaaS ● MLaaS 	Supervised Learning: <ul style="list-style-type: none"> ● Genetic Algorithms ● Generative Adversarial Networks

2.3.1 On-field Operations

On-field AI tasks complementing an IoT context include unsupervised learning with Self-Organized Maps (SOM) and neural networks. Such computational tasks would not significantly burden the energy, data, and computational constraints of the IoT gateway. The middleware needs to enable priority to unsupervised learning operations for the localized IoT infrastructure, since the effort for greater computation tasks should be done remotely where resources are more plentiful, thus adding to system redundancy [14].

2.3.2 Off-field Operations

Off-field AI tasks accompanying an IoT context include supervised learning using complex algorithms, such as Genetic Algorithms (GAs). AIaaS (AI-as-a-service) and MLaaS (machine learning-as-a-service) infrastructures are suitable since they are tasked with heavy-duty compute and resource needs [15], [16]. Tailoring AIaaS and MLaaS solutions include denormalized databases suited for long-term archiving and monitoring of IoT data. This is essential for big data tasks such as long-term trending analysis and predictive forecasting capabilities relying on large datasets for statistical probabilities.

3 Applications of Biomimetic Middleware Solutions

3.1 Integration of IoT with Motion Capture

The application of biomimetic design in middleware can be observed from IoT solutions in the field of human motion tracking. This field of research has evolved to the point where sensing technologies are commercially embedded such as Apple FaceID, Microsoft Kinect and Sony SoftKinetic. These platforms facilitate AR and VR applications for domestic and industrial applications.

The importance of consumer adoption should not be underestimated, as adoption drives economies of scale and mainstream adoption. Thus, combining commercial motion capture technologies with IoT provides the potential for rapid deployment, while also reducing the total cost of ownership concerns. The momentum of adoption leads to acceptance and familiarity as part of broader IoT middleware design.

Examples of motion capture systems that are common in consumer gaming and entertainment are shown in Figure 2. They include arcade systems, set-top boxes, and interactive multimedia where an immersive visual communication medium can complement IoT-based solutions for environmental monitoring applications.



Figure 2

Current motion capture systems for consumer applications

In addition, the professional arena has also been complemented with motion capture technologies where sophistication and high precision levels are required. Vendor solutions from North America and the European Union include Contemphas, GaitTrack, Qualisys and TekScan. These tools have a high outlay along with recurring maintenance expenses that constrain broader adoption.

Hence consumer-based motion capture solutions are best matched for IoT middleware application, because greater adoption of IoT with M2M communications will take place as 5G rollouts become commonplace. Minimizing maintenance concerns such as cost of replacement will increase the adoption rate and end user accessibility.

3.2 End User Factor within IoT Middleware

The IoT middleware platform must be developed to account for quality control, especially in the field of motion capture and annotation analysis to ensure system implementation flexibility.

Connecting the consumer arena when factoring the number of motion tracking systems available in the marketplace, as well as the proprietary nature of professional motion capture systems, means that a complementary and practical application must reasonably adopt mainstream design principles.

Thus, the complete IoT-based solution integrating biomimetic middleware with motion capture sensors must aim to be technology and vendor agnostic. The solution should feasibly adopt open source software and technologies for broader developer adoption and ease integration with newly evolving IoT development platforms.

Therefore, the middleware IoT infrastructure is not simply glue logic to combine components into a common space, but handle massive-scale IoT heterogeneous concerns in an ubiquitous manner. Wider reach of an IoT-based BMM solution is

achieved when it provides a M2M communications mechanism, as well as professional and consumer interactivity in a seamless manner.

3.3 Innovations in IoT Middleware Research

The conception of the BMM technology platform in the scope of motion capture should consider cooperation with academic and institutional organizations for scientific research and innovation. This is achieved by building the IoT middleware framework with a customizable architecture that is not linked to an industry or commercial design goal.

The place where application-specific analysis is done at the AIaaS and MLaaS backend, such that separation is ensured between computational processors and IoT nodes. Since there are many motion capture applications that can be applied with IoT, including television broadcasts, motion pictures, sports physiotherapy, and tele-medicine, the functional separation of processing concerns is noteworthy in this research.

In this work, as a case study, we explore the application of biomimetic principles to middleware for analysis of healthcare employees. The practical piecemealing of operations in the healthcare domain means the middleware infrastructure is segmented into component-level work tasks for logical deployment.

Hence, the case study will examine the daily requirements of healthcare employees. By combining biomimetic principles using IoT, there is the potential to accommodate workplace training needs in alliance with occupational therapists including physiotherapists.

3.4 Case Study Adopting BMM IoT Middleware

3.4.1 Healthcare Employee Training and Analysis

3.4.1.1 Lifting Practice and Analysis Problem Space

Investigative research conducted by the Wrocław Medical University identified that employees would benefit from a posture analysis system to identify incorrect lifting practice. The worldwide increase in back injuries resulting from lifting objects greater than 25 kg has led to costs associated with employee downtime including compensation and rehabilitation [9].

The emotional and financial burden is anticipated to rise as population aging occurs in modern society, placing further stress on existing employee workloads. The best way to manage this emerging issue is through improving training and rehabilitation protocols, thus enforcing positive lifting practices in medical facilities.

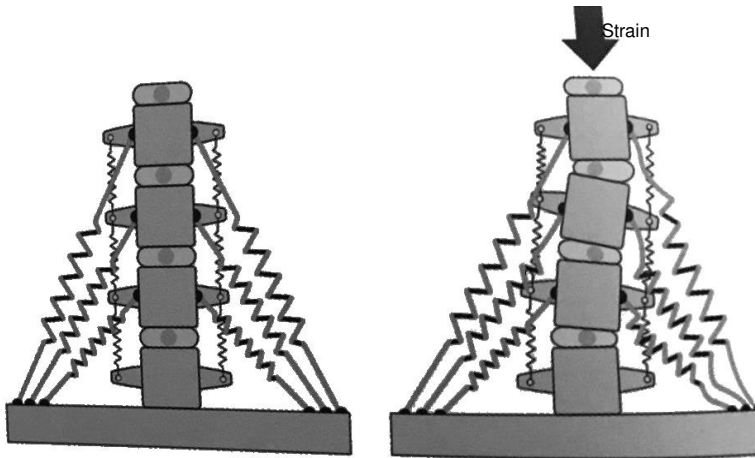


Figure 3

Depiction of back strain resulting from incorrect lifting technique [4]

Thus, as patient care duties inevitably increase over the coming years, designing a remote healthcare employee resource is a practical option where AI analysis can be conducted at a centralized facility. Therefore, an IoT-based solution coupled with BMM principles is key to managing motion capture resources. Hospitals and medical clinics can achieve positive employee productivity through training resources coupled with IoT solutions.

The IoT BMM platform must encapsulate the known possible postures when carrying heavy objects. The AIaaS and MLaaS backend infrastructure would contain the comprehensive training database capturing the main points where injury risk is known for an integrated medical facility.

The main points that are captured from an IoT-based lifting rehabilitation framework can be summarized as follows [11]:

- The employee preparing to initially bend forward to the patient;
- The employee adjusting their gait to ensure a proper grip on the lying patient;
- The stage where load-bearing takes place, as the employee starts to lift the patient and perform the act of transference; and
- The final point where the employee places the patient on a different source, such as another bed, stretcher or wheelchair.

Risks of Repetitive Strain Injury (RSI) increase dramatically when improper lifting techniques are applied by healthcare employees. To counteract this problem, longer-term monitoring and training is essential to evaluate lifting practice regularly, not only to assess the capabilities of employees to carry properly but provide longitudinal health studies [4], [9].

The IoT platform must consider the use of client interfaces, such as mobile devices and tablets, to enable healthcare employees to interact with the training system. This provides a quantitative assessment of the lifting diagnosis of each employee, but remotely diagnose issues at the central training facility. Hence, the employee can proactively track their learning progress on their own device in conjunction with their local doctor.

Additionally, the healthcare employee would also allow for qualitative feedback to the IoT motion capture platform to ensure a virtuous loop for iterative improvement to the system. Consultation with user interactivity experts is important to design the platform in a manner that is beneficial to the employee and consultant physiotherapist who provide constructive feedback and ensure positive lifting practice.

The lifting technique framework should not be a means of punitive judgment, but rather an additional tool to offer continuous liaison with relevant healthcare stakeholders. The goal is to ensure harm minimization resulting from a back injury, while improving morale and workplace productivity through proper training methods.

3.4.1.2 Combining IoT BMM with Human Activity Recognizers for Healthcare Employees

The core IoT infrastructure deals with analyzing and recognizing human gait through specific motion capture algorithms. This offers results that are state-of-the-art, especially for challenging gait recognition tasks processed in the AIaaS and MLaaS cloud-based computational layer:

- Classifying data sequences into key movements using the Histogram of Gradients (HoG) for human activity recognition; and
- Adoption of neural network techniques to further optimize activity recognition by eliminating false positives.

The main aspect of the IoT BMM design is to incorporate lifting analysis for gait analysis by distinguishing on-field and off-field computational processing requirements methodically. These requirements can be distinguished as follows:

- Loading and preparing gait recognition information classified by time series, ensuring the data can be visually explored by the employee in consultation with their physiotherapist;
- Identified lifting issues are structured in a manner that allows employees to evaluate results while offering a guided reference for patient lifting best practices; and
- Offer potential for mobile deployment where network connectivity is intermittent or unreliable, thus improving the portability of the IoT platform in remote areas.

The issues of understanding the kinematic actions of the healthcare employee must be factored into the research, especially when multiple objects are involved. Visual interference impacts recognition accuracy, so this concern must be considered for additional testing purposes when the platform is rolled out for a healthcare workplace.

Furthermore, research must also consider support vector machine or neural network approaches when the employee undertakes a maneuver and adjusts their position for a specific context, such as distinguishing the difference between carrying a child or an elderly patient.

3.4.1.3 Development Approach and Current Results

The development of the lifting analysis platform involved a hybridized approach where cloud services were augmented with the local client infrastructure. This method sought to balance the needs of the end-user while satisfying the needs of the medical institution where the experiment was conducted. The biomimetic design principles used to design the platform fulfilled the following system requirements:

Local Client Processing

- Identify components that required immediate local processing, in order to serve immediate client needs:
 - Data feeds that must be immediately presented to the end-user due to minimum latency needs, such as VR imaging presented to the medical patient;
 - Data that cannot be transmitted due to potential network bandwidth limitations or restrictions, especially where signal strength is weak for a wireless Internet connection.

Remote Cloud Processing

- Determine main features or functions that can be processed off-site onto the cloud infrastructure:
 - Data points that can be safely backed up in order to prevent information loss due to unforeseen circumstances, such as the case where the laptop computer is accidentally lost whilst in transit between medical facilities;
 - Data elements that can be processed remotely in order to mitigate processing constraints on the local computer since the laptop will have processing power limitations compared to a desktop workstation.

Table 3 summarizes the component-level identification of the rehabilitation platform regarding operational requirements:

Table 3
Hybrid Architecture for Rehabilitation Platform sourced from [13]

Operational Location	Platform Components	Reasoning/Rationale
Local Client Operations	<ul style="list-style-type: none"> ● Oculus Rift VR and Leap motion sensor hardware in C#: <ul style="list-style-type: none"> ○ Unity SDK 2018.1.6; ○ MonoDevelop environment; ○ Blender graphics toolkit. 	<ul style="list-style-type: none"> ● Graphics processing and rendering of the gait simulation and training was done on the experimental kit; ● VR gear and laptop were running directly at the external medical premises.
Remote Cloud Operations	<ul style="list-style-type: none"> ● Remotely hosted Cloud Infrastructure: <ul style="list-style-type: none"> ○ Fully managed virtual machine platform 	<ul style="list-style-type: none"> ● Safely backup of statistical data; ● Patient information deleted prior to cloud storage other than user ID assignment.

As the rehabilitation exercises were conducted, the patients were assigned grades for their motor coordination ability, determined by their ability to conduct a routine grasping task of an object in space. Notably, while improvements were not exhibited by all patients, the overall trend indicates increasing familiarity with Virtual Reality technology by the patients enhances their user experience and positive engagement.

From the in-depth results examined in detail by Marzec et al. [13], a nominal improvement was observed especially for patients who had difficulty releasing objects in an active manner, as they were able to release objects after comprehensively using the VR rehabilitation platform as observed in Table 4. Thus, there is promise in the design principles of the experimental environment – warranting further study for the combined approach of simulated and physical rehabilitation of poststroke patients.

Table 4
Poststroke Rehabilitation Observations extracted from [13]

Patient	Initial State Prior to VR Training	Final State After VR Training
Case I	Actively releasing grasp/letting go of object	Actively releasing grasp/letting go of object
Case II	Not actively letting go of object	Actively releasing grasp of object
Case III	Not actively letting go of object	Actively releasing grasp of object

The experimental limitations for future consideration include the need for data security and increasing the test sample size to verify the efficacy of the rehabilitation approach [13]. Data security is essential to ensure personally identifiable information is maintained for patient privacy, through Public-key Cryptography, so that the patient and doctor are only privy to such information.

Furthermore, as the experiment is extended to more patients, the end results will verify the platform and its hybridized modular architectural approach.

Conclusions

This paper aims to provide an overview and analyze the benefits of adopting the biomimetic approach to middleware for IoT-based platforms, with an emphasis on dealing with the dynamic relationship between on-field and off-field machine learning functions. The data processing quality of the IoT sensor source, such as motion data captured from medical employees, should consider qualitative and quantitative user concerns to ensure broad acceptance of IoT in society while also mitigating apprehension to new technology.

End-user needs should always be accommodated when designing IoT biomimetic middleware as a quality attribute. This is achieved by knowing the domain context so that IoT middleware design composition manages heterogeneous IoT integration and accommodates end-user needs of security, reliability, and usability. Thus, this ensures the wide adoption of IoT-based BMM for a variety of different system frameworks.

The principles of biomimetics offer the primary framework of connecting different components within a context that is user-centric while accommodating future advances in IoT technologies that influence system design and architecture – this is examined by the case study with the emergence of consumer motion capture systems.

The study highlights the essential drivers for a common IoT biomimetic middleware framework, along with the design principles for future IoT applications. The flow of information from architectural through to biomimetic design show that IoT is the critical path as next-generation cellular networks guide tomorrow's information economy.

In conclusion, the understanding of complementary approaches, including learning-based ML methodologies such as neural networks and genetic algorithms, as well as training datasets, have a real-world impact on the operations of multi-modal IoT systems. Furthermore, performance optimization is needed for biomimetic design principles governing IoT infrastructure management.

References

- [1] Bantz, D. F., Bisdikian, C., Challener, D., Karidis, J. P., Mastrianni, S., Mohindra, A., Shea, D. G., Vanove, M. (2003), *Autonomic personal computing*, *Autonomic Computing*, Vol. 42, No. 1, IBM Press
- [2] Bass, L., Clements, P., Kazman, R. (2012), *Software Architecture in Practice*, 3rd Edition, Boston: Addison-Wesley. ISBN 978-0-321-81573-6
- [3] Britton, C., Bye P. (2004), *IT Architectures and Middleware: Strategies for Building Large, Integrated Systems*, Addison Wesley Professional

-
- [4] Carneiro, P., Braga, A. C., Barroso, M. (2017), Work-related musculoskeletal disorders in home care nurses: Study of main risk factors, *International Journal of Industrial Ergonomics*, 61: 22-28, <http://doi.org/10.1016/j.ergon.2017.05.002>
- [5] Chaczko, Z. C. (2009), *Towards Epistemic Autonomy in Adaptive Biomimetic Middleware for Cooperative Sensornets*. PhD Thesis, University of Technology, Sydney, Australia
- [6] Chaczko, Z. C., Aslanzadeh, S. (2011), C2EN: Anisotropic Model of Cloud Computing, *International Conference on Systems Engineering, Proceedings of 21st International Conference on Systems Engineering, ICSEng 2011, Las Vegas, USA*, pp. 467-473
- [7] Chaczko, Z. C., Chiu, C., Aslanzadeh, S., Dune, T. (2011), *Software Infrastructure for Wireless Sensor and Actuator Networks, Proceedings of 21st International Conference on Systems Engineering, ICSEng 2011, Las Vegas*, pp. 474-479
- [8] Clements, P., Bachmann, F., Bass, L., Garlan, D., Ivers, J., Little, R., Merson, P., Nord, R., Stafford, J. (2010), *Documenting Software Architectures: Views and Beyond, 2nd Edition*, Boston: Addison-Wesley. ISBN 978-0-321-55268-6
- [9] European Council Directive – 90/269/EEC, European Union Health and Safety Requirements for Manual Load Handling, <http://eur-lex.europa.eu/legal-content/EN/TXT/?uri=CELEX%3A31990L0269>
- [10] Godinez, M., Hechler, E., Koenig, K., Lockwood, S., Oberhofer, M., Schroeck, M. (2010), *The Art of Enterprise Information Architecture: A Systems-Based Approach for Unlocking Business Insight*, IBM Press
- [11] Health and Safety Executive, U.K. Government, *Moving and Handling Case Studies in Health and Social Care*, <http://hse.gov.uk/healthservices/moving-handling-case-studies-research.htm>
- [12] Krakowiak, S. (2009), *Middleware Architecture with Patterns and Frameworks*
- [13] Marzec, M., Olech, M., Klempous, R., Nikodem, J., Kluwak, K., Chiu, C., Kołcz, A. (2019), *Virtual Reality Poststroke Rehabilitation with Localization Algorithm Enhancement, Virtual and Augmented Reality in Education Conference, Lisbon, Portugal*, <http://www.msc-les.org/conf/vare2019/>
- [14] McConnell, S. (1999), *After the Goldrush – Creating a True Profession of Software Engineering*, Microsoft Press
- [15] Pressman, R., Maxim, B. (2014), *Software Engineering: A Practitioner's Approach, 8th Edition*, McGraw Hill

- [16] Systems Engineering Competency Maturity Model – Architecture Papers (1995), Software Engineering Institute, Carnegie Mellon University

Statistical Analysis of Machinery Variance by Python

Joao Gabriel Ostrowski¹, József Menyhárt^{2*}

¹University of Debrecen, Faculty of Engineering, Mechanical Engineering Department, Ótemető u. 2-4, 4028 Debrecen, Hungary
E-mail: ostrowski@mailbox.unideb.hu

^{2*}Corresponding author, University of Debrecen, Faculty of Engineering, Department of Air and Road Vehicles, Ótemető u. 2-4, 4028 Debrecen, Hungary,
E-mail: jozsef.menyhart@eng.unideb.hu

Abstract: Based particularly on data technologies, information is rapidly evolving in engineering. In mechanical engineering, maintenance is benefiting the most from data innovations, the reduction of maintenance costs, and the improvement of system availability. Modern reliability engineering targets uncertainty with advanced statistics and data science. This paper explores maintenance descriptive analytical techniques to determine whether variations between porosity percentage in batches from two similar machines are due to randomness, suggesting technical issues on machinery. The finding is backed by statistical analysis, hypothesis testing, and data mining. Python 3 was used following best practices of data science and data visualization as the main toolset to explore the working data, execute the proposed statistical analysis, and make conclusions. The findings were promising reinforcing the importance of advanced statistics for reliability studies. As a conclusion, we failed to reject the null hypothesis suggesting that there was no apparent difference between sample means. With a confidence of 95%, the difference is explained by natural variations and randomness inherent to the fabrication process.

Keywords: reliability engineering; python programming; statistical analysis; maintenance optimization

1 Introduction

Information is evolving in engineering, based particularly on data technologies that facilitated information flow through departments making processes more efficient. Applied examples include live feedback data from sensors, live feed for stock control, predictive maintenance schemes, etc. Cloud implementations for Big Data streamline and Data Science play a prominent role in the introduction of Industrial Internet of Things in modern factories [1].

In mechanical engineering, maintenance is the most advanced field regarding new data technologies including such giants as IBM and Google worked extensively in applied cases for the industry, aiming at common business goal requirements, minimizing costs and late maintenance while maximizing machinery availability, production output, and customers' satisfaction [2]. Although most of the field development encompasses Maintenance Predictive Analytics through Machine Learning implementations, models fail to predict events when there is no past data detailing a similar occurrence, the adoption of Maintenance Descriptive Analytics in which Modern Reliability Engineering takes part, applying advanced statistics [3]. The focus of this research is to explore some new approaches to the statistical methodologies applied to support optimized maintenance planning in industrial environment.

1.1 The S.M.A.R.T Methodology

The S.M.A.R.T methodology was used as a business best practice to define the goals of this research. First, defined by George T. Doran [4], consultant and former Director of Corporate Planning for Washington Water Power Company, S.M.A.R.T. is an acronym to define goals and objectives in a clear and data-driven manner. According to Paul J. [5], an effective goal must be:

- Specific: A goal should be clear and specific, otherwise it is not possible to focus on efforts or feel truly motivated to achieve them. The five "W" questions (what, why, who, where, which) provide a large scale of support to gain maximum specificity;
- Measurable: It is only possible to plan a timeline of activities if one can perceive when tasks start and come to end. Such need becomes attainable by tracking progress, for tracking, there must be some measurable parameters;
- Achievable: A goal needs to be realistic and attainable to be successful. In other words, it should stretch and push barriers for a challenge while still remaining approachable.
- Relevant: This step ensures that the goal matters to the business are in line with other relevant goals.

Time-based: Every goal needs a target date to have a deadline to focus on and something to work toward.

In line with Peter Drucker's management concepts [6], such methodology started to be widely applied on analytics and data projects due to its attention to measurable results, which clarifies the base for effectivity analysis.

1.2 Goal

According to the previous guideline, the goal of this paper is in connection with reliability engineering objectives according to Connor, P. [7]:

- Goal 1: Evaluation of the variations in porosity percentage of two different machines based on their sensor data set to determine if the difference is due to randomness or some underlying causes. The required confidence level of the analysis is 95%. The analysis should be carried out in a month.

1.3 Foundations of Reliability Engineering

A brief introduction of reliability engineering as a discipline and its roots are rooted in the military due to the necessity of cost-effective systems, and a comparison between reliability and quality frameworks.

1.4 Military Roots of Reliability Engineering

Technology is known to develop exponentially due to military efforts, and the reliability engineering as a discipline was a necessary step by the United States during the 1950s as an attempt to reduce the increasing failure rates and improve the availability of military equipment. Due to the rapid development of electronic devices embedded in systems, the US Department of Defense (DOD) set up the Advisory Group of Reliability of Electronic Equipment (AGREE) report in 1952. The report consisted of strict rules regarding a test of thousands of hours applying high stress, cyclical, high and low temperatures, vibration and switching. [26]

In 1965, the DOD issued the MIL-STD-785 Reliability Programs for Systems and Equipment integrating the standardization for several liable engineering activities, meanwhile, the AGREE routine was accepted by NASA and all major high technology purchasers and suppliers. European countries followed up on the reliability progress by 1990s with a series of Reliability standards that became integrated into the International Standards Organization (ISO), ISO/IEC 60 300 e.g. [26]

1.5 Reliability and Quality

Reliability and quality, despite their distinctive concepts, are both attributes used interchangeably in several cases. Regarding the user level, it is commonly associated with technological products including computers, smartphones, or house appliances. On the other hand, from an industrial point of view, the idea is attributed to machines and parts.

There is no discussion when it comes to the increasing reliability required by modern society, upon a purchase one expected the item to function as described

for the longest time period as possible, avoiding new purchases and substitutions. This is exactly where reliability engineering differs from the old fashioned quality control paradigm, a time dimension was also taken into consideration. In other words, while quality is assessed against a set of specifications, which define conforming or non-conforming parts, a binary distribution of good and bad.

As an uncertain science, the main objective of reliability engineering reveals whether an item will work over a certain period of time, which can be answered by distributions of probabilities. As in its core, reliability is defined as *"the probability that an item will perform a required function without failure understated conditions for a stated period of time"*. [27]

In the words stated by James R. Schlesinger, Former US Secretary of State for Defense, "reliability is engineering in its most practical form". According to Connor, P. the priorities of such science can be listed as follows [30]:

- 1 To apply engineering knowledge and specialist techniques to prevent or to reduce the likelihood or frequency of failures;
- 2 To identify and correct the causes of failures that do occur, despite the efforts to prevent them;
- 3 To determine ways of coping with failures that do occur, if their causes have not been corrected;
- 4 To apply methods for estimating the likely reliability of new designs, and for analyzing reliability data.

2 Mathematical Methods and Tools

The methods used to quantify reliability include the mathematics of probability and statistics. As mentioned above, reliability engineering handles uncertainty. Understanding that variation is part of engineering and inherent to all manufacturing processes is the necessary step for controlling and minimizing unexpected events. Statistical methods provide the means for analyzing, understanding, and controlling variation. [28]

2.1 Box Plot Graph Construction and Analysis

A box and whisker plot often called a box plot displays the five-number summary of a set of data. The five-number summary is the minimum, first quartile, median, third quartile, and maximum. [28]

In a box plot, we draw a box from the first quartile to the third quartile. A vertical line goes through the box at the median. The whiskers go from each quartile to the minimum or maximum.

One common measure of spread for data analysis is the interquartile range (IQR), which is calculated as $Q_3 - Q_1$ and provides a measure of spread that is independent of the distribution mean.

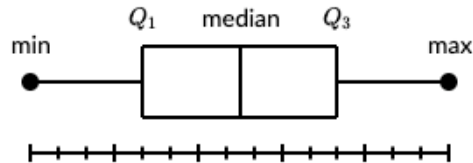


Figure 1

Representation of the five-number summary of a box plot

2.2 Outliers Detection through the Interquartile Range (IQR) Rule

For a rough symmetric dataset, both mean and standard deviation are good descriptive statistics to improve understanding around the dataset, however, for a skewed distribution or distributions that are not normal, the median and the interquartile range are more robust metrics to rely on for extracting insights. Since standard deviation is a function of the distribution mean, it is also heavily influenced by outliers, which are data points that do not fit the overall distribution adding noise to it.

Outliers can be visualized, and boxplots are great in this sense, or one could use mathematical techniques for identifying them. One of the techniques commonly found in the industry and statistical libraries for coding is the interquartile range rule [8].

The IQR rule used shows that a datapoint is an outlier if it is more than $1.5 \times IQR$ above the third quartile or below the first quartile. Said differently, low outliers are below $Q_1 - 1.5 \times IQR$ and high outliers are above $Q_3 + 1.5 \times IQR$.

2.3 Normality Test

An important decision point when working with a sample of data is whether to use parametric or nonparametric statistical methods. [9] [29]

The simpler form would assume that data have known and specific distribution, often a Gaussian, or normal, distribution. If a data sample does not follow a known distribution, then the assumptions of parametric statistical tests are not valid and nonparametric statistical methods must be used. Thus, normality tests are applied to working data sets for checking its correlation to a normal distribution. For the scope of this research, graphical and statistical methods were applied to check the normality of working data [9].

There are two common graphical methods for the normality test, the histogram plot, and the quantile-quantile plot, or QQ plot. The histogram with a Gaussian kernel density estimation was achieved by using the seaborn library under the `.distplot(kde=True)` command. For validation, the kernel density should be visual to a Gaussian distribution.

The QQ plot was executed by the statsmodel library under the command `qqplot(line='s')`. The QQ plot generates an idealized distribution and plots the compared data as a scatterplot above a 45 degrees line representing the desired distribution. There are plenty of excellent Python visualization libraries available, including the built-in matplotlib. However, we can use some alternative libraries. Seaborn is a popular data visualization library for Python programming language. Seaborn is an important Python visualization library built on top of matplotlib. It can give the similar information like ggplot2. It gives us the capability to create amplified data visuals. This helps us understand the data by displaying it in a visual context to unearth any hidden correlations between variables or trends that might not be obvious initially. Seaborn has a high-level interface as compared to the low-level of Matplotlib. [17-20] [24] [25]

Statsmodels is a Python package/library that allows engineers or users to explore data, estimate statistical models, and perform statistical tests during their work. An extensive list of descriptive statistics, tests, plotting functions, and result statistics are available for different types of data and each estimator. It complements SciPy's stats module. Statsmodels is part of the Python programming language. It is oriented towards data analysis, data science and statistics. Statsmodels is built on top of the numerical libraries NumPy and SciPy. The statsmodels integrate with Pandas for data handling and uses Patsy for an R-like formula interface. The graphical functions are based on the Matplotlib library. [17-20] [24] [25]

A perfect approximation using this method implies all datapoints from the sample aligned with the idealized line. When the datapoints tend to go above the idealized normal, distribution line the distribution is right-skewed, contrarily, the distribution is left-skewed when the observations tend to be below the normal line as exemplified in Figure 2 [10].

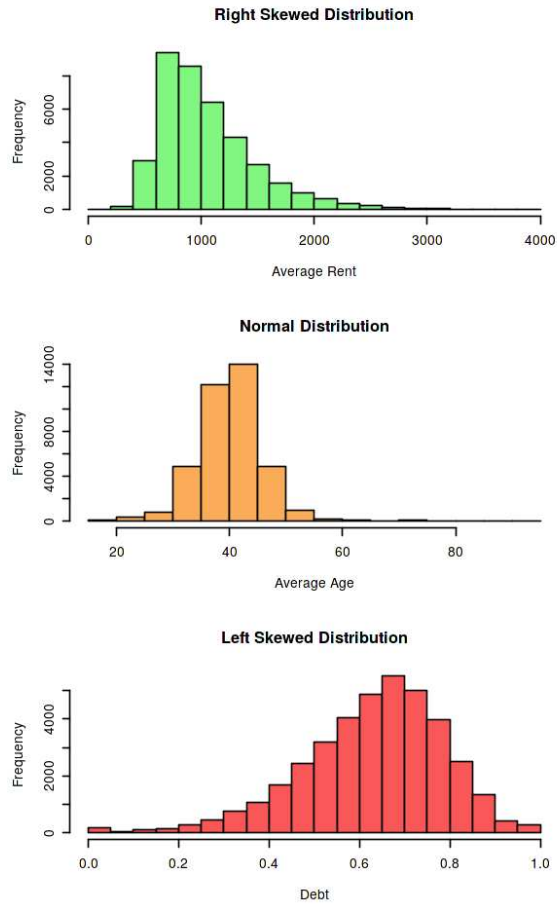


Figure 2
Examples of QQ Plot distributions

The statistical methods are diverse in the coding field, which differs on the preliminary assumptions and considerations upon the tested data. For the research scope, an algorithmic version of the Shapiro-Wilk normality test was applied by using the `scipy.stats` library under the command `shapiro()`.

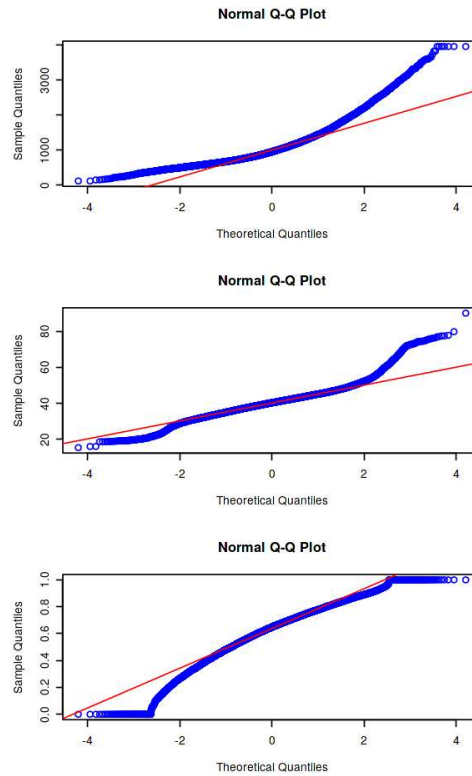


Figure 3
Examples of QQ Plot distributions

2.4 Central Limit Theorem

One of the reasons why normal distribution appears regularly when dealing with applied statistics must complete with the central limit theorem. One of the most fundamental and profound concepts in statistics [11], the central limit theorem is the core for several statistical activities involving using a sample for making inferences over a large and unknown population. It demonstrates that the sampling distribution of the sample means can be approximated as a normal distribution if the number of samples n is large enough, for statistical purposes $n > 30$ [12].

The versatility of the theorem is that it holds its principle for every random variable distribution, being normally distributed or not. Figure 4 illustrates the concept from a non-normal distribution use case.

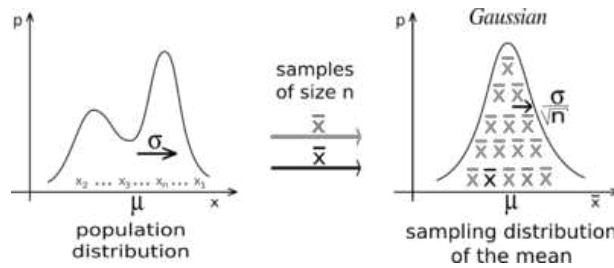


Figure 4
Central limit theorem use case

2.5 T-test for Difference of Two Sample Means

Testing the hypothesis that the mean of a sample is the same as that of an assumed population is a very common statistical analysis use case. When this is the case and when the true population mean (μ) and standard deviation (σ) are known this is a typical z test. On the other hand, when parameters from the original population are not given the test and classified as a t-test using sample statistics as approximation parameters and it has the variation corrected based on the Student-t distribution. [31-34]

Generally, the hypothesis being tested in a t-test suggests the difference between means of two sample means with relatively small sample sizes. The assumptions of the test are the following [31-34]:

- Data points are independent;
- Data points are accurately recorded;
- The sample size is small, usually less than 30.

The statistical test is then evaluated according to Equation 1.

$$Ttest = \frac{(x_1 - x_2) - d}{SE_{\bar{x}}} \quad (1)$$

$$SE = \sqrt{\frac{s_1^2}{n_1} + \frac{s_2^2}{n_2}} \quad (2)$$

The t-statistic is then compared to a t-table or applied to a t Distribution Calculator [13] together with the calculated degrees of freedom (DF) associated with the sample sizes for obtaining the p-value which resembles the probability of observing a result as extreme as the one observed in the experiment. The obtained p-value is then compared to the experimental confidence level to accept or reject the null hypothesis and reach conclusions. [31-34]

3 Methods

The technology used to process analysis varies according to the purpose and can be summarized as follows:

- Python 3.2 was used by specific libraries such as Pandas and Numpy for structured data handling and summary statistics, Matplotlib and Seaborn for visualizations, Statsmodels and Scipy for specific statistical tests;

3.1 Goal 1 - Porosity Analysis

Briefly reviewing the goal definition, for the given data set of machine porosity, a study is necessary to understand whether the porosity occurrence is due to processual randomness. The action plan consists of:

- Exploratory data analysis for better understanding the working data;
- Validation of the underlying distribution of the sample;
- State null hypothesis and alternative hypothesis for the experiment;
- Evaluation of sample confidence intervals (CI) at 95% confidence level;
- Two-sample t-test statistical test.

Table 1
First 4 samples of Machine Porosity data set [29]

Sample Number	Machine A - Percent porosity [%]	Machine B - Percent Porosity [%]
Sample 1	1.72	1.78
Sample 2	1.73	1.99
Sample 3	1.74	1.68
Sample 4	1.53	1.69

As a good practice of data analysis, the initial focus is on EDA execution or Exploratory Data Analysis for getting a better sense of the working data. The working data is a small machine sensor dataset with 20 observations for each machine. Summary statistics are presented below as well as the visualization of population distribution for Machine A and Machine B as a frequency plot (Figure 4) and a box plot (Figure 5).

Table 2
Summary statistics for Machine A and Machine B working data [29]

	Machine A	Machine B
Mean [%]	1.730	1.771
Median [%]	1.745	1.760
Max [%]	1.790	1.990
Min [%]	1.530	1.680
Std Dev [%]	0.063246	0.074302

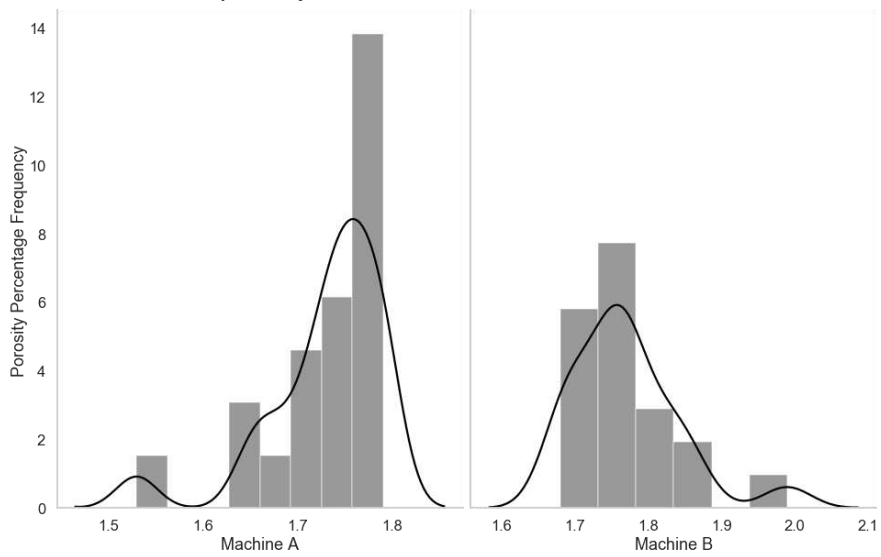


Figure 5
Porosity percentage frequency distribution

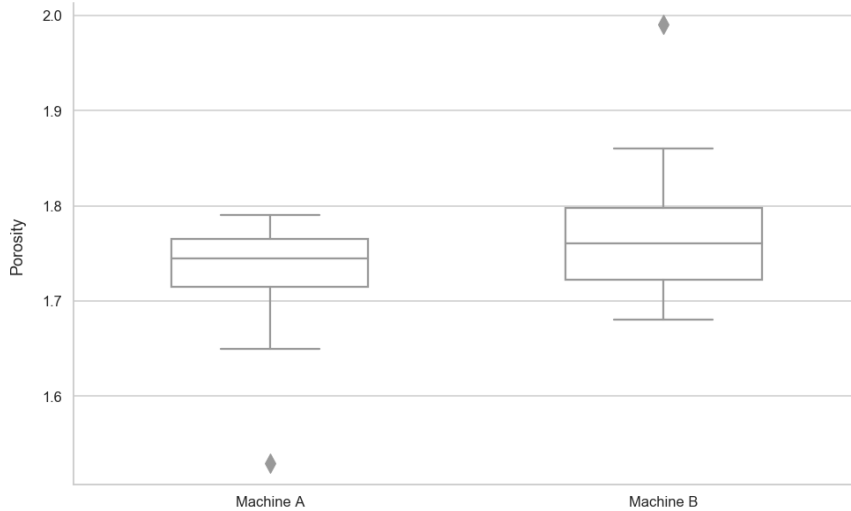


Figure 6

Box plot visualization from Machine A and B working data

It is a common assumption for engineering processes that the population of a production process follows a normal distribution, and provided that n is large enough (>30) it is possible to assume that the means of samples coming from such population are also normally distributed. A normality test was executed for both distributions in order to confirm if the dataset could be approximated and treated as a normal distribution since such consideration allow simplified statistical tests for testing the hypothesis.

From Figure 5 two different outliers are detected by using the $1.5 \times IQR$ rule, which made both samples to fail upon a Shapiro-Wilk test due to the small n of 20. However, after treating the outliers, overwriting both with the mean value of each sample, both samples passed the normality test. Figure 6 shows the resulting QQ plot graphical method for normality estimation for both machines after removing outliers.

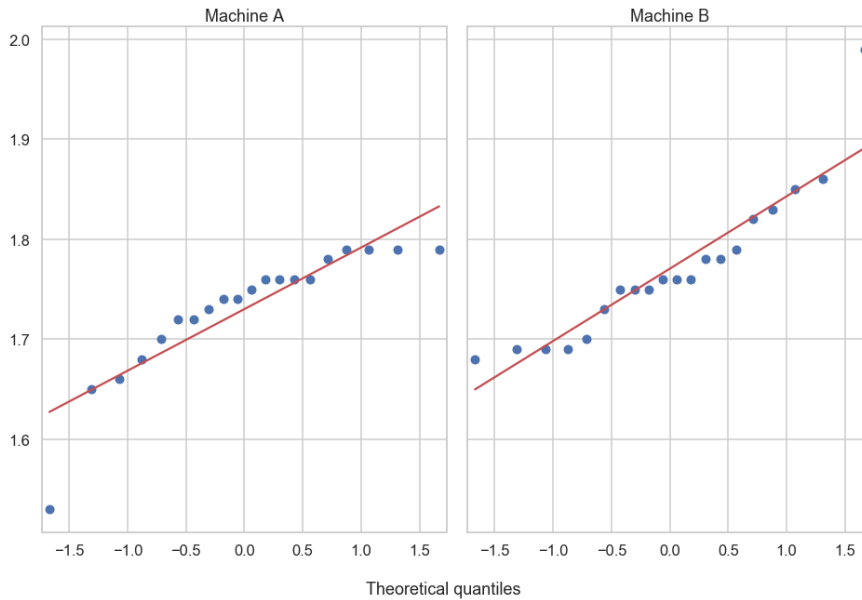


Figure 7

QQ plot for machines A and B after removing outliers

For the Two-sample t-test, the null hypothesis (H_0) under analysis is that both samples come from a common distribution, and therefore are similar having their mean difference is zero. In other words, the different machines have no impact on the porosity percentage of produced parts. Additionally, the alternative hypothesis (H_a) is that the mean difference between samples is different from zero, meaning that samples come from different populations. Hypothesis statements summarized in Table 3.

Table 3
Summarized hypothesis

Set	Null Hypothesis	Alternative Hypothesis
1	$\mu_1 - \mu_2 = 0$	$\mu_1 - \mu_2 \neq 0$

As an experiment best practice, the first assessment is completed by looking at an eventual overlap of CI at 95% confidence level, which would reinforce the null hypothesis. Figure 8 presents a clear overlap between sample means at 95% confidence level.

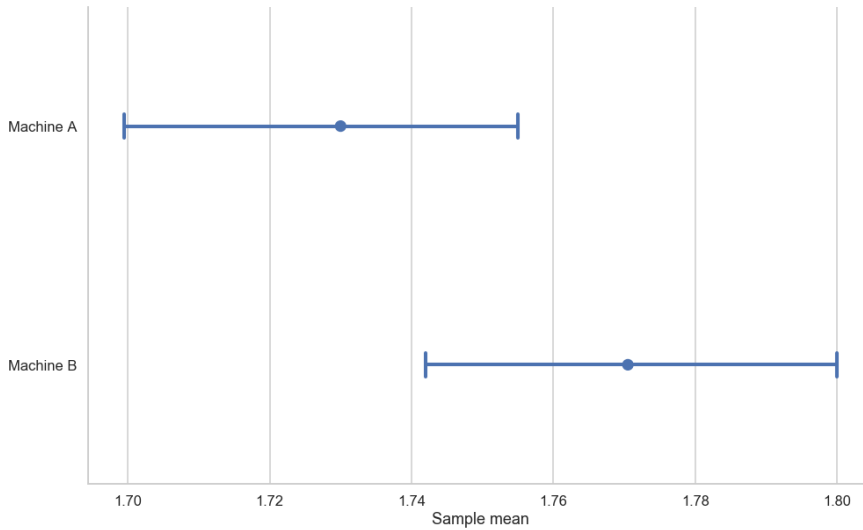
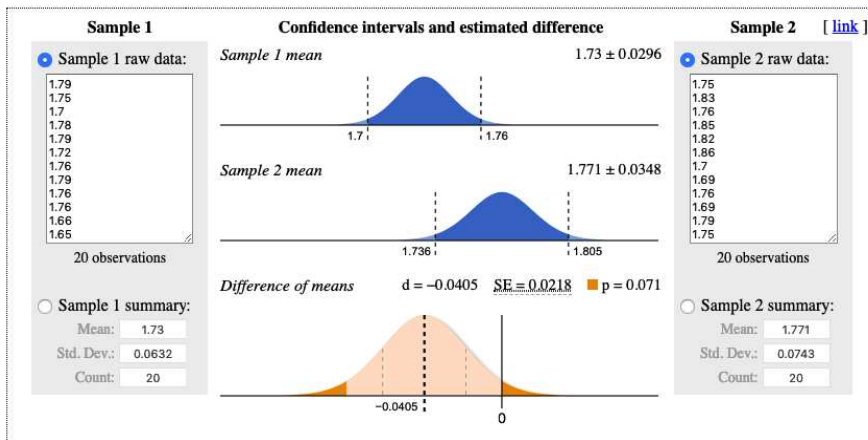


Figure 8

The confidence interval for sample means

The standard error of the mean difference is calculated and evaluated at a Z score of 1.96, covering 95% confidence level. Results are summarized in Figure 9 which are obtained by using Miller's A/B test calculator [14].



Verdict: No significant difference

Hypothesis: $d = 0$ $d \leq 0$ $d \geq 0$

Confidence: 95%

Figure 9

T-test summary from Evan's Awesome A/B Tools

Similar results were obtained using statsmodel T-test function considering equal variance and n number of samples under the command `stats.ttest_ind(equal_var=False)`.

Conclusion

Since the advent of data technologies, engineers need to be prepared to face data integration and analysis tasks which will require a lot more cognitive skills and deep work [15] to generate intelligence and insights as outputs to improve maintenance processes. [21-23]

Most of the meaningful insights by the analysis is derived from adjacent areas of engineering, supporting the idea of a more complete professional who is able to design, implement, carry out an audit, and analyze data.

The purposed goal emphasized statistical and data analysis, covering the entire pipeline from data extraction, transformation, and load (ETL) to p-value determination for reaching conclusions and business suggestions. The intuition built refines inspection and maintenance planning, where better-informed decisions are made aided by data-driven processes. Understanding such a mindset will gradually direct the industry towards modernization as it is already happening with modern industrial revolutions, such as the Industrial Internet of Things (IIoT) [17].

Understanding the mathematics of reliability allow leaders not to see future events, but the distribution of the most likely and desired outcomes in a way companies can prioritize better actions.

In conclusion, in a world where processes are growing complex with many different human and processual interactions understanding how to deal with uncertainty is an important skill for the modern engineer.

The method can be further refined by other soft computing methods. The Support Vector Machine method is well suited for analysing and grouping large amounts of data. The most promising method seems to be fuzzy logic, which provides an opportunity to examine so-called fuzzy sets. This is essential for a modern technical system. There are several operational and maintenance cases where operators have unequivocal data or perceptions. In this case, statistics-based machine learning is needed to make decisions.

Modern maintenance systems run on a real-time basis these days providing the fastest data reporting that helps maintainers take the fastest action. Modern enterprise management systems such as SAP and Oracle provide the ability to store and analyse data. The solution in this article can be implemented in any enterprise management system provided there is sufficient hardware capacity to perform complex calculations. Increased IT demand requires financial investment, which is not worth for every enterprise. This decision is always an economic decision and may be different for every company.

References

- [1] Boyes, H., et al. (2018) The industrial internet of things (IIoT): An analysis framework. *Computers in Industry*, Volume 101, 2018, pp. 1-12
- [2] Ageeva, Y. (2018, June 17) Predictive Maintenance Scheduling with IBM Watson Studio Local and Decision Optimization. In *Towards Data Science*. Retrieved 08:48, March 12, 2019, <https://towardsdatascience.com/predictive-maintenance-scheduling-with-ibm-data-science-experience-and-decision-optimization-25bc5f1b1b99>
- [3] Karim, R. et al. (2016) Maintenance Analytics – The New Know in Maintenance. *IFAC-PapersOnLine*, Volume 49, Issue 28, pp. 214-219
- [4] Doran, G. T. (1981) There's a S.M.A.R.T. Way to Write Management's Goals and Objectives. *Management Review*, 70, 35-36
- [5] Meyer, P. J. (2003) *Resources Attitude Is Everything: If You Want to Succeed Above and Beyond.*, Published January 1st 2003 by Paul J. Meyer Resources, ISBN: 9780898113044
- [6] Bogue, R. (2018) "Use S.M.A.R.T. goals to launch management by objectives plan". *TechRepublic.*, Retrieved February 13, 2020, <https://www.techrepublic.com/article/use-smart-goals-to-launch-management-by-objectives-plan/>
- [7] Connor, P. D. T. (2012) *Practical Reliability Engineering*. Wiley, Fifth Edition
- [8] Upton, G., Cook, I.: *Understanding Statistics*, Publisher: OUP Oxford, 1996, ISBN 9780199143917
- [9] Brownlee, J. (2018) *A Gentle Introduction to Normality Tests in Python*. In *Machine Learning Mastery*. Retrieved 17:29, February 18, 2019, <https://machinelearningmastery.com/a-gentle-introduction-to-normality-tests-in-python/>
- [10] Bachmann, J. (2018, September 01) *Statistical Analysis: A frequentist approach*. In *Kaggle Kernels*. Retrieved 20:47, March 11, 2019, <https://www.kaggle.com/janiobachmann/statistical-analysis-a-frequentist-approach>
- [11] Brooks, D. G.: *The Sampling Distribution and Central Limit Theorem*, 2nd edition, Amazon Books, CreateSpace Independent Publishing Platform (December 31, 2012) ISBN-13: 978-1530441617
- [12] Stat Trek. (2019, March 06) *Central Limit Theorem*. In *Statistics Dictionary Stat Trek*. Retrieved 20:42, March 06, 2019, https://stattrek.com/statistics/dictionary.aspx?definition=central_limit_theorem

- [13] Stat Trek. (2019, March 07) T-distribution calculator. In Statistics Dictionary Stat Trek. Retrieved 19:03, March 06, 2019, <https://stattrek.com/online-calculator/t-distribution.aspx>
- [14] Miller, E. (2019, March 03) Evan's Awesome A/B Tools. In [evanmiller.org](http://www.evanmiller.org). Retrieved 13:36, March 03, 2019, <http://www.evanmiller.org/ab-testing/t-test.html>
- [15] Newport, C. (2016) *Deep Work: Rules for Focused Success in a Distracted World*. Grand Central Publishing, Fifth Edition
- [16] Boyes, H., et al. (2018) *The industrial internet of things (IIoT): An analysis framework*. *Computers in Industry*, Volume 101, 2018, pp. 1-12
- [17] Singh, S.: *Become a Data Visualization Whiz with this Comprehensive Guide to Seaborn in Python*, Retrieved: February 13, 2020, <https://www.analyticsvidhya.com/blog/2019/09/comprehensive-data-visualization-guide-seaborn-python/>
- [18] statsmodels 0.11.0: *Statistical computations and models for Python*, Retrieved: February 13, 2020, <https://pypi.org/project/statsmodels/>
- [19] statsmodels 0.11.0: *statsmodels*, Retrieved: February 13, 2020 <http://www.statsmodels.org/stable/index.html>
- [20] patsy: *Describing statistical models in Python*, Retrieved: February 13, 2020, <https://patsy.readthedocs.io/en/latest/index.html>
- [21] Mankovits T., Szabó T., Kocsis I., Páczelt I.: *Optimization of the Shape of Axi-Symmetric Rubber Bumpers* *Strojnicki Vestnik -Journal of Mechanical Engineering* 60:(1) pp. 61-71 (2014)
- [22] Deák K., Mankovits T., Kocsis I.: *Optimal wavelet selection for manufacturing defect size estimation of tapered roller bearings with vibration measurement using Shannon Entropy Criteria*, *Strojnicki Vestnik -Journal of Mechanical Engineering* 63 : 1 pp. 3-14, 12 p. (2017)
- [23] Sziki G. Á., Sarvajcz K., Szántó A., Mankovits T.: *Series Wound DC Motor Simulation Applying MATLAB SIMULINK and LabVIEW Control Design and Simulation Module*. *Periodica Polytechnica - Transportation Engineering & pp.* 1-5, 5 p. (2019)
- [24] Kordic, B., Popovic, M., Ghilezan S.: *Formal Verification of Python Software Transactional Memory Based on Timed Automata*, *Acta Polytechnica Hungarica*, Vol. 16, No. 7, 2019, ISBN 1785-8860
- [25] Horváth Á.: *The Cxnet Complex Network Analyser Software*, *Acta Polytechnica Hungarica*, Vol. 10, No. 6, 2013, ISBN 1785-8860
- [26] O'Connor, P. D. T.; Kleyner, A.: *Introduction to Reliability Engineering, Practical Reliability Engineering*, Fifth Edition. 2012 John Wiley & Sons, Ltd. Published 2012 by John Wiley & Sons, Ltd.,

- https://media.wiley.com/product_data/excerpt/28/04709798/0470979828-54.pdf
- [27] Huff, A. M.: Reliability Of a Lunar, Western Kentucky University, Retrieved February 13, 2020, https://digitalcommons.wku.edu/cgi/viewcontent.cgi?article=1302&context=stu_hon_theses
- [28] HSC: Numeracy for Science - Mathematics is fundamental to science, Retrieved February 13, 2020, <https://investigatingssciencehsc.com/numeracy-in-science/>
- [29] DiazEIE419Q3 - Percent Porosity Machine A Machine B Sample, Retrieved February 13, 2020, <https://www.coursehero.com/file/23869487/DiazEIE419Q3/>
- [30] Chowdavaram, GUNTUR – 522019., R.V.R. & J. C. COLLEGE OF ENGINEERING, Regulations (R-17), Scheme of Instructions, Examinations and Syllabi For Two Year M.Tech. Degree, Programme in MACHINE DESIGN
- [31] NCSS Statistical Software: Chapter 206, Two-Sample T-Test, Retrieved February 13, 2020, https://www.ncss.com/wp-content/themes/ncss/pdf/Procedures/NCSS/Two-Sample_T-Test.pdf
- [32] NCSS Statistical Software: Chapter 207, Two – Sample T-Test from Means and SD's, Retrieved February 13, 2020, https://ncss-wpengine.netdna-ssl.com/wp-content/themes/ncss/pdf/Procedures/NCSS/Two-Sample_T-Test_from_Means_and_SDs.pdf
- [33] Demetriadis, S.: Data Analysis and Hypothesis Testing Using the Python ecosystem, t-Test & ANOVAs, Aristotle University of Thessaloniki, Retrieved February 13, 2020, <http://pytolearn.csd.auth.gr/dnld/sdemetri@UVa2016-StatTests.pdf>
- [34] plotly – Graphing Libraries: T-Test in Python/v3, Retrieved February 13, 2020, <https://plot.ly/python/v3/t-test/#two-sample-t-test>

Multi-Robot Workspace Allocation with Hopfield Networks and Imprecise Localization

Mert Turanli, Hakan Temeltas

Control and Automation Engineering Department, Istanbul Technical University,
ITU Ayazaga Campus, Istanbul, 34469, Maslak, Turkey
turanim@itu.edu.tr, hakan.temeltas@itu.edu.tr

Abstract: With the increased use of robots with different performance characteristics in areas such as search and rescue, patrolling and surveillance, the control of multiple robots with unequal capabilities have gained a lot of interest among robotics researchers. Also, the uncertainty of the sensors utilized on the robots for localization has made the problem of imprecise localization attractive. This paper aims to present the development and implementation of a multi-agent collaboration algorithm under localization uncertainty using Hopfield neural networks, guaranteed power Voronoi diagrams (GPVD or GPD), and coverage control. The agents are considered non-holonomic wheeled mobile robots under the assumption that their locations are not known precisely, but they are known to be in uncertain circles. The workspace is partitioned with a Guaranteed Power Voronoi Diagram (GPVD or GPD) algorithm which takes imprecise localization into account. Also, it is assumed that the actuation capabilities of the robots are different from each other and the agents do not know those performances beforehand. The performance parameters of the robots are learned by using the collaboration algorithm with Hopfield Neural Network (HNN) and then passed to the GPD algorithm. The GPD algorithm together with the HNN provides workspace partitioning for the robots so that the agents with poor actuation performances take smaller regions from the workspace while the agents with strong performances take greater regions. Thus, a collaborative coverage task is achieved which enables the robots to deploy themselves to an optimal configuration minimizing the total coverage cost. The simulation results in MATLAB show the efficiency of the algorithm. The experimental results with the Robot Operating System (ROS) are given. The results obtained are satisfactory since the algorithm has faster convergence and has the capability to assign the regions from the workspace considering the imprecise localization resulting from sensor characteristics. Finally, the algorithm is compared to the base collaboration method, important performance improvements had been observed.

Keywords: Workspace allocation; Coverage control; Guaranteed Power Voronoi Diagrams; Hopfield Neural Network

1 Introduction

The Multi-agent collaboration and coordination problems have been well studied in robotics literature over the last decades. Autonomous agents deploy themselves over the area to maximize sensor coverage. The Voronoi-based coverage control method became quite important due to its application potential in practice, for example, surveillance and security uses, patrolling and environmental monitoring applications, dealing with the deployment and allocation problems at the same time.

The definition of the Voronoi-based coverage control problem is autonomous self-deployment of the agents in the environment so that the optimal coverage configuration can be achieved. The Voronoi-based coverage control accomplishes the dynamic workspace partitioning by making use of Voronoi diagrams. Another definition of the coverage is to observe every point of a given region or to see it with a sensor having a field of view [11].

To summarize the new ideas of this paper with respect to the literature, in the previous method, which is about the adaptation to the performance variations of multiple robots [22], a non-linear estimator was used to enable the robots to learn their own parameters. In this work, a faster and more robust estimator based on HNN is utilized instead. Also, the localization uncertainty coming from sensors such as laser scanners or odometry is taken into consideration by using Guaranteed Power Voronoi Diagrams. In the base work, the localization uncertainty is not taken into consideration where the authors did the workspace partitioning by using the Power Voronoi Diagrams.

The contributions of the work are further explained in the Contributions section.

1.1 Related Studies

Several self-deployment algorithms taking localization uncertainty [21], [14], [19], [28] into account exist in the literature using Guaranteed Voronoi Diagrams [6] and their variants. Also, a Power-Voronoi-based collaboration algorithm is studied by the authors [23]. Pierson, A. and the others investigated inter-robot trust adaptation in response to the relative performances by using multi-robot sensor coverage [24]. A multi-robot cooperative coverage algorithm is proposed in which the robots are spraying a large field by performing task allocation and coordination [10]. Additionally, Hopfield Neural Networks are well studied by the authors for estimating the system parameters online in robotics [1] and control [3], [9] applications.

In the work [20], a multi-agent dynamic coverage method with anisotropic sensing footprints is proposed. Safety and convergence guarantees are taken into consideration. The agents are forced to search an area of interest collaboratively with local and global coverage strategies. Avoidance strategies are also developed.

In a recent paper [27], a framework for distributed coverage control for mobile sensors is discussed. In the multi-agent problem, the locational optimization is considered a special case of optimizing Kullback-Leibler divergence where space is density function space. The distributed coverage control laws are then formulated by minimizing distance functions. For a possible metric for distance functions, L^2 distance is utilized. A mobile sensor network coverage problem is studied in another work [4]. The sensors have different velocity constraints and the effect of the measurement errors is investigated. In the study of the authors [16], the agents accomplish the persistent coverage task in a distributed way. The control law is cooperative, and the environment is structured. It is proven that no collision occurs between agents nor with obstacles.

Also, there are many other related papers especially in the robotics and engineering areas that can be briefly summarized. In the work [15], a genetic algorithm approach is given to a networked high-performance drilling process. The algorithm is used for optimal tuning of linear controllers and the mutation part takes care of doing a search among the different linear controllers. Simulation and experimental results are given. In another paper [12], two open research surgical robot platforms are discussed. The paper gives the aims and related problems in the robotic surgery field. It also briefly introduces the research platforms. In the paper [8], the virtual technologies in engineering practice are discussed. The complex engineering product and related activities are created on the system level computer. The research results in the field of virtual technology are given. The paradigm in the virtual engineering area shifts to the Virtual Engineering Space (VES) approach. A new concept Knowledge Content Background (KCB) is introduced. In another work [26], a method for generating the optimal path for a traveling robot in a partially unknown environment is introduced. The method can handle both static and dynamic obstacles and a comparison with the Particle Swarm Optimization method is presented. In the study [30], a device for parallel robot investigations is given. The size of the elements of the device can be changed so that different robots can be realized. By reconfiguring the device, different characteristics can be tested. The main aim of the device is the construction studies. In the paper [31], the control problems in the surgical robotics area are discussed. For the precision in control methods used, the interaction between the manipulated tissues and the tool should be modeled. In the paper, the design and modeling of telesurgical systems is presented and possible control methods are summarized.

1.2 Contribution

The contribution of the paper is that it uses a coverage collaboration algorithm that calculates the weights of the agents automatically according to their actuation performances [22] under localization uncertainty [21], [14], [6] with HNN estimator [1, 3]. To the best of our knowledge, this is the first work in the

literature that uses an HNN estimator and takes the localization uncertainty into account in a coverage collaboration algorithm at the same time. The net contribution of this work is that it provides faster convergence for the multi-agent systems using Voronoi partitioning-based collaboration approaches under localization uncertainty by using HNNs. This enables the algorithm to compensate different capabilities of the agents such as actuation by assigning the areas from the workspace to the agents according to their performances and to account the imprecise localization.

1.3 Paper Organization

The paper is organized as follows. The first section gives the introduction, related studies and the contribution of the work. In the second section, the formal problem statement, preliminary information about workspace partitioning with Voronoi Diagrams, HNNs and locational optimization will be given. In the next section, the coverage control algorithm with HNNs and adaptation to performance variations will be investigated. In the fourth section, the stability analysis of the control and estimation algorithm will be discussed. After, MATLAB simulation results are given with different case studies. The next section gives the experimental setup and results. In the last section, the conclusions of the work will be explained.

2 Problem Formulation

In this section, preliminary information about Guaranteed Power Voronoi diagrams, HNNs, and locational optimization are presented.

The formal statement of the problem is as follows. Consider a team of n non-holonomic wheeled mobile agents. The aim is to maximize coverage according to locational optimization function by performing collaboration among the agents. The collaboration is achieved by estimating the actuation performances of the agents with HNNs which are not known beforehand. Then, the regions of the agents are assigned automatically by giving the performance parameters to the GPD algorithm. In the resultant configuration, the agents with strong actuators take larger portions from the workspace, while smaller regions are assigned to the robots with weak actuators.

In the N -dimensional space $S \subseteq \mathbb{R}^N$ is defined as a convex region. The positions of the robots are not known precisely, but known to be within an uncertain circle.

2.1 Guaranteed Power Voronoi Diagrams

The Guaranteed Power Voronoi Diagrams (GPD or GPVD) [14] are the types of Voronoi diagrams in which the power distance is used and the generator points are known to be in uncertain regions.

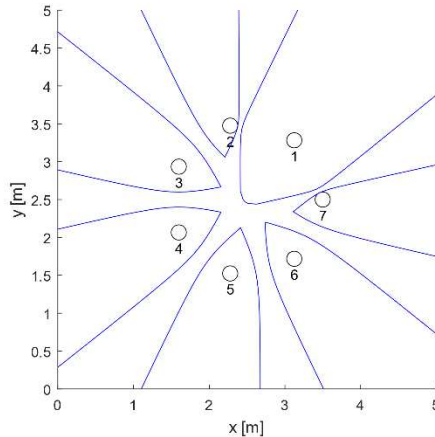


Figure 1

Example Guaranteed Power Diagram (GPVD) with the weight $w_1 = 0.5$

The distance function is defined similarly to the one in the Guaranteed Voronoi Diagrams [6]. The main difference is that the distance function is a power distance in a guaranteed sense. The bisector is a hyperbola when the weights are zero. The definition of the GPV-cell is given below where r_i $r_i r_i$ is the radius of the uncertainty circle and w_i is the weight of the cell:

$$V_i^g = \left\{ p \in S \mid (\|p - p_i\| + r_i)^2 - w_i \leq (\|p - p_j\| - r_j)^2 - w_j, \right. \\ \left. i \neq j, j = 1, 2, \dots, n \right\} \quad (1)$$

Figure 1 gives an example of GPVD. The region of the first region is greater than the other ones since the weight of the first cell is given as 0.5.

2.2 Locational Optimization

Let us define $S \subseteq R^N$ as a bounded environment, $\phi: R^N \rightarrow R^+$ as a density function, and $\ell: R^+ \rightarrow R$ as a non-decreasing performance function. Then, the locational optimization function \mathfrak{S} is given as below:

$$h(q, p_i, w_i) = \ell(\|q - p_i\|) - w_i \quad (2)$$

$$\mathfrak{S}(p_1, p_2, \dots, p_m) = \sum_{i=1}^m \int_{V_i} h(q, p_i, w_i) \phi(q) dq \quad (3)$$

Here, the V_i is defined as Voronoi region i , m gives the number of the site points, w_i represents the weight of the i^{th} cell and the site point of the corresponding Voronoi cell is given as p_i , as it can be viewed in Figure 2.

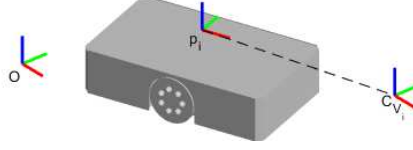


Figure 2

The position of the robot and the centroid location

The mass M_{V_i} and centroid C_{V_i} of a Voronoi region can be defined as given below [13]:

$$Y_i(h, q) = \int_{V_i} h dq \quad (4)$$

$$C_{V_i} = \frac{1}{M_{V_i}} Y_i(q \phi(q), q) \quad (5)$$

$$M_{V_i} = Y_i(\phi(q), q) \quad (6)$$

The performance function is taken as $\ell(\|q - p_i\|) = \|q - p_i\|^2$. So, the locational optimization function \mathfrak{S} can be written as below:

$$\mathfrak{S}(p_1, p_2, \dots, p_m) = \sum_{i=1}^m \int_{V_i} h(q, p_i, w_i) \phi(q) dq \quad (7)$$

The partial derivatives of the function \mathfrak{S} are taken with respect to p_i to find the closed-form solution of the locational optimization function. Then, it can be shown that the locational optimization function given in (7) can be minimized by using the centroid positions given in (5). As a result, the solution is the result where the positions are equal to the centroid locations of the agents.

For the holonomic case $\dot{p}_i = u_i$, the coverage control law is given for i^{th} agent as:

$$\dot{p}_i = u_i \quad (8)$$

$$u_i = K_p(C_{V_i} - p_i) \quad (9)$$

Here, p_i gives the position of the i^{th} agent where K_p is a positive-definite gain matrix.

2.3 Hopfield Neural Networks

The Hopfield Neural Network as presented in [1], is a non-autonomous non-linear dynamical system in continuous time that is able to estimate the parameter vector according to the parameterization of a given dynamical system. Similar to other online parameter estimators, it is able to give the time-evolving estimate of the parameters of the actual dynamical system.

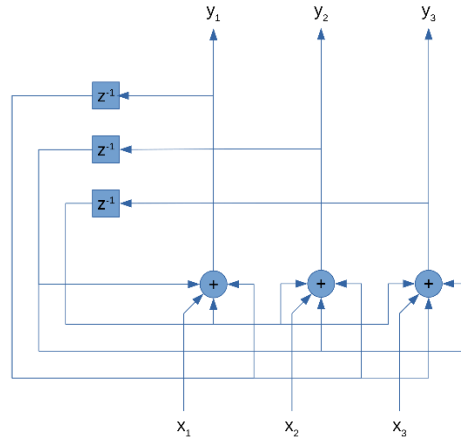


Figure 3

A Hopfield Neural Network with three neurons

Figure 3 gives an example of a Hopfield Network with three neurons. The network is in discrete-time and the previous values of the outputs y_i of the neurons are fed back to the inputs x_i of the neurons.

Since the parameterization of the system is given in the design stage of the HNN, there is no need to train the network. Only the convergence parameters should be adjusted in order to perform a fast and robust estimation. The weights of the network are automatically calculated according to the parametrization of the system. Also, the state vector in the network and the resulting differential equation enables the parameter vector to converge to the real parameter values.

Consider a Hopfield Neural Network of M neurons. Let x_i be the total input to neuron i , s_j be the state or output of the neuron j , W_{ij} be the weight associated with the connection from neuron j to neuron i and I_i be the bias of the neuron i . Then, the state equations of the HNN can be given as:

$$\frac{dx_i}{dt}(t) = -(\sum_{j=1}^M W_{ij}(t)s_j(t) + I_i(t)) \quad (10)$$

$$s_i(t) = \alpha \tanh\left(\frac{x_i(t)}{\beta}\right) \quad (11)$$

The total input-state relation is given as in (11) where $\alpha, \beta > 0$ and $i \in M$.

$$\frac{dx}{dt}(t) = -(W(t)s(t) + I(t)) \quad (12)$$

$$s(t) = \alpha \tanh\left(\frac{x(t)}{\beta}\right) \quad (13)$$

The matrix representation of the HNN is defined in (12) and (13).

In this work, in order to find the performance parameters of the agents, the Hopfield Neural Network is used to perform online parameter estimation.

The choice of the utilization of the HNN as a parameter estimator is made since other approaches like classification with neural networks have accuracy limitations.

3 Coverage Control with Agents with Unequal Actuation Capabilities

In this section, the point-offset control law for non-holonomic robots is given. Then, the parameter estimation with HNN is explained. After, the adaptation to actuation performance variations algorithm is introduced.

The actuation performances are defined as different capabilities of the agents. For example, weak motors and wheel slip can be counted as weak actuation performances, besides powerful motors and favorable terrain are the examples of the strong actuation capabilities. The collaboration algorithm learns the performance variations of the agents by estimating model parameters without prior knowledge and compensates them by giving large regions to the powerful agents and smaller regions to the weak ones.

3.1 The Control Law

The control of the agents is a crucial issue in the coverage collaboration task. After the agent calculates its own centroid location, a control law driving the agent to the position should be executed. In other words, a control law should be selected and designed in order to perform the desired coverage task successfully.

In the literature, there are many works about non-linear controllers for robotics applications. To summarize the recent ones, a stochastic nonlinear model predictive control (MPC) [7], a nonlinear MPC trajectory controller [18], a feedback linearization controller for trajectory tracking for a flexible robot [2], a nonlinear high accuracy feedback linearization control of flexible robots [5] are the related control papers in the literature that are suggested to the reader.

The selected structure of the control law consists of the non-holonomic point-offset control law and the coverage controller given in equation (9). The point-offset controller for the non-holonomic agents consists of a reference point P and a distance l from the center of the robot [17, 25] to the point P . The velocity of the reference point P can be transformed to the linear (v) and angular (ω) velocities by using the matrix equation given below where θ is the heading angle of the robot:

$$\begin{pmatrix} v \\ \omega \end{pmatrix} = \begin{pmatrix} \cos\theta & \sin\theta \\ -\frac{\sin\theta}{l} & \frac{\cos\theta}{l} \end{pmatrix} \begin{pmatrix} \dot{x} \\ \dot{y} \end{pmatrix} \quad (14)$$

After substituting the velocities from the coverage control law in (9) with the (14), the control law becomes:

$$u_i = K_p \begin{pmatrix} \frac{\cos\theta_i}{l} & \frac{\sin\theta_i}{l} \\ -\frac{\sin\theta_i}{l} & \frac{\cos\theta_i}{l} \end{pmatrix} (C_{V_i} - p_i) \quad (15)$$

The K_p is selected so that the control law gives a fast and stable response. Also, the controller is designed in continuous time, but for the discrete-time, a high sampling rate is selected [29] according to the kinematics having in mind that the trajectories calculated by the robots and the dynamics of the robots are slow. The design process of the controller is iterative. First, a high sampling rate is chosen empirically and then the controller gains are adjusted under the physical limits of the robots. The chosen gains are validated by performing a simulation. The process is repeated iteratively until the resulting stable gains are found. The simulation results in the related sections show that the sampling rate is sufficient for the kinematics of the agents under the physical constraints of the robots.

In order for the robot to avoid the collisions, the center P should be checked against collisions with radius $\rho = l + r_{robot}$, where r_{robot} is the radius of the robot.

3.2 Parameter Estimation with HNNs

In order to estimate parameters of the system given in (8), the system should be rewritten in linear in parameters (LIP) form:

$$\dot{p}_i = K_p (C_{V_i} - p_i) \quad (16)$$

$$\dot{p}_i = K_p C_{V_i} - K_p p_i \quad (17)$$

$$p_i = -K_p^{-1} \dot{p}_i + C_{V_i} \quad (18)$$

$$y = p_i - C_{V_i} = -K_p^{-1} \dot{p}_i \quad (19)$$

$$y = - \begin{pmatrix} 1/K_{p,1} & 0 \\ 0 & 1/K_{p,2} \end{pmatrix} \dot{p}_i \quad (20)$$

$$y = \begin{pmatrix} -\dot{p}_{i,x} & 0 \\ 0 & -\dot{p}_{i,y} \end{pmatrix} \begin{pmatrix} 1/K_{p,1} \\ 1/K_{p,2} \end{pmatrix} \quad (21)$$

Then, the parameter estimation vector is defined as follows:

$$\theta_{est} = \begin{pmatrix} 1/K_{p,1} \\ 1/K_{p,2} \end{pmatrix} \quad (22)$$

The LIP form of the system becomes:

$$A = \begin{pmatrix} -\dot{p}_{i,x} & 0 \\ 0 & -\dot{p}_{i,y} \end{pmatrix} \quad (23)$$

$$y = p_i - C_{V_i} \quad (24)$$

$$y = A \theta_{est} \quad (25)$$

The weight matrix W and bias I in equation (12) can be calculated as in the following equations:

$$W = A^T A \quad (26)$$

$$I = -A^T y \quad (27)$$

$$\hat{\theta}_{est} = \begin{pmatrix} s_1(t) \\ s_2(t) \end{pmatrix} \quad (28)$$

$$\hat{K}_i = \begin{pmatrix} 1/\hat{\theta}_{est,1} \\ 1/\hat{\theta}_{est,2} \end{pmatrix} \quad (29)$$

By using (12), (13) together with (23), (24), (26) and (27) the parameters of the closed-loop system (16) can be estimated online. The estimated parameters can be calculated by using the equations (28) and (29).

The equation (12) can be implemented by using numerical integrators.

As explained in Section 2.3, there is no need to train the network because the parametrization of the system dynamics is already given.

For the testing results of the HNN, the reader is referred to the given source code and dataset in the following repository: <https://github.com/mertturani/hnn/>

3.3 Estimating the GPVD Weights

The adaptation algorithm in this section is based on the algorithm in work [22]. Assuming that \hat{K}_i is obtained by using (28) and (29) after the estimation, the values of the parameter vector \hat{K}_i is transferred to the weight estimator. The output of the weight estimator is passed to the GPD workspace partitioning algorithm.

For the weight w_i of the agent i , the adaptation law is:

$$\delta_i = w_i - f(\hat{K}_i) \quad (30)$$

$$\dot{w}_i = -k_\omega \sum_{j \in N_i} (\delta_i - \delta_j) \quad (31)$$

where k_ω is a positive coefficient and N_i represents the neighbors of the agent i . The function $f(\hat{K}_i)$ is related to the desired performance and chosen as $f(\hat{K}_i) = \|\hat{K}_i\|$.

Assuming that \hat{K}_i is obtained for the agent i , the weights are calculated by using the estimation law in (30) and (31). For the implementation, a numerical integrator should be used in order to calculate the estimated weight value.

4 Stability Analysis

To prove the stability of the control and estimation laws, first, a Lyapunov function candidate should be defined as given below for $V_3: \theta_{est} + (-c, c)^M \rightarrow \mathbb{R}$:

$$V = V_1 + V_2 + V_3 \quad (32)$$

$$V_1 = \sum_i \frac{1}{2} \|C_{V_i} - p_i\|^2 \quad (33)$$

$$V_2 = \sum_i w_i \quad (34)$$

$$V_3 = \sum_i -\frac{1}{2c} \sum_{j=1}^M \ln \left(\left(1 + \frac{\tilde{\theta}_{est(i,j)}}{c - \theta_{est(i,j)}} \right)^{c - \theta_{est(i,j)}} \left(1 - \frac{\tilde{\theta}_{est(i,j)}}{c + \theta_{est(i,j)}} \right)^{c + \theta_{est(i,j)}} \right) \quad (35)$$

where $\tilde{\theta}_{est(i,j)} = \theta_{est(i,j)} - \hat{\theta}_{est(i,j)}$ and $\hat{\theta}_{est(i,j)}$ is defined as the output of the j^{th} neuron of the parameter estimator of the i^{th} agent. Also, c is a positive constant [1].

First, if we consider the state vector as $x_i = (C_{V_i} - p_i \quad w_i \quad \tilde{\theta}_{est(i)})^T$, it can be seen that $V(x = 0) = 0$. Also, $V_3(x) > 0$ as given in proof in [1]. So, $V(x) > 0$.

Taking the derivative of the Lyapunov function yields:

$$\dot{V}_1 = \sum_i -(C_{V_i} - p_i)^T \dot{p}_i \quad (36)$$

$$\dot{V}_2 = \sum_i -(C_{V_i} - p_i)^T K_p (C_{V_i} - p_i) \leq 0 \quad (37)$$

The first term is negative semi-definite.

$$\dot{V}_3 = \sum_i -k_\omega \sum_{j \in N_i} \left((w_i - f(\hat{K}_i)) - (w_j - f(\hat{K}_j)) \right) = 0 \quad (38)$$

Also, the second term is zero. Taking the derivative of the third term becomes:

$$\dot{V}_3 = \sum_i -\frac{1}{c\beta} \tilde{\theta}_{est(i)}^T W_i \tilde{\theta}_{est(i)} \leq 0 \quad (39)$$

where W_i is the weight matrix for i^{th} agent and clearly positive semi-definite. For $\beta > 0, c > 0$ the third term is negative semi-definite.

The trajectories and estimation errors are bounded since the $\dot{V} \leq 0$. The weights are bounded since the $\sum_i w_i$ becomes a stable filter as given in the proof in [22]. To complete the proof, the following theorem is introduced from [1]:

Theorem 1: The equilibrium point $\tilde{\theta}_{est(i)}^* = 0$ is globally asymptotically stable if $I \subset [t_0, \infty)$ and $\bigcap_{t \in I} \ker(A(t)) = \{0\}$.

From the Theorem 1 and the proof in [1], it can be concluded that for a non-degenerate interval $t \in I$, the equilibrium point $\tilde{\theta}_{est(i)}^* = 0$ is globally uniformly asymptotically stable and the equilibrium point is unique.

From LaSalle's Invariance Principle, the largest invariant set defined by $\dot{V} = 0$ should be found. $\dot{V} = 0$ occurs only when $C_{V_i} = p_i$ and $\tilde{\theta}_{est(i)} = 0$. These equilibrium points are unique, and the case corresponds to the case that the tracking and estimation errors become zero. From the control and estimation laws, it can be concluded that the set is an invariant set. Thus, the system is globally asymptotically stable.

Corollary 1: In the steady-state, the estimation vector converges to its real value and $w_i - f(K_i)$ converges to a common value for all agents [22]:

$$\lim_{t \rightarrow \infty} (\hat{K}_i) = K_i \quad (40)$$

$$\lim_{t \rightarrow \infty} (w_i - w_j) = f(K_i) - f(K_j) \quad (41)$$

From the stable filter theory, in the steady-state, the weights converge to their final values, as stated in the referenced paper [22]. Also, from (41) the value of $w_i - f(K_i)$ converges to a common value for all agents.

The stability analysis is done in continuous time since the nonlinear systems are continuous in nature. However, the implementation is carried out in discrete-time and for this purpose, a high sampling rate is selected [29] according to the kinematics of the agents since the trajectories of the robots and the dynamics of the agents are slow and the dynamics are neglected in design. Also, the numerical integrations in the estimators are converted into discrete-time trapezoidal integrations in order to get accurate results in discrete-time.

5 Simulation Results

The simulations are done in MATLAB environment with the map sizes of 5x5 and 10x10 meters. The parameters in the simulation are $k_\omega = 0.2$, $K_p = \text{diag}([1 \ 1])$, $r_{robot} = 0.11$, $l = 0.1$, $\alpha = 3000$ and $\beta = 1$. Also, the uncertainty radius is given as $r_i = 0.1$ meters.

The simulation is performed with 15 agents. In Figure 4 and Figure 5, the position errors and the coverage cost are given, respectively. The position errors of the robots asymptotically converge to zero and the coverage cost is settled to a minimum value after the coverage task is completed.

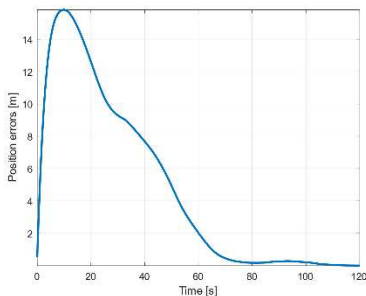


Figure 4
Position errors

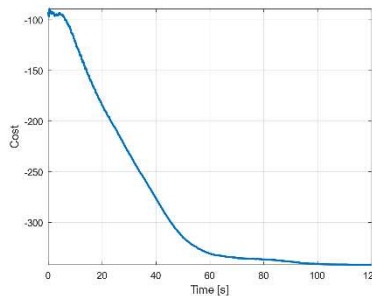


Figure 5
Coverage cost

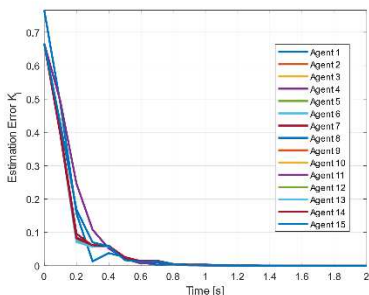


Figure 6
Parameter estimation errors

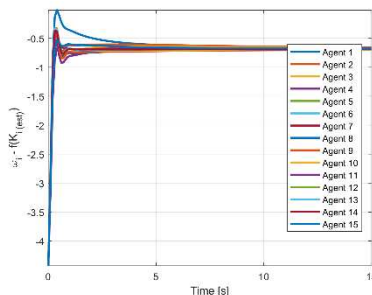


Figure 7
The value of $w_i - f(\hat{K}_i)$

Figure 6 shows the asymptotic convergence of the parameter estimation errors of the Hopfield Network, obeying Theorem 1.

In Figure 7, the value of $w_i - f(\hat{K}_i)$ is given which converges to a common point among the agents as given in the Corollary 1.

Figure 8 and Figure 9 represent the weight of agents and the trajectories, respectively. The weight of the first agent has a lower value than the other agents since it has a degraded performance different from the other ones. The trajectories of the agents converge to the optimal coverage positions, as seen in Figure 9.

Table 1 shows the region ratios of the agents at the end of the simulation. The region of the first agent is smaller than the regions of the other agents.

The results show that the HNN estimator outperforms well compared to the base method [22] which is a non-linear adaptive estimator. The HNN provides faster convergence and more robust estimation according to the simulation results, as it can be seen from the parameter estimation errors. As a result, the coverage time can be improved.

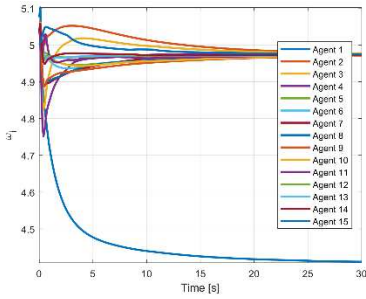


Figure 8
The weights of the agents

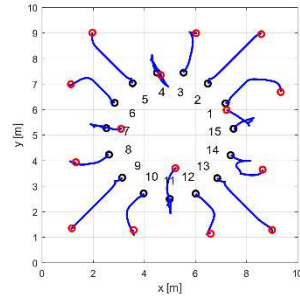


Figure 9
The trajectories of the agents

Table 1

Region ratios of the agents at the end configurations

Agent	Region Ratio	Agent	Region Ratio
1	0.0349	9	0.0592
2	0.0560	10	0.0661
3	0.0537	11	0.0688
4	0.0602	12	0.0614
5	0.0669	13	0.0496
6	0.0572	14	0.0652
7	0.0527	15	0.0629
8	0.0615	-	-

6 Experiments

The experiments were carried out with two Turtlebot 2 agents in 2x2 meter environment. The first agent had a 10% actuation performance degradation. The agents start at initial configurations and perform the collaborative coverage task.

6.1 Experimental Setup

The experiments were carried out with two Turtlebot 2 agents in ITU Robotics Laboratory. The computers on the robots are Acer Aspire E11 with Intel Celeron N2940 processors and 4 GB of memory running Ubuntu 14 and ROS Indigo. The Turtlebot 2 agents are differential drive robots having a maximum velocity of 0.65 m/s and a maximum payload of 5 kg. The weight of the robot is 6.3 kg.



Figure 10

The initial configurations of the robots (ITU Robotics Laboratory)

Figure 10 illustrates the experimental setup in the ITU Robotics Laboratory. The localization information is taken from the wheel odometry of the robots. The ROS driver “kobuki_node” is used for the Turtlebots. The communication between the agents is performed by using publisher/subscriber architecture and ROS topics. The robots are connected to a 450 Mbps Wi-Fi N access point.

The ROS master computer is a laptop PC running Ubuntu and ROS Kinetic. The computers on the robots are connected to the ROS master node over the Wi-Fi network.

6.2 Experimental Results

The experiment starts with a ROS node named as Coverage node running for each agent separately in a decentralized way. Each node estimates its own \hat{K}_i vector from its own motion by using HNNs by using (12) and (13) and then calculates the weight of the agent by using (30) and (31). The node then passes the weights to the GPD algorithm. After the centroid locations are found by using the GPV-cells and the non-holonomic control law is executed. The obtained velocities are sent to the corresponding topic of the agent.

The coverage node is running on the controller PC of the agent on ROS real-time in a distributed way. The robots communicate with each other and estimate their own performance parameters, estimate the weights and calculate the GPD regions. Then, they execute the control law after finding the centroid positions.

The experiment is repeated three times and the results are given in the table of region ratios.

Figure 11 shows the overall coverage cost of the agents for the first experiment. The cost converges to its local minima as the coverage task completes. Also, in Figure 12, the estimation errors show asymptotical convergence to zero.

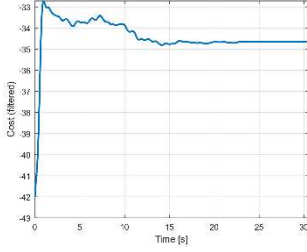


Figure 11
Coverage cost

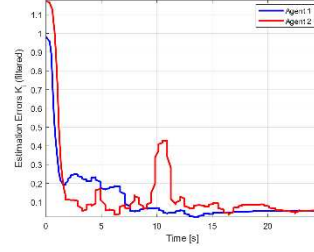


Figure 12
Estimation errors

Figure 13 illustrates the value of $w_i - f(\hat{R}_i)$. As given in Corollary 1, the value converges to the same value among the agents. Lastly, Figure 14 depicts the weight values calculated by the online estimator. As expected, the weight of the first agent is less than the other agent.

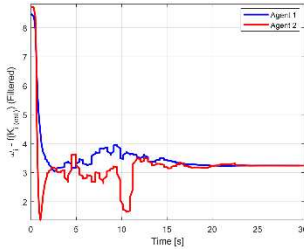


Figure 13
The value of $w_i - f(\hat{R}_i)$

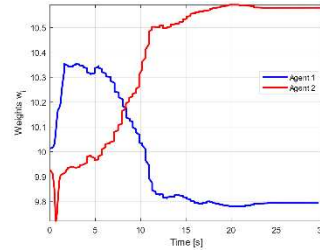


Figure 14
The weights of the agents

In Figure 15, the trajectories of the two agents are given. The black circles denote the initial configurations while the red circles show the final configurations.

At the end configuration, the obtained regions are given in Figure 16 for the first experiment. The region ratio of the first agent is less than the second one. In the first experiment, the α parameter is taken as $\alpha = 6000$.

At the last configuration, the obtained region ratios are given in Table 2 for the second, third, and fourth experiments. Here, in the three experiments, the Hopfield parameter α is taken as $\alpha = 3000$. The region ratio of the first agent is less than the other agent in each experiment. The results taken from the three experiments are similar. The distributed algorithm assigns the weights to the agents according to their performances. The video of the experiment can be viewed at: <https://web.itu.edu.tr/turanlim/video/exp-tb2.mp4>.

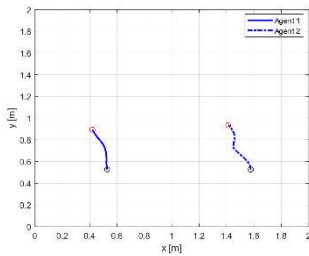


Figure 15

The trajectories of the agents

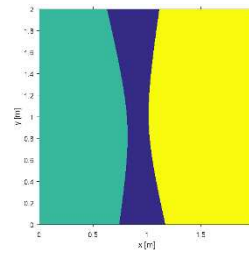


Figure 16

The GPD plot obtained from the first experiment

Table 2

Region ratios of the agents at the end configuration with HNN of three experiments

Agent	Region Ratio Experiment 1	Region Ratio Experiment 2	Region Ratio Experiment 3
1	0.1950	0.1917	0.2120
2	0.6484	0.6534	0.6342

Similar results were obtained in experiments compared to the MATLAB simulations. The agents with greater actuation performances take greater regions than the weaker ones. Also, the estimation errors show that the HNN estimator outperforms well compared to the base method [22] which is a non-linear adaptive estimator.

Conclusion

In the paper, a coverage collaboration algorithm for non-holonomic wheeled mobile agents which learns the actuation performances of the agents by using HNNs and allocates the areas of the workspace to the agents according to their performances under localization uncertainty is introduced. The robots do not know their performances beforehand. By estimating their own performances, they perform the collaborative coverage task by minimizing the locational optimization function. Meanwhile, the GPD algorithm is used to take the positioning uncertainty of the agents into account. Also, the control law drives the robots to their optimal configurations. So, the optimal coverage is accomplished in a decentralized manner. The simulation results in MATLAB show the efficiency of the algorithm. The results are verified with field experiments done with the ROS. The algorithm provides faster convergence and a more robust estimation performance compared to the base method in the literature. Also, it takes the localization uncertainty into account coming from the localization sensors.

References

- [1] Alonso, H., Mendonça, T. and Rocha, P. Hopfield neural networks for on-line parameter estimation. *Neural Networks*, 22(4):450-462, 2009

- [2] Ansarieshlaghi, F. and Eberhard, P. Trajectory Tracking Control of a Very Flexible Robot Using a Feedback Linearization Controller and a Nonlinear Observer. In *ROMANSY 22--Robot Design, Dynamics and Control*, Springer, pp. 26-33, 2019
- [3] Atencia, M. and Joya, G. Hopfield networks: from optimization to adaptive control. In *Neural Networks (IJCNN), 2015 International Joint Conference on*, pp. 1-8, 2015
- [4] Dou, L., Song, C., Wang, X., Liu, L. and Feng, G. Coverage Control for Heterogeneous Mobile Sensor Networks Subject to Measurement Errors. *IEEE Trans. Automat. Contr.*, 63(10):3479-3486, 2018
- [5] Eberhard, P. and Ansarieshlaghi, F. Nonlinear Position Control of a Very Flexible Parallel Robot Manipulator. In *IFTToMM World Congress on Mechanism and Machine Science*, pp. 155-162, 2019
- [6] Evans, W. and Sember, J. Guaranteed voronoi diagrams of uncertain sites. In *20th Canadian Conference on Computational Geometry*, pp. 207210, 2008
- [7] Gonçalves, L. M. G., Basso, G., Dórea, C. E. T. and Nascimento, T. P. Stochastic Nonlinear Model Predictive Mobile Robot Motion Control. In *2018 Latin American Robotic Symposium, 2018 Brazilian Symposium on Robotics (SBR) and 2018 Workshop on Robotics in Education (WRE)*, pp. 19-25, 2018
- [8] Horváth, L. and Rudas, I. J. Information content driven model for virtual engineering space. *Acta Polytechnica Hungarica*, 15(2):7-32, 2018
- [9] Hu, Z. and Balakrishnan, S. N. Parameter estimation in nonlinear systems using Hopfield neural networks. *J. Aircr.*, 42(1):41-53, 2005
- [10] Janani, A., Alboul, L. and Penders, J. Multi robot cooperative area coverage, case study: spraying. In *Conference Towards Autonomous Robotic Systems*, pp. 165-176, 2016
- [11] Leitner, J. and others. Multi-robot formations for area coverage in space applications. 2009
- [12] Li, Y., Hannaford, B. and Rosen, J. The Raven Open Surgical Robotic Platforms: A Review and Prospect. *Acta Polytechnica Hungarica*, 16(8), 2019
- [13] Luna, J. M., Fierro, R., Abdallah, C. T. and Wood, J. An Adaptive Coverage Control for Deployment of Nonholonomic Mobile Sensor Networks over Time-Varying Sensory Functions. *Asian J. Control*, 15(4):988-1000, 2013
- [14] Mahboubi, H., Vaezi, M. and Labeau, F. Mobile sensors deployment subject to measurement error. In *Vehicular Technology Conference (VTC Fall), 2014 IEEE 80th*, pp. 1-6, 2014

- [15] Martiñán, D., Caballero, B. and Haber, R. Optimal tuning of a networked linear controller using a multi-objective genetic algorithm. Application to a complex electromechanical process. In *2008 3rd International Conference on Innovative Computing Information and Control*, p. 91, 2008
- [16] Mellone, A., Franzini, G., Pollini, L. and Innocenti, M. Persistent Coverage Control for Teams of Heterogeneous Agents. In *2018 IEEE Conference on Decision and Control (CDC)*, pp. 2114-2119, 2018
- [17] Michael, N. and Kumar, V. Planning and control of ensembles of robots with non-holonomic constraints. *Int. J. Rob. Res.*, 28(8):962-975, 2009
- [18] Nascimento, T. P., Dórea, C. E. T. and Gonçalves, L. M. G. Nonlinear model predictive control for trajectory tracking of nonholonomic mobile robots: A modified approach. *Int. J. Adv. Robot. Syst.*, 15(1), 2018
- [19] Nowzari, C. and Cortés, J. Self-triggered coordination of robotic networks for optimal deployment. *Automatica*, 48(6):1077-1087, 2012
- [20] Panagou, D., Stipanović, D. M. and Voulgaris, P. G. Distributed dynamic coverage and avoidance control under anisotropic sensing. *IEEE Trans. Control Netw. Syst.*, 4(4):850-862, 2017
- [21] Papatheodorou, S., Stergiopoulos, Y. and Tzes, A. Distributed area coverage control with imprecise robot localization. In *Control and Automation (MED), 2016 24th Mediterranean Conference on*, pp. 214-219, 2016
- [22] Pierson, A., Figueiredo, L. C., Pimenta, L. C. A. and Schwager, M. Adapting to performance variations in multi-robot coverage. In *Robotics and Automation (ICRA), 2015 IEEE International Conference on*, pp. 415-420, 2015
- [23] Pierson, A., Figueiredo, L. C., Pimenta, L. C. A. and Schwager, M. Adapting to sensing and actuation variations in multi-robot coverage. *Int. J. Rob. Res.*, 36(3):337-354, 2017
- [24] Pierson, A. and Schwager, M. Adaptive inter-robot trust for robust multi-robot sensor coverage. In *Robotics Research*, Springer, pp. 167-183, 2016
- [25] Pierson, A. and Schwager, M. Bio-inspired non-cooperative multi-robot herding. In *Robotics and Automation (ICRA), 2015 IEEE International Conference on*, pp. 1843-1849, 2015
- [26] Purcaru, C., Precup, R. E., Iercan, D., Fedorovici, L. O., David, R. C. and Dragan, F. Optimal robot path planning using gravitational search algorithm. *Int. J. Artif. Intell.*, 10(13 S):1-20, 2013
- [27] Razak, R. A., Sukumar, S. and Chung, H. Distributed Coverage Control of Mobile Sensors: Generalized Approach using Distance Functions. In *2018 IEEE Conference on Decision and Control (CDC)*, pp. 3323-3328, 2018

- [28] Sharifi, F., Zhang, Y. and Aghdam, A. G. A distributed deployment strategy for multi-agent systems subject to health degradation and communication delays. *J. Intell. Robot. Syst.*, 73(1-4):623-633, 2014
- [29] Slotine, J.-J.E., Li, W. and others. Applied nonlinear control. Prentice hall Englewood Cliffs, NJ, 1991
- [30] Somló, J., Varga, G. D., Zenkl, M. and Mikó, B. The ‘Phantom’ Delta Robot A New Device for Parallel Robot Investigations. *Acta Polytechnica Hungarica*, 15(4), 2018
- [31] Takács, Á., Kovács, L., Rudas, I., Precup, R.-E. and Haidegger, T. Models for force control in telesurgical robot systems. *Acta Polytechnica Hungarica*, 12(8):95-114, 2015

The Residual Variable in Decision Diagrams

Jan Lucansky, Peter Pistek, Marian Maruniak

Institute of Computer Engineering and Applied Informatics, Slovak University of Technology in Bratislava, Ilkovičova 2, 842 16 Bratislava 4, Slovak Republic,
jan.lucansky@stuba.sk, peter.pistek@stuba.sk, maruniak09@student.fiit.stuba.sk

Abstract: We propose a novel method for binary-based decision diagrams (DD) which uses a residual variable. A new type of DD – Residual Variable in decision diagram (RViDD) allows to work without the use of the lowest and the most numerous level of nodes but at the same time preserves all the fundamental characteristics of DD. Thanks to these properties, it allows the use of all existing algorithms for optimization with only slight or no modification. In this paper we present the required characteristics for providing compatibility between DD using different decompositions and RViDD as well as the exchange of residual variable without the necessity of constructing a new RViDD. Proposed method was experimentally validated on benchmark circuits with various types of experiments. We use exhaustive (all input variable combination) comparative between reduced and ordered DD and RViDD with the average improvement up to 17.55%. Since optimization of DD is a NP-complete problem, we also include the usage of evolutionary algorithm for RViDD in comparison to more effective algorithms.

Keywords: BDD; KFDD; decision diagrams; residual variable

1 Introduction

The idea to use Decision Diagrams (DDs) in computer science is a longstanding one. The widespread use of DDs started with [1] when a set of algorithms for constructing and operating on DDs as data structures was introduced. Since then, DDs have come a long way and numerous applications have been found with the byproduct of numerous forms of DDs [2]. Some of these applications, nowadays, include, but are not limited to, formal verification, logic synthesis, test generation, classification techniques or network security. One of the areas that has greatly benefited from the use of DDs is circuit design. With conventional technologies slowly approaching their physical limits and with continuous emphasis on high speed and low power requirements, the need for optimizing circuits at design level becomes more and more important and DDs are a natural way to achieve that. A good example can be found in [3] where Binary DDs (BDD) have been used to optimize logical circuits based on multiplexers (multiplexer trees) or in [4], where BDDs are used for synthesis of optical circuits. Another example of their ongoing

importance can be found in [5], where DDs are used for the design of reversible and quantum circuits. The problem of power consumption increased in importance in the last years and is usually highlighted on system level. Today, as IoT devices use many sensors, it is essential to lower energy consumption as much as possible at any level of abstraction [6]. It is worth mentioning that DDs are not the only alternative and several types of graphs can be used as SAT solvers [7].

An extensive research regarding the use of various types of DDs has already been done. Among the most popular ones are BDDs, which are based on Shannon decomposition of Boolean function. As mentioned in [8], only 2 types of decomposition have an impact on DD area reduction – Shannon and Reed-Muller (sometimes called Davio). DDs that make use of Davio decomposition, either its positive or negative form, are called Functional DDs (FDD) and a combination of both types of decomposition results in Kronecker Functional DD (KFDD). Applying reduction techniques and respecting a certain order of variables for input functions results in Reduced Ordered DD, which based on the decomposition used can result in either ROBDD, ROFDD or ROKFDD. Keeping track of these abbreviations becomes hard to remember and sometimes counterintuitive (accurately called “alphabet soup” in [2]). The need for various types of DD prevails as each type and mainly the decomposition used has its own advantages with regards to the input function. Experimental results suggest that BDDs are more suitable for reduction of control functions and KFDDs perform better with symmetric data functions. Moreover, there are many types of logic gates represented by DD, e.g. BDD nodes can be directly transformed into 2:1 multiplexers and used to construct a multiplexer tree. Several advanced techniques with various different gates can also be found in [9] and [10]. For the purpose of this paper, suppose the Reduced and Ordered notification to be implicit.

Scaling remains a major problem for all types of DD. The ordering complexity for an input function with n variables is factorial, the input Boolean function contains 2^n bits and was proven to be a NP-complete problem [11]. To be absolutely sure that the chosen order is the most suitable one for reduction, all order combinations should be tested. Several methods and heuristics from static variable ordering to complex ordering algorithms were combined with DD in order to address scaling problems. Promising results were achieved with Evolutionary Algorithms (EA), which can be used not only for area reduction, but to simultaneously focus on optimization of multiple parameters, such as Average Path Length (APL) or power consumption. APL is critical for circuit’s delay when the majority of paths have equal probability of being traversed. The delay can have the highest priority among given parameters at all levels of abstraction [12].

To further increase the number of types of DD, we propose yet another type of DD with yet another abbreviation – RViDD. This type of DD exploits the advantages of Residual variable used at the lowest level of DD and effectively decreases the complexity of $n+1$ variable input to that of n variable input by replacing one variable with an exact logic value representation. We present the experimental results achieved with a combination of Residual variable and EA.

2 Preliminaries

The input for DD is a Boolean function (B-function) $f: B_n \rightarrow B$ over a set of variables X_n denoted as $f(x_0, x_1, \dots, x_{n-1}) = y$. Variables are ordered based on significance from left to right, denoted by their index, where the order of input variables corresponds to the decreasing weights assigned to the variables from left to right, starting from the weight of 2^{n-1} for variable x_0 down to the weight of 2^0 for x_{n-1} . Any B-function f specified by its binary vector y and a fixed variable ordering can be easily expressed as a DD [3]. For easier transformation to residual function, the given B-function can be represented by modified truth table shown in Table 1.

Table 1
Modified truth table of B-function

x_1	x_2	...	x_{n-2}	x_{n-1}	y	
					x_0	$\overline{x_0}$
0	0	...	0	0	$f(2^{n-1})$	$f(0)$
0	0	...	0	1	$f(2^{n-1}+1)$	$f(1)$
0	0	...	1	0	$f(2^{n-1}+2)$	$f(2)$
.	
.	
.	
1	1	...	1	0	$f(2^n-2)$	$f(2^{n-1}-2)$
1	1	...	1	1	$f(2^n-1)$	$f(2^{n-1}-1)$

The modification of given function to a function of residual variables can be done by representing the binary vector of function as a canonical matrix (1). Such matrix [13] contains $2^{(n-1)}$ columns of two rows. Each column represents a pair of values x_0 (bottom row) and $\overline{x_0}$ (top row) of the function.

$$(B(x_0, x_1, \dots, x_{n-1})) = \begin{pmatrix} f(0) & f(1) & \dots & f(2^{n-1}-2) & f(2^{n-1}-1) \\ f(2^{n-1}) & f(2^{n-1}+1) & \dots & f(2^n-2) & f(2^n-1) \end{pmatrix} \quad (1)$$

Decomposition of B-function takes the input binary vector y of length 2^n and produces an output of 2 vectors of length $2^{n/2}$. Shannon decomposition for variable x_i effectively splits the vector in half based on the value of variable, the true half for $f_{x_i}(x)$ and the false half for $f_{\overline{x_i}}(x)$. Similarly, positive Davio decomposition outputs 2 vectors consisting of the false half and an eXclusive OR (XOR) of both halves, and negative Davio decomposes the vector into the true half and a logical XOR of both halves. Decomposition functions are shown in formula (2), (3) and Figure 1.

Variable x_i is a chosen variable with decomposition applied to it.

$$f_0 = f_{\bar{x}_i}(x); \quad f_1 = f_{x_i}(x); \quad f_2 = (f_0 \oplus f_1) \quad (2)$$

$$S = f_0 \cdot f_1; \quad pD = f_0 \oplus x_i \cdot f_2; \quad nD = f_1 \oplus \bar{x}_i \cdot f_2 \quad (3)$$

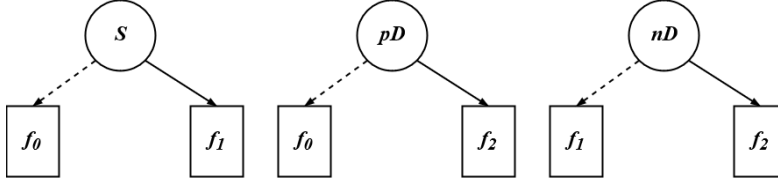


Figure 1

Three types of decompositions – Shannon (S), positive Davio (pD) and negative Davio (nD) from Formula 2 and 3

DD is a directed acyclic graph consisting of one root node, several intermediate nodes and up to two terminal nodes representing logical values true and false, usually labeled 1 and 0 respectively. Each non-terminal node is labeled by a Boolean variable x_i , depending on its position in the input order. Non-terminal nodes in unoptimized DD have one ingoing edge (with the exception of root node) and two outgoing edges labeled low and high representing the value of function f_i according to decomposition of the parent node. Each non-root non-terminal node is a root to a separate diagram called subdiagram.

DD optimization methods can be divided into two categories [14]:

1. DD ordering – results in Ordered Decision Diagram (ODD), which respects a given order of input variables. Variable ordering has a major impact on effectiveness of DD reduction.
2. DD reduction – when applied on ODD, results in Reduced ODD (ROBDD/ROKFDD) which has a lower node count than unreduced DD. Completely reduced DD represents a canonical form of DD. RODD respects three rules:
 - a. Uniqueness (Type I) – no two distinct nodes u and v represent the same variable, have the same decomposition and have the same left and right successor. Reduction is applied when $var(u) = var(v)$, $dec(u) = dec(v)$, $left(u) = left(v)$, $right(u) = right(v)$ which implies $u = v$.
 - b. Non-redundancy for Shannon node (Type S) – no variable node u has identical left and right successor. Reduction is applied when $left(u) = right(u)$.
 - c. Non-redundancy for Davio node (Type D) – no variable node u has the right successor equal to terminal node 0. Reduction is applied when $right(u) = 0$.

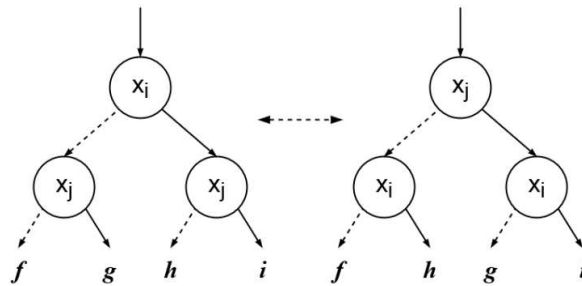


Figure 2

Exchange of adjacent variables in DD

As was already mentioned, the creation of an optimal DD has exponential increase in complexity. To further optimize a DD, an optimal input variable ordering has to be found. For circuits consisting of larger number input variables, searching the entire space of possibilities becomes unrealistic in acceptable time. Several methods were explored in ordering complexity mitigation with various degrees of reduction in final node count (size) of RODD. These methods can be separated into categories based on the complexity of underlying algorithm.

Basic methods are simple modifications in variable ordering. One such example is the exchange of adjacent variables on the same level in DD. The goal of exchanging variables at k and $k+1$ level for the DD G of function f is to transform G to DD G' of function f . The only difference between variable ordering π and π' is only at levels k and $k+1$ and can be expressed as $\pi(k) = \pi'(k+1)$ and $\pi(k+1) = \pi'(k)$. Exchange of adjacent variables does not affect the upper and lower levels in DD and is illustrated in Figure 2 [15].

In heuristic methods, the ordering of variables will be determined according to the information available about the issue before the construction of DD itself. Force algorithm [15] belongs among the best known algorithms in this category. The idea behind Force is simple - the algorithm computes the forces acting upon each variable and displaces the variables in the direction of the forces acting upon them. In Force, a CNF formula is viewed as a hypergraph, where the formula's variables correspond to vertices and clauses correspond to hyperedges. The algorithm itself determines two values during execution and iteratively uses them to order the variables. Another heuristic method [16] is based on the proven assumption that the number of nodes in a particular level of DD depends only on the arrangement of variables at lower levels. The algorithm of this method sequentially places all the variables to the first level and determines to which of them it received the least number of nodes. This variable (or several variables) is saved for the chosen level and the remaining variables are tested at upper levels. This process is repeated until the final DD is obtained. Algorithm complexity remains exponential, but provides better parameters than iterating through all possible variable orderings.

The third and final category consists of alternative methods based on evolutionary algorithms (EA). EA belong to a state-of-art in optimization algorithms. The core term of EA is population, which represents a set of chromosomes. Chromosome can be either the input order of variables or decompositions represented as a vector of genes, such as $\{x_0, x_5, x_6, x_3, x_2, x_1, x_4, x_7\}$. In this case, each gene is a variable in particular order (chromosome) of given population of orders. A population of a specific stage of EA is called generation. Initial population, or the first generation, is created using randomly generated chromosomes, which are then sorted through based on their fitness value to form a new generation.

After creating a population, a fitness value is calculated for each chromosome. The underlying algorithm of fitness calculation depends on the targeted problem. An example of multi-parametric fitness formula can be seen in (4) where A_r , P_w and A_p are the coefficients setting percentage weights of optimized parameters and their sum $A_r + P_w + A_p$ should be equal to 1 at all the times. The formula also contains 3 parameters (area, power consumption and APL) that have their orderings normalized to range $(0, 1)$.

$$fitness = A_r \times area_normalized + P_w \times power_normalized + A_p \times apl_normalized \tag{4}$$

Most fit chromosomes, then have a certain probability of genetic operations being applied to them to increase the diversity of current generation and decrease the chance of getting stuck in a local optimum. Some forms of EA also introduce a technique called elitism which ensures the preservation of the best chromosomes across generations in order to make sure subsequent generations never provide worse, and therefore useless, results than the previous generations.

Chromosomes of the current generation are selected based on their fitness value. At this point, EA starts to populate a new generation by selecting chromosomes from current generation and applying genetic mutation and crossover. A genetic mutation in vector of variables (chromosome) is to invert a random gene in chromosome. This operation is implemented as a swap of the variable on a random position and the variable positioned on the complementary position. For example, a mutation in chromosome of length 8, at position 2, is illustrated in Figure 3.

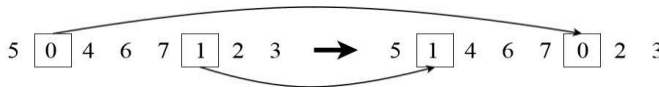


Figure 3
Mutation example

The second genetic operation called crossover causes two selected chromosomes to be cut at the same randomly chosen point and exchange their segments. In some variations, two points can be randomly selected in one chromosome and the

segment between these two points is then replaced with the segment on the same position in paired chromosome. Since a simple exchange of the parts of variable orderings can violate the uniqueness of each variable, this operation usually has to be corrected. Variables that are already present in the unchanged part of chromosome are replaced with unused variables. Crossover is illustrated in Figure 4, where variable 5 in the first chromosome and variable 6 in the second were corrected.

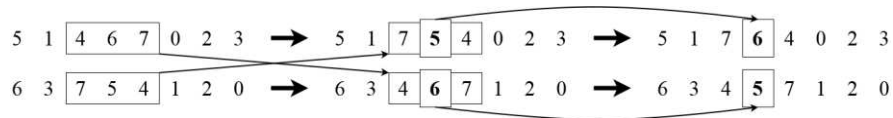


Figure 4

Crossover example

EA starts with the creation of a new population (in this work we also reuse previous generations several times) and keeps applying mutation and crossover on selected chromosomes with predefined probability. The size of population as well as the probability of EA operations are a subject to research themselves and can vary depending of the application of EA.

Several variations of EAs exist. For example, Particle Swarm Optimization (PSO) [17] is a population-based stochastic technique inspired by social behavior of bird flocking or fish schooling. In PSO, the potential solutions called particles fly through the problem space by following the current optimum particles. Particles learn from their past experiences, learn from experience of others and finally converge near the solution, which may be the best or a suitably good solution after satisfying a definite termination criterion. The particles sense their proximity to a good solution using a fitness function [18]. Another variation of EA with interesting results is modified memetic algorithm (MMA) [18]. The key feature of MMA is the use of various techniques of local search. While the gene that passes on the offspring cannot be changed (except for mutations) in the classic EA, memes transmit information among themselves so as to best suit the evaluation function (for example through local searches) in MMA which happens through knowledge of the solution's local space.

All the previously mentioned, algorithms share the same feature, which is that they primarily focus on size reduction. Number of nodes in DD is directly proportional to the size of represented circuit and has impact on other parameters as well, e.g. if the DD (and most notably BDD) is used as representation of a multiplexer tree, each node corresponds to a multiplexer and the dynamic power consumption of entire circuit can be easily estimated [19].

3 Residual Variable

If n variable B-function is to be implemented using the complexity of DD with $n-1$ variables, one of the input variables must to be available in both direct and complemented form. The input variable order has to be modified in a way where this particular variable has the highest weight in binary vector.

Definition 1 – If the presences in a function of n variables are identified (e.g. by their order in truth table), it is possible to assign a weight to these variables. The variable with the highest weight can then be removed from the vector of variables and replaced with logic value in direct and complemented form. Such variable is called a *residual variable* (RV). An arbitrary variable may be a RV if it is available both in direct and complemented form, otherwise the transformation of RViDD to a specific circuit would require an additional NOT logic gate.

Definition 2 – If RV is identified in a function of n variables, the circuit representation of this function can be transformed into a circuit representation of function with $n-1$ variables where the RV is connected to the data input.

Definition 3 – DD for the function f with n variables is called RViDD (Residual Variable in DD), if one variable is the residual variable and it is also a terminal node of RViDD.

To create a DD with $n-1$ variables, the existing procedure repeats decomposition until it reaches the level defined by the formula 5 with chosen variable x_n

$$f_{x_{n-1}=c}(x_0, \dots, x_{n-1}) := f((\text{vector } n-1), c) \quad (5)$$

In formula 5, c is a constant, $x_{n-1} = c$, ($c \in \{0, 1\}$) and *(vector $n-1$)* contains corresponding substitution of 0s and 1s according to the given order of variables x_0, \dots, x_{n-1} in the upper levels of DD and its particular propagation path. for given variables x_0, \dots, x_{n-1} is obtained.

In the case where the decomposition of input function is stopped one iteration earlier, formula 5 is transformed into formula 6.

$$f_{x_{n-2}=c}(x_0, \dots, x_{n-2}, x_{n-1}) := f((\text{vector } n-2), c, x_{n-1}) \quad (6)$$

In formula 6, c is a constant, $x_{n-2} = c$, ($c \in \{0, 1\}$) and *(vector $n-2$)* contains corresponding substitution of 0s and 1s according to the given order of variables x_0, \dots, x_{n-2} in the upper levels of DD and its particular propagation path. It is possible by using this method to achieve up to four final states, or rather substitution rules, which depend on the value c and x_{n-1} . Substitution rules take 2 input values and provide 1 output value, which represents RV, as shown in Table 2, where v_1 represents $f((\text{vector } n-2), x_{n-1})$, v_2 represents $f((\text{vector } n-2), \overline{x_{n-1}})$ and u_i represents value of i -th leaf in RViDD.

Table 2
Substitution rules for residual functions

Rule	v_1	v_2	u_i
0	0	0	0
1	0	1	x_{n-1}
2	1	0	$\overline{x_{n-1}}$
3	1	1	1

Using formula (2), (3) and rules in Table 2, final states of RV obtained with every decomposition are shown in Table 3 for any chosen residual variable (x_i).

Table 3
Final states of residual variable x_i for every decomposition

f_0	f_1	f_2 ($f_0 \oplus f_1$)	Function value			Final state		
			S	pD	nD	S	pD	nD
0	0	0	0.0	$0 \oplus x_i, 0$	$0 \oplus \overline{x_i}, 0$	0	0	0
0	1	1	0.1	$0 \oplus x_i, 1$	$1 \oplus \overline{x_i}, 1$	x_i	x_i	x_i
1	0	1	1.0	$1 \oplus x_i, 1$	$0 \oplus \overline{x_i}, 1$	$\overline{x_i}$	$\overline{x_i}$	$\overline{x_i}$
1	1	0	1.1	$1 \oplus x_i, 0$	$1 \oplus \overline{x_i}, 0$	1	1	1

Example 1: Suppose the input B-function f_i with 4 variables in given order $f_i(x_2, x_0, x_1, x_3) = 1000010001011011$ where variable x_2 is chosen as RV. For simplicity, only Shannon decomposition is used. Truth table and its modified version for f_i are shown in Table 4. Results in column y can be expressed as a canonical matrix B_i of resulting values (7). The first row represents vector v_1 from Table 2 and the second row represents values from vector v_2 .

$$(B_i(x_2, x_0, x_1, x_3)) = \begin{vmatrix} 1 & 0 & 0 & 0 & 0 & 1 & 0 & 0 \\ 0 & 1 & 0 & 1 & 1 & 0 & 1 & 1 \end{vmatrix} \tag{7}$$

Using substitution rules in Table 2, canonical matrix (7) can be expressed as a vector Z_i of residual functions (8). Notice that the length of vector Z_i is half the length of input vector f_i . Same steps apply for all decomposition types (Table 3).

$$(Z_i(x_2, x_0, x_1, x_3)) = (\overline{x_2}, x_2, 0, x_2, x_2, \overline{x_2}, x_2, x_2) \tag{8}$$

3.1 Replacement of Residual Variable

Since RViDD is a new type of DD, it is important to maintain properties for basic reduction rules in order to reuse existing reduction and optimization algorithms developed mainly for BDD or KFDD. As a consequence, main features of DD

with any type of decomposition are preserved and the DD can be directly compared to RViDD in terms of various factors, such as size (node count).

Table 4
Modified truth table for f_i from Example 1

x_2	x_0	x_1	x_3	y
0	0	0	0	1
0	0	0	1	0
0	0	1	0	0
0	0	1	1	0
0	1	0	0	0
0	1	0	1	1
0	1	1	0	0
0	1	1	1	0
1	0	0	0	0
1	0	0	1	1
1	0	1	0	0
1	0	1	1	1
1	1	0	0	1
1	1	0	1	0
1	1	1	0	1
1	1	1	1	1

→

x_0	x_1	x_3	y	
			x_2	$\overline{x_2}$
0	0	0	0	1
0	0	1	1	0
0	1	0	0	0
0	1	1	1	0
1	0	0	1	0
1	0	1	0	1
1	1	0	1	0
1	1	1	1	0

Transformation of DD node at the first level to RViDD node is done according to rules in Table 3 where the residual functions are replaced with corresponding final state of RV (Figure 5). This transformation applies to all decompositions since their final states are equal for each input. Upper levels of RViDD remain unchanged and identical to their DD counterpart.

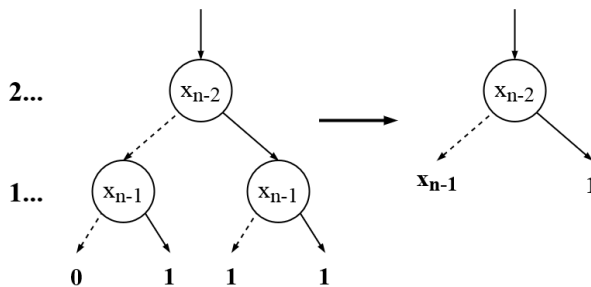


Figure 5
Example of transformation of DD node to RViDD node

An important feature in reduction, is the exchange of adjacent variables. Although the exchange itself is not very efficient, it serves as the basis for many algorithms. If adjacent variables are exchanged (levels i and j) then variable ordering of given function is modified from $f(x_0, \dots, x_i, x_j, \dots, x_{n-1})$ to $f(x_0, \dots, x_j, x_i, \dots, x_{n-1})$ without disrupting upper and lower levels. This approach remains unchanged if none of the variables is positioned at the first level, i.e. none of the variables is a RV.

Replacing RV with another variable requires a few more steps. While terminal nodes in DD can only have 2 values $\{0,1\}$, which lead up to 4 possible states $\{00,01,10,11\}$, RViDD has 4 values $\{0,1, x_i, \overline{x_i}\}$, which lead up to 16 possible states. Exchanging residual variable therefore has to follow rules in Table 2 and the final state after exchange can be achieved by simply deconstructing the RV into B-functions, swap the variables as in DD and construct RViDD again by substituting the terminal level functions with newly chosen RV. Rules for exchanging RV are shown in Table 5, where only different outcomes are displayed, rules with identical outcomes or outcomes where RV is simply replaced by a new one (while maintaining position and negation of RV) are omitted.

Table 5
Rules for exchanging residual variable

Before exchange	After exchange	Before exchange	After exchange
Binary vector (v_1, v_2, v_3, v_4)	Binary vector (v_1, v_3, v_2, v_4)	Values (u_1, u_2)	Values (u'_1, u'_2)
00,10	01,00	$0, \overline{x_i}$	$x_j, 0$
00,11	01,01	$0, 1$	x_j, x_j
01,00	00,10	$x_i, 0$	$0, \overline{x_j}$
01,01	00,11	x_i, x_i	$0, 1$
10,10	11,00	$x_i, \overline{x_i}$	$1, 0$
10,11	11,01	$\overline{x_i}, 1$	$1, x_j$
11,00	10,10	$1, 0$	$\overline{x_j}, \overline{x_j}$
11,01	10,11	$1, x_i$	$\overline{x_j}, 1$

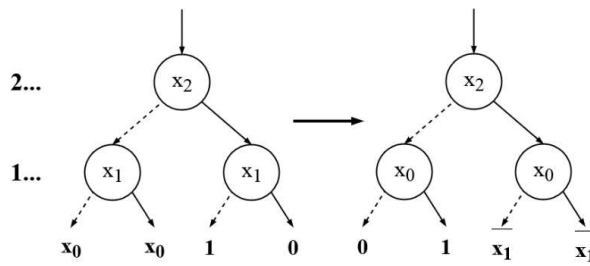


Figure 6
Replacement of residual variable in RViDD

Replacing RV allows the modification of existing RViDD, which is more efficient than constructing a new one with a different RV. Since the replacement of RV needs to perform more operations than a common exchange of variables at adjacent levels in DD, it can be used in conjunction with basic methods to find the variable that appears to be most suitable for the position of RV. Although it requires more steps, this appears to be the only drawback in computation time of synthesis in RViDD. Example of RV replacement is shown in Figure 6.

3.2 RViDD Construction

Important advantage of RV is the fact that the final states (Table 3) are equal for every decomposition. This automatically preserves the ability to apply reduction rules to nodes in RViDD. Reduction rule I can still be applied to any 2 nodes with 2 identical successors. Reduction rule S can be used on any Shannon node that has 2 identical successors, even if both of them are RV, e.g. the right successor of x_2 node in RViDD in Figure 6. Reduction rule D applies to any Davio node whose right successor is equal to terminal value 0.

Example 2: Suppose the input B-function f_2 with 4 variables $f_2(x_2, x_1, x_3, x_0) = 0101011010011001$. Unreduced BDD for f_2 is shown in Figure 7.

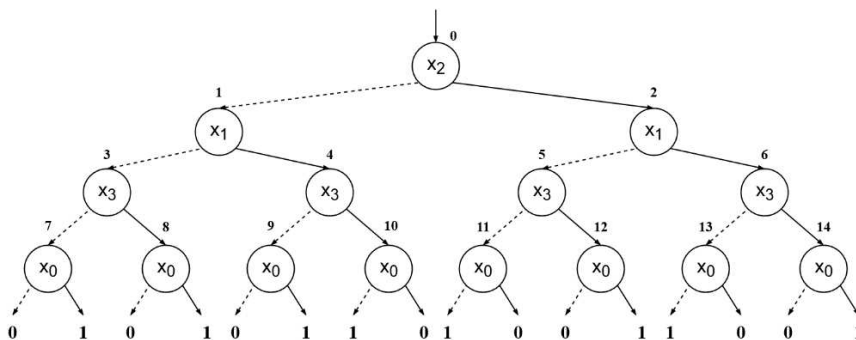


Figure 7
BDD for f_2 from Example 2

Variable x_0 is chosen as RV. Following the same steps presented in Section 2 - Example 1, a modified truth table is constructed with vector of residual functions Z_2 (9). For simplicity, only Shannon decomposition is used. Unreduced RViBDD for f_2 is shown in Figure 8. Recursively applying reduction rules results in reduced RViBDD shown in Figure 9.

$$(Z_2(x_2, x_1, x_3, x_0)) = (x_0, x_0, x_0, \overline{x_0}, \overline{x_0}, x_0, \overline{x_0}, x_0) \quad (9)$$

Figure 7 shows all nodes for the complete unreduced DD. With top-to-bottom construction approach (synthesis) of DD, reduction rule I can be applied on any node which shares characteristics with an already existing node – the same level, variable, decomposition and identical successors. This eliminates the need to synthesize entire subdiagram of the reduced node.

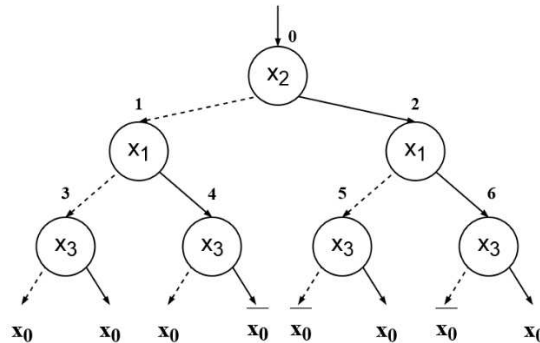


Figure 8

Unreduced RViBDD for f_2 from Example 2

From Figure 7 and 8 it can be seen that RViBDD has half the node count of BDD thanks to omitting the most numerous first level and replacing it with RV. Reducing RViBDD is subject to the same reduction approach as DD but with lower node count, therefore the time of reduction should be, in theory, halved.

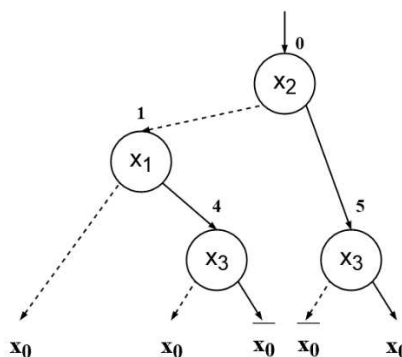


Figure 9

Reduced RViBDD for f_2 from Example 2

Constructing RViDD follows the same steps as a regular DD construction with any decomposition. Thanks to properties of RV, reduction rules remain unchanged and can be applied equally to DD and RViDD, which makes RV an important contributor to size reduction in binary-based DDs. For DDs using only Shannon decomposition, terminal values can be directly derived and the input B-function can be immediately replaced with vector of residual functions, even before DD construction. Thus the construction cost is minimized right after ordering phase. Davio decompositions have a slight disadvantage, since the terminal values cannot be directly estimated from the input function. The DD has to be constructed first and only once the state of the first level is known can the RV be applied. Although it has virtually no impact on construction time, it still lowers the number of nodes to check for reduction rules by removing the most numerous level.

4 Experimental Results

The advantages RV brings to DD optimization were verified on benchmark circuits LGSynth'93 [20]. The use of RV shows significant improvement in size reduction as well as the expected improvement in synthesis time. As was already mentioned in Section 3.2, RV effectively halves the size of DD and therefore lowers the number of nodes that need to be checked for reduction suitability in each iteration. Table 6 shows results achieved using only Shannon decomposition so the use of different decomposition methods does not obscure the actual impact of RV itself. Columns BDD and RViBDD show the number of nodes of reduced and ordered DD and columns Size imp. and Time imp. indicate the improvement in size and synthesis time respectively. Benchmarks marked with * used n orders instead of $n!$, where n is the number of variables.

The average improvement in time needed for synthesis of reduced and ordered RViBDD compared to BDD is 40.7% and in some cases rises up to 81.38%. The size reduction shows improvement between 6.06% and 33.33%. It is important to mention the possibility where the initial check on the most numerous level will not apply any RV and the computation time may slightly increase. As can be seen, this does not happen often and average computation time is lower in almost every case. Presented results were achieved using a new algorithm that combines RV, basic reduction rules and EA with following parameters:

- Check all possible orders and decomposition for functions with < 8 input variables
- Population size: 500 (< 12 input variables), 200 (≥ 12 and < 21 input variables) or 100 (≥ 21 input variables)
- Crossover probability: 80%
- Mutation probability: 20%

- Elitism: 1%
- Iterations (population count): 100

Table 6
Residual variable impact on BDD

Benchmark	BDD	RViBDD	Size imp. [%]	Time imp. [%]
parity*	31	29	6.45	-
cm151a*	44	30	31.82	-
cm152a*	21	14	33.33	-
sao2	103	96	6.8	45.13
9sym	33	31	6.06	41.28
sqrt8	35	32	8.57	40.45
rd84	71	64	9.86	43.13
misex1	62	49	20.97	20.41
Inc	96	81	15.63	43.15
5xp1	76	59	22.37	34.94
xor5	9	7	22.22	30.64
con1	15	12	20	81.38
squart5	47	34	27.66	31.64
rd53	29	24	17.24	39.41
majority	7	6	14.29	29.23
Average	45.27	37.87	17.55	32.05

The overall percentage improvement in size reduction in RViDD for chosen benchmarks is shown in Table 7. Columns *S*, *pD* and *nD* show the improvement of reduced and ordered RViDD against unreduced and unordered DD with the respective decomposition. Column *RViKFDD* shows the improvement when all 3 decompositions are combined with RV. It is obvious that the combination of all decomposition methods provides the best results with average of 87.24% in comparison to single decomposition used. RViKFDD takes advantage of EA not only for population of orders, but for vector of decompositions as well (each variable has exactly 1 decomposition assigned) using the same parameters mentioned above with 2 exceptions – no fitness function and no elitism.

Table 7
Residual variable impact on size reduction in [%] with various decompositions

Benchmark	S	pD	nD	RViKFDD
misex1	89.64	85.62	89.43	90.7
Inc	92.02	89.46	89.66	92.12
5xp1	90.13	87.58	87.58	90.92
xor5	77.42	80.65	80.65	87.1
con1	87.23	84.04	85.11	88.3
squart5	86.29	85.48	84.27	87.5

rd53	74.19	78.49	78.49	80.65
majority	80.65	77.42	77.42	80.65
Average	84.70	73.59	84.08	87.24

Table 8
Comparison of various algorithms in size reduction

Benchmark	BDD	RViBDD	RViKFDD	PSO	MMA	Sifting
cordic	209	144	102	105	-	93
cm150a	32	31	31	32	-	33
mux	32	31	31	32	-	33
cm151a	32	30	29	32	-	34
sao2	103	96	96	91	85	92
9sym	33	31	25	-	33	33
sqrt8	35	32	31	33	33	42
rd84	71	64	46	-	59	59
misex1	62	49	44	36	36	41
Inc	96	81	80	79	61	68
5xp1	76	59	56	68	68	82
con1	15	12	11	16	15	18
squar5	47	34	31	37	37	38
rd53	29	24	18	-	23	23

Subsequent generations of decomposition chromosomes were chosen randomly. Choosing the fitness of a certain decomposition is dependent on the input function and order of variables, which is not known during population creation.

Newly proposed algorithm with RV was compared in matter of size with PSO, MMA and Sifting, a method presented in [21]. This comparison is shown in Table 8 (using the same EA parameters as in Table 6). Column BDD shows reduced and ordered BDD and is a clear indication that on its own, the Shannon decomposition is not sufficient enough to achieve optimal results. Columns RViBDD and RViKFDD show reduced and ordered results for their respective DD with RV applied. It is again proved that a combination of all decompositions provides better results than using a single decomposition. Applying RV provides improvement not only in comparison to BDD, but also to other current methods in field. Combination of RV and several decompositions shows better results in 10 out of 14 cases.

RV improvement in multi-parametric optimization of underlying circuits is shown in Table 9. Since the number of nodes has usually the highest priority among all parameters, input values for fitness functions were chosen accordingly:

- Number of nodes: 98%
- Average Path Length (APL): 1%
- Power Consumption (PC): 1%

Achieved results could be optimized in other ways choosing different parameter, e.g. if power consumption holds a higher level of importance in comparison to area of circuit, its impact value could be higher and that of a size parameter could be lower (the sum always has to add up to 100%).

Table 9

RV impact on Power Consumption and Average Path Length using Shannon decomposition

Benchmark	In	Out	Size	PC min.	PC max.	PC diff.	APL min.	APL max.	APL diff.
cordic	23	2	144	28.36	30.38	6.66	11.75	14.09	16.63
cm150a	21	1	31	11.63	15.38	24.39	3.06	4.13	25.85
mux	21	1	31	15.38	15.38	0	3.06	3.06	0
t481	16	1	36	14.86	14.86	0	4.15	4.15	0
parity	16	1	29	14.5	14.5	0	15	15	0
cm151a	12	2	30	11.25	14.75	23.73	5.25	6.5	19.24
cm152a	11	1	14	7	7	0	3.25	3.25	0
sao2	10	4	96	23.52	28.88	18.54	10.33	12.36	16.44
9sym	9	1	31	10.22	11.22	8.92	7.13	8.13	12.31
sqrt8	8	4	32	13.43	14.23	5.65	9.94	11.31	12.15
rd84	8	4	64	24.52	24.52	0	22.36	22.36	0
misex1	7	7	49	18.91	20.44	7.49	16.75	19.06	12.13
inc	7	9	81	30.06	33.27	9.63	20.75	25.16	17.52
5xp1	7	10	59	27.82	29.5	5.69	21.66	23.34	7.23
con1	6	2	12	5.26	5.26	0	4.25	4.56	6.85
xor5	5	1	7	3.5	3.5	0	4	4	0
squar5	5	8	34	13.7	14.65	6.5	15.38	17	9.56
rd53	5	3	24	10.1	10.1	0	11.25	11.25	0

Columns In, Out and Size represent the number of inputs and outputs for each benchmark and the size of RViBDD (only Shannon decomposition was used in this table). Columns PC min., PC max. and PC diff. display the minimal and maximal achievable power consumption (PC) and their difference in [%]. PC is shown in relative value independent of technology used in circuit synthesis and is directly proportional to the number of switches performed in circuit. This value was estimated based on formulas presented in [19]. The final trinity of columns marked as APL min., APL max. and APL diff. display the minimal and maximal achievable values for APL and their difference in [%]. The highest achieved improvement was 24.39% in PC and 25.58% in APL, while the average improvement for all tested benchmarks comes down to 6.24% in PC and 9.47% in APL. It can be observed that symmetric functions have little to no improvement in both parameters due to limited changes in structure of DD during variable reordering.

Conclusions

We have proposed a novel solution for the optimization of binary-based Decision Diagrams (DD), by introducing new type of DD. Our RViDD (Residual Variable in Decision Diagrams) uses one input variable as a residual variable which can be utilized as another type of a terminal node. Thanks to this modification, the optimized RViDD has almost half the nodes, compared to unoptimized DD with the same variable ordering.

We proved that the same basic reduction rules can be used as well for RViDD as for DD without any modification. Another well-known rule – exchange of adjacent variables – remains also applicable with only a small modification in the level of terminal nodes. We called this procedure “replacement of residual variable” where residual variable (RV) can be replaced by any other input variable which might prove to be necessary during optimization phase. Replacement of RV leads up to 16 different possible states (compared to 4 in DD) out of which only 8 lead to other than simple 1:1 swapping of the old RV for a new one.

During experimental phase we chose several known types of DD (BDD, FDD, KFDD) and created their equivalents with residual variable (RViBDD, RViFDD, RViKFDD). Our focus was on comparison of three parameters, primarily on number of nodes, but also on energy consumption and average path length (APL). In average our solution (residual variable in DD) has 17.55% less nodes than the solution without residual variable. Because RV can change the most suitable decomposition for given benchmark circuit, a test comparing its impact on various decompositions is presented. It is not a surprise that the best solution is based on RViKFDD which uses all types of decompositions. Based on the previous experiment, we were able to tell that residual variable is suitable for all types of decomposition, because there were no exceptions (results with smaller improvement).

We also tried to use more complicated optimization process by involving evolutionary algorithm. We compared it with Sifting method (as reference), Particle swarm optimization (PSO) and Modified memetic algorithm (MMA). Even though evolutionary algorithm is not superior for PSO and MMA in every case, our solution (RViBDD) was better in 8 cases (10 for RViKFDD) out of 14 benchmarks with improvement up to 22.51%. This proves the impact residual variable has in optimization process.

The Residual variable also shows the positive impact on multi-parametric optimization (number of nodes, power consumption and Average Path Length (APL)). In average, dynamic power consumption of any underlying circuit should be decreased by 6.24%. This is achieved by lowering the number of switches performed in the circuit when traversing the diagram. APL improvement moves around 9.47% for all tested benchmarks, which also shows RV can (positively) affect the symmetry of the circuit, should it be one of the desired attributes.

While all the presented results display a positive influence of residual variable on DD optimization, there is still room for improvement. One such case would be to introduce the logic of Free DDs [22] where the rule that each path from root to terminal nodes has to follow the same order of variables is relaxed. Although this greatly increases the complexity of the used algorithm, it is expected to bring an even further decrease, in all observed parameters.

Acknowledgement

This work was supported by the Cultural and Educational Grant Agency of the Slovak Republic (KEGA 011STU-4/2017) and ITMS 26240220084.

References

- [1] R. Bryant, "Graph-Based Algorithms for Boolean Function Manipulation," in *IEEE Transactions on Computers*, Vol. C-35, No. 8, pp. 677-691, Aug. 1986, doi:10.1109/TC.1986.1676819
- [2] R. E. Bryant, "Binary decision diagrams and beyond: enabling technologies for formal verification," *Proceedings of IEEE International Conference on Computer Aided Design (ICCAD)*, San Jose, CA, USA, 1995, pp. 236-243, doi:10.1109/ICCAD.1995.480018
- [3] P. Pistek, "New multiplexer-based switching circuits synthesis methods." in *Information Sciences and Technologies*, Vol. 7, No. 1, pp 19-27, 2015
- [4] A. Deb, et al, "Synthesis of Optical Circuits Using Binary Decision Diagrams." *Integration*, Vol. 59, pp. 42-51, May 2017, doi:<https://doi.org/10.1016/j.vlsi.2017.05.001>
- [5] R. Wille, P. Niemann, A. Zulehner and R. Drechsler, "Decision diagrams for the design of reversible and quantum circuits," *2018 International Symposium on Devices, Circuits and Systems (ISDCS)*, Howrah, 2018, pp. 1-6, doi:10.1109/ISDCS.2018.8379626
- [6] *Technology Roadmap for Semiconductors: Design. 2015:* <https://www.semiconductors.org/resources/2015-international-technology-roadmap-for-semiconductors-itrs/> (accessed June 1, 2016)
- [7] B. Nagy, "Optimal Boolean Programming with Graphs." in *Acta Polytechnica Hungarica*, Vol. 16, No. 4, 2019, doi:10.12700/APH.16.4.2019.4.12
- [8] B. Becker and R. Drechsler, "How many decomposition types do we need? [decision diagrams]," *Proceedings the European Design and Test Conference. ED&TC 1995*, Paris, France, 1995, pp. 438-443, doi:10.1109/EDTC.1995.470359
- [9] L. Amarú, P. Gaillardon and G. De Micheli, "Majority-Inverter Graph: A New Paradigm for Logic Optimization," in *IEEE Transactions on Computer-Aided Design of Integrated Circuits and Systems*, Vol. 35, No. 5, pp. 806-819, May 2016, doi: 10.1109/TCAD.2015.2488484
- [10] L. Amarú, P. Gaillardon and G. De Micheli, "BDS-MAJ: A BDD-based logic synthesis tool exploiting majority logic decomposition," *2013 50th*

- ACM/EDAC/IEEE Design Automation Conference (DAC), Austin, TX, 2013, pp. 1-6, doi: 10.1145/2463209.2488792
- [11] B. Bollig and I. Wegener, "Improving the variable ordering of OBDDs is NP-complete," in *IEEE Transactions on Computers*, Vol. 45, No. 9, pp. 993-1002, Sept. 1996, doi: 10.1109/12.537122
- [12] R. Gerov, Z. Jovanovic, "Parameter Estimation Method for the Unstable Time Delay Process." In *Acta Polytechnica Hungarica*, Vol. 16, No. 3, 2019, doi: 10.12700/APH.16.3.2019.3.6
- [13] P. Pistek, M. Kolesar and K. Jelemenska, "Optimization of multiplexer trees using modified truth table," 2010 International Conference on Applied Electronics, Pilsen, 2010, pp. 1-4
- [14] R. Ebdndt, G. Fey, R. Drechsler, "Advanced BDD Optimization" (1. ed.). Netherlands: Springer, 2005, 222p, ISBN 978-0-387-25453-, doi: 10.1007/b107399
- [15] M. Rice, S. Kulhari, "A Survey of Static Variable Ordering Heuristics for Efficient BDD/MDD Construction". University of California, CA, USA, Tech. Rep., 2008 [Online] Available: shorturl.at/cCGMR
- [16] S. J. Friedman and K. J. Supowit, "Finding the optimal variable ordering for binary decision diagrams," in *IEEE Transactions on Computers*, Vol. 39, No. 5, pp. 710-713, May 1990, doi: 10.1109/12.53586
- [17] A. Mitra and S. Chattopadhyay, "Variable ordering for shared binary decision diagrams targeting node count and path length optimisation using particle swarm technique," in *IET Computers & Digital Techniques*, Vol. 6, No. 6, pp. 353-361, November 2012, doi: 10.1049/iet-cdt.2011.0051
- [18] S. Rehan, M. Bansal, "Performance Comparison among Different Evolutionary Algorithms in terms of Node Count Reduction in BDDs" in *International Journal of VLSI and Embedded Systems*, Vol. 4, pp. 491-496, July 2013
- [19] R. Marcolescu, R. Marcolescu, M. Pedram, "Efficient Power Estimation for Highly Correlated Input Streams," 32nd Design Automation Conference, San Francisco, CA, 1995, pp. 628-634, doi: 10.1145/217474.217601
- [20] K. McElvain, "LGSynth93 Benchmark Set: Version 4.0", 1993. Distributed by NC State University. Available: <https://ddd.fit.cvut.cz/prj/Benchmarks/IWLS93.7z>
- [21] R. Rudell, "Dynamic variable ordering for ordered binary decision diagrams," *Proceedings of 1993 International Conference on Computer Aided Design (ICCAD)*, Santa Clara, CA, USA, 1993, pp. 42-47, doi: 10.1109/ICCAD.1993.580029
- [22] J. Bern, J. Gergov, C. Meinel and A. Slobodova, "Boolean manipulation with free BDD's. First experimental results," *Proceedings of European Design and Test Conference EDAC-ETC-EUROASIC*, Paris, France, 1994, pp. 200-207, doi: 10.1109/EDTC.1994.326915

Predictive Control of Switched Reluctance Motors for Aircraft Electrical Actuators Applications

Reyad Abdel-Fadil^{1,2}, László Számel¹

¹Budapest University of Technology and Economics, Department of Electric Power Engineering, Egry József u. 18, H-1111 Budapest, Hungary

²Aswan University, Electrical Engineering Department, Abu El-Reish Qebly, Aswan Faculty of Engineering st., 81542 Aswan, Egypt
Reyad.abdelfadil@aswu.edu.eg, szamel.laszlo@vet.bme.hu

Abstract: Aircraft applications require high reliability, high availability, and high power density, while aiming to decrease weight, complexity, fuel consumption, operational costs, and environmental impacts. Modern electric driving systems can meet these demands and provide significant technical and economic enhancements over traditional mechanical, hydraulic, or pneumatic systems. Due to the high reliability of Switched Reluctance Motors (SRMs), it can be used for aircraft electromechanical actuators to replace the conventional actuators. This paper presents Model Predictive Control (MPC) for the actuators system to drive flight control surfaces in modern civil aircraft. In this study, the actuators system with nonlinear SRM is modeled, simulated, and controlled using a predictive control technique. The predictive control algorithm is applied for a three-phase controlled rectifier to provides a fixed DC voltage for actuators supply bus, and for SRM's symmetrical power converter to drive the surface of the actuator. The performance of the proposed system is tested using a simulation model in PSIM software, and the controller is programmed using C language. Obtained results confirm the effectiveness of the suggested system to drive aircraft electromechanical actuators satisfactorily for either tracking demanded motor speed or desired actuator deflection angle.

Keywords: Switched Reluctance Motor; Model Predictive Control; Current Control; More Electric Aircraft; Aircraft Electrical Actuators

1 Introduction

In recent years, electrically powered equipment in the aerospace industry is increasing, these types of aircraft referred to as "More Electric Aircraft" (MEA) [1-3]. Although this trend has many benefits such as reliability, aviation safety, efficiency, and improved aircraft maintenance capability, it faces some challenges that must be overcome such as power supply for high-power electrical equipment

and high-performance motors for electric actuation systems, and power converters with high accuracy controllers. Aircraft actuators are used to control the aircraft during take-off, flight, landing, and taxi by moving the flight control surfaces (rudder, aileron, and spoiler). The flight control surfaces actuators of the conventional civil aircraft are powered through three independent hydraulic systems, that are considered complex to install and costly to maintain. Therefore, modern aircraft use high-power electrical actuators with ratings of up to 50 kW to solve the hydraulic system's problems [4], and the concept of replacing the hydraulic systems with electrical systems has been associated with MEA concept. Previous and recent studies and research have confirmed that MEA provides aircraft manufacturers and operators with significant cost benefits due to reductions in system complexity and overall weight of the aircraft [5]. The flight actuators can be divided into two main technologies: the first is Fly-By-Wire (FBW) in this technology, actuators are powered hydraulically but controlled by electrical signals. The second is Power-By-Wire (PBW), where the flight actuators are powered and controlled using electrical power [1].

The control surfaces of large conventional civil aircraft such as Airbus (A320) and Boeing (B777) are hydraulically actuated, and most of these actuators are controlled by an electrical signal (FBW technology). But hydraulic systems are expensive, and their weight contributes to most fuel consumption. Therefore, many research and development activities have proposed various systems and components as a solution to replace hydraulic power with electric power aims to reduce the overall weight of the system, reduce complexity, and increase efficiency. Recently, with the developments in high-performance motors, power electronics devices, and control techniques, the use of electrically powered actuators (PBW technology) has gradually increased in civil aircraft. Electrically powered actuators can be divided into two main configurations: the first is Electro-Hydrostatic Actuator (EHA) with fluidic gearing between the motor and the actuated surface, the second is the Electro-Mechanical Actuator (EMA) with mechanical gearing [6], the EHA and EMA configurations will be discussed in Sections 2.

Electric actuators system can be operated efficiently by using high-performance electric motors with a suitable power converter and optimal control strategy. There are many types of electric motors that can be used to drive the flight control actuators such as DC motor which introduced in [7, 8]. Recently, the researches tended to use different types of electric motors with the application of advanced control strategies to reduce the cost, overcome the disadvantages of traditional methods, and improve the overall performance. One of these motors is the Switched Reluctance Motor (SRM) because it has several advantages such as simple construction and material composition, high starting torque, high-speed ranges, higher reliability, low inertia, and the low manufacturing cost [9, 10]. But the most significant challenges to be overcome if using SRM are the problem of torque ripples and the complexity of the control. The main idea of the SRM is that

the phase currents are switched ON and OFF according to the rotor position data, by sequential currents that switching into the motor windings, the rotor rotates to align itself with the minimum reluctance position, because of this movement the torque will be generated [11, 12].

Generally, the current controller of SRMs can be implemented by using the Hysteresis Current Control (HCC) method with high switching frequencies electronics elements or by using the Pulse Width Modulation (PWM) method. The main advantages of HCC are robustness and easy to implement with analog elements, but on the other hand, it causes a residual current ripple. Regarding the PWM controller, although this method needs a modulator to calculate ON and OFF times, the switching frequency will be known and controllable. In this study the Model Predictive Control (MPC) is used for the current controller, this method directly generates the switching signals for the converter switches without the need for a modulator. Predictive control technique uses the system model to predict the future values of control variables, the predicted values are applied to the control unit to determine the best performance possible based on pre-defined criteria [13].

The most important advantages of predictive control are that it depends on the system itself to generate the controller equation, and with predictive control help, the controller's cascaded structure can be avoided to achieve high-performance and rapid transient response [14]. Also, this control strategy is an ideal strategy for motor drives applications because of robustness, flexibility, and ease of understanding [15-19]. However, the MPC faces some difficulties such as the need for large memory size to store calculated data and comparisons between different actions to determine the optimal procedure. Also, this type of control is highly sensitive to any changes in system parameters, especially parameters that are used directly in prediction equations. In addition, the MPC typically operates at high switching frequencies which leads to high switching losses [20]. Also, in case of including more than objective in the cost function equation of the MPC, the weighting factors of the objectives must be optimized according to the desired performance, and the optimization method must be selected carefully to achieve the best performance. several models of optimal control have been introduced which can contribute to optimizing the controller objectives [21-24].

This work aims to contribute to increasing the use of the SRM in electric vehicles, especially in more electric aircraft's applications, by utilizing these motors to drive the aircraft's flight control surfaces actuators, due to the several advantages of the SRM. Meanwhile, this work tried to overcome the operation problem of the SRM, such as torque ripples, by using advanced control techniques (MPC) to reduce the torque ripples, taking into consideration optimization of the average switching frequency and the maximum stator current to reduce the system losses.

2 Aircraft Electrically Powered Actuators

2.1 Electro-Mechanical Actuator (EMA)

The configuration of the EMA is shown in Fig. 1, and this type of actuators can be used to drive the inboard spoiler surfaces of aircraft. The bi-directional power converter is used in this type of electric actuators to supply the motor with demanded power, this power is utilized to moves the spoiler surface through a mechanical transmission with a gearbox, and a ball-screw mechanism. Regarding the control unit, as can be seen from the actuator configuration diagram, the controller takes the error signal of the actuator surface deflection angle and processes this signal and generate the gating signals of the power switches to feed the motor with the required power. As a result, the motor rotates at a suitable speed and specific torque to drive the ball-screw and change the actuator surface to reach the desired deflection angle [25].

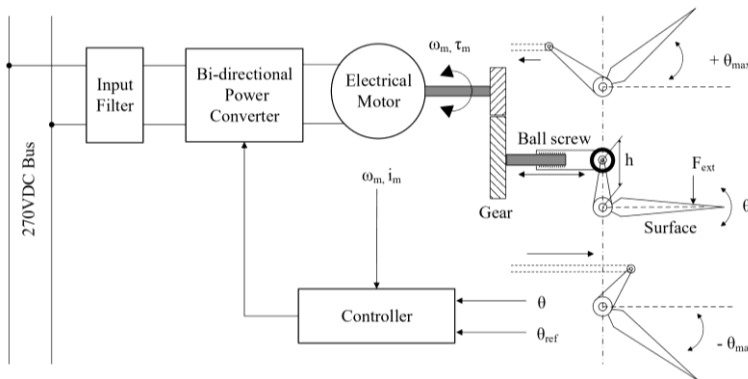


Figure 1
Electro-mechanical actuator configuration

2.2 Electro-Hydrostatic Actuator (EHA)

The EHA has standard hydraulic bypass valves to guarantee ease use of traditional active-standby or active-active actuator architectures. It is closely similar to conventional centralized hydraulic actuators in operating. Thus, the EHA is more suitable for primary flight control. The EHA can consume low quiescent power when operating in standby mode [26], and it is capable of performing a quick response at startup using an efficient electrical system. Moreover, EHA is more efficient than hydraulic actuators, and its efficiency is up to 70%, while the efficiency of the conventional actuators is typically 50% maximum. As shown in Fig. 2, the EHA is driven by an electric motor. The reference deflection angle

(θ_{ref}) is determined according to the desired position of the actuator surface and compared to the actual deflection angle (θ) then the error signal of the deflection angle is processed by the control unit to generate the optimal states of the power converter switches. The power converter unit regulates voltage, and current applied to the electric motor to rotate in both directions and provide a specific torque to drive the pump, thus moving the piston in the required direction. The piston movement and the arm will change the angle of the deflection of the surface to reach the desired position in both directions. The power converter is connected to the 270 VDC bus through the filter to mitigate the high-frequency harmonics generated in the system. The EHA is chosen for this study because it used not only in aerospace actuators but also in many industrial applications.

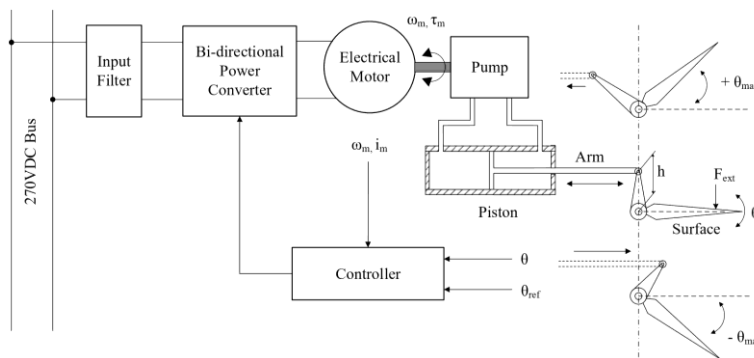


Figure 2

Electro-hydrostatic actuator configuration

3 Transformer Rectifier Unit Control

The on-board electric power system of modern aircraft has 400VAC variable frequency (400 - 800) Hz synchronous generators connected to the main AC bus. In order to provide a fixed 270 VDC voltage for actuators supply bus, it is important to select the power converter topology and its control technique appropriately. In aircraft applications, the Transformer Rectifier Unit (TRU) converts the AC voltage generated by the generators to a suitable DC voltage which can be used by the electrical components incorporated into the system such as an electrical actuator. This section will discuss the control of the power converter that can meet the requirements of high-performance TRU. The studied three-phase AC/DC converter topology with the proposed control scheme is shown in Fig. 3.

The converter uses six bi-directional switches. It is assumed that all switches are ideal and the characteristics of all circuit elements are linear and time-invariant.

Assuming a balanced three-phase supply:

$$i_{sa}(t) + i_{sb}(t) + i_{sc}(t) = 0 \rightarrow i_{sc}(t) = -i_{sa}(t) - i_{sb}(t) \quad (1)$$

Thus, the rectifier current i_r :

$$\begin{aligned} i_r &= s_a(t)i_{sa}(t) + s_b(t)i_{sb}(t) + s_c(t)i_{sc}(t) \\ &= (s_a - s_c)i_{sa}(t) + (s_b - s_c)i_{sb}(t) \end{aligned} \quad (2)$$

where s_a , s_b , and s_c are the switching states of the corresponding phases.

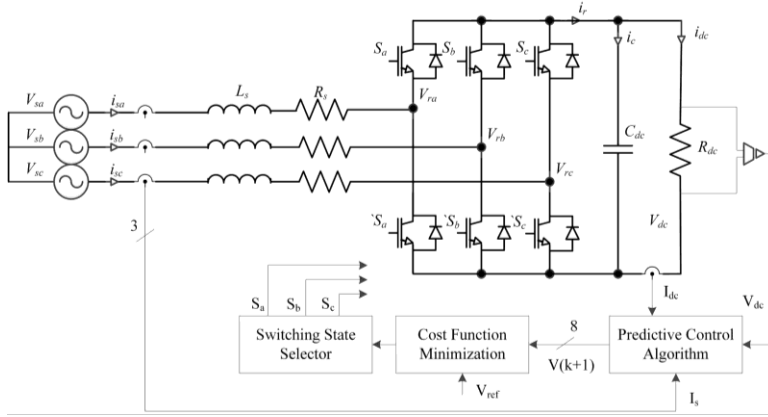


Figure 3

Three-phase voltage-source AC/DC converter

The governing equations of the system to obtain a dynamic model for the rectified voltage $V_{dc}(t)$ and the currents on the DC side can be deduced as:

$$i_c(t) = i_r(t) - i_{dc}(t) = C_{dc} \frac{dv_{dc}(t)}{dt} \quad (3)$$

$$C_{dc} \frac{dv_{dc}(t)}{dt} = (s_a - s_c)i_{sa}(t) + (s_b - s_c)i_{sb}(t) - i_{dc}(t) \quad (4)$$

The predicted DC voltage $V_{dc}(k+1)$ can be calculated using the discrete-time equation as:

$$V_{dc}(k+1) = \frac{T_s}{C_{dc}} [(s_a - s_c)i_{sa}(t) + (s_b - s_c)i_{sb}(t) - i_{dc}(k)] + V_{dc}(k) \quad (5)$$

Where $V_{dc}(t)$ is the rectified DC bus voltage, C_{dc} is the output capacitor, $V_{dc}(k)$ and $V_{dc}(k+1)$ the current and future capacitor voltages, T_s is the sampling time, and $i_{dc}(k)$ is the load current.

The proposed MPC algorithm for AC/DC power converter control is built as the flow chart demonstrates the main steps in Fig. 4. The predictive voltage controller must achieve the smallest voltage error with fast dynamics. So, a suitable cost function is used to measure and minimize the predicted voltage error by selecting the optimal switches states. The cost function (g) considers the absolute error between the reference voltage V_{ref} and the predicted voltage $V_{dc}(k+1)$.

$$g = |V_{ref} - V_{dc}(k+1)| \quad (6)$$

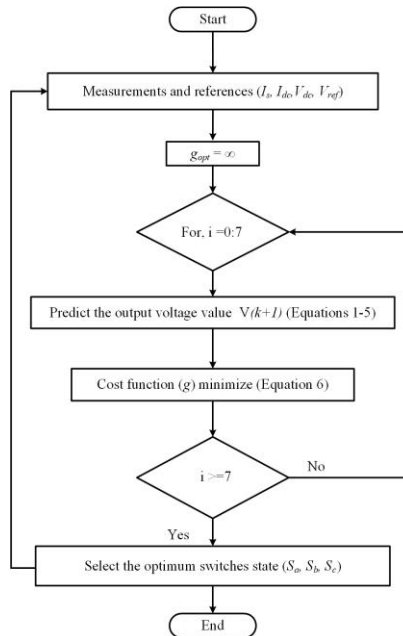


Figure 4

The predictive control algorithm of the AC/DC power converter

4 Current Control of SRM

There are several types of applications where the load on the SRM varies with speed over large ranges. These applications may require accurate speed control and good dynamic responses, as in aircraft actuators. In electrical actuators, the SRM is driven by the power converter to provides four quadrants operation mode, and the controller feedback signal can be the actuator surface position or motor shaft speed. During this study, the nonlinear model of SRM (6/4) is simulated, and the power converter topology is the symmetrical converter type that is controlled by predictive control techniques.

The predictive current control uses the equivalent circuit equations of the motor model to predict the future value of the stator current. There are many methods to establish the non-linear model of SRM, such as look-up table and interpolation techniques, neural network techniques, and analytical methods. In this work, the Look-up table technique is used to find the different values of the machine inductance according to the rotor position and phases current. Therefore, the equations of the SRM can be written as [27, 28]:

$$\begin{aligned} V &= R_s I + \frac{d\{L(\theta, I)I\}}{dt} = R_s I + L\{\theta, I\} \frac{dI}{dt} + I \frac{d\theta}{dt} \frac{d\{L(\theta, I)\}}{dt} \\ &= R_s I + L\{\theta, I\} \frac{dI}{dt} + \frac{d\{L(\theta, I)\}}{dt} \omega_m I \end{aligned} \quad (7)$$

$$L\{\theta, I\} \frac{dI}{dt} = V - R_s I + \frac{d\{L(\theta, I)\}}{dt} \omega_m I \quad (8)$$

where V represents the phase voltage, R_s describes phase resistance, while L symbolizes a mutual inductance, $\psi=L\{\theta, I\}$ represents the flux linkage per phase according to the position of the rotor θ and phase current I , and ω_m is the motor angular speed in radians/sec.

By applying the discrete-time form, the future values of the motor phases current $I(k+1)$ can be calculated from equation (8) as follows:

$$L\{\theta, I\} \frac{I(k+1) - I(k)}{dt} = V(sg) - R_s I + \frac{d\{L(\theta, I)\}}{dt} \omega_m I \quad (9)$$

$$I(k+1) = \frac{T_s}{L\{\theta, I\}} (V(sg) - R_s I + \frac{d\{L(\theta, I)\}}{dt} \omega_m I) + I(k) \quad (10)$$

where $V(sg)$ is voltage vector according to the switches status of the power converter, in this case, there are 27 different voltage vectors, $I(k)$ motor phases current, and T_s symbolizes the sampling time.

In this study, the significant objective of the controller is to maintain the stator current close to the reference current, which is usually set by a speed control loop, leading to the minimization of the motor shaft torque ripples. The further objectives that will be considered in the cost function equation are a reduction of the average switching frequency and minimize the copper losses in stator windings. It is necessary for the control algorithm to produce the smallest possible values of the current error, optimize the average switching frequency, and minimize the copper losses. Therefore, the cost function is calculated for all possible voltage vectors/switches stats of the power converter, because there are three states for each phase (+Vdc, 0, -Vdc) and this study used a three-phase motor, so the possible switches stats are $3^3 = 27$. Then determine the optimal stats

according to the controller objective function. Equation (11) represents the cost function (g). The cost function g is calculated for all n=27 different voltage vectors V_g according to switching vector S_g , and the voltage vector that minimizes cost function (g) will be applied to the motor phases in the next time interval. Figure 5 illustrates the flow chart that describes how the proposed current control algorithm was built.

$$g = |I_{ref} - I_j(k+1)| + \lambda_1 \sum_{j=1}^3 |I_j(k+1)| + \lambda_2 |S_g(k+1) - S_g(k)| \quad (11)$$

where λ_1 and λ_2 are the weight factors for copper losses and switching times respectively, and $1 > \lambda_1 > 0$ and $1 > \lambda_2 > 0$.

Generally, the three controller objectives can be adjusted in the cost function by tuning the weighting factor of each objective to reach the optimal required performance according to the application. In this study case, the weights factors were set to $\lambda_1 = 0.03$ and $\lambda_2 = 0.0025$.

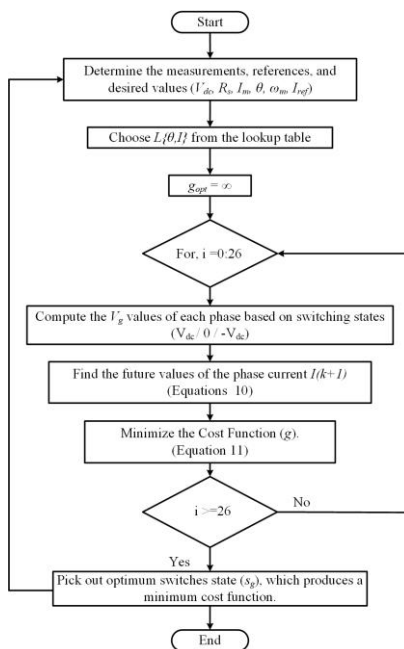


Figure 5

The proposed MPC algorithm for SRM current control

The proposed control method requires a reference current to be followed by the predicted current with the smallest possible error value. Therefore, the actual deflection angle of the actuator surface is used as a feedback signal, and the deflection angle error signal is determined by comparing the actual and desired

deflection angle. Then, this error signal can be used as an input variable to a linear controller (PI) to produce the reference signals for the current control loop. The reference current signal can be generated using the actuator position control loop, as mentioned earlier, or by the motor speed control loop as well. The generated reference current is distributed to each phase according to the rotor position data θ_m in the phases commutation block. With the help of DC voltage V_{dc} , phase current $I(k)$, phase inductance $L\{\theta, I\}$, and motor speed ω_m or rotor position data θ_m , we can determine the future values of the phase current $I(k+1)$ using equation (10). The switches state selector block will select the optimal state for all power switches of the converter according to the cost function equation that reduces the error between the calculated current and desired current to the smallest possible value, leading to reducing the error in the deflection angle of the actuator surface. To ensure the minimization of the cost function, the controller algorithm does a number of iterations equal to all possible switches state, in this study the number of iterations equals 27 as illustrated before, then it calculates the difference between the desired and the expected values, which determined using the system model, taken into account the other terms of cost function such as average switches frequency. On each iteration, the algorithm stores the switches state if it makes the cost function is smaller than the previous values. The overall configuration of the flight control surface's actuation system, including SRM and predictive control, is illustrated in Fig. 6. And The simulation model of mechanical transmission for EMA is shown in Fig. 7 [29]. This model takes into consideration, inertia, damping, the stiffness of the ball screw mechanism, stiffness of the bearing structure, and surface dynamics.

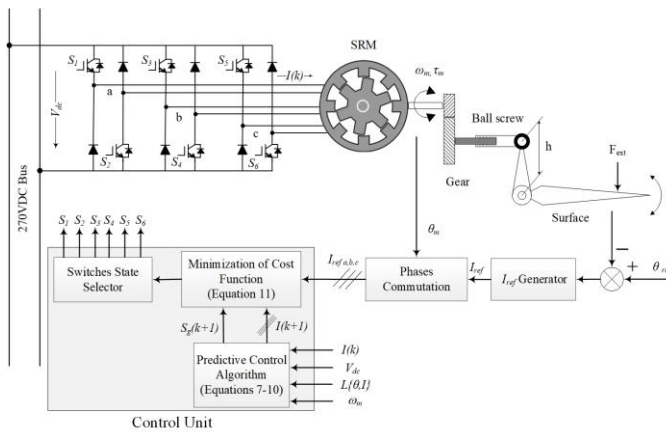


Figure 6

The configuration of the flight control surface actuation system with SRM and MPC

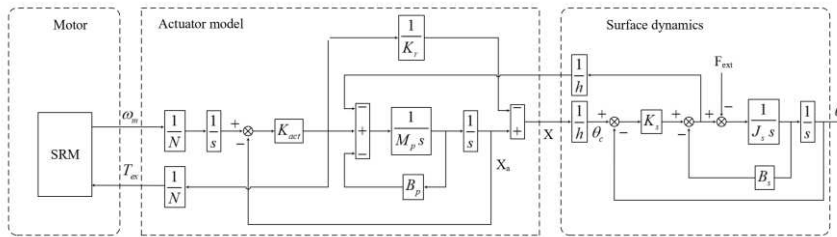


Figure 7

EMA simulation model

5 Simulation Results and Discussions

In this study, a 60 kW 6/4 SRM model with nonlinear characteristics is simulated, and the motor's parameters listed in Table 1 [30, 31]. The proposed system is simulated using PSIM software, and the MPC is programmed by C-Code.

Table 1
SRM simulation parameters

Parameter	Values	Parameter	Values
Rated power	60 kW	Aligned inductance	23.62 mH
DC supply voltage	250 V	Rotation speed	1000 rpm
Maximum current	450 A	Moment of inertia	0.05 kg.m ²
Stator resistance	0.05 Ohm	Number of rotor poles	4
Unaligned inductance	0.67 mH	Number of stator poles	6

The actuators are normally connected to the 270 VDC bus, and hence the TRU is used to provide a regulated DC voltage. In this study, the three-phase 6-switch IGBT controlled rectifier is used in TRU, and the actuator is driven by SRM with a bi-directional symmetrical converter to produce deflection in both directions. The three-phase rectifier and symmetrical converter are controlled by predictive control technique. To perform a complete simulation model of the proposed system the electric system of the Boeing-787 is taken as a study case, which considered one of the modern types of MEA. The B787 electrical power system composites from four identical channels, each channel has four buses: main AC bus (variable frequency), secondary AC bus, 270 VDC, and 28 VDC. A single channel of the power distribution system used in this study is shown in Fig. 8 [32]. The 270 VDC bus feeds about half of the total electric load of the aircraft, and one of the most important loads powered by this bus is the electric actuators.

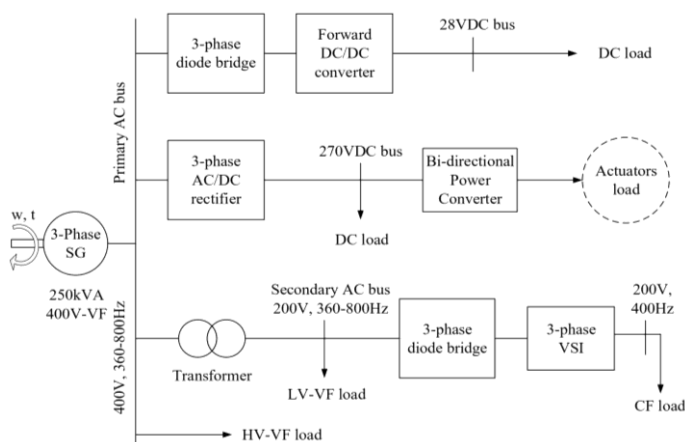


Figure 8

A single channel of MEA power distribution system

5.1 The 270 VDC Bus Control

The actuation system is designed to control the deflection angle of the actuator surface from the maximum positive to maximum negative values. Therefore, the power converter is controlled to act as a bi-directional converter according to the operating conditions, and the SRM will operate in four-quadrant operation mode. Continuous regulation of the DC bus helps the power converter to operate efficiently in both directions, and the predictive control of the TRU should provide a regulated DC voltage during all operating conditions. Figure 9 shows the 270 VDC voltage profile with EMA dynamic load under different operating conditions. It can be observed that voltage was regulated satisfactorily and within the allowable limits according to the aircraft standards (MIL-STD-704F) [33].

Although there are small overshoot/undershoot when the reference signal changes sharply, the voltage value remains within standard limits during a complete operating cycle, and It is better than the results were obtained in case of using the linear controller (PID) for the AC/DC converter at the same operating conditions. A comparison between the converter performance with each of the two controllers (PID, and MPC) is listed in Table 2.

Table 2
AC/DC converter performance (PID Vs MPC)

Performance Controller	Over/Undershoot (%)	Ripples (%)	Settling time (ms)
PID	15.6	1.85	25
MPC	10.76	0.88	9.7

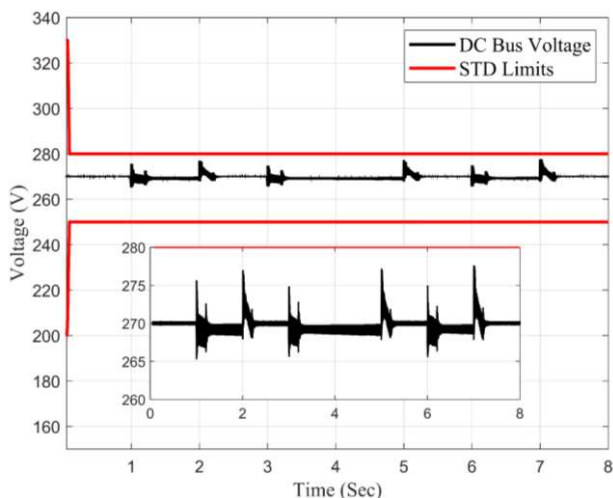


Figure 9
The 270 VDC bus voltage profile with EMA load

5.2 SRM Control

This part is divided into two main stages, the first one is the comparison between the torque ripples of the motor using MPC and using HCC to verify the effectiveness of MPC to control the SRM with small current and torque ripples, the obtained results verifies the ability of predictive current control algorithm to reduce the motor phase current ripples compared with traditional methods. Because of the direct effect of the phases current on motor torque, the motor torque ripples during the conduction period and motor average torque will be minimized by using a predictive current control algorithm. Table 3 summarizes the comparison between MPC and HCC at different loading conditions regarding the average torque ripples, average switching frequency, and the copper losses.

Table 3
SRM torque ripples (HCC Vs MPC)

Control method \ Performance	Average torque (%)	Switching frequency (kHz)	Copper losses (W)
HCC (Load torque = 10Nm)	17	6.52	29.2
MPC (Load torque = 10Nm)	6	5.19	29.05
HCC (Load torque = 20Nm)	12	6.15	54.75
MPC (Load torque = 20Nm)	5	4.8	54.52

The second stage is applying MPC to the aircraft actuator system, and study the overall system performance. Figure 10 shows the response of these currents, as a result of the movement of the actuator in both directions, the sequence of motor

phases has been changed, the currents waveform in case of the positive and negative deflection angle are shown in Fig. 10-a and Fig. 10-b, respectively.

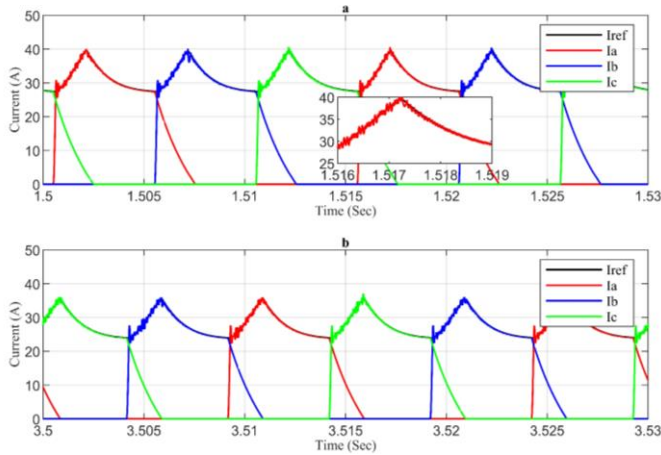


Figure 10

Motor phases current (a) positive deflection angle (b) negative deflection angle

From the obtained results we can note that the three phases current tracks the reference current signal generated from speed or position control loop in both directions with small ripples, which confirm the effectiveness of the proposed current controller algorithm.

Figure 11 shows the speed of the motor at possible different operating conditions, and the reference speed signal is set to provide the motor rotation in both directions and to give the trapezoidal shape of the actuator deflection angle. It can be seen that the actual speed tracks the reference signals in the complete operation period. Three snapshots of the motor speed profile are taken and zoomed to verify MPC performance. By zooming the speed signal, we can see the peak values of the overshoot and undershoot in both directions are about 10 rpm (1%), which confirms the effectiveness of MPC in aircraft electric actuators. But it should be noted here that the MPC causes some ripples in the steady-state.

The main objective of this work is to control the deflection angle of the flight control surfaces. Therefore, the performance of the deflection angle for a complete operating period (from 0 to $\pm\theta_{max}$) is shown in Fig. 12. Two snapshots of the deflection angle have been taken to show the maximum and final position of the deflection angle. As we see, the actual deflection angle follows the reference one with a small error, this error is less than 0.2° , which represent 0.4%. These results demonstrate the possibility used of the proposed system to control the deflection angle of the flight control surfaces with satisfactory performance.

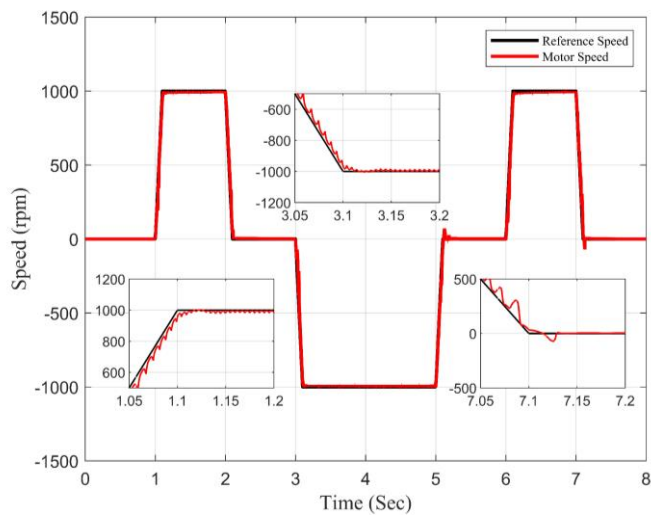


Figure 11

Motor speed performance with a zoom at different speed values

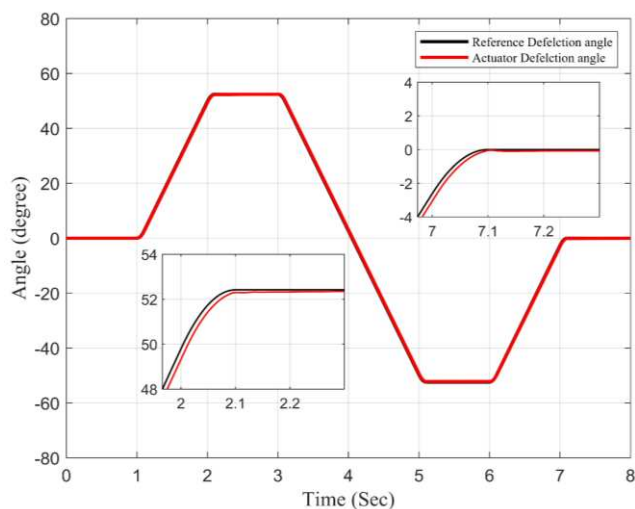


Figure 12

A complete cycle of the EMA deflection angle using MPC with a zoom at different edges

It is known that the main challenge of using SRM in many applications is the problem of torque ripples. But thanks to the predictive current control technology of the SRM proposed in this work, the torque ripples have been reduced as explained previously in Table 3. Figure 13 shows the torque performance of the SRM during a complete cycle of the deflection angle.

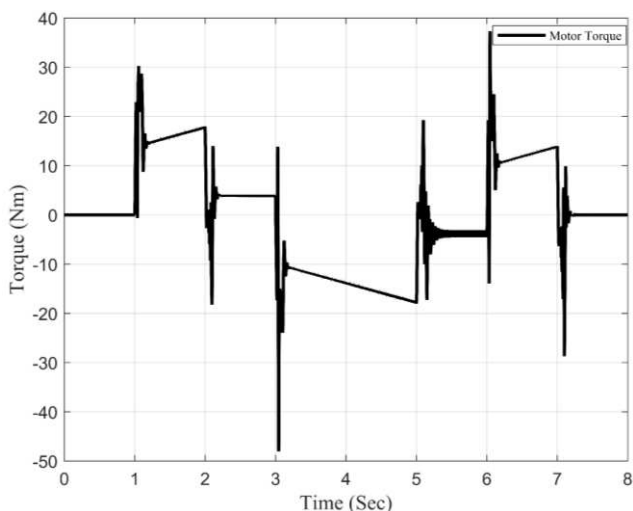


Figure 13

SRM torque for a complete cycle of the deflection angle

From the SRM torque diagram, we can observe that the torque of the motor increases when the deflection angle of the actuator surface increases due to the external forces that affect the surface as the wind force. Then the torque becomes constant when the surface reaches its new position. Next, the same behavior occurs in the negative period of the deflection angle during the actuator surface return to zero position. Finally, the torque returns to zero again when the surface reaches its zero position at the end of the cycle. This diagram also shows that the MPC can effectively control the SRM with small values of torque ripples to drive the flight control surface actuators.

Conclusions

In this study, the authors built a simulation model for the SRM-based flight control actuator for modern civil aircraft applications. The electric motor control unit is designed using predictive control technique, and the MPC was also used for TRU controller to regulate the 270 VDC bus for actuators supply. With the help of MPC, TRU provides a fixed DC voltage under the actuator dynamic load effects at transient and steady-state operating conditions. Using the predictive current control for SRM, the motor speed, and the flight control surface deflection accurately track the desired signals. The proposed control algorithm produces a small overshoot/undershoot in the motor speed about ± 10 rpm (1%) with small ripples in the motor torque, and the maximum error in the deflection angle around 0.4%. The obtained results demonstrate the effectiveness of the proposed system in aircraft electrical actuators. These results confirm that the MPC techniques provide a good response of the motor speed controller, with acceptable torque ripples values in all operating conditions, and produce the desired deflection angle

for flight control surfaces in both directions accurately. Of the above, we can conclude that the SRM controlled by MPC can efficiently drive the flight control surfaces actuators, for civil aircraft applications.

References

- [1] Ian Moir and Allan Seabridge, "Aircraft systems: mechanical, electrical, and avionics subsystems integration," 3rd ed., John Wiley&Sons, 2008
- [2] A. Eid, M. Abdel-Salam, H. El-Kishky, and T. El-Mohandes "Simulation and transient analysis of conventional and advanced aircraft electric power systems with harmonics mitigation," *Electric Power Systems Research*, Vol. 79, No. 4, pp. 660-668, 2009
- [3] Reyad Abdel-Fadil, Ahmad Eid, and Mazen Abdel-Salam, "Electrical distribution power systems of modern civil aircrafts," in *2nd International Conference on Energy Systems and Technologies*, Cairo, Egypt, pp. 201-210, 2013
- [4] D. R. Trainer and C. R. Whitley, "Electric actuation - power quality management of aerospace flight control systems," in *International Conference on Power Electronics, Machines and Drives*, Sante Fe, NM, USA, pp. 229-234, 2002
- [5] Richard M. Crowder, "Electrically powered actuation for civil aircraft," in *IEE Colloquium on Actuator Technology: Current Practice and New Developments*, pp. 5/1-5/3, 1996
- [6] K. P. Louganski, "Modeling and analysis of a dc power distribution system in 21st Century airlifters," M.Sc., Virginia Polytechnic Institute and State University, 1999
- [7] R. Abdel-Fadil, A. Eid, and M. Abdel-Salam, "Fuzzy Logic Control of Modern Aircraft Actuators," in *3rd International Conference on Energy Systems and Technologies*, Cairo, Egypt, pp. 149-158, 2015
- [8] R. Abdel-Fadil, A. Eid, and M. Abdel-Salam, "Control and Performance Investigation of Modern Civil Aircraft Actuators using Model Predictive Control," in *The 17th International Middle East Power Systems Conference (MEPCON'15)*, Cairo, Egypt, 2015
- [9] T. J. E. Miller, "Electronic Control of Switched Reluctance Machines," First Edition, Newnes, Oxford, UK, 2001
- [10] K. Vijayakumar. R. Karthikeyan, S. Paramasivam. R. Arumugam, and K. N. Srinivas, "Switched Reluctance Motor Modeling, Design, Simulation, and Analysis: A Comprehensive Review," *IEEE Transactions on Magnetics*, Vol. 44, No. 12, pp. 4605-4617, 2008
- [11] R. Krishnan, "Switched Reluctance Motor Drives :Modeling, Simulation, Analysis, Design, and Applications", 1st ed., CRC Press, Germany, 2001

- [12] R. Abdel-Fadil and L. Számel, "State of the Art of Switched Reluctance Motor Drives and Control Techniques," in *Twentieth International Middle East Power Systems Conference*, Cairo, Egypt, pp. 779-784, 2018
- [13] Patricio Cortés, Marian P. Kazmierkowski, Ralph M. Kennel, Daniel E. Quevedo, and José Rodríguez, "Predictive control in power electronics and drives," *IEEE Transactions on Industrial Electronics*, Vol. 55, No. 12, pp. 4312-4324, 2008
- [14] Jose Rodriguez and Patricio Cortes, "Predictive control of power converters and electrical drives," 1st ed., John Wiley&Sons, Ltd, US, 2012
- [15] R. Haber, R. Bars, and U. Schmitz, "Predictive control in process engineering, from the basics to the applications," 1st ed., WILEY-VCH Verlag GmbH&Co, Germany 2011
- [16] G. Abbas, U. Farooq, and J. Gu and M. U. Asad, "Constrained model based predictive controller for a high-frequency low-power DC-DC buck converter," *International Journal on Electrical Engineering and Informatics*, Vol. 5, No. 3, pp. 316-339, 2013
- [17] L. Tarisciotti, P. Zanchetta, A. Watson, J. C. Clare, M. Degano, and S. Bifaretti, "Modulated model predictive control for a three-phase active rectifier," *IEEE Transactions on Industry Applications*, Vol. 51, No. 2, pp. 1610-1620, 2015
- [18] R. Abdel-Fadil and L. Számel, "Enhancement Of the Switched Reluctance Motor Performance for Electric Vehicles Applications Using Predictive Current Control," in *2018 International IEEE Conference and Workshop in Óbuda on Electrical and Power Engineering (CANDO-EPE)*, Budapest, Hungary, pp. 195-200, 2018
- [19] S. Vazquez, J. Rodriguez, M. Rivera, L. G. Franquelo, and M. Norambuena, "Model Predictive Control for Power Converters and Drives: Advances and Trends," *IEEE Transactions on Industrial Electronics*, Vol. 64, No. 2, pp. 935-947, 2017
- [20] A. Eid, R. Abdel-Fadil, and M. Abdel-Salam, "Performance and Power Quality Improvements of MEA Power Distribution Systems using Model Predictive Control," *International Review of Aerospace Engineering*, Vol. 10, No. 1, pp. 31-40, 2017
- [21] A. Árpád Takács, Levente Kovács, Imre J. Rudas, Radu-Emil Precup, and Tamás Haidegger, "Models for Force Control in Telesurgical Robot Systems," *Acta Polytechnica Hungarica*, Vol. 12, No. 8, pp. 95-114, 2015
- [22] K. K. Tan, S. Zhao and J.-X. Xu, "Online automatic tuning of a proportional integral derivative controller based on an iterative learning control approach," *IET Control Theory Appl.*, Vol. 1, No. 1, pp. 90-96, 2007

- [23] Rafael Pedro Alvarez Gil1, Zsolt Csaba Johanyák, and Tamás Kovács, “Surrogate Model based Optimization of Traffic Lights Cycles and Green Period Ratios using Microscopic Simulation and Fuzzy Rule Interpolation,” *International Journal of Artificial Intelligence*, Vol. 16, No. 1, pp. 20-40, 2018
- [24] S. Preitl, R. Precup, Z. Preitl, S. Vaivoda, S. Kilyeni, and József K. Tar, “Iterative Feedback And Learning Control. Servo Systems Applications,” *IFAC Workshop ICPS'07*, Cluj-Napoca, Romania, pp. 16-27, 2007
- [25] X. Du, R. Dixon, R. M. Goodall, and A. C. Zolotas, “Modelling and control of a high redundancy actuator,” *Mechatronics*, Vol. 20, No. 1, pp. 102-112, 2010
- [26] C. A. Constantino, L. S. Góes, and F. J. Moreira, “High frequency modeling of a hydraulic actuation flight control system,” in *9th Brazilian Conference on Dynamics Control and their Applications*, Serra Negra, Brazil, pp. 1080-1090, 2011
- [27] C. Li, G. Wang, Yan Li, and Aide Xu, “An improved finite-state predictive torque control for switched reluctance motor drive,” *IET Electric Power Applications*, Vol. 12, No. 1, pp. 144-151, 2018
- [28] V. Jambulingam, “Mathematical Modeling and Simulation of Switched Reluctance Motor,” *International Journal for Research in Applied Science&Engineering Technology*, Vol. 4, No. VI, pp. 441-446, 2016
- [29] V. B. Blaignan and V. A. Skormin, “Stiffness enhancement of flight control actuator,” *IEEE Transaction on Aerospace and Electronic Systems*, Vol. 29, No. 2, pp. 380-390, 1993
- [30] C. Li, G. Wang, Y. Fan, and Yan Li, “Adaptive RBF Neural Network Controller Design for SRM Drives,” in *35th Chinese Control Conference*, Chengdu, China, pp. 6092-6097, 2016
- [31] N. Saha, and S. Panda, “Speed control with torque ripple reduction of switched reluctance motor by Hybrid Many Optimizing Liaison Gravitational Search technique,” *Engineering Science and Technology, an International Journal*, Vol. 20, No. 3, pp. 909-921, 2017
- [32] R. Abdel-Fadil, A. Eid, and M. Abdel-Salam, “Fuzzy logic control of modern aircraft electrical power system during transient and steady-state operating conditions,” in *IEEE International Conference on Power Electronics, Drives and Energy Systems*, Mumbai, India, pp. 1-6, 2014
- [33] Navy-AS: “Aircraft electric power characteristics (MIL-STD-704F),” Department of defense-USA, 2013

Generations and Emotional Intelligence A Pilot Study

**Renáta Machová¹, Tibor Zsigmond¹, Kornélia Lazányi²,
Veronika Krepszová¹**

¹ J. Selye University, Faculty of Economics, Department of Management,
Hradná st. 21, 945 01 Komárno, Slovakia
machovar@ujss.sk, zsigmond@ujss.sk, krepszovav@ujss.sk

² Óbuda University, Keleti Faculty of Business and Management, Dean Office,
Tavaszmező u. 17, 1084 Budapest, Hungary
lazanyi.kornelia@kgk.uni-obuda.hu

Abstract: Emotional intelligence is at the heart of our research. Our aim was to examine the differences that exist between generations, based on the views of their representatives. In the theoretical portion we dealt with defining emotional intelligence and presenting it from the leaders' aspect. Finally, each generation is introduced. In our paper we set up 2 hypotheses, which are cross-tabulated and / or analyzed with the help of related statistical methods. In the end, both our hypotheses proved to be true. This article contains 2 figures and 2 tables. Our paper ends with a section on conclusions, in which we summarize our research, results and outline our findings.

Keywords: emotional intelligence; generations; workplace

1 Introduction

This article is about emotional intelligence. We chose this topic in order to demonstrate the presence of emotional intelligence in the 21st Century. Emotional intelligence plays an important role in everyday life. We do not notice it, but our emotions determine our actions. It also affects our personality and personal relationships. That is why we would like to show how this is present at the workplaces of each age group. A job is the place where we spend most of our time, and where we meet and work with many people every day. It is important to get along well with others and that our emotions do not adversely affect our relationships or hinder our work.

In the theoretical part we introduced the concept of emotional intelligence. Within this, we introduced the individual points of view and then we approached the topic

from the perspective of the leaders. Finally, we introduced the individual generations, respectively their characteristics.

In the practical part, we examined the relationship between emotional intelligence and belonging to an age group. The research was carried out with the help of a questionnaire, which was transmitted by the snowball sampling method. Respondents were grouped by generation, and their responses were summed up and compared. For comparison, we used diagrams, which were explained below, and finally conclusions were drawn. Our goal with this method of analysis was to demonstrate emotional intelligence and generational differences in the workplace.

2 Theoretical Background

Emotional intelligence is present in every person's life and in every area of our existence. It influences our own lives, our decisions, and at the same time helps to establish and maintain relationships with other people. With respect to ourselves, it helps us draw conclusions from a particular event or control our emotions in a given situation and make the necessary and appropriate decisions based on it. Emotional intelligence is a part of social relationships, even as it helps to build human relationships, to recognize the emotions of others, and to put ourselves in the role of the person and thus outline the processes that can take place in that person.

2.1 Emotional Intelligence

The word emotion comes from the Latin word "motore", it means to move. The word "e" indicates that it is moving. So emotions go hand in hand with the urge to act. This has been retained by evolution [10]. Salovey and Mayer [28] define emotional intelligence as "the subset of social intelligence that involves the ability to monitor one's own and others' feelings and emotions, to discriminate among them and to use this information to guide one's thinking and actions." [19] This view was used by Schutte *et al.* [29] while developing a valid measurement for emotional intelligence. According to Neale *et al.* [24] our emotions influence the way we act, make decisions, or judgments, so they affect everything we do. Joseph and Newman [14] distinguished two interpretations of the EI: "1) as set of specific competencies for recognizing and controlling individual emotions and 2) as a grab bag of constructs that contribute to job performance but are not redundant with cognitive ability." Emotions provide individuals with essential regulation and orientation in their function, which aims to facilitate adaptation to certain conditions [37]. Emotional intelligence is increasingly present in everyday life. It can be found in social contacts such as human relationships and leadership activities. It is essential for controlling and managing the emotions of ourselves,

others, and groups. Emotions have a big impact on the quality of relationships within a business. This can only be formed and developed by internal factors [26]. Emotional intelligence (EI) is today a vital concept in the field of psychology. It extends its influence into the world of work and, through it, into each workplace, thus giving rise to a global concept. The EI can partly intervene in business problems, as it affects executives. Therefore, companies and enterprises treat this issue as a key issue and consider it to be a basic operational factor of an organization, even though it is not a sort of a physical concept [6]. Developing emotional intelligence brings benefits and enhances performance. This can help you communicate more effectively with others, have a better personal connection, have a stronger empathic ability, have better career prospects, and have more confidence in managing change. In addition, it contributes to several other things e.g., more respect for others, less power play in the workplace, less stress, more confident and positive thinking and increased creativity [24]. Workplaces are undergoing change. They not only judge individuals how smart they are, i.e. how developed their cognitive intelligence is, but also by how they treat others and themselves. This standard is used to judge who to employ, who to promote and who to send. According to [9] the new standard takes the appropriate intellectual ability and expertise as basic, and instead focuses on personal qualities such as initiative, empathy, adaptability and persuasion [1] [32].

The main factor influencing emotional intelligence is, according to researchers, the environment itself, as it often has a profound effect on an individual's level of emotional development. Environmental influences can guarantee the development of emotional intelligence, but the opposite is also true, it can also hinder it. For example, the mood in the workplace significantly determines the emotional intelligence of the manager or subordinates. Environmental impulses make it difficult to enhance emotional intelligence. The most influential effect for people is their own cultural environment, which has a great influence on the development and formation of emotional intelligence. One of the most important phenomena today is the examination of the importance of organizational culture. Organizational culture provides an opportunity to promote workplace results and create a positive workplace atmosphere. The goal of organizational culture is to create internal integrity, support external adjustment, and reduce the uncertainty of organizational members [3]. Conflict management appears as a factor that directly or indirectly influences the development of organizational culture, which is closely related to a person's emotional intelligence. Its purpose is to develop a method that enables organizational conflicts to be handled in situations where two people's efforts are incompatible. Conflict management is influenced by the general characteristics of the individual, the emotional state of the participants in the given situation, the organizational atmosphere and the relationship between the participants in the confrontation. In addition, perception of individuals' intentions and motivations also have an impact. Smart and successful individuals seek problem solving and collaboration, while the unsuccessful ones seek ruler type solutions [3] [18] [22] [32].

Emotional intelligence is increasingly important in human management. EQ is not equal to personality, it is a combination of countless abilities and competencies that influence behavior, radiance and personal style. This type of intelligence plays an important role in the workplace as it plays a decisive role in behaving in a communication situation and in dealing with people. Emotional intelligence is the closest to empathy. The latter allows us to recognize the emotions of others and it enables us to gauge their thinking and behavior. In emotional management, control of mood and behavior is essential in stressful, complex situations. EQ contributes to expressing our appreciation to others, and it also lays the foundation for effective communication. While IQ helps in individual task solving, EQ plays an important role in the development of employee relationships. Individuals with a higher level of emotional intelligence can better manage their own feelings and thus be better at achieving their goals. According to research, those with lower EQs have done worse work than sales teams that have done better in this area. In the world of work, it is extremely important to motivate others. In a leadership role, it is essential for someone to know and influence the subordinates' thinking [3] [32] [41].

2.2 Aspects of Emotional Intelligence

The key to success is to be aware of emotions, learn how to control and manage them, and furthermore understand the others' feelings. Therefore, emotional intelligence crosses two perspectives. One is the self-knowledge of an individual in order to understand his or her goals, motivations, behaviors, and reactions. The second step is to understand people's feelings and behaviors. These are also called intrapersonal and interpersonal skills. We as individuals are centered in the intrapersonal intelligence. It is the ability to understand what is happening in us and to act accordingly. Interpersonal intelligence is related to the people around us. That is being aware of how we intercept and understand the actions and emotions of others [24].

Emotional intelligence can be developed in all areas, i.e. all attitudes can be changed. Research has shown that it takes at least 21 days to change an attitude. A real change requires elements of the KASH model. These include knowledge (K), attitude (A), skills (S) and habits (H). Most trainings are almost exclusively focused on knowledge transfer and skill development, so they are intended to shape the thinking brain. However, sustainable change can be achieved by changing behavior and habits as well, by which the emotional brain is concerned [24]. Understanding and controlling the emotional side of the brain is required to improve emotional intelligence and decision making. This can be done by developing five key skills. If we are able to calm down and relieve stress quickly, will help us to stay balanced, focus on tasks no matter what challenges we face or how stressful we are. Emotional awareness is the ability to relate to our emotions. Without emotional awareness, we cannot fully understand our own motivations

and needs or communicate effectively with others. A good communicator needs more than just verbal skills. This is non-verbal communication. You need to keep the attention of others and build a confidential relationship with others. You should also be able to read and respond accurately to non-verbal signals that other people send. Humor and the use of toys to tackle challenges is also important. Humor, laughter, and play are natural remedies to ease the burden. Positive conflict resolution and confidence building skills support the previous four emotional intelligence skills. Therefore, is very important to handle stress, to stay emotionally aware, to communicate not just verbally, to use humor and play, and by all these you will be better able to handle emotionally charged situations, and to recognize and eliminate many problems before they spread [8].

Goleman [10] first divides emotional intelligence into two parts. In his view, personal skills are the responsibility for treating ourselves, while social competencies are responsible for managing social relationships. He further breaks down these two skills, providing the right foundation for developing emotional intelligence. So, based on these principles, the first step is to measure the work. It has to be focused on skills that help the employee perform well. The next step is to assess the individual, which involves examining the weaknesses and strengths of the person and then developing them. Feedback is important, as the personal characteristics assessed are emotionally charged, so special attention should be paid to their formulation. The next is the assessing the needs for change. It is important to observe the individual's aspiration for development and their attitude to change. Motives, that is, motivation that helps individuals to complete successful learning processes. The more you strive for personal development, the better you will achieve it. It is necessary to set an example, set role models for individuals. These role models possess the ability to develop and stand as a good example. Encouraging participants and supporting the organizational environment also greatly contribute to the successful acquisition of skills. Providing affirmative feedback is also helpful as individuals need validation and recognition. They need to feel that their efforts for change are not in vain. Finally, evaluation should not be forgotten. It is necessary to evaluate development and make sure that changes are permanent [3] [38].

Emotional intelligence plays an important role in an organization, because an organization must select its employees based on their emotional intelligence and organize the level of growth of employee training. People with high levels of emotional intelligence are more balanced and stable than people with lower levels of emotional intelligence. This intelligence is linked to the various relationships within the organization. It also influences leadership, work balance, conflict management, and stress management. In addition, it also reduces employee turnover. It has a great impact on the behavior of employees at work. It enhances employee tolerance and makes them feel good with their co-workers. Personal or workplace skills contribute about 20% to personal success in life, while emotional intelligence contributes to it 80%. It is easier to train someone in the technical part

of their job than to develop their intellectual intelligence. There is no emotional skill at a young age. And, there is also a tendency according to which it takes more dedication to acquire technical skills, leaving very little time and opportunity for social skills or emotional intelligence. Understanding emotions is very important in an organization for success and humanity [7] [24] [27].

2.3 Emotional Intelligence in Leadership

The natural way of a leadership is one that is based on emotional intelligence. An advanced personality is the basis of an effective leadership. Development of emotional intelligence is an essential task of leadership training. A certain level of intelligence – the general intellectual ability – is essential for the leader, because the knowledge acquired is rapidly obsolete today, and only the intelligent person can see through the complex mesh of problems [11]. A person with a high EQ is ideal for leadership, because it includes skills such as controlling the impulse, controlling impatience, controlling the mood, preventing frustration, suppressing thinking, developing empathy and hope [2]. The most important qualities of a leader are being able to know and control one's own spiritual phenomena and to be able to establish contacts. According to Goleman [11], in the face of an increasingly fierce competition in a globalized marketplace, the ever-changing demands of increasingly high-quality customers in a hierarchical organization cannot be met by management alone. Therefore, it is not disputed that an emotionally advanced leader is needed. It is the primary task for leaders to make sure that those who are under leadership feel comfortable. Therefore, management is primarily an emotional enterprise. The emotionally intelligent leadership style influences how the organization works. There are six leadership styles with emotional intelligence that can produce both positive and negative effects [3] [21] [23] [41].

Leaders with a vision are compassionate, have a high level of self-confidence and are often initiators of change. Affiliate leaders are also compassionate, capable of networking and handling conflict well. The democratic leader supports collaboration and teamwork, communicates confidently, and yet is often an excellent audience. The counsellor leader is emotionally conscious, compassionate, and able to recognize and utilize the strengths of others. The coercive leader builds on his/her own position of power, instructs others to pursue his/her own intentions, and has no compassion. A results-oriented leader sets high standards that he or she follows. Proactive and highly performance-centered people tend to control or criticize those who cannot achieve their own high standards and do not support their development [3] [12] [13] [21].

The basic and most important dimension of leadership is influencing emotions, which is a natural part of leadership. It is the leader who is expected to give encouragement and guidance, and thus the individual who controls the emotions

of the community. Its role is to manage collective emotions in a positive direction and to eliminate the blocking impulse of wrathful moods. The natural leaders do not confine themselves only to have the work done by subordinates. Subordinates also expect emotional support and compassion from the leader, which is an emotional relationship based on support. If the superiors generate optimistic emotions, then everyone gives the best of their knowledge and being. This situation is called resonance. When a manager evokes negative emotions, it results in dissonance and dismantles the emotional basis that motivates the employee to perform. The groups mostly consider the emotional reaction of their leader to be the determining factor. So the leader sets up emotional norms. If the designated leader does not have enough emotional intelligence, the group will not consider him / her to be a credible leader and will therefore start to trust another manager. This person becomes the actual leader. Another style is represented by the resonant leader. He /she is the one who attunes him/herself to the subordinates' negative feelings and is able to turn them to be rather optimistic. He/she speaks honestly and convincingly. As a result, the workgroup takes on the enthusiasm and the creativity of their leader. The outburst of anger and the fear of indifference are the characteristics of a dissonant leader. Unfortunately, this is not an uncommon phenomenon in the workplace [11] [17] [21].

Coaching is the most powerful method of communication. The proper method applied effectively is able to raise awareness. It helps to improve people's performance, which improves the productivity of the group and the organization. The essence of coaching is to develop the individual's abilities in a positive way and manages to show the most of them. It gets the best out of individuals. The goal of coaching is to develop awareness and responsibility. One should not be mistaken coaching for advising. For example, telling someone what to do is not considered as coaching. During this process, we do not provide any advice and ready solutions. Nor can it be confused with mentoring, personal counselling, professional counselling or training [24]. The Coach-ee, the subject of the coaching, needs knowledge that cannot be solved by taking over the coach's own knowledge. The task is to get the necessary knowledge and bring out the hidden skills with the help of the coach [39]. People need to see not their performance but their ability [39].

Coaching can be applied in areas such as employee motivation, problem solving, team building, teamwork, training, planning and evaluation, task performance, praise and evaluation, managing human relationships, delegating, delegating, and distributing tasks [39].

Employees of an emotionally intelligent organization are productive, motivated and effective. They are committed to their goals. In many organizations, work is done in teams. The emotional intelligence exhibited by team members is crucial to team performance. This emotional intelligence helps team members to unite and be effective in operations. They are able to work together most effectively and

bring better results to the organization as a whole. A team that does not show signs of emotional intelligence cannot operate successfully.

Team members have the opportunity to get to know each other before starting work, this is team building. In case of negative behavior, the cause should be identified and corrective action taken. Decisions must be made on the basis of the views of all team members. All members should be supported in their activities. If any problem arises, the focus should be on solving the problem, not troubleshooting [2]. Teambuilding is an ongoing process that assists the team. Not only do team members share their expectations for group assignments, they also trust and support each other and respect the personality and mindset of other individuals. The role of a Teambuilder is to lead the team towards cohesion. Empowering teams and employees allows people to make decisions about their work. Good team-building skills can bring employees together for a common goal and create greater productivity gains. Thus, it is the responsibility of the Teambuilder to ensure that all team members participate in the mission of the companies for which teambuilding is very important [15] [17] [41].

2.4 Generations

Today, there are six generation groups in the world, which are considered to be six distinctly different groups of people. We can say that these generations love something else, have a different lifestyle and have different qualities. This characterization is not entirely true as they share some common impulses, experiences, decades of living together, have same acquaintances, and group problems. They differ in a sense, that these problems were not experienced by them in the same way. Generation groups can also be differentiated in the workplace as their work is done in a different way. Before the 21st Century, there was a widening gap in the workplace between generations of active workers. The change is justified by the fact that industrial society has been gradually replaced by the information society and later by the knowledge society, which has completely redefined the way people communicate. The Internet has simplified the process of obtaining information, but it has changed the way people interact and generational conflicts have appeared, since the information society has created a virtual society. Newer generations have already acclimatized to this virtual society, so they move more confidently here than in reality. As a result of this impulse, however, older generations often feel excluded from the new world. The six generations are divided and demarcated as follows: Veteran generation 1925-1945, Baby Boom generation 1946-1964, X generation 1965-1979, Y generation 1980-1994, Z generation 1995-2010, Alpha generation after 2010. However, only the characteristics of the generations we are investigating are described below [4] [5] [16] [33] [40].

Members of the Baby Boom generation were already in a more relaxed socio-economic situation than their parents, but even more than their children. Work had a predetermined working time of when to start and finish. They were in good contact with their colleagues and talked to each other and therefore knew each other well. Their privacy was not ensnared by workplace expectations. The amount of work was determined. They knew the boss personally, had a possible or partial human contact with him, therefore was not just an unknown one. This is the last generation where hierarchy defined the principle of operation. Changes have begun with this age group. A consumer society has evolved, and Monday night slideshow watching has taken the place over family conversations. Technical devices, cars, TVs, washing machines, refrigerators have appeared. More and more things helped the baby boomers' lives, dropping into a world they were not prepared for. The world continued to expand, with television being broadcast daily and expanding with more channels. They wanted to meet the expectations of the West, so they rushed and worked more and more. And their children experienced that their parents were doing everything for them, but the price of that was that their parents were less at home. When they got home, they were anxious and full of doubts [16] [33] [35] [40].

Generation X is already part of the explosion of information technology. Its members were present when the computer took over the place of typewriters, but they still loved to write letters by hand and speak on the phone as in e-mail. They had less and less time for old chat meetings. Generation X worked a lot because it had to earn money incessantly, with the result that it rarely had fun. The majority of those in the workplace adapted to change and shaped their lives accordingly. The rush, the profit and loss accounts and the bonuses were strong constraints on their lives. As a result, the time spent on rest and relaxation decreased [35]. Anxiety became a part of their life and they had to deal with it constantly. There was no good-old honesty among the group of friends either. They were constantly in a hurry and rush, even on weekends, trying to bring in their back things and backlogs. Tired of falling in bed in the evenings, they got to the hamster wheel in which they spun more and more [36]. Based on these, we can say that the main motivation for this generation in their work was money and the salary. Their great mission was to create a stable existence, to create material negligence for their families and for themselves. Professional development was not one of their key goals, but those who wanted to progress, were usually pursuing a significant amount of overtime and doing extra work. Generation X is characterized by greater patience and work discipline than younger generations. They were able to shut down external factors and were able to handle many things at once. In their work, they relied on the intellectual knowledge they had acquired, unlike later generations, where Internet and IT played a greater role, and therefore did not feel the need to possess such profound information [5] [16] [32] [40].

Digitization was part of the life of Generation Y. They are the ones who had been most influenced by the achievements of the digital explosion and the Internet.

Children of this age group used sophisticated technologies such as computers, video games and video players. This did not seem to cause them any effort. When new technology arrived, their parents often turned to the children to teach them [34]. From a young age, social media and a constant online presence was part of their daily lives. Members of the age group acquired almost all information on the Internet. According to their slogan "what was not found here did not even exist". Generation Y is the biggest challenge for companies. They are motivated by money, success, career, but they are not characterized by loyalty, reliability, adaptability and obedience. If they have the opportunity, they look for new challenges and they do not hesitate to move on. This can be explained by the fact that they had to make decisions and perform tasks early. Today's consumer society shows that it is not talent by which someone should chose, but rather potential earnings. They are not emotionally attached to their workplace. This age group has not learned that work involves effort. Thus, the new digital generations are not fully aware how much work is needed to be done to be able to buy for example the digital devices in their hands. Generation Y still has ambitions and is willing to do it for them while Generation Z sits at home waiting for a miracle. This age group includes self-realization, belonging somewhere, fun and public events [4] [5] [16] [31] [33] [40].

The members of the generation Z are still college students, but tomorrow they are the new workforce. This is the only age group born into a technologically saturated world. This is a formally educated generation. Digital technology is present in every aspect of their lives, and they have learned to use it at a young age [20]. Generation Z doesn't have to learn how to handle digital devices because they already know that. For them, it is a basic training. They are the ones who are never alone, they can be online anytime and anywhere, and can talk about their thoughts, themselves and their emotions. They have two forms of identity: one is personal identity and the other is social identity. Their personal identity comes from attributes that made them unique, such as their personal characteristics, special interests, and favorite activities. In contrast, family members, friends, and neighbors contribute to their social identity [25]. The biggest difference in the age groups is that members of the Z generation become adults later, despite the fact that they are mentally more mature than their age. However, smart and intelligent they may seem, emotionally it is almost impossible for them to process violent or aggressive information. A major component of early maturity is the extent of aggression seen on screen. Young people today stay at home with their parents, start to work and set up their own family later. [4] [5] [33] [36].

3 Aims and Methodology

We decided to divide the respondents into four main groups based on generations: Baby Boom, Generation X, Generation Y and Generation Z. In addition, there are two generations, the Veteran and the Alpha, but these two generations have not been dealt with in the research because the "veterans" are likely no longer working, while members of the latter group are not yet working. We wanted to compare how the four different generational groups still living and working together change their views on the topic.

The questionnaire was prepared online and snowball method was used. It was filled in voluntarily and anonymously. Data were collected between December 29, 2018 and March 10, 2019. The questionnaire was completed by 204 respondents. We can say that the number of respondents in the four different groups became almost identical, which meant that the answers were easy to compare.

At the beginning of the questionnaire, we used introductory questions. The next set of questions was already regarding the main topic of emotional intelligence. First of all, we observed the communication link between the employer and the employee. Next, we analysed satisfaction with workplace activities and the importance of work appreciation, that is, verbal praise. We wanted to know the extent to which material assets, professional recognition, development opportunities and a good work environment matter. By completing a web-based (gyorseqtests.hu) emotional intelligence test, we were able to assess the mean value of the subjects' emotional intelligence. At the end of the questionnaire, we inquired about the respondents' demographic data.

During our research we set up 2 hypotheses:

Hypothesis 1: Relationship between age group and perception of emotional intelligence

H₀: There is no relationship between age group and perception of emotional intelligence.

H₁: There is a relationship between age group and perceptions of the importance of emotional intelligence.

Hypothesis 2: The level of emotional intelligence is influenced by age group

H₀: There is no relationship between age group and the level of emotional intelligence.

H₁: There is a relationship between age group and the level of emotional intelligence.

The responses received were aggregated using Microsoft Excel, and the SPSS statistical program was used to test our hypotheses.

4 Results

In this part of the paper, we present the results of a questionnaire research on emotional intelligence. In addition, issues related to emotional intelligence were divided into generational groups. Out of the 204 fillers, 61% are women and 39% are men. The fillers were divided into generation groups. This was important, because we wanted to compare how different generations perceive the role of emotional intelligence in the workplace. We used only four generations in the research, because they are currently active in the labor market. 24.5% of the respondents belong to the Baby Boom, 26% to the X, 25% to the Y and 24.5% to the Z Generation. We wanted to check how do these values relate to real labor market rates. According to the data [30] we can see that our results relate to real labor market rates.

Table 1

Real labor market rates – employees by age group and generations used in the study (2019/Q3) [30]

Generation	Age group	Number of employees (thousand)	Percent of employees of the total workforce
Z	15-24	139.8	5%
Y	25-34	607.3	23%
Y+X	35-44	752.9	29%
X	45-54	635.8	25%
Baby-boom + Veteran	55+	449.3	17%
	Slovakia	2585.1	100%

We also tested the highest level of education. For this question, five options were identified for the respondents. The rate of those with the highest level of education attained a primary school was 2%. They were the least. Secondary education (high school, vocational secondary school and vocational school) was the most marked (46%). The proportion of students still in tertiary education is 12%, while 35% with university degrees. Only 5% of the respondents indicated that they are postgraduate students.

In terms of occupational status, 2% of those who filled in said they were owners and 7% were self-employed. Another 8% work as managers, while most (80%) work as subordinates. The other option was marked by 3%. We also examined the size of the companies they work for. Micro-enterprises are of 38% (0-9 employees), 28% of small enterprises (10-49) and 34% of medium-sized enterprises (50-249). None of our fillers worked for a large company. The duration of the employment relationship was also examined. Only 14% of those who filled in said they had worked for the company for less than 1 year. 33% reported 1 to 5 years, and 13% reported 5 to 10 years. Most fillers (41%) had been with the same company for more than 10 years.

In our first hypothesis (Relationship between age group and perception of the importance of emotional intelligence), we made a cross-table. The age group was an ordinal (independent) variable, because we can arrange them in series. To assess the importance of emotional intelligence, however, we used a question in our questionnaire asking our respondents whether emotional or cognitive intelligence they consider more important. This variable is nominal and dependent. Based on our responses, we have obtained the following results.

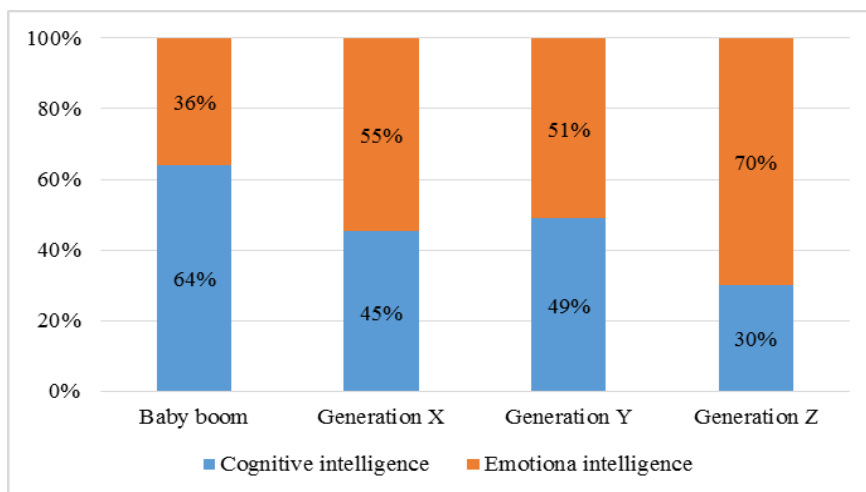


Figure 1

Which intelligence is more important? – By generations

Thus, according to the figure, cognitive intelligence is considered more important by the oldest generation examined, whereas the vast majority of younger ones marked the emotional one. However, in order to prove that our result was not merely a coincidence, we needed further investigation. For this, we performed a Pearson Chi-square test, the results of which are presented in the following table.

Table 2

Contains the result of the H1 testing

	Value	df	Asymp. Sig. (2-sided)
Pearson Chi-Square	11,746 ^a	3	,008
Likelihood Ratio	11,987	3	,007
Linear-by-Linear Association	9,575	1	,002
N of Valid Cases	204		

The degree of freedom in our case was 3, while the significance level was 95% (0.05). The Chi square value was 11.746, while the critical value for degree of freedom and significance of 0.05 was 7.815 according to the table. The empirical significance (P) is 0.008. Thus, overall, the Chi-square we measured is less than critical, and empirical significance is less than significance. Based on these results, we must reject the null hypothesis (no relationship between the two variables) and we have to accept the alternative hypothesis (the relationship between the two variables). Our first hypothesis – the relationship between age group and perception of the importance of emotional intelligence – can be considered as true.

We also made a cross-tabulation of our second hypothesis (the level of emotional intelligence is influenced by age group). The age group was an ordinal (independent) variable because we can arrange them in series. The magnitude of emotional intelligence was examined in 3 categories:

- Low – 0-25
- Medium – 26-50
- High – 51-75

This variable is also considered to be ordinal, but also dependent. Based on the answers of our respondents, we have obtained the following results.

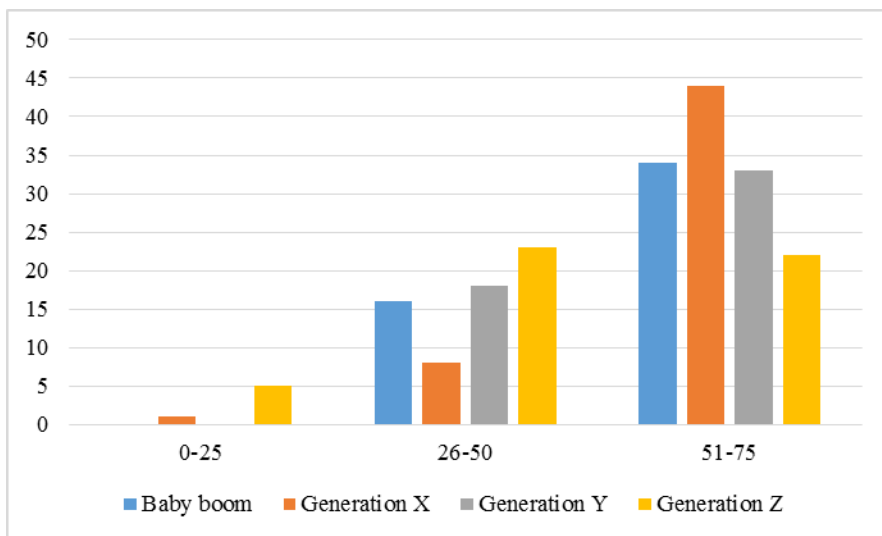


Figure 2
EQ score by generations

According to our results, individuals of Generation X have the highest level of emotional intelligence, while those of Generation Z have the lowest level of emotional intelligence. However, in order to prove that our result was not merely a

coincidence, we needed further investigation. This time we wanted to perform the Pearson Chi-square test, but according to the results of the SPSS program, more than 20% of the cells had values less than 5. In this sense, we cannot use the Pearson Chi-square test.

Table 3
Contains the result of the H2 testing

	Value	df	Asymp. Sig. (2-sided)
Pearson Chi-Square	25,734 ^a	6	,000
Likelihood Ratio	26,438	6	,000
Linear-by-Linear Association	12,046	1	,001
N of Valid Cases	204		

a. 4 cells (33,3%) have expected count less than 5. The minimum expected count is 1,47.

In this case, we need to look at the results of the likelihood ratio. Our significance remained at 0.05. The significance (P) value we have for the likelihood ratio is 0.000, which is less than the defined significance. In this case, we must reject the null hypothesis (no relationship between the two variables) and accept the alternative hypothesis (the relationship between the two variables). Our second hypothesis, according to which the level of emotional intelligence is influenced by age, can be considered as true.

Conclusions

In the first part of our article, we briefly introduced the theory of emotional intelligence. For this we used Hungarian, Slovak and English literature. Emotional intelligence can be found in everyday life such as social contacts. It affects human relationships and leadership activities. It is essential for recognizing, controlling and managing the emotions of ourselves and others. Our emotions affect our environment as they have a profound effect on our emotional development. Environmental influences can guarantee the development of emotional intelligence, for example, the mood in the workplace significantly determines the emotional intelligence of the manager or of subordinates. This intelligence plays an important role in the workplace as it plays a crucial role in communication and in situations that affect behavior and the way people are treated. The closest thing to emotional intelligence is empathy. This allows us to recognize the emotions of others and to be able to gauge their thinking and behavior. In this work we present two aspects of emotional intelligence, its presence in organizations and its measurement, which consists of 16 different steps. We went on to do more with leaders and coaching. In the last subchapter of the theoretical part, we mention the

6 generational groups, but in our paper we only dealt with 4 generations (Baby Boom, X, Y and Z), as their members are still active and Already in the job market. For the 4 generations, we have highlighted the most important traits in the workplace. In our research, we identified 2 main hypotheses that examined each generation for emotional intelligence.

Based on our results, both hypotheses were accepted, after confirming the appropriate statistical evidence. Our results indicate that there is a relationship between age group and perceptions of the importance of emotional intelligence, and that the level of emotional intelligence is actually influenced by age group. Furthermore, it has been found that although the youngest (Generation Z) consider emotional intelligence to be more important than cognitive, they still have lower emotional intelligence than their older (Baby Boom, Generation X and Y) counterparts.

Acknowledgement

This work was supported by the Collegium Talentum 2019/2020 Programme of Hungary.

References

- [1] C. Anyakoha: Job analysis as a tool for improved organizational performance of SMEs in Lagos, Nigeria. *Central European Journal of Labour Law and Personnel Management*, 2019, Vol. 2, No. 1, pp. 7-16, ISSN 2644-4542, DOI: 10.33382/cejllpm.2019.02.01
- [2] B. Arora: Importance of Emotional Intelligence In The Workplace. *International Journal of Engineering and Applied Sciences*, 2017, Vol. 4, Iss. 4, pp. 43-45, ISSN: 2394-3661
- [3] L. Balázs: *Emotional Intelligence*, Z-Press Publishing Ltd., 2014, ISBN 9789639493728
- [4] A. Bencsik, G. Horváth-Csikós, T. Juhász: Y and Z Generations at Workplaces. *Journal of Competitiveness*, 2016, Vol. 8, Iss. 3, pp. 90-106, ISSN 1804-1728, DOI: 10.7441/joc.2016.03.06
- [5] S. Berkup: Working with generations X and Y in generation Z period: Management of different generations in business life. *Mediterranean Journal of Social Sciences*, 2014, Vol. 5, No. 19, pp. 218-229, ISSN 2039-2117, DOI: 10.5901/mjss.2014.v5n19p218
- [6] K. Buvaneswari: A study of emotional intelligence and work related variables among business executive. *EPR International Journal of Economic and Business Review*, 2013, Vol. 1, Iss. 1, pp. 10-21, ISSN 2347-9671
- [7] Gy. Csapai, Sz. Berke: Emotional factors influencing managerial growth, In A. Csata *et al.* (ed.) 12th Annual International Conference on Economics

- and Business, Editura Risoprint, 2015, pp. 392-398, ISBN 978-973-53-1565-8
- [8] C. Ezigbo: Develop Emotional Intelligence as a MindTool for Leadership Effectiveness and Employee Career Development. *Research on Humanities and Social Sciences*, 2013, Vol. 3, No. 4, pp. 1-9, ISSN 2225-0484
- [9] D. Goleman: Working with Emotional Intelligence, Bantam, 2000, ISBN 978-0553378580
- [10] D. Goleman: Emotional Intelligence: Why It Can Matter More Than IQ, Bantam, 2005, ISBN 978-0553383713
- [11] D. Goleman, R. Boyatzis, A. McKee: Primal Leadership. Unleashing the Power of Emotional Intelligence, Harvard Business Review Press, 2013, ISBN 9781422168035
- [12] M. Hitka, S. Lorincová, L. Ližbetinová: Manager's data in human resource management from the perspective of the work position. *Acta Oeconomica Universitatis Selye*, 2017, Vol. 6, No. 2, pp. 69-80, ISSN 1338-6581
- [13] M. Hitka, S. Lorincova, G. P. Bartakova, L. Lizbetinova, P. Starchon, C. Li, E. Zaborova, T. Markova, J. Schmidtova, L. Mura: Strategic Tool of Human Resource Management for Operation of SMEs in the Wood-processing Industry. *Bioresources*, 2018, Vol. 13, No. 2, pp. 2759-2774, ISSN: 1930-2126
- [14] D. L. Joseph, D. A. Newman: Emotional intelligence: An integrative meta-analysis and cascading model, *Journal of Applied Psychology*, 2010, Vol. 95, No. 1, pp. 54-78, ISSN 0021-9010, DOI: 10.1037/a0017286
- [15] D. Kannaiah, R. Shanthi: A Study on Emotional Intelligence at Work Place. *European Journal of Business and Management*, 2018, Vol. 7, No. 24, pp. 147-154, ISSN 2222-2839
- [16] A. Kolnhofer-Derecskei, R. Zs. Reicher, Á. Szeghegyi: Transport Habits and Preferences of Generations — Does it Matter, Regarding the State of The Art? *Acta Polytechnica Hungarica*, 2019, Vol. 16, No. 1, pp. 29-44, ISSN 1785-8860, DOI: 10.12700/APH.16.1.2019.1.2
- [17] K. Lazanyi, M. Fulop: Why don't we trust others? *Acta Oeconomica Universitatis Selye*, 2017, Vol. 6, No. 1, pp. 61-70, ISSN 1338-6581
- [18] S. Lorincová: Human resource and corporate culture: Gender-based differences in the assessment. *Central European Journal of Labour Law and Personnel Management*, 2018, Vol. 1, No. 1, pp. 28-45, ISSN 2644-4542, DOI: 10.33382/cejllpm.2018.01.03
- [19] J. D. Mayer, R. D. Roberts, S. G. Barsade: Human Abilities: Emotional Intelligence, *Annual Review of Psychology*, 2008, Vol. 59, No. 1, pp. 507-536, ISSN 1545-2085, DOI:10.1146/annurev.psych.59.103006.093646

-
- [20] M. McCrindle: *The ABC of XYZ: Understanding the Global Generations*, Australia, McCrindle Research Pty Ltd, 2014, ISBN 978-1742230351
- [21] M. Minárová: *Managers in SMEs and their emotional abilities*. *Acta Oeconomica Universitatis Selye*, 2015, Vol. 4, No. 1, pp. 83-92, ISSN 1338-6581
- [22] L. Mura: *Current situation in Family Businesses. Managerial trends in the development of enterprises in globalization era*, 2017, pp. 178-185, ISBN 978-80-552-1739-0
- [23] L. Mura, A. Ključnikov, M. Tvaronavičiene, A. Androniceanu: *Development Trends in Human Resource Management in Small and Medium Enterprises in the Visegrad Group*. *Acta Polytechnica Hungarica*, 2017, Vol. 14, No. 7, pp. 105-122, ISSN 1785-8860, DOI: 10.12700/APH.14.7.2017.7.7
- [24] S. Neale, L. Spencer-Arnell, L. Wilson: *Emotional intelligence coaching*, Kogan Page, 2009, ISBN 978-0749463564
- [25] J. Palfrey, U. Gasser: *Born digital: Understanding the first generation or digital natives*, Basic Books, 2010, ISBN 978-0465018567
- [26] J. Poór: *Internationalization and Globalization in Human Resource Management*, CompLex Publishing, 2013, ISBN 9789632952871
- [27] S. Saini: *Emotional Intelligence at Workplace – A Conceptual Study*. In *International Journal of Management Studies*, 2018, Vol. 5, Iss. 3, pp. 53-56, ISSN 2231-2528, DOI: 10.18843/ijms/v5i3(5)/08
- [28] P. Salovey, J. D. Mayer: *Emotional Intelligence, Imagination, Cognition and Personality*, 1990, Vol. 9, No. 3, pp. 185-211, ISSN 0276-2366, DOI:10.2190/dugg-p24e-52wk-6cdg
- [29] N. S. Schutte, J. M. Malouff, L. E. Hall, D. J. Haggerty, J. T. Cooper, C. J. Golden, L. Dornheim: *Development and validation of a measure of emotional intelligence*, *Personality and Individual Differences*, 1998, Vol. 25, No. 2, pp. 167-177, ISSN 0191-8869, DOI: 10.1016/S0191-8869(98)00001-4
- [30] Slovstat: *Employees by age group*, Available on <http://datacube.statistics.sk/#!/view/sk/VBD_SK_WIN/pr3115qr/v_pr3115qr_00_00_00_sk>, [accessed 09.03.2020]
- [31] G. Statnickè, R. Jegelavičiūtè: *Influence of teaching methods on the self-leadership expression of the millenium generation students*. *Acta Oeconomica Universitatis Selye*, 2017, Vol. 6, No. 1, pp. 137-154, ISSN 1338-6581
- [32] A. Szabó, B. Kun., R. Urbán, Zs. Demetrovics: *Initial results on the domestic application of the wong and law emotional intelligence scale*

- (wleis-hu), *Mental Hygiene and Psychomatics*, 2011, Vol. 12, No. 1, pp. 1-15, ISSN 1419-8126, DOI: 10.1556/Mental.12.2011.1.1
- [33] G. Szabó-Szentgróti, M. Gelencsér, E. Szabó-Szentgróti, Sz. Berke: *Generational impact in workplace conflicts*, *Leadership science*, 2019, Vol. 50, No. 4, pp. 77-88, ISSN 0133-0179, DOI: 10.14267/VEZTUD.2019.04.08
- [34] D. Tapscott: *Grown up digital. How the net generation is changing your world*, McGraw-Hill, 2009, ISBN 978-0071508636
- [35] A. Tari: *Generation Y*, Jaffa Publishing Ltd., 2010, ISBN 9789639971202
- [36] A. Tari: *Generation Z*, Tericum Publishing Ltd., 2011, ISBN 9789639633926
- [37] M. Vágnerová: *Basics of psychology*, Karolinum, 2005, ISBN 978-80-246-0841-9
- [38] D. Vlacseková: *Comparative analysis of motivation of civil servants and public servants in the local state administration – case study of Slovakia*. In: *Central European Journal of Labour Law and Personnel Management*, 2019, Vol. 2, No. 1, pp. 74-93, ISSN 2644-4542, DOI: 10.33382/cejllpm.2019.02.06
- [39] J. Whitmore: *Coaching for Performance. The Principles and Practice of Coaching and Leadership*, Nicholas Brealey Publishing, 2017, ISBN 978-1473658127
- [40] R. Zemke, C. Raines, B. Filipczak: *Generations at Work: Managing the Clash of Veterans, Boomers, Xers and Nexters in Your Workplace*, Amacom, 2000, ISBN 978-0814404805
- [41] J. Žul'ová, M. Švec, A. Madleňák: *Personality aspects of the employee and their exploration from the GDPR perspective*. In: *Central European Journal of Labour Law and Personnel Management*, 2018, Vol. 1, No. 1, pp. 68-77, ISSN 2644-4542, DOI: 10.33382/cejllpm.2018.01.05